Optimization of Electromagnetic Follow up Observations and Localization of Gravitational Wave Signals from Compact Binary Coalescences

Man Leong Chan

Submitted in fulfillment of the requirements for the Degree of
Doctor of Philosophy

School of Physics and Astronomy
College of Science and Engineering
University of Glasgow

November 1, 2018

Abstract

Many gravitational wave sources will produce electromagnetic signals as they emit gravitational waves. An important example is binary neutron star mergers. The joint observations and discoveries of the electromagnetic signatures of these gravitational wave sources can produce substantial scientific benefits in physics, astrophysics and cosmology. To maximize the scientific outcomes of such gravitational events as much as possible, the detections of their electromagnetic signatures are necessary. The first detection of the inspiral signals from binary neutron stars by LIGO and VIRGO, and the observations of the associated electromagnetic counterparts throughout the electromagnetic spectrum have served an excellent example. These detections and discoveries have also ushered in a new era of both gravitational wave astronomy and multi-messenger astronomy.

However, using gravitational wave interferometric detectors, the sky location estimates of the gravitational wave signals from binary neutron star can span a few hundreds square degrees, unless there are three or more detectors observing the event simultaneously. The large sky localization error poses a challenge for astronomers scanning the localization error to look for the electromagnetic signals of these gravitational wave events. The electromagnetic counterparts may also not be readily detectable depending on the distance and orientation of the sources, which presents further difficulties in detecting their signals.

To alleviate the situation, we develop an algorithm to maximize the detection probability of the electromagnetic counterparts of gravitational wave events. The algorithm we develop is able to generate an observing strategy that optimizes the probability of successful electromagnetic follow-up observations given limited observational resources. This is achieved by using a greedy algorithm for tiling the sky location error and Lagrange multiplier for assigning observation times to observation fields. The analysis with the algorithm also allows an estimate of the detection probability. In Chapter 3, we present a proof-of-concept demonstration of this algorithm to four telescopes Subaru-HyperSuprimeCam, CTIO-Dark Energy Camera, Palomar Transient Factory and Pan-Starrs, for three different simulated binary neutron star events, assuming kilonova to be the target electromagnetic counterpart. By applying the algorithm to telescopes with arbitrary field of view and sensitivity within a range, we provide an insight into the potential of future telescopes and other telescopes not directly included in our analysis. Moreover, the algorithm is applied to the design of a space based mission, the Einstein Probe, to find the optimal combination of the size of field of view and the sensitivity.

The localization of gravitational wave sources, which is determined both by the gravitational wave signals and the detectors, is an important factor to the success of electromagnetic follow-up observations. We investigate the localization of binary

neutron star mergers detected with the Einstein Telescope and Cosmic Explorer. Compared to the existing detectors, the improvement in the sensitivity of the Einstein Telescope and Cosmic Explorer in the low frequency band has many important implications. One of them is the considerable increase in the length of the in-band duration of the signals from binary neutron stars, which is useful in localizing the sources. In Chapter 4, using a Fisher matrix approach, we estimate the sky localization error of binary neutron stars as a population and distributed at various distances. As the extended in-band duration of signals also increases the possibility of identifying and releasing the presence of a signal prior to merger, known as early warning, we investigate the prospect for early warning of binary neutron star merger events with these detectors.

While the Einstein Telescope and Cosmic Explorer hold promising future for gravitational wave astronomy, they are not likely to be operative until the 2030s. In the literature, detectors designed with more advanced technologies than LIGO and VIRGO are proposed to fill the gap in time. We estimate the localization of binary black holes with two such detectors in Australia and China and seconds generation detectors such as LIGO, LIGO India, VIRGO and KAGRA.

In chapter 5, we study electromagnetic observations of binary neutron star mergers with the Large Synoptic Survey Telescope. The Large Synoptic Survey Telescope is a telescope designed with large size of field of view and excellent sensitivity in its observing bands. Such a telescope provides a promising prospect for multimessenger astronomy with gravitational waves. With its sensitivity and field of view, the telescope is expected to enable electromagnetic follow-up observations with shorter exposure time and fewer observation fields than many existing telescopes. We define a simple procedure for electromagnetic follow-up observations triggered by gravitational waves using the telescope. Taking advantages of the Fisher matrix approach in Chapter 4 for the sky location estimates, we quantify the observation time necessary for the telescope to perform electromagnetic follow-up observation of binary neutron star mergers detected with different networks of gravitational wave detectors.

Contents

List of Figures

List of Tables

Acknowledgements

I would like to thank my supervisor Prof. Ik Siong Heng, Dr. Chris Messenger and Prof. Martin Hendry. They are excellent mentors from whom I have learned a lot both in science and many other aspects of life. I count myself lucky for having had their mentorships and I am forever indebted for their guidance, help and support throughout my Ph.D. study.

I am also grateful to Prof. Graham Woan and Dr. Yiming Hu for the help and support I received from them during my Ph.D. study. I would like to express my sincere gratitude to Daniel Williams, Dr. Matthew Pitkin, Dr. David Keitel and Dr. Jamie Scott. I have benefited a lot from their expertise and knowledge on many technical problems that I had.

I would like to thank the rest of the Glasgow IGR group, especially Brynley Pearlstone, Joe Bayley, Hunter Gabbard, Rachel Gray, Fergus Hayes, Laurence Datrier, Dr. John Veitch, Dr. Natalia Korsakova, Sheena Barclay, Mark Fletcher, Marc Aftalion, Alastair Doye, Hafizah Isa, Andreas Noack, Dr. Raymond Robie, Andrew Spencer, Simon Tait, Karl Toland, Zeno Tornasi, Peter Wakeford, Jennifer Wright and former IGR member Dr. Jade Powell. I have had many meaningful discussions with them that have inspired ideas in me.

From the LIGO and Virgo collaborations I wish to express my sincere gratitude to Prof. YenBei Chen, Dr. Eric Howell, Prof. David Blair, Dr. Michael Coughlin and Dr. Xilong Fan for their help and support with my research. I am also thankful to SFC for funding my thesis and the Scottish University Physics Alliance.

Last but not least, I am grateful to my family, especially Chan Wai Keng, Chan Fong Chai, Chan Sio Pan, Chan Ngok Cheng, Laurent Faton and Chan Wei Man. I am tremendously grateful to my encouraging parents, who have continuously been supportive of me, and my beloved wife, Ku Tim Tai, who is always patient with me and has always been the source of my motivations, while I was pursuing my own aspirations. Without them, this thesis would have not been possible.

Declaration

I, Man Leong Chan (also known as Mervyn Chan), confirm that the work in this thesis is my own work.

In Chapter 1, I present a background on gravitational wave astronomy with references given for informations and figures from other sources or when it is appropriate.

Chapter 2 is a background of multimessenger astronomy with binary neutron stars and an introduction to the electromagnetic follow-up observation campaign for GW170817. Appropriate references have been given to figures and information that are from other sources.

In Chapter 3, the work presented was carried out with Dr. Yiming Hu, Dr. Chris Messenger, Prof. Ik Siong Heng, and Prof. Martin Hendry. Most of this work is published in the Astrophysical Journal [1]. The algorithm developed has also been included as an component in a Python toolkit developed by Coughlin, M. W. et al and has been published in [2]. The work on the Einstein Probe in this Chapter is the result of collaboration with Prof. Ik Siong Heng. It is an application of the developed algorithm based on the information on the Einstein Probe publicly available and via private communication with Dr. Weimin Yuan.

In Chapter 4, the work presented from Section 4.1 to Section 4.3 was carried out with Dr. Chris Messenger, Prof. Ik Siong Heng and Prof. Martin Hendry. We have also benefited substantially from the discussions we had with Prof. Chen Yen Bei and Dr. Xilong and their valuable insights. The work is published in Physical Review D [3]. The work presented in Section 4.4 is the result of collaboration with Dr. Chris Messenger, Prof. Ik Siong Heng and Prof. Martin Hendry, Dr. Eric Howell, and Prof. David Blair. The work presented in this thesis is my own work and is part of the work in a paper published in MNRAS [4].

The work in Chapter 5 is the result of collaboration with Dr. Chris Messenger, Prof. Ik Siong Heng and Prof. Martin Hendry. The summary presented in Chapter 6 is my own.

Chapter 1

Introduction to Gravitational Wave Astronomy

1.1 Gravitational wave astronomy

In 1915, Albert Einstein published the General Theory of Relativity (GR) [5]. In GR, the presence of masses determines the curvature of space-time, and the curvature of space-time determines the motion of masses. The curvature of space-time is represented by the tensor $G_{\mu\nu}$ and governed by the stress energy tensor $T_{\mu\nu}$. These two tensors have the following relationship,

$$T_{\mu\nu} = \frac{c^4}{8\pi G} G_{\mu\nu}, \tag{1.1}$$

where G is the gravitational constant, c the speed of light, and μ and ν indicate the position of tensor elements in a tensor. When an axis-asymmetric mass with quadrupole moment accelerates, ripples in space-time propagating outward at the speed of light will be generated. These ripples are known as gravitational waves (GWs). For an observer at a large distance, the curvature of space-time can be linearized and locally described by the metric tensor $g_{\mu\nu}$, given by

$$g_{\mu\nu} = \eta_{\mu\nu} + h_{\mu\nu}, \tag{1.2}$$

where $\eta_{\mu\nu}$ is the Minkowski metric describing a flat space-time in which energy is absent. It is defined as

$$\eta_{\mu\nu} = \begin{pmatrix} -1 & 0 & 0 & 0 \\ 0 & 1 & 0 & 0 \\ 0 & 0 & 1 & 0 \\ 0 & 0 & 0 & 1 \end{pmatrix}. \tag{1.3}$$

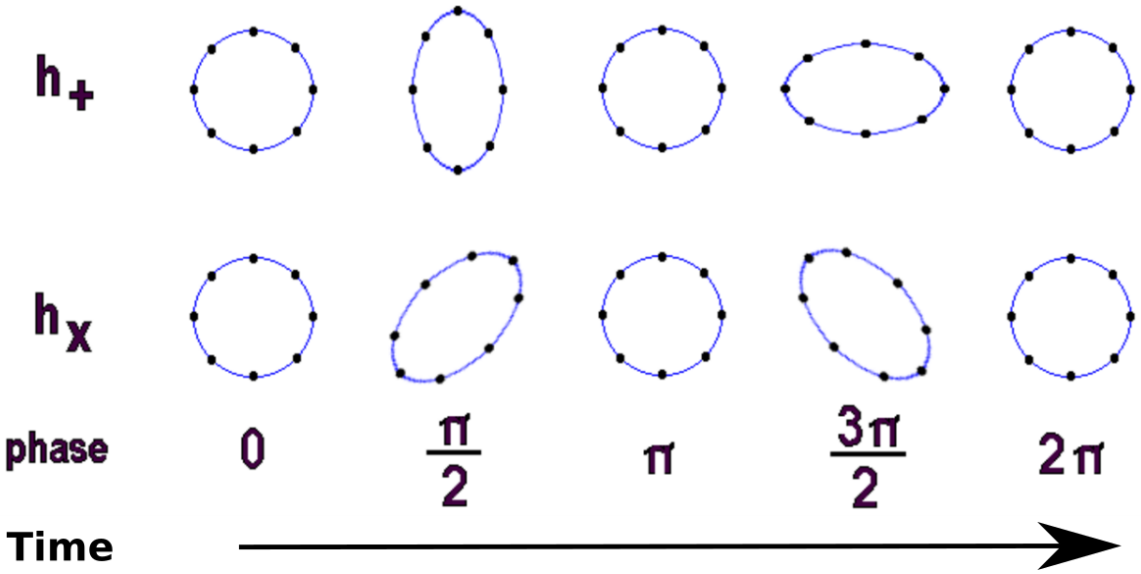

Figure 1.1: An illustration of the effect a linearly polarized GW on the distance between test masses. The upper row shows the effect of h_+, and the lower the effect of $h_\times$. The black dots arranged in a ring represent free falling test masses. As a GW moves into the page, the space will be stretched and squeezed. Reproduced from [9].

$h_{\mu\nu}$ describes a small deviation from the flat metric $\eta_{\mu\nu}$. Using the transverse traceless gauge [6, 7, 8], $h_{\mu\nu}$ can be written as

$$h_{\mu\nu} = \begin{pmatrix} 0 & 0 & 0 & 0 \\ 0 & h_+ & h_\times & 0 \\ 0 & h_\times & -h_+ & 0 \\ 0 & 0 & 0 & 0 \end{pmatrix}, \tag{1.4}$$

where h_+ and $h_\times$ are two GW polarization states. The effects these two polarization states on free falling test masses are visualized in Figure 1.1. The amplitude of an observed GW is characterized by the fractional change ΔL in the distance L between two test masses when the GW passes, given by

$$h = \frac{\Delta L}{L}. \tag{1.5}$$

Hulse and Taylor made the first indirect detection of GWs from the binary pulsar PSR1913-16 [10]. The orbital evolution of the binary system has been recorded over a course of more than 30 years [11]. Figure 1.2 plots the shrinkage in the period compared to the values predicted up to 2005 by GR. This orbital evolution could not be entirely explained via energy loss due to electromagnetic (EM) emission. By taking energy dissipation through GWs, however, the observed values and the predicted values have been very consistent and only deviated by 0.2% [11].

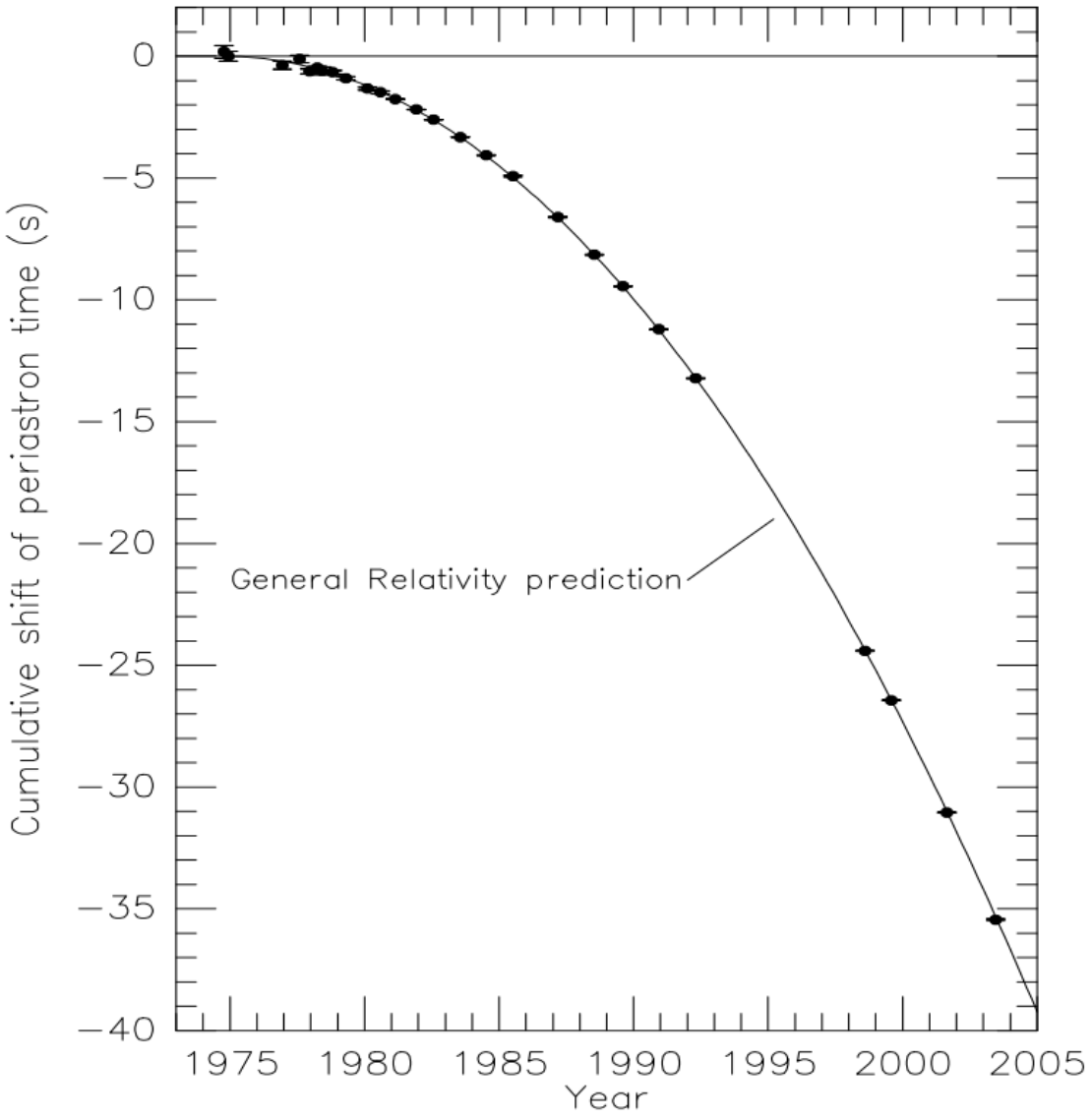

Figure 1.2: The orbital evolution of the binary system PSR B1913+16. The dots are the data obtained from observation. The curve is the values predicted by GR. Reproduced from [11].

GWs provide complementary information to observations in the EM spectrum. First, GWs are direct probe of large-scale regions of their origins as GWs are produced by the entire masses and momentum of an accelerating system with quadrupole moment. Moreover, GWs interact very weakly with matter. This allows GWs to travel through space unhindered and carry information about their astrophysical origins and even the earliest stage of the Universe that is otherwise inaccessible. Given that in the Universe, only $\sim 4\%$ masses are baryonic, and the rest are matter or energy that do not emit electromagnetically, GW is expected to be a probe that will allow us to directly study the larger part of the Universe and to make serendipitous discoveries that are currently unknown to us [7].

1.2 Sources of gravitational waves

According to GR, accelerating axis-asymmetric object with quadrupole moment would generate GWs as it moves. However, unlike EM radiation, where positive and negative charges generates EM dipoles, the lack of negative charge of mass and the conservation of momentum prevents gravitational radiation via dipole moment of mass distribution. The first order moment of mass distribution that is allowed to generate GWs is quadrupole [7, 12]. GWs observed on the earth is expected to be weak. For example, it is estimated that two masses of 10^3kg each rotating about an axis at a rate of 10 times per second will generate GWs with amplitude $h \sim 5 \times 10^{-43}$ if all the velocity is non-spherical [7]. As a result, GWs that originate from massive celestial objects can possibly be detectable. In this section, possible detectable sources of GWs will be discussed.

1.2.1 Continuous waves

Continuous waves are expected to be emitted by spinning neutron star (NS). Remnants from stars as massive as up to $\sim$ 2 $M_\odot$[1] may form NS [13]. In order for a NS to emit GW, the NS has to have an axi-asymmetry. This axi-asymmetry can be idealized to be deformation of, or a bump on the surface. An axi-asymmetrical NS will emit GW at the frequency twice that of its rotation frequency. The amplitude can be expressed as [7],

$$h \sim \frac{4}{5}(2\pi R f)^2 \frac{\epsilon M}{r}, \tag{1.6}$$

where ϵ is fractional ellipticity, f the frequency of the spin of the NS, R the radius, M the mass of the NS and r the distance. A typical NS has mass of 1.4 $M_\odot$ and radius of 10km.

One possible source of this type is the Crab pulsar, whose observed short spindown time would require a large value of ϵ [7], although it is generally believed that ϵ larger

[1] $M_\odot$: solar mass

than 10^{-6} is not supported [14]. The amplitude of a GW from the Crab pulsar will be very weak (e.g. $\mathcal{O}(10^{-25})$ or lower) [15, 16]. This maybe observable to ground-based detectors only if the observation time is long enough. Successful observation of continuous GWs will help determine or constrain the equation of state of NS and understand NS glitches [17]. There is currently no detected continuous GW. But the non-detection of such GW has produced upper limits for the emission and thus ϵ [18, 15, 19].

1.2.2 Binary systems

Systems of two compact objects (i.e. white dwarf (WD), NS, or black hole (BH)) orbiting around their common mass center are binary systems. Binary systems consisting of NS and/or BH are also known as compact binary coalescences (CBCs) and are a detectable source to ground-based detectors such as Laser Interferometric Gravitational Wave Observatory (LIGO) and Virgo at their respective design sensitivities (i.e. Advanced LIGO (aLIGO) and Advanced Virgo (AdVirgo)).

A typical GW emitted by a CBC can be divided into three characteristic phases. The first phase is called inspiral. During this stage, the orbital motions of the two bodies will cause the binary to lose energy, which will be carried away by GWs. The loss of energy will then cause the orbit to shrink. At this stage, for system of equal masses, the frequency of the GW signal is determined by the masses of the binary and the distance between the two bodies [20]. As the two bodies move closer, the frequency and the amplitude of the GW emitted will slowly increase. During inspiral, NS and BH can be assumed to be point masses, so this phase will end when the system reaches the last stable orbit, after which stable orbits cannot be supported [20, 21]. This happens when the frequency of the GW emitted by the system is $\simeq 4400(\mathrm{M}_\odot/M)\mathrm{Hz}$, where M is the total mass of the binary [7]. The remaining time before the system enters the next phase is given by [22]

$$\tau_\mathrm{c} = \frac{5}{256}\frac{c^5}{G^{\frac{5}{3}}}\frac{(\pi f_\mathrm{s})^{-\frac{8}{3}}}{\mathcal{M}^{\frac{5}{3}}}, \tag{1.7}$$

where τ_c is the time to merger for a compact binary system, c the speed of light, G the gravitational constant, and f_s the starting frequency considered for the GW. $\mathcal{M}$ is the chirp mass and is defined as,

$$\mathcal{M} = \frac{(m_1 m_2)^{\frac{3}{5}}}{(m_1 + m_2)^{\frac{1}{5}}}. \tag{1.8}$$

The masses of the two components of the binary are denoted as m_1 and m_2 in the above equation. Figure 1.3 shows the time to merger for $1.4\mathrm{M}_\odot - 1.4\mathrm{M}_\odot$ as a function of f_s. For comparison, $10\mathrm{M}_\odot - 10\mathrm{M}_\odot$ and $30\mathrm{M}_\odot - 30\mathrm{M}_\odot$ binary black hole (BBH) are also plotted. The waveform of this phase is well understood and modeled using

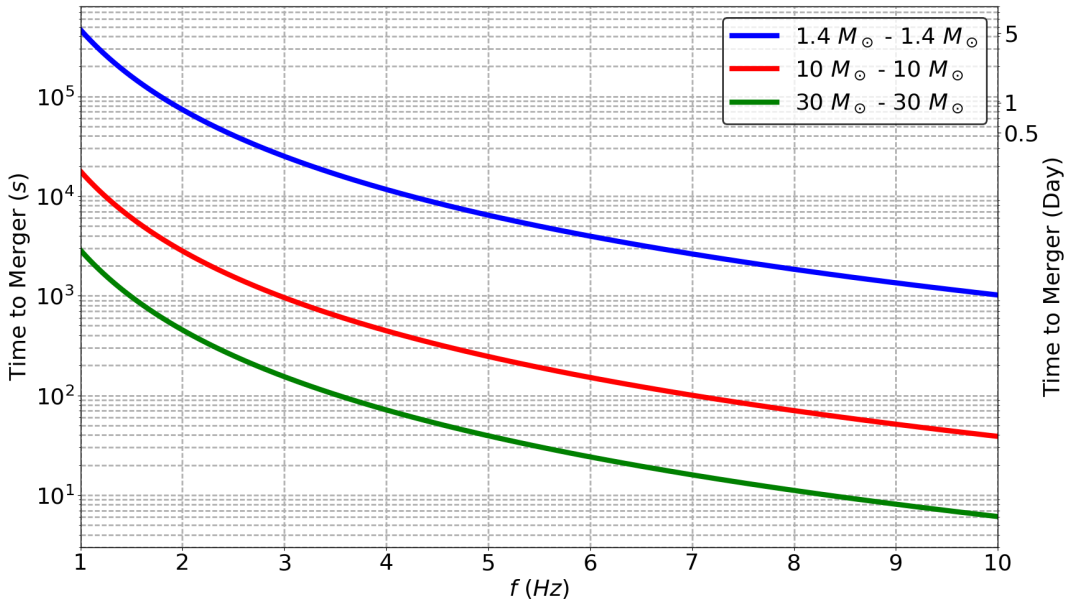

Figure 1.3: The time to merger as a function of starting frequency f_s for $1.4M_\odot - 1.4M_\odot$ BNS (blue), $10M_\odot - 10M_\odot$ BBH (red) and $30M_\odot - 30M_\odot$ BBH (green).

post-Newtonian approximations. The amplitude of a GW from a CBC in a circular orbit is given by [7],

$$h \sim \frac{1}{r}\mathcal{M}^{\frac{5}{3}}\Omega^{\frac{2}{3}}, \tag{1.9}$$

where Ω is the orbital angular velocity. The system will then enter the next phase known as merger, where the two bodies are so close that they collide into each other. This stage is highly relativistic and involves strong gravity, possibly tidal deformation and disruption effect [21]. The computation of the exact waveform of this phase requires numerical simulations [23, 24]. After the binary has merged together and a new NS or BH is formed, a signal called ringdown will be emitted [25, 26]. The ringdown waveform can be constructed by combining perturbative calculations in GR with numerical relativity waveforms [27, 28, 29, 30, 31, 32, 33, 34]. It can also be obtained by applying the Effective One Body formalism [23, 35] . An example GW signal from BBH is shown in Figure 1.4.

BNS and BBH are considered examples of the primary sources of GW for ground-based interferometric detectors for the reasons that the amplitudes of their signals are strong enough to be detectable and that a portion of their signals fall within the detectable frequency range of the detectors. There are currently 5 detections of BBH merger and 1 detection of BNS. The detections of these GW events will be discussed more in Section 1.5.

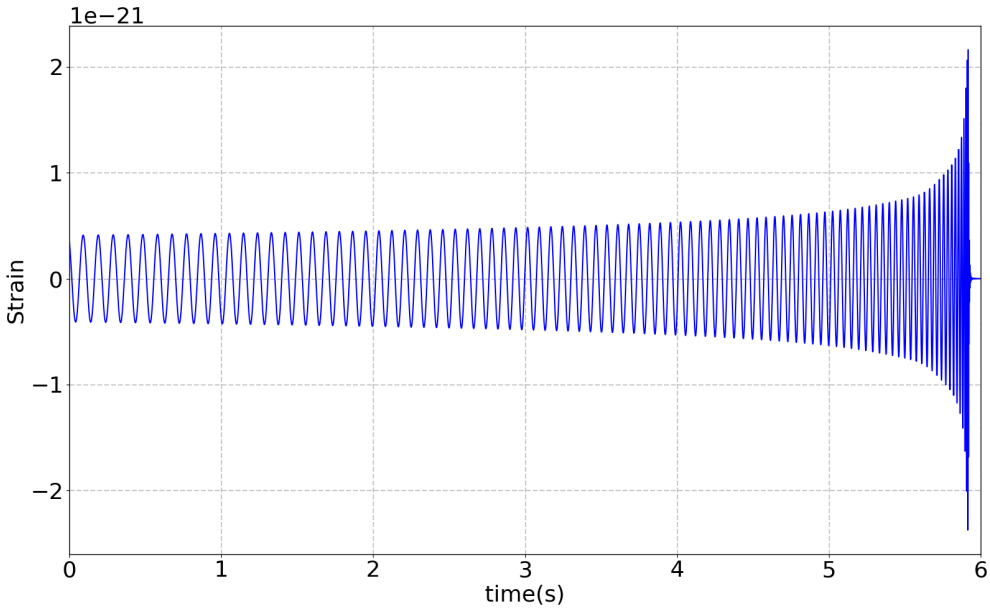

Figure 1.4: An example waveform of the GW signal from a $30M_{\odot}-30M_{\odot}$ BBH merger at 400Mpc. The plotted signal starts at 10Hz and lasts for $\sim$ 6s. This waveform is produced using lalsimilation IMRPhenomB (lalsimulation is a package in python for general purpose routines for gravitational waveforms and noise generation [36]).

1.2.3 Bursts

Burst GWs usually refer to transient GW signals that are complex and not well modeled. Unlike well modeled GWs, such as inspiraling signals of CBC, matched filtering cannot be used to search for burst signals due to the lack of knowledge of their exact waveforms as matched filtering is a technique that requires the pre-calculation of a bank of waveforms (see Section 1.6.1). Sources that fall into this category include BH or NS mergers with high mass ratios or eccentricity [37] and core collapse supernovae (CCSNe) [38].

Stars with masses more than $\sim 9M_{\odot}$ are expected to collapse to form supernova due to the loss of gravitational potential during the collapse [39] and generate detectable GWs for ground-based interferometric detectors [40, 41]. GWs from galactic supernovae are rare events and are predicted to occur at a rate of one per 30 - 100 years [42, 43]). CCSNe are considered promising sources of multimessenger astronomy as they will emit electromagnetically and gravitationally. The physical processes that happens in a supernova and the exact mechanism that drive the supernova to explode are still not completely understood. GWs are produced from inside the core, and are therefore likely to convey direct information crucial to the understanding of the explosion mechanism of CCSNe.

There are multiple models for the explosion mechanism of CCSNe such as neutrino-

driven mechanism, thermonuclear mechanism and magnetorotational mechanism [44]. With different assumptions of the physics inside the cores of CCSNe, a number of different catalogs in the literature [45, 46, 47, 48, 49, 50, 51] contain predicted waveforms that significantly alter in the strain amplitude, signal morphology and duration of the GWs from CCSNe. For example, the amplitude and duration of a GW from neutrino-driven CCSN can be up to orders of magnitudes different from that from rotating core-collapse CCSN. Therefore, detecting and classifying GWs from CCSNe would be necessary to the determination of the explosion mechanism. In the literatures, principle component analysis has been applied to CCSN waveform in an attempt to identify the explosion mechanism of CCSNe [52, 53].

1.2.4 Stochastic background

Stochastic background GWs of astrophysical origin can arise due to a superposition of GWs from sources such as isolated core-collapse NSs, WDs or a population of CBCs. These GW sources are so weak that they cannot be distinguished amongst the background created by the entire population. The detections of these signals would provide information on the physical properties of the source populations, and the history of star formation [54].

Stochastic background GWs of cosmological origin is expected to be generated in the very early stage of the Universe after gravitons decoupled from the primordial plasma. The observations of these GWs will provide information on the physics at energy higher than could be achieved on earth and may provide direct information about the birth of the Universe [7]. Stochastic background of cosmological origin is currently the only known probe that allows us to probe the very early stage of the Universe (10^{-30}s after the Big Bang) [7, 21].

Both astrophysical and cosmological stochastic background are expected to be very weak GWs (the estimate rate of CBC after the observations of GW150914 and GW151226 suggests that astrophysical stochastic background may be louder than previous expectation [55]), but could be detectable to space-based GW detector such as the Laser Interferometer Space Antenna (LISA) (a brief introduction of LISA will be given in Section 1.3.5). Search for stochastic background GWs in aLIGO sensitive frequency range also produces constrain and upper limit on the dimensionless energy density of these GWs in this frequency range [55].

1.3 Gravitational wave detectors

Experiments looking for GW signals were pioneered by Joseph Weber when he first attempted to directly detect GWs with his bar antennae in the 1960s [56, 57]. Over the years, new methods and design of GW detectors have been developed and proposed to increase the bandwidth and sensitivity of GW detectors. In this section, we will briefly discuss the detectors.

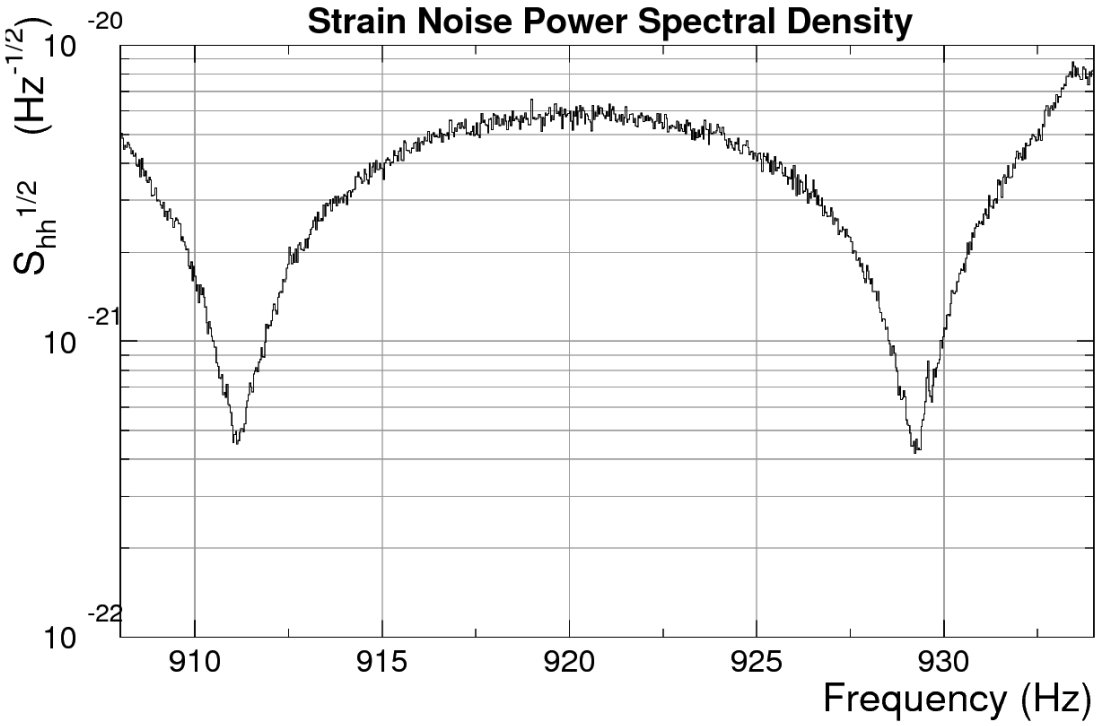

Figure 1.5: The ASD of Auriga. Reproduced from [64].

1.3.1 Bar antenna

The first GW detectors were bar antennae built by Joseph Weber in the 1960s [56]. The bar antennae were cylinders made of aluminum 1.5 meter long and 0.66 meter in diameter. A bar detector of length L will stretch and squeeze causing a change ΔL in the length of the bar when a GW of amplitude h passes if the frequency of the GW is at or close to the resonant frequency of the bar. The amplitude h of the GW is then given by Eq. 1.5.

In the 1970s, Weber claimed that he had detected GWs from CCSNe [58], and subsequently he claimed regular detections of GWs from the center of the milky way galaxy [59]. Although no other experiment was able to repeat the detection [60, 61], more advanced technologies have been applied to the building of bar detectors over the years. These include building more massive bars and operating the detector in a cryogenic or ultra-cryogenic temperature. There are still two groups operating bar detectors: the Roma group and the Auriga group [62, 63]. These detectors operate at ultra-cryogenic temperature ($T = 100$ mk). In general, bar detectors are very narrow band instrument and have difficulty to achieve the sensitivity required to detect GW. Figure 1.5 shows the amplitude spectral density (ASD) of Auriga as an example. It can be seen that only two narrow bands have reached the sensitivity of $\mathcal{O}(10^{-21})$.

1.3.2 Interferometric detectors

In 1962, the idea of using laser interferometry to observe GWs was outlined by Michael Gertsenshtein and Vladislav Pustovoit in Russia [65]. This was later independently proposed by many including Weiss [66]. Existing GW detectors that are based on laser interferometry include aLIGO, AdVirgo, GEO600 and the Japanese Kamioka Gravitational wave detector (KAGRA).

LIGO is comprised of two detectors built in Hanford and Livingston in the USA [67]. The construction of LIGO started in 1995 [68]. Multiple upgrades were designed from the beginning to improve the sensitivity of the two detectors. LIGO with the initial design sensitivity known as initial LIGO (iLIGO) began operation in the 2002 [69]. After the completion of Science Run 5, the LIGO detectors were upgraded to an enhanced version known as Enhanced LIGO, with the first Enhanced LIGO run Science Run 6 starting in 2009. The laser power of Enhanced LIGO was increased from 10W to 35W. Enhanced LIGO was two times as sensitive asiLIGO. One year later, Enhanced LIGO underwent further major upgrades associated with aLIGO, which is 10 times more sensitive than Enhanced LIGO [70]. This was soon followed by a 3km interferometer in Europe known as VIRGO [71, 72]. The construction of VIRGO began in 1996 and its first and second Science Run started in 2007 and 2009 respectively [73]. VIRGO was upgraded to AdVirgo in 2015, and performed a joint observing run with aLIGO in August 2017 [74]. GEO600 is a British and German collaborative GW detector located in Hannover with 600m arm length [75, 76]. The construction of it started in 1995 with its first science run in 2002. KAGRA refers to the Japanese interferometric GW detectors located underground in the Kamioka Mine with 3km arm length [77]. This project began in the 1990s and is based on the success of a 300m interferometer located at the Mitaka campus of the National Astronomical Observatory of Japan known as TAMA 300 [78]. Detectors such as aLIGO, AdVirgo, KAGRA and GEO600 are known as second generation (2G) detectors.

Since like aLIGO, many 2G prototype interferometers and the existing interferometric GW detectors except GEO600 utilize a kind of resonant optical cavities known as the Fabry-Perot cavity (explained below) as interferometer arms [79, 80, 81, 82, 83], the optical layout of aLIGO is shown in Figure 1.6 as an example of the configuration of an interferometer. A beam of laser light is split into two beams by the beam splitter and travel along the two 4-km-long arms. The two 4-km-long arms are actually Fabry-Perot cavities, which allows the light in an interferometer to reflect between the input test mass and the end test mass in each arm back and forth [82]. One of the purposes of implementing Fabry-Perot cavities as arms is to improve the sensitivity by increasing the round trip of the laser light beam in an interferometer. After being reflected by the test masses, the beams will be recombined and interfere to form an interference pattern. When an incoming strain of a GW signal passes the two arms of a detector, depending on the polarization angle of the wave, the length of the two arms of an interferometric detector will stretch and squeeze. The change in length is

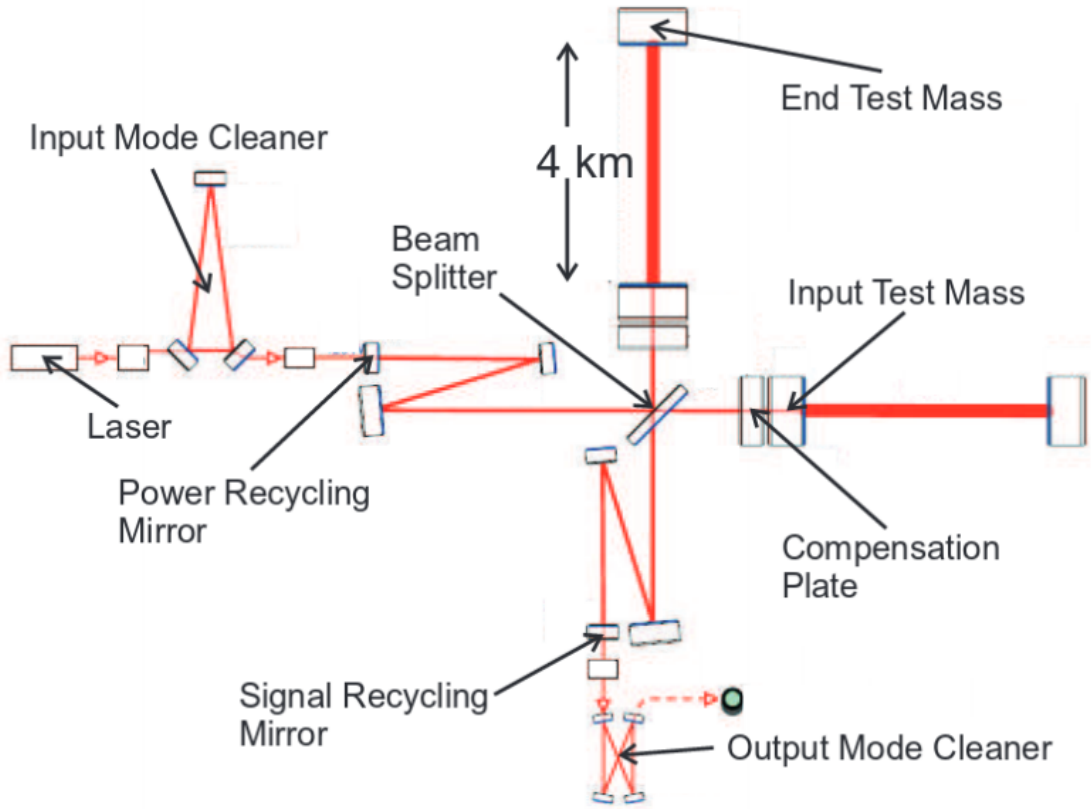

Figure 1.6: The optical layout of aLIGO. The laser beam from the laser will travel through the input mode cleaner before its split by the beam splitter and becomes two beams. The beams will then enter the two Fabry-Perot cavities separated by the input and end test masses and reflect between the input and end test masses back and forth. The beams will then be recombined to form an interference pattern. The passage of an incoming GW, given a proper polarization angle, will create a shift in the phase, which will be reflected in the interference pattern. Reproduced from [70].

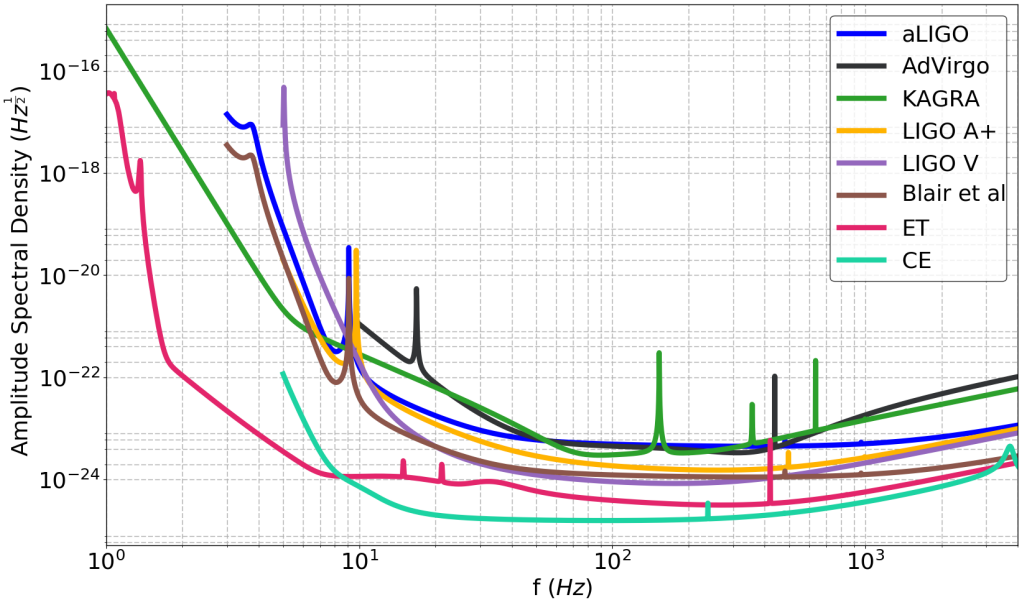

Figure 1.7: The ASD for aLIGO (Hanford, Livingston, India) (Blue), AdVirgo (Black), KAGRA (Green), LIGO A+ (Yellow), LIGO Voyager (Purple), Blair et al (Brown), ET (Cherry) and CE (Light green), aLIGO and AdVirgo are at their respective design sensitivities.

measured by laser light as the strain of the incoming wave and can be expressed as,

$$h = \frac{2\Delta L}{L}, \tag{1.10}$$

where ΔL is the change in the arms's length due to the passage of the GW and L the length of the arms. The change in length will result in a change of the interference pattern of the two laser beams. From Eq. 1.10, it can be seen that given a GW strain, the change in the arms' length ΔL will be larger if the length of the arms is longer. Therefore, in addition to increasing the round trip, another way by which the sensitivity of an interferometer can be increased is extending the arms' length. The design sensitivities of aLIGO, AdVirgo and KAGRA are shown as a blue, a black, and a green line respectively in Figure 1.7 (other lines shown in the plot will be explained later). To show the difference in sensitivities between detectors, Figure 1.8 plots the ratio of the sensitivity of detectors to the design sensitivity of aLIGO.

Interferometric detectors are essentially sensitive to the entire sky with a few blind spots. The sensitivity in every different direction in the sky (i.e. the antenna pattern) is given by

$$\begin{aligned} F_+ &= \tfrac{1}{2}(1+\cos^2\theta)\cos 2\phi\cos 2\psi - \cos\theta\sin 2\phi\sin\psi \\ F_\times &= \tfrac{1}{2}(1+\cos^2\theta)\cos 2\phi\sin 2\psi + \cos\theta\sin 2\phi\cos\psi, \end{aligned} \tag{1.11}$$

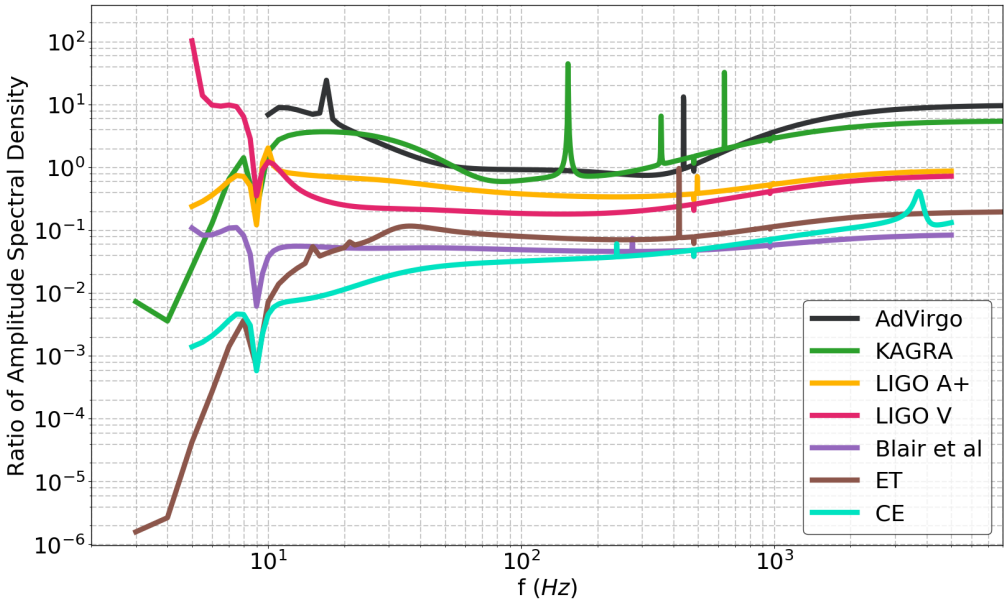

Figure 1.8: The ratio of the ASD of one detector to that of aLIGO at its design sensitivity to show the difference in ASD between detectors. AdVirgo (Black), KAGRA (Green), LIGO A+ (Yellow), LIGO Voyager (Cherry), Blair et al (Purple), ET (Brown) and CE (Light green).

where F_+ and $F_\times$ are the antenna pattern functions for the two polarizations. The equations assume that the interferometric detector is at the center of a spherical coordinate system, and θ and ϕ are the azimuthal angle and polar angle of the source respectively, and ψ is the GW polarization angle. An example is given in Figure 1.9. The measured GW strain is given by therefore

$$h = F_+(\theta, \phi, \psi)h_+ + F_\times(\theta, \phi, \psi)h_\times, \tag{1.12}$$

where h_+ and $h_\times$ are the two polarization states defined in Section 1.1.

1.3.3 Future detectors

To push the sensitivity of the LIGO detectors further, upgrade plans for aLIGO such as A+ and Voyager have been proposed [84]. A+ is considered to be a minor upgrade for aLIGO that targets quantum noise and coating thermal noise. The installation began in around 2017-2018. This upgrade includes the implementation of several technologies such as frequency dependent squeeze [85] and more advanced mirror coatings, and detector components such as heavier test masses, replacement of suspensions and larger laser beam size. The goal of this upgrade is to extend BNS inspiral signal range 1.7 times further than that for aLIGO at its design sensitivity.

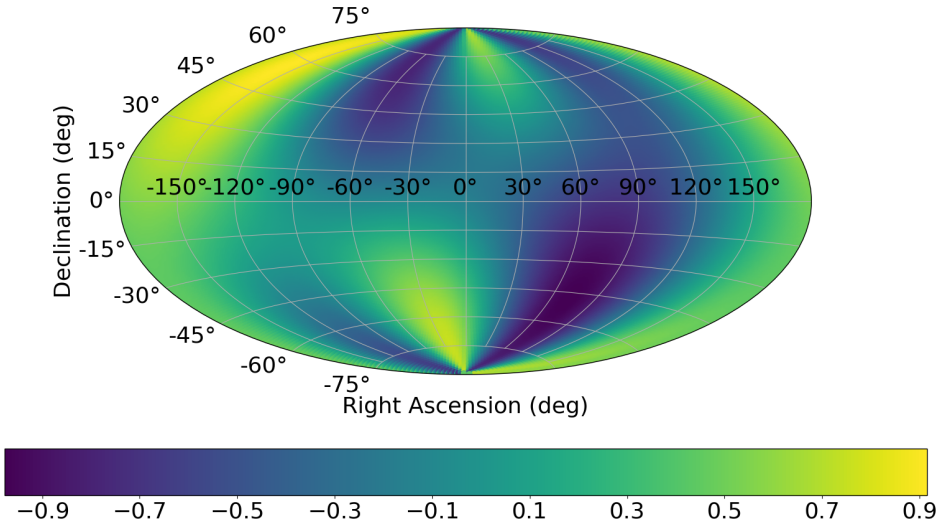

(a)

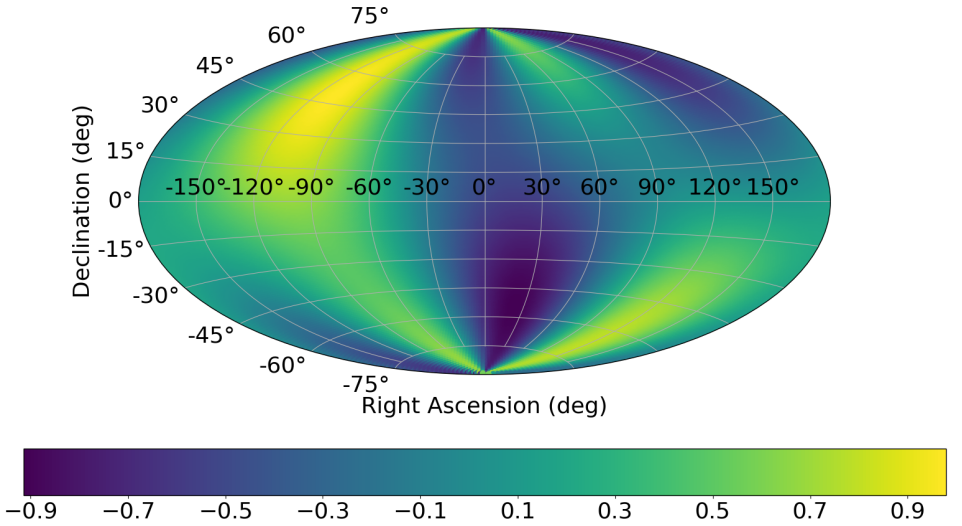

(b)

Figure 1.9: The antenna pattern of aLIGO as an example. Panel a and b show F_+ and $F_\times$ at $\psi = \pi/8$ respectively.

Compared to A+, Voyager is proposed to be a more major upgrade for aLIGO that aims to reduce the limiting noise of aLIGO beyond A+. Voyager is the last upgrade scheme for LIGO, and may involve operating the detector at cryogenic temperature [86, 87]. The aim is to extend BNS range further by a factor of 3. The simulation and experimentation for LIGO Voyager are currently underway with the goal of LIGO Voyager being operative in $>$ 2025. The design sensitivities of LIGO A+ and LIGO Voyager are represented as a yellow and a purple line respectively in Figure 1.7. The comparison of the ASDs of these detectors with aLIGO is shown in Figure 1.8.

In addition to the two exiting LIGO detectors in Hanford and Livingston, project of building a third LIGO detector in India has been approved by the India government [88]. This detector should begin operation and join the existing international network by 2025 [88]. Such a location should bring improvement in sky localization of detected GW signals by a factor of ~ 3 [89].

As we will discuss in the next section (Section 1.3.4), there are also proposals and designs for building detectors with sensitivity ~ 10 times better than the advanced detectors. These detectors are known as third generation (3G) detectors. However, it is expected that 3G detectors will not be operational until at least the 2030s [84]. To bridge the gap in time between 2G and 3G detectors, Blair et al proposed building two detectors in China and Australia [90]. These detectors are designed with more advanced technologies than 2G detectors such as test mass of 80kg and with arms 8km long. Modeling shows that these detectors can be ~ 4 times as sensitive as aLIGO. The design sensitivity of such a detector is shown in Figure 1.7. The comparison between the sensitivity of a Blair et al detector and the design sensitivity of aLIGO is shown in Figure 1.8.

1.3.4 Third Generation Detectors

Although 2G detectors such as aLIGO and AdVirgo have achieved the sensitivity necessary to detect GWs and plans for upgrade have been proposed (see Section 1.3.3), improving the sensitivity throughout the frequency band relevant to ground-based GW detectors even further is still desirable and has practical implications.

Sensitivity improvement in the most sensitive frequency band of 2G detectors (a few tens Hz to a few hundreds Hz) should effectively increase the signal-to-noise ratio (SNR) of a CBC event, which should in turn improve the estimate of sky localization and some of the system parameters (it is possible, however, for some other parameters that SNR alone is not an accurate indicator of the amount of information that can be extracted from the observation since different parameters can have different spectral dependence). Moreover, events with high SNRs (i.e. SNR $>$ 50) are required for the tests of strong field gravity [91, 92, 93]. Study such as that of individual cores of NSs or the quasi-normal modes of BH is usually only possible with events of SNR larger than 50 [94, 95, 96, 97]. Better sensitivity also enables observations of GWs and measurements of the cosmological parameters via GWs beyond the horizon of

aLIGO and AdVirgo.

On the other hand, improvement in the low frequency band of 1Hz - 10Hz is also important. As seen in Figure 1.3, CBC systems spend a huge amount of time at low frequencies, improvement in this frequency band will considerably extend the in-band duration of their signals from the order of seconds/minutes to the order of hours/days depending on the masses and distances of the systems. The in-band duration of a GW from a given compact binary system in a detector can be obtained by replacing the starting frequency f_s with the low frequency cut-off of the detector in Eq. 1.7. Such a long duration helps with the estimation of the parameters of, and the localization of the GW source (see Chapter 4 for localization of BNS mergers). For example, for a BNS merger observed with aLIGO, integrating signal from 10Hz instead of 20Hz improves the measurement accuracy of the masses of the system by a factor of 2, while doing so may only increase 1% of the SNR [94].

Additionally, a detector sensitive enough to observe GW in 1Hz - 10Hz can open a window to GWs at this frequency range. One example would be intermediate mass black hole (IMBH), of which the existence has yet to be corroborated through observations [95, 98]. As discussed in Section 1.2.2, the frequency of the GW signals emitted by a compact binary is increasing until it reaches the last stable orbit when the frequency is $\simeq 4400(\mathrm{M}_\odot/M)$Hz. For IMBHs with $10^2\mathrm{M}_\odot$ - $10^4\mathrm{M}_\odot$, this occurs at $\sim$ 1Hz - $\sim$ 10Hz.

Two proposed 3G detectors, i.e. the ET and CE are currently in their design and development stages [84, 94]. The current design of the ET employs the ET-D geometrical configuration as discussed in [94]. As shown in Figure 1.10, the detector will consist of 3 individual interferometers. The opening angle of each interferometer is 60° and they will be placed in such a formation that they form an equilateral triangle. This triangular shape design was considered to be the optimal strategy to achieve the sensitivity goal [100] and allows the ET to solve the polarization states of an incoming GW. For the ET, gravitational gradient noise and seismic noise (see Section 1.4 for a brief discussion of the noise sources) will be suppressed by building the detector underground with arms 10km [101]. Cryogenic technologies and the use of new material for suspension fibers will also be introduced to mitigate thermal and coating noise [101]. Mirrors as heavy as 120 kg will be used to reduce radiation pressure. The input power of laser in the interferometers will also be increased to 500 Watts. In addition, the ET will employ a design known as the xylophone configuration, in which each of the ET's interferometric detectors will be complemented by another interferometer that is optimized for low frequency [102, 103]. The design sensitivity for the ET is shown in Figure 1.7 and its comparison with the design sensitivity of aLIGO in Figure 1.8. However, it needs pointing out that the sensitivity curve shown in Figure 1.7 actually refers to a single interferometer with the xylophone design, and arms of 10 km and opening angle of 90°. The noise curve for an interferometer in a triangular ET would be equal to the curve shifted up by approximately 15% [102].

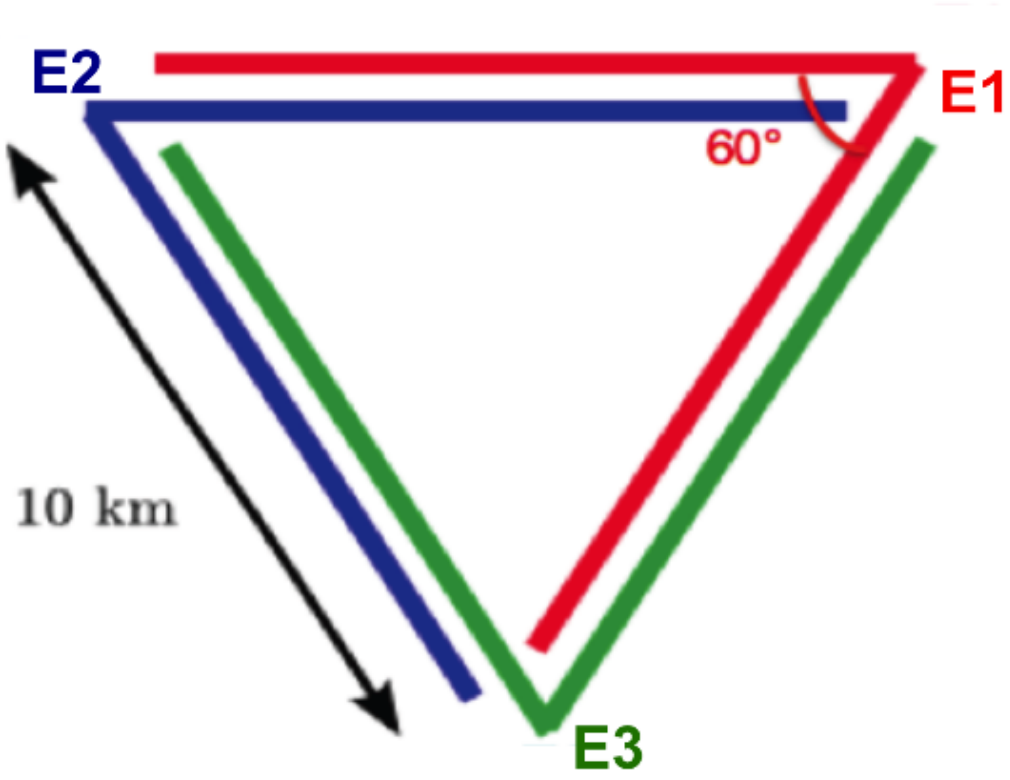

Figure 1.10: The geometrical configuration of ET-D proposed for ET. ET will be consisted of three individual V-shaped interferometers with 10km long arms (red, blue and green). The opening angle of each interferometer is 60° and each interferometer is rotated by 120° relative to each other forming an equilateral triangle. Reproduced from [99].

The antenna pattern functions of the ET can be expressed as [99]

$$\begin{aligned} F^1_+(\theta,\phi,\psi) = & -\tfrac{\sqrt{3}}{4}[(1+\cos^2\theta)\sin 2\phi\cos 2\psi \\ & +2\cos\theta\cos 2\phi\sin 2\psi], \\ F^1_\times(\theta,\phi,\psi) = & \tfrac{\sqrt{3}}{4}[(1+\cos^2\theta)\sin 2\phi\sin 2\psi \\ & -2\cos\theta\cos 2\phi\cos 2\psi], \\ F^2_{+,\times}(\theta,\phi,\psi) = & F^1_{+,\times}(\theta,\phi+\tfrac{2\pi}{3},\psi), \\ F^3_{+,\times}(\theta,\phi,\psi) = & F^1_{+,\times}(\theta,\phi-\tfrac{2\pi}{3},\psi), \end{aligned} \tag{1.13}$$

similar to Eq. 1.11, the above equations assume that the detector is at the center of a spherical coordinate system, where θ and ϕ are the azimuthal angle and polar angle of the source respectively, and ψ is the GW polarization angle. The superscripts $k = (1, 2, 3)$ indicate the k^{th} interferometer. The antenna pattern functions of each interferometer of the ET's is identical to an interferometer with 90° opening angle but 75% the arm length .

The current design of CE is similar to a 2G detector with arms extended to 40km and more advanced technologies [84]. The presented sensitivity curve of CE (displayed in Figure 1.7, see Figure 1.8 for the comparison between CE, and aLIGO at its design sensitivity) is obtained with existing technologies and well defined extrapolations from them as a means to compute a lower limit [84]. As CE will be built with the most advanced technologies available at the time for the final design stage, the sensitivity curve computed should not be considered the design target of CE [84]. The antenna pattern of CE can be computed using Eq. 1.11. CE is expected to be operational after $\sim$ 2035. Compared to 2G detectors, the sensitivities of 3G detectors in the relevant frequency range are better by a factor of 10 - 30, and even more for frequency $\leq$ 10Hz (see Figures 1.7 and 1.8).

1.3.5 The Laser Interferometer Space Antenna

LISA is a European Space Agency and NASA mission, which aims to build a space-based interferometric detector that is scheduled to be launched in 2034 [104]. As illustrated in Figure 1.11, LISA consists of three separate spacecrafts, oriented in such a way that they form an equilateral triangle with 2.5×10^6 km long sides. Each spacecraft contains two test masses. LISA will be sensitive to GWs in the frequency range from 10^{-4}Hz to 10^{-1}Hz [104]. The design sensitivity of LISA is shown in Figure 1.12. Being sensitive to this frequency band will open up a new window in astronomy as this frequency range is below the frequency range observable with ground-based detectors. For example, GWs created by the entire population of WD binaries in the milky way and binaries of super-massive BHs in the universe are expected to be observable to LISA. It is also possible that LISA will observe stochastic background GW created in the very early stage of the Universe (i.e., cosmological stochastic background) [107, 108]. In 2015, an European Space Agency spacecraft known as

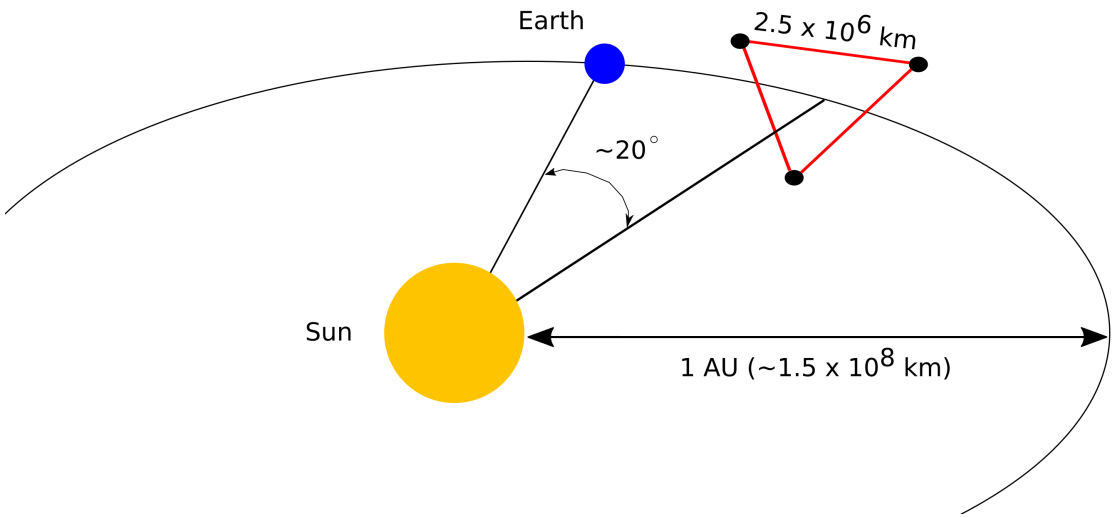

Figure 1.11: The configuration of LISA and its position relative to the Sun and the Earth. Reproduced from [105]. This figure is not to scale.

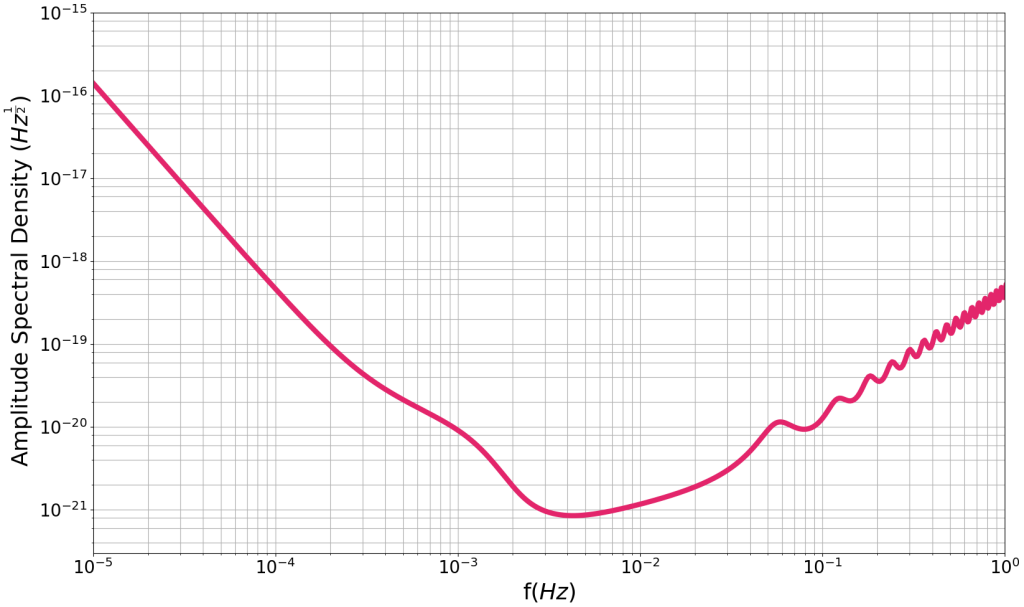

Figure 1.12: The design sensitivity of LISA [106].

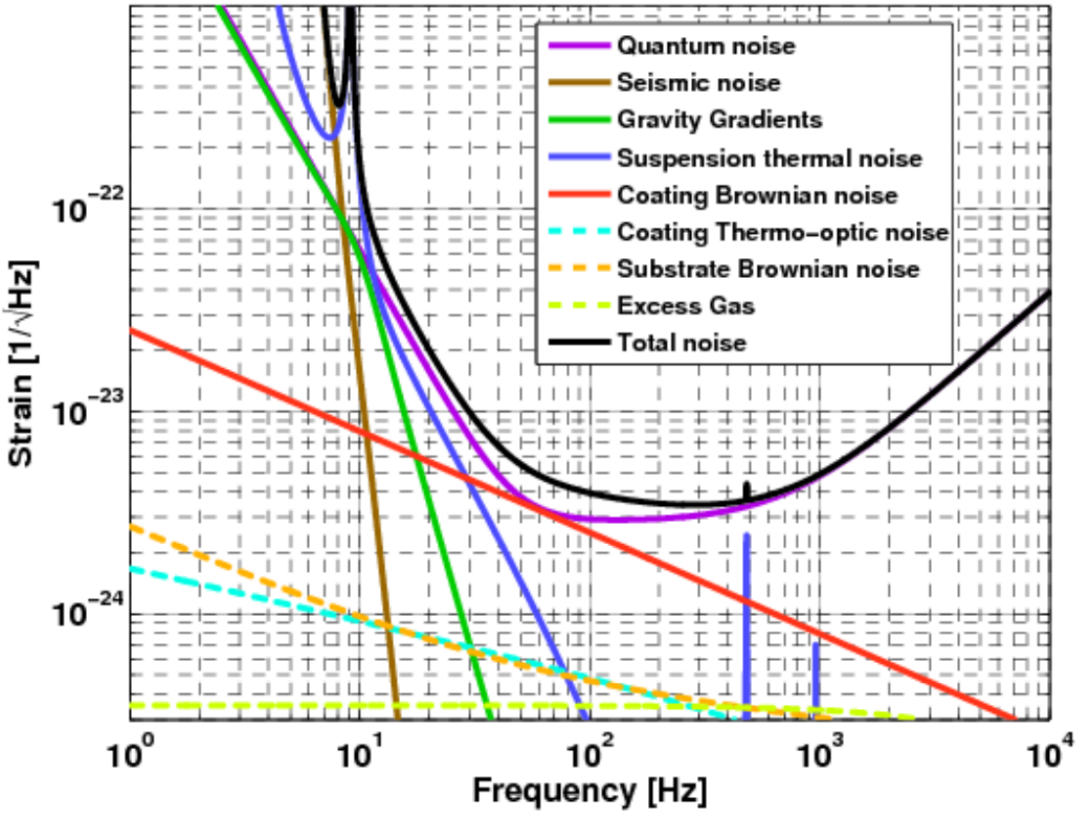

Figure 1.13: The sources of noise in the frequency band from 1Hz to 10Hz and their contributions to the noise budget in aLIGO.

LISA Pathfinder was launched to test the technologies needed for the LISA mission and has demonstrated that the LISA mission is viable [109, 110].

1.4 Noise Source

In an interferometric detector, a number of different noise sources limit the sensitivity of the detector in different frequency bands [111], so the performance of an interferometric detector can be characterized by the ASD of its noise background. As an example, the sources of noise and their contributions to the total noise expected in aLIGO at its design sensitivity is shown in Figure 1.13. This section will discuss the factors that limit the sensitivity of an interferometer. Successful detection of GWs demands the understanding and characterization of these noise sources.

1.4.1 Gravitational gradient noise

For frequency $\leq$ 20Hz, gravitational gradient noise is a contributor of noise [112, 113]. Gravitational gradient noise is the noised produced by time-changing Newtonian gravitational forces acting on the test masses of an interferometric detector due to fluctuations in the local gravitational field [114]. It is shown as a green line in Figure 1.13. The causes of this noise include seismic waves (i.e. Rayleigh waves), oceanic dynamics and ground water movements, human activity, the passage of clouds above or objects hitting the interferometer building and changes of atmospheric mass density [115, 113, 116].

Gravitational gradient noise causes perturbations of the test masses in interferometers and is difficult to be shielded against and isolated from. In fact, noise of gravitational gradient prevents experiments looking for GW signals at frequencies $<$ 1Hz to be carried out on earth [108]. To avoid noise of this type as much as possible, site selection for interferometric detectors has to take into account seismic stability. For example, to minimize gravitational gradient noise, KAGRA is built in an underground location. The current design of the ET also proposes the use of an underground location for reducing gravitational gradient noise [94]. It is suggested that Rayleigh waves is reduced exponentially with underground depth by $e^{\frac{-4d}{\lambda}}$, where d denotes the depth of the underground location and λ the wavelength of seismic wave[115]. Also, operating the detector in space will isolate the detector from seismic gravitational gradient noise, e.g., LISA [105].

In addition to site selection, techniques to mitigate gradient noise such as monitoring and subtracting local gravitational field fluctuations in real time are currently being developed [102, 115]. For such a technique to be effective, it is necessary to place an array of seismometers around the detector that measure the seismic motion. The effect of gravitational gradients on the test masses is then to be modeled and then subtracted from the detector output signals.

1.4.2 Seismic noise

The coupling of the motion of the ground in the surrounding area with an interferometer will also introduce motion of the test masses, which would then result in noise in the interferometer. For frequency between 1 - 10Hz, human activity and wind are the contributors to seismic noise. For example, the passage of trains could cause the loss of $\sim$ 40 min of data acquisition time each day at iLIGO Livingston [117]. In addition, oceanic waves are known to produce seismic noise below 1Hz [113, 118]. A location on Earth can have seismic noise at the level of $\sim 10^{-7} f^{-2} \mathrm{m/Hz}^{\frac{1}{2}}$ even if the location is considered to have relatively low seismic noise [119]. For the detection of a GW with strain $\sim 10^{-21}$ at $\sim$ 100Hz, a reduction of seismic noise by $\sim$ 8 orders of magnitude is required. To suppress seismic noise, suspension of the test masses is implemented [108, 120, 121, 122, 123]. In addition, systems that actively attenuate and mitigate

motion of the test masses are in place. For example, aLIGO uses sensors to monitor and register movement in the suspension system and to counteract movements that are detected [124]. Seismic noise for aLIGO at the design sensitivity is represented as a brown line in Figure 1.13.

1.4.3 Thermal noise

Noise is also produced by the thermally driven motion of molecules within the suspensions and the coatings of the test masses and the test masses themselves. This noise is dominant in the frequency band from $\sim$ 10Hz to $\sim$ 100Hz (shown as blue, red, cyan and orange lines in Figure 1.13). The magnitude of such noise is determined by the heat-flow damping, mechanical energy dissipation of the material and components [125]. To keep thermal noise as low as possible, it is preferable to use low mechanical loss materials for test masses, suspensions and mirror coatings. The term mechanical loss refers to the property of a material that determines the energy storage characteristics around resonant frequencies. Interferometers use fused silica as a material with intrinsically low mechanical loss to reduce thermal noise [126, 127].

1.4.4 Quantum noise

Quantum noise is a primary factor limiting the strain sensitivity of a ground-based interferometer detector for frequency above 10Hz. it actually comprises of two independent noises, i.e., radiation pressure noise and photon shot noise. The trade-off between these two noises form a fundamental limit in the sensitivity based on Heisenberg uncertainty principle [128]

Radiation pressure noise is associated with radiation pressure, which is created from the transfer of the momentum of the photons of the laser light in an interferometer to the test masses after hitting the test masses. One possible origin of the radiation pressure noise is the statistical uncertainty in the number of photons of the laser beam in each arm after being split by the beam splitter. Since each photon in the original beam is scattered independently, there will be a binomial distribution of the number of the photons N in each arm that is anti-correlated [129]. This results in a statistical fluctuation $\propto \sqrt{N}$ from the radiation pressure.

The statistical variation in the photoelectric current at the output port of an interferometer is the reason responsible for the presence of photon shot noise. The statistical variation 0in the photoelectric current is caused by the fluctuation in the number of incident photons in a detected photocurrent, which is assumed to follow a Poisson distribution with $\sqrt{N}$ uncertainty, where N is the number of incident of photons per unit observation time [129]. Lowering shot noise is achieved by increasing the power of the laser beam or the observation time [129, 21].

However, increasing laser power also means increasing the pressure of photons hitting the mirrors at the end of the arms and thus increases radiation pressure noise.

Table 1.1: Masses and distances of detected BBH mergers

Event	MassM$_\odot$			Distance(Mpc)
	Primary mass	Secondary mass	End Product	
GW150914	$36.0^{+5.0}_{-4.0}$	$29.0^{+4.0}_{-4.0}$	$62.0^{+4.0}_{-4.0}$	410^{+160}_{-180}
GW151226	$14.2^{+8.3}_{-3.7}$	$7.5^{+2.3}_{-2.3}$	$20.8^{+6.1}_{-1.7}$	440^{+180}_{-190}
GW170104	$31.2^{+8.4}_{-6.0}$	$19.4^{+5.3}_{-5.9}$	$50.7^{+5.9}_{-5.0}$	880^{+450}_{-390}
GW170608	12.0^{+7}_{-2}	$7.0^{+2.0}_{-2.0}$	$19.0^{+5.0}_{-1.0}$	340^{+140}_{-140}
GW170814	$30.5^{+5.7}_{-3.0}$	$25.3^{+2.8}_{-4.2}$	$55.9^{+3.4}_{-2.7}$	540^{+130}_{-210}

The masses of the bodies in the detected BBH mergers and that of the end product, as well as their distances. All quoted numbers are at 90% confidence interval from [130, 131, 132, 133, 134].

As such, there is a fundamental limit to the reduction of the combination of this noise. For an operating frequency of an interferometer, there will be optimistic power of laser beam minimizing these radiation pressure noise and shot noise. This limit of sensitivity is called the Standard Quantum Limit, which stems from the Heisenberg uncertainty principle [108]. A purple line representing quantum noise is displayed in Figure 1.13.

1.5 Detected gravitational waves

In September 2015, the two interferometric detectors of LIGO made the first direct detection of GWs. The observed signal of the GWs, referred to as GW150914, swept in the frequencies from 35Hz to 250Hz and is consistent with the waveform for inspiral, merger and ringdown predicted by GR [130]. The GWs were inferred to come from the merger of two BHs with $\sim 36M_\odot$ and $\sim 29M_\odot$ at $\sim$ 410Mpc. The result of the merger formed a BH with $\sim 62M_\odot$. This indicates that $\sim 3M_\odot$ equivalent energy was carried away by GWs. This strain data of this event observed at the two aLIGO detectors is shown in Figure 1.14. Also shown in the figure is a time-frequency representation of the strain data. The EM follow-up observation of this event will be discussed in Chapter 2. For all the detected BBH mergers, the masses of the bodies of are given in Table 1.1,

Three months later in December, the two LIGO detectors made the second detection, referred to as GW151226 [131]. The signal was from two smaller BHs, and the final product was of smaller BH (see Table 1.1). The signal was observed in the two LIGO detectors for $\sim$ 1s, with $\sim$ 55 cycles sweeping in the frequencies from 35Hz to 450 Hz. It is also inferred that at least one BH had a spin larger than 0.2.

During LIGO's second observing run, three more observations of GWs from BBHs were made. These GWs were designated to be GW170104, GW170608 and GW170814

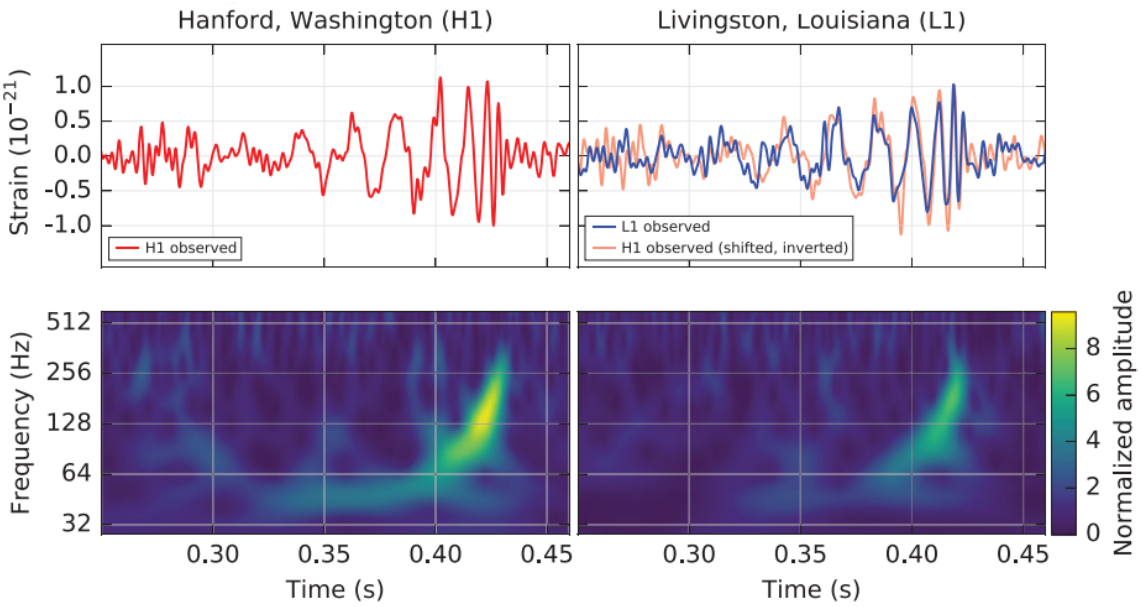

Figure 1.14: The GW signals of GW150914. The top left panel shows the strain of GW150914 observed at aLIGO Hanford. The top right panel shows that observed at aLIGO Livingston (blue). For visual comparison, the strain observed at Hanford is also presented in light orange in the top right panel. To account for the difference between the arrival times at the detectors, the strain observed at Hanford is shifted by ~ 6.9ms. It is also inverted to account for the detectors' relative orientations. The bottom row shows a time-frequency representation of the strain data. Reproduced from [130].

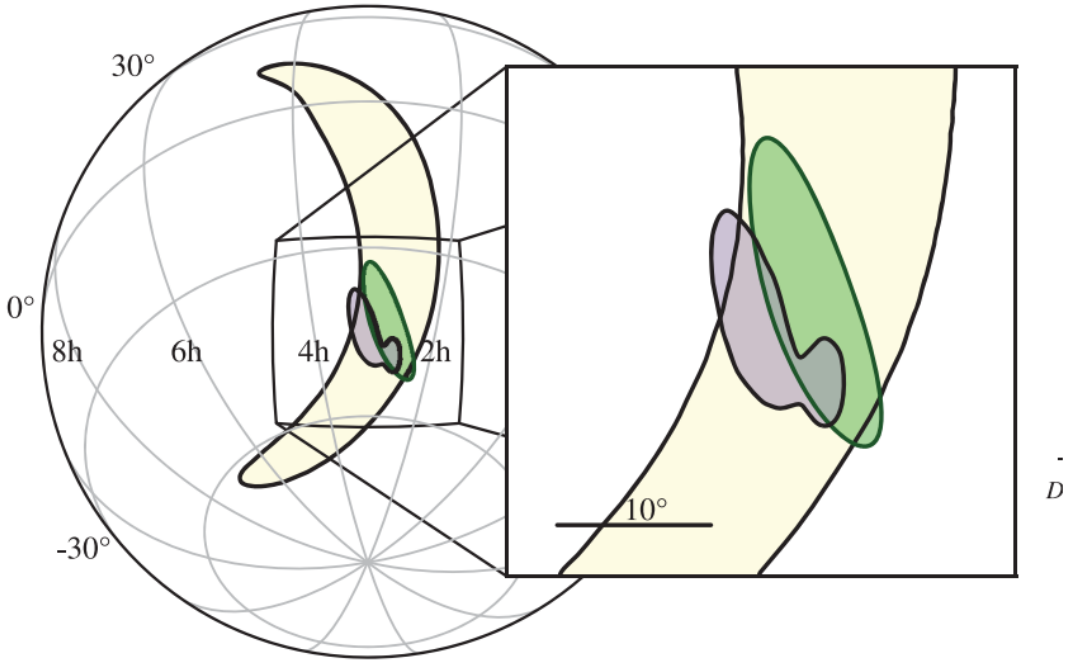

Figure 1.15: The 90% credible region of GW170814. The yellow stripe shows the rapid localization using only the data from aLIGO. The green oval shows the localization after including the data from AdVirgo. The purple area shows the full Bayesian localization. Reproduced from [134].

[132, 133, 134]. GW170608 was so far the lightest observed BBH systems [133]. Although GW170814 was similarly produced by two stellar BHs, it is the first event observed with three detectors together - aLIGO and AdVirgo [134]. The joint detection with 3 detectors significantly improved the sky localization of the event. Figure 1.15 shows the difference between the localizations with and without the data from AdVirgo. Using only the two LIGO detectors, the 90% credible region would be 1160 $\deg^2$, while combining the data from all three detectors reduced the 90% credible region to be 60 $\deg^2$. A network of three detectors also enabled the test of GW polarizations from the detector response of the three detectors.

On the 17th of August, 2017, the network of aLIGO and AdVirgo made the first observation of the inspiral signal from a BNS system. This GW event was later designated to be GW170817. The two NSs in the detected BNS system were inferred to have masses in the range $0.86 - 2.26 M_\odot$ if no spin was assumed. If the spin components of the NSs were present, the masses of the two NSs were inferred to be in the range $1.17 - 1.60 M_\odot$ [135]. The distance of this event was inferred to be relatively close - only $\sim$ 40Mpc. The remnant of the BNS could be a short-lived or long-lived neutron star, which might or might not collapse to a BH. Similar to GW170814, a network of three detectors also enabled relatively accurate localization.

As the presence of NS in a binary system would enable emission in the EM spectrum, the localization with three detectors also facilitated the EM follow-up observations of this event [136]. This will be discussed more in Chapter 2. The discoveries of these GWs have opened up a new window on the sky and ushered in a new era of GW astronomy.

1.6 Data analysis

As it is too difficult to solve the Einstein equations analytically, post-Newtonian approximation approach has been developed to find approximate solutions to the equations. In post-Newtonian approximation, the lowest order for emission of GWs is the quadrupole formula. Quadrupole radiation is known to be weak. Given the facts that sources of GWs are usually located at large distance and that GWs interact only weakly with matter, detecting GWs and extracting information from the detected signals can be difficult, especially for events with relatively low SNRs.

Data analysis with Bayesian inference is important in GW astronomy both in detecting GW signals and extracting information from the signals [137]. In this section, the technique for searching for GW, matched filtering, will be introduced. We will then discuss Bayes' theorem and the Fisher matrix or the Fisher information matrix (FM) in the context of estimating uncertainty on the parameters of GW signals.

1.6.1 Search for gravitational waves

For well modeled signals, i.e. the inspiral signals from CBCs and continuous waves from NSs, a statistical technique known as matched filtering has been employed to search for GWs in the data and to measure the SNRs of the signals and the parameters of the sources. Matched filtering examines the data to determine whether a signal consistent with the waveform of an astrophysical origin is present in the data by correlating the observed data with the waveform. This approach requires to pre-calculate a bank of waveform templates [138, 139, 140]. These waveform templates will then be cross correlated with the data of a detector.

Assuming the data output in the time domain is $x(t)$, if the data contains a signal $h(t)$ and the noise $n(t)$, we have the following expression,

$$x(t) = h(t) + n(t). \tag{1.14}$$

Here, we assume that the noise $n(t)$ is additive. If we further assume that the noise is stationary and Gaussian, we can express the spectral properties of the noise using the one-sided spectral density of the noise [138], given by

$$S(f) = 2\int_{-\infty}^{\infty} \kappa_n(t) e^{2\pi i f t} dt, \tag{1.15}$$

where f is positive frequency, and $\kappa_n(t)$ is the autocorrelation function $E[n(t)n(t')] = \kappa_n(t-t')$. Next, we will define the scalar product as

$$(x|h) = 4\mathcal{R}\int_0^\infty \frac{\tilde{x}(f)\tilde{y}^*(f)}{S(f)}\mathrm{d}f, \tag{1.16}$$

where we use $\mathcal{R}$ to denote the real part of a complex, a tilde the Fourier transform and asterisk the complex conjugate of a complex. The expression for matched filtering is then given by [138]

$$\log\Lambda[x] = (x|h) - \frac{1}{2}(h|h), \tag{1.17}$$

where Λ is the likelihood of the data x given the presence of signal h. The aim of this process is to find the waveform that fits the data with the highest possible SNR. The optimal SNR is defined as

$$\rho^2 = 4\int_0^\infty \frac{|\tilde{h}(f)|^2}{S(f)}\mathrm{d}f. \tag{1.18}$$

The best fit of the signal is found when the data's correlation with respect to the waveform's parameters is maximized. If the SNR of a signal is larger than some pre-set threshold, the signal will be recorded as potential candidate. Under the assumption that the noise in the data is stationary and Gaussian, matched filtering can recover weak signals in noisy data by accumulating SNR over a board bandwidth of the detector.

However, matched filtering can be computationally expensive as interferometric detectors will acquire months to year worth of data in a run. It is also not guaranteed that matched filtering will rule out all false alarms caused by noise-mimicked signal. To rule out this type of false alarm, coincidence of the same signal at multiple detectors will be sought to increase the confidence in a detection. Algorithm such as null stream in which data from a network of detectors are shifted in the time domain and combined linearly has also been developed to identify false alarm caused by glitches of detectors [141]. This indicates that reliable and confident detection of GWs require coincident observations of the same signal at multiple detectors and data analysis techniques will need to be able to work with data from multiple detectors. Additionally, current ground-based interferometric detectors can monitor almost the entire sky at any given time (see Figure 1.9 for an example of the antenna pattern of an interferometric detector). They are also broadband instruments being sensitive to frequencies from $\sim$ 10Hz to $\sim$ 1000Hz. This means that searches for GW signals will have to carry out searches that cover the entire sky and a board frequency range. These are the motivations for developing efficient and less computationally expensive methods [142, 143].

1.6.2 Bayesian Inference and Bayes Theorem

Bayesian inference is a statistical inference method that naturally allows one to perform statistical tasks and estimation based on incomplete information. In astronomy, Bayesian inference can be used to determine the probability of an event occurring based on the information in the past. Once the result of an observation or an experiment is available, Bayesian inference can also be applied to infer or extract information from the observation or the experiment, as well as to to update the probability of a hypothesis. In addition, when there are two models competing to describe the same event or system, determining which model is favored by the data can be done using Bayesian inference.

In the context of Bayesian inference, one uses Bayes' theorem to achieve the above goals, which can be written as

$$p(\boldsymbol{\theta}|d, \mathcal{M}, I) = \frac{p(d|\boldsymbol{\theta}, \mathcal{M}, I)p(\boldsymbol{\theta}, \mathcal{M}|I)}{p(d, \mathcal{M}|I)}. \tag{1.19}$$

Interested readers are referred to [144] for an example proof of this equation. In the above equation, we use the symbol p to denote probability distribution function. Vector $\boldsymbol{\theta}$ represents the physical quantities of a system, $\mathcal{M}$ a model that describes the system, d the observation or the data taken in an experiment and I the background information or relevant prior knowledge. Readers should not be confused $\mathcal{M}$ with chirp mass of a CBC defined in Section 1.2.2.

On the left hand side of Eq. 1.19, $p(\boldsymbol{\theta}|d, \mathcal{M}, I)$ is known as the posterior distribution. It describes how the probability of $\boldsymbol{\theta}$ is distributed given d, $\mathcal{M}$, and I. The posterior distribution function captures all the information about $\boldsymbol{\theta}$ that one can infer given d, $\mathcal{M}$ and I. On the right hand side, the term $p(\boldsymbol{\theta}, \mathcal{M}|I)$ is the probability distribution function for $\boldsymbol{\theta}$ in $\mathcal{M}$ given I. It represents one's knowledge prior to collecting d and allows one to fold this knowledge in the process of inference and estimation. This term is therefore known as the prior distribution. The term, $p(d|\boldsymbol{\theta}, \mathcal{M}, I)$, is the probability distribution function for the data, given $\boldsymbol{\theta}$, $\mathcal{M}$ and I. It actually evaluates how likely the data d is, given $\boldsymbol{\theta}$, $\mathcal{M}$ and I, which thus acquires its name the likelihood. The denominator $p(d|\mathcal{M}, I)$ is referred to as the marginal likelihood or the evidence, which is given by

$$p(d|\mathcal{M}, I) = \int d\boldsymbol{\theta} p(\boldsymbol{\theta}, \mathcal{M}|I)p(d|\boldsymbol{\theta}, \mathcal{M}, I). \tag{1.20}$$

Using Bayes' theorem (i.e. Eq. 1.19) is therefore straightforward to combine one's knowledge and new knowledge from new data or observation. To put it in simple terms, Bayes' theorem states the following common sense: the posterior, or the degree of belief in $\boldsymbol{\theta}$ being true in the model $\mathcal{M}$, is updated by an observation or experiment, weighted by the prior knowledge.

Bayesian inference has been widely used in GW astronomy for parameter estimation, given incomplete information. For example, given a problem of parameter

estimation, one can find the most probable values of the $\boldsymbol{\theta}$ under the model $\mathcal{M}$ by evaluating the posterior distribution function $p(\boldsymbol{\theta}|d, \mathcal{M}, I)$. The most probable values or the best bit are found when the posterior distribution function is maximized. In the situation where $p(\boldsymbol{\theta}|d, \mathcal{M}, I)$ is continuous, one can also estimate the probability P that $\boldsymbol{\theta}$ are in the interval $[\boldsymbol{\theta}_1, \boldsymbol{\theta}_2]$ by performing an integration,

$$P(\theta_1 \leq \theta \leq \theta_2) = \int_{\boldsymbol{\theta}_1}^{\boldsymbol{\theta}_2} p(\boldsymbol{\theta}|d, \mathcal{M}, I) d\boldsymbol{\theta}. \tag{1.21}$$

One should not be confused by the upper case P, which indicates the probability, and lower case p, which is symbol for probability distribution function (PDF). In practice, using numerical techniques, the posterior distribution function and Eq. 1.21 can be computed using numerical techniques if the analytical solution does not exist.

In the cases where one is only concerned or interested in a certain subgroup of the parameters $(\theta_1, \theta_2, ..., \theta_m)$ (assuming there are n parameters in $\boldsymbol{\theta}$, and $m < n$), the posterior distribution function can be integrated over the rest of the parameters to find the PDF for $(\theta_1, \theta_2, ..., \theta_m)$. Such a manipulation is known as marginalization and is defined as follows:

$$p(\theta_1, \theta_2, ..., \theta_m|d, \mathcal{M}, I) = \int p(\boldsymbol{\theta}|d, \mathcal{M}, I) d\theta_{m+1} d\theta_{m+2} ... d\theta_n. \tag{1.22}$$

In reality, one may need not only to estimate the most probable values under a model but also to decide the most probable model among a number of alternative models. Such a problem is known as model selection. Bayes' theorem can be written as

$$p(\mathcal{M}|d, I) = \frac{p(d|\mathcal{M}, I) p(\mathcal{M}|I)}{p(d|I)}, \tag{1.23}$$

The term $p(\mathcal{M}|I)$ can be interpreted as the prior distribution function for the model given the background information I, and $p(\mathcal{M}|d, I)$ as the posterior distribution function for the model $\mathcal{M}$ given the data and the background information I. The posterior distribution function captures our degree of belief in the model $\mathcal{M}$ being true. So using Bayes' theorem, one can decide how much more likely a model is than the alternative by evaluating the odds ratio, which is defined as the ratio of the degree of belief in one model to the alternative as

$$O_{1/2} = \frac{p(\mathcal{M}_1|d, I)}{p(\mathcal{M}_2|d, I)} = \frac{p(\mathcal{M}_1|I)}{p(\mathcal{M}_2|I)} \times \frac{p(d|\mathcal{M}_1, I)}{p(d|\mathcal{M}_2, I)}, \tag{1.24}$$

where $\mathcal{M}_1$ and $\mathcal{M}_2$ indicate model 1 and model 2. In some text, $\frac{p(d|\mathcal{M}_1, I)}{p(d|\mathcal{M}_2, I)}$ is referred to as the Bayes factor [144, 145]. We know that $\mathcal{M}_1$ is favored if the ratio is larger than 1 or disfavored if the ratio is less than 1.

1.6.3 Fisher matrix

The FM, named after the statistician Ronald Fisher, is a statistical tool that measures the amount of information about unknown parameters that is carried by an observable. The FM is defined as [138]

$$\Gamma_{ij} = \mathrm{E}\left[\frac{\partial \log\, p(d|\boldsymbol{\theta},\mathcal{M},I)}{\partial\theta_i}\frac{\partial \log\, p(d|\boldsymbol{\theta},\mathcal{M},I)}{\partial\theta_j}\middle|\boldsymbol{\theta}\right], \tag{1.25}$$

where Γ_{ij} is the FM, and $p(d|\boldsymbol{\theta},\mathcal{M},I)$ is the likelihood function as defined in Section 1.6.2. The FM describes on average how strong the dependence of the likelihood function on the parameters is. If the log of the likelihood function is twice differentiable with respect to $\boldsymbol{\theta}$, the FM can also be expressed using the second derivatives,

$$\Gamma_{ij} = \mathrm{E}\left[-\frac{\partial^2 \log\, p(d|\boldsymbol{\theta},\mathcal{M},I)}{\partial\theta_i\partial\theta_j}\middle|\boldsymbol{\theta}\right]. \tag{1.26}$$

It can be seen from Eq. 1.26 that the FM for a measurement or data d described by unknown parameters $\boldsymbol{\theta}$ is the expectation value of the second derivatives of the log of the likelihood function conditioned on the true values of $\boldsymbol{\theta}$.

If $\tilde{\boldsymbol{\theta}}$ is the measurement error of $\boldsymbol{\theta}$ and $\hat{\boldsymbol{\theta}}$ is an unbiased estimator of $\boldsymbol{\theta}$, we have

$$\tilde{\boldsymbol{\theta}} = \hat{\boldsymbol{\theta}} - \boldsymbol{\theta}, \tag{1.27}$$

and the covariance matrix, given by,

$$\mathrm{cov}_{ij} = \mathrm{E}[\tilde{\boldsymbol{\theta}}\tilde{\boldsymbol{\theta}}^{\mathrm{T}}], \tag{1.28}$$

where the superscript T indicates transpose. For an unbiased estimator, the Cramer-Rao bound states that the following inequality holds

$$\mathrm{cov}_{ij} \geq \Gamma_{ij}^{-1}. \tag{1.29}$$

In the situation where the SNR is high enough, the above equation becomes

$$\mathrm{cov}_{ij} = \Gamma_{ij}^{-1}. \tag{1.30}$$

In order words, the matrix inverse of the FM presents the lower bounds on the variances of the parameter estimators and is equal to the covariance matrix for high enough SNR. The FM can therefore be used to test how small the variance on an estimator can be.

In data analysis for GW astronomy, the FM is a widely used statistical tool[146, 147, 148, 149, 150, 151, 152, 153, 154]. It is employed to evaluate the quality of astrophysical information obtainable from observations of GW signals and to estimate how accurately information about the parameters can be extracted (see Chapter 4 for an application of the FM to the estimate of the localization of CBC). In the context

of GW astronomy, assuming the likelihood function is Gaussian, the mathematical definition of the FM (from Eq. 1.25) is given by

$$\Gamma_{ij} = 2\int_0^\infty \frac{\frac{\partial\tilde{h}^*(\boldsymbol{\theta},f)}{\partial\theta_i}\frac{\partial\tilde{h}(\boldsymbol{\theta},f)}{\partial\theta_j} + \frac{\partial\tilde{h}^*(\boldsymbol{\theta},f)}{\partial\theta_j}\frac{\partial\tilde{h}(\boldsymbol{\theta},f)}{\partial\theta_i}}{S(f)}\mathrm{d}f. \tag{1.31}$$

where $\tilde{h}(\boldsymbol{\theta}, f)$ is signal strain in the frequency domain and $\tilde{h}^*(\boldsymbol{\theta}, f)$ the complex conjugate. The power spectrum density is denoted by $S(f)$ and $\partial\tilde{h}(\boldsymbol{\theta}, f)/\partial\theta_i$ indicates the partial derivative of $\tilde{h}(\boldsymbol{\theta}, f)$ with respect to the i^{th} unknown parameter θ_i.

In the literature, the estimates from the FM have been reported to be more optimistic than techniques or methods that completely explore the likelihood, e.g. Monte Carlo Markov Chain (MCMC). However, this is often due to the abuse or misuse of the FM in situations where the SNR is too low. In the moderate to high SNR regime in which the Cramer Rao lower bound is valid [155, 156, 157], estimates from the FM are a good indicator of the expected uncertainty on parameters. In addition, complete simulations of MCMC are usually too computationally expensive to carry out, while the FM is low to moderate in computational cost.

Chapter 2

Multi-Messenger Astronomy with Binary Neutron Stars

Multi-messenger astronomy refers to the study of astronomy based on the coordinated observations across different bands and messengers from the same source. These messengers could be cosmic rays, neutrinos, EM radiations and GWs [7]. The observation of GWs and other messengers from GW sources has been of great importance in GW astronomy because the information obtained from the observations of GWs and the associated EM signatures are complementary to each other [7, 158].

Detecting the EM emission of a GW trigger will help establish the association between the GW trigger, the EM emission and its progenitor as was the case of GW170817 and its associated EM counterparts [136, 159, 160, 161, 162, 163, 164, 165, 166, 167]. A joint detection of the GW and its EM signatures will provide a better understanding of the progenitor's local environment and the progenitor itself [158, 168, 169]. The detection of both the EM signatures and GW may also improve the understanding of the emission mechanism (e.g. CCSNe [170]). In addition, a successful EM follow-up observation will increase the confidence in and improve the localization of the GW detection, or reduce the SNR required to claim a detection of GW [7]. This is also true even when merely the time and the direction of GWs and other messengers are correlated [168]. Moreover, detecting the EM signatures of CBCs will allow for a measurement of the redshift z of the sources that enables the use of the GWs during inspiral as a precise probe of the luminosity distance of their progenitors independent from the EM signals. The measurement of z and the luminosity distance from GW data can then be used to constrain cosmological constants and the Hubble constant in a way that is independent but complementary to other probes such as EM emission [171, 172, 173, 174].

Broadly speaking, there are three types of coordinated observations in GW astronomy using GWs and other kinds of messengers. The first type of coordinated observations is known as triggered searches. In a triggered search, information from observed transient EM signals such as gamma-ray bursts (GRBs) [175, 176, 177, 178,

179, 180, 181, 182], soft-gamma repeater flares [183, 184], pulsar glitches [185] or CCSNe [186, 40] is used to facilitate the search for signals of GWs. For example, the information about the time and the sky location of the EM emission can be used to define an on-source window for the search of GW in the data of a GW detector [40]. Any potential signal candidates found in the data stream will have to be consistent with the arrival time and the sky location of the EM source [7]. This approach is useful in improving the search sensitivity and reducing the background noise. Since the data in a detector is in the form of time-series collected during observation and stored, triggered search can also be conducted after an observation when the data have been collected. However, triggered search requires that the involved observing instruments are operational during the on-source window. Incomplete coverage of the on-source window by GW detectors may reduce the sensitivity of this search approach [7, 40].

On the other hand, it is possible to use the information from a GW candidate such as timing and sky location for the search of the EM counterparts [139, 187, 188, 189, 190, 191]. This is known as follow-up searches. However, since interferometers are not pointing instruments, the sky localization of GW events can be poor making follow-up searches a challenge to achieve. This will be discussed more later in this chapter, Chapters 3 and 5.

In addition, there is a class of coordinated observations referred to as parameter refinement [7]. During an observation period of interferometric detectors, radio observations can be used to monitor the change in the frequency of pulsars [192, 193, 194]. This is helpful in searching for the GWs from known pulsars as the change in frequency recorded can be used to reduce the parameter space that must be searched.

In this chapter, we focus on multi-messenger astronomy with CBCs with an emphasis on GW170817. We will begin in Section 2.1 by briefly describing the process with which GW alerts and sky maps are shared with partners of EM astronomers. Four localization algorithms used to facilitate searches for EM counterparts of GW sources are discussed in Section 2.2. We will then describe the expected EM counterparts from BNS mergers in Section 2.3 along with the relevant observation activities for GW170817, which will be followed by a short introduction to the EM follow-up observations for the two detected BBH mergers, GW150914 and GW151226 in Section 2.4.

GW170817 is the first event that a source is observed both electromagnetically and gravitationally [136]. The discovery of the short GRB by *Fermi* Gamma-ray Burst Monitor (*Fermi*-GBM) [166] and that of BNS merger candidate by LIGO and VIRGO [135] started a series of follow-up observations covering a broad EM spectrum from gamma-ray to radio emission (see below). The results of this EM follow-up observation campaign are consistent with and supportive of the hypothesis that GW170817 was a BNS merger in the galaxy NGC4993 [136]. The observation of the EM counterparts also made possible a measurement of the redshift of the system, which later was used to constrain the Hubble constant [174]. With these discoveries,

multi-messenger astronomy has entered a new era in which GW is used as an active probe of astronomical sources along with other messengers.

2.1 Electromagnetic follow up observations with aLIGO and AdVirgo

Facilitating and enabling multi-messenger observations of GW events with a wide range of astronomical telescopes and instruments are one of the main goals of aLIGO and AdVirgo as a scientific collaboration. To meet this goal, aLIGO and AdVirgo have designed a dedicated program of EM follow-up observation for the purpose of sharing information on GW event candidates with EM partners enrolled in this program [195].

When a significant GW candidate is identified solely based on the apparent signal significance, aLIGO and AdVirgo will provide a preliminary alert to the EM partners [190, 136, 195]. At this point, information on only the estimate of the arrival time and the signal significance about the candidate will be provided [195, 196, 197, 198, 199, 200, 201]. This will then be followed by a validation check of the preliminary alert. A rapid sky localization will be provided to the EM partners if the event candidate can be localized for the purpose of prompt EM follow-up [190, 136, 195]. A more refined sky localization of the GW candidate will be made available to the EM partners along with more information on the GW such as the masses and distance of the system in a few hours or more [190, 136, 195]. Since the threshold for generating GW candidate is set to be low, it is also possible for an alert to be retracted at any stage of the process described above if examination or human intervention determines that the GW candidate is likely to have an origin other than astrophysical [195].

Many teams of astronomers with access to ground-based and space-based instruments joined the program during aLIGO's first and second observing run and have performed EM follow-up observations for the detected BBH mergers and the BNS merger [190, 136]. These observations will be briefly introduced in later sections.

2.2 Localization Algorithms

Sky localization of a GW candidate refers to the construction of a posterior probability distribution for the sky position of the GW candidate. Sky localization is mainly achieved via timing triangulation using the time difference in the arrival times of the sources at the detectors in a network. Information such as the phases and polarizations of the waves can also help improve the localization [202, 203, 204]. A sky map accurately showing the probable sky locations of a GW event given the information available is essential for EM follow-up observations of a GW trigger as it provides guidance to astronomers on directions of pointing and imaging.

Unfortunately, interferometers are not directional instruments and their perfor-

mance is usually very poor when it comes to the localization of GW sources unless there are three or more detectors in a network. With the two aLIGO detectors, the 90% credible regions for CBC signals are expected to be large, probably spanning hundreds square degrees [205]. For example, as mentioned above, the 90% credible regions were as large as $\sim 600\text{deg}^2$ and $\sim 1400\text{deg}^2$ on the sky for GW150914 and GW151226 respectively [130, 131]. There was improvement in localizing GW sources with AdVirgo joining the observing runs [134, 135] and more improvement can be expected when more detectors such as KAGRA and LIGO India start to join the global network [150]. However, for sources at large distance, sky localization error may still be large. The sizes of the fields of view (FOVs) of many telescopes are the order of $\mathcal{O}(1)$ deg^2, leading to a huge mismatch between the FOVs and the localization error. Moreover, many EM counterparts will peak in luminosity and then fade away on a time scale from seconds to days or weeks. For example, short GRBs will only last for ~ 2s. Optical afterglow may be observable on a timescale of days to weeks depending on the distance and the viewing angles. Kilonova may also be detectable for a few days depending on the opacity and the distance [206]. Given the typical expected distances of these objects, searching for the potentials EM counterparts associated with a GW trigger in the sky error region is not a task easy to achieve.

Therefore, in many situations, to increase the chance of successful EM follow-ups, it is desirable to have prompt and accurate reconstruction of the sky location of GW events with low latency. However, there is a trade-off between the speed and the accuracy of the localization. In this section, a short overview of four algorithms used for the reconstruction of sky location of GW events is presented.

2.2.1 Bayesian Triangulation and Rapid Localization

Bayesian Triangulation and Rapid Localization (BAYESTAR) [207] is an algorithm dedicated to produce rapid sky localization for CBC events. BAYESTAR has applied several techniques to reduce the runtime for an analysis and the reconstruction of the sky location of a GW trigger while maintaining a high accuracy.

Firstly, it takes advantage of the fact that almost all the information on the sky location of a GW is captured in the estimates of the arrival time, the amplitude and the phase of the GW on its arrival at each detector [207]. This means ignoring other intrinsic parameters of the GW source such as its mass will not seriously compromise the localization accuracy. This is helpful in reducing the dimensionality of the localization problem. Coupled with the assumption that detector noise is Gaussian, this allows the use of an easy likelihood function to which Bayesian inference is applicable [207]. In addition, considering only a few parameters at each detector implies there is no need to compute the post-Newtonian waveforms allowing fast evaluation of the likelihood function. BAYESTAR is also parallelized and can further reduce the runtime for an analysis by running on multiple threads simultaneously. It is reported that BAYESTAR can produce sky maps that are approximately as accurate as the

full MCMC parameter estimation within 10 seconds of a detection [207].

For GW170817, BAYESTAR was used to generate rapid sky position reconstruction of the source. The combination of the data from both aLIGO and AdVirgo allowed a precise sky localization of the event to an area of $28\,\mathrm{deg}^2$ at 90% confidence level, and an estimate of the distance of 40^{+8}_{-14}Mpc [135]. A sky map showing the location constraints on the sky position of GW170817 is given in Figure 2.1. The well-constrained sky position estimate of the event, as well as the temporal coincidence between the GW candidate and the detection of GRB 170817A, sparked an extensive observing campaign across the EM spectrum [136].

2.2.2 Coherent WaveBurst

Coherent WaveBurst (cWB) [208] is both an archived search and a real time search algorithm designed for the coherent detection and sky location reconstruction of transient GW signals. This algorithm makes minimal assumptions about the morphology of the waveform and is thus suitable for any un-modeled GW transient signals [209, 208]. For signals that better match the assumptions, the performance will be better [190].

The detection of a GW signal with cWB is done by first whitening the data. A wavelet transform (i.e. Wilson-Daubechies-Meyer transform [210]) will then be applied to the data to present the data in the time-frequency domain that spans the entire frequency range that the detectors are sensitive [208, 211]. To identify a GW candidate, the data in the time-frequency domain from all detectors in a network will be first combined. cWB will then construct an energy map of the combined whitened data. The energy is defined as the sum of the square of the data maximized over the arrival times at detectors. The identification of a GW candidate is then achieved by identifying the areas in the time-frequency domain with energy exceeding detector noise with the assumption that the noise is Gaussian. Combining the data before the identification of any candidates has the advantage of avoiding having the sensitivity limited by the least sensitive detector in the network as the combined SNR will become the statistics based on which a signal is picked up rather than a single detector SNR. The identified area in the time-frequency domain will be used for analysis and the extraction of the key parameters including signal waveform and sky location.

To reconstruct the sky location of a GW event, a maximum likelihood calculation will be carried out over all possible GW signals at each point in the sky with *ad hoc* constraints that reduce the signal space to approximate a posterior probability distribution [208, 209]. Because the sky localization will be degenerate if there are only two detectors in a network, the use of prior will be important for the sky location reconstruction of GW sources. cWB uses an astrophysically motivated prior to break the degeneracy [208]. This prior comes from the expectation that quieter signal will occur more often than louder signals. This implies that a signal is more likely to happen in the part of sky to which the detector response is larger.

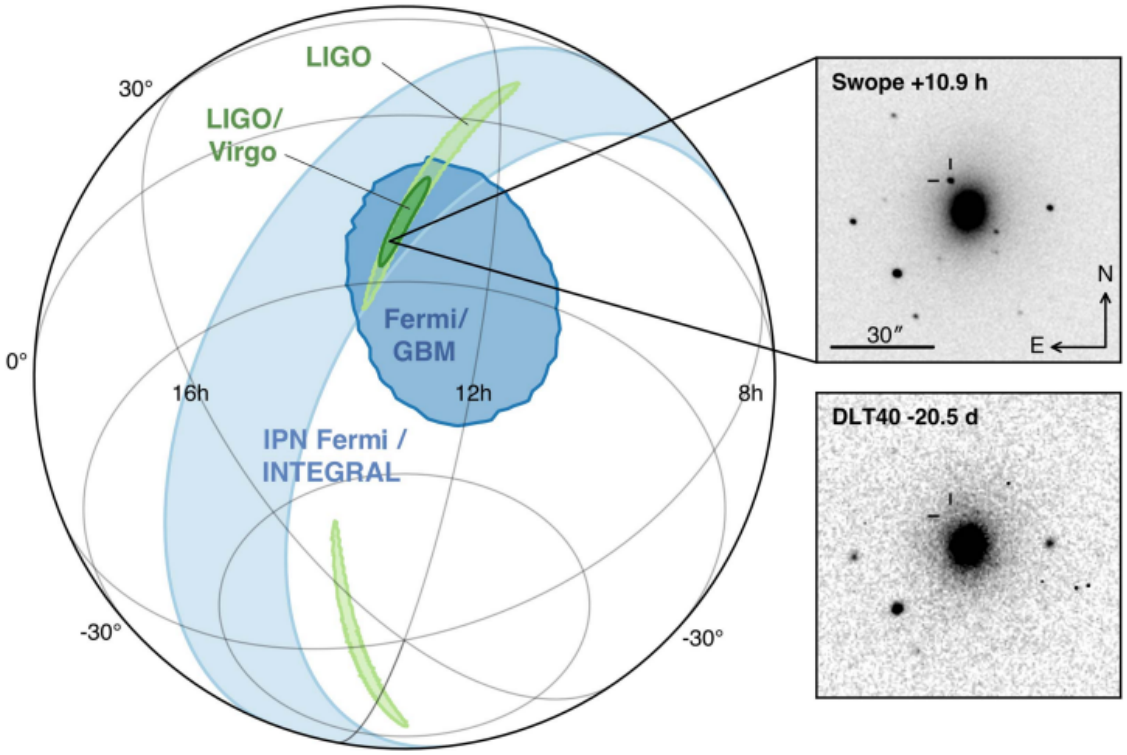

Figure 2.1: The sky location reconstruction for GW170817 and GRB170817A. The localization error shown in dark green is the localization achieved using the data from both aLIGO and AdVirgo. The light green shows that using only the data from aLIGO. The localization for the short GRB detected by *Fermi*-GBM is shown in dark blue. Localization via triangulation using the data from INTEGRAL and *Fermi*-GBM is shown in light blue. The upper and bottom panels on the right are the Swope optical discovery image taken at 10.9 hr after the merger and the DLT40 pre-discovery image taken 20.5 days prior to merger, showing the location of the host galaxy NGC 4993. The position of the transient in both images is marked using a reticle. Reproduced from [136].

2.2.3 LALInferenceBurst

LALInference Burst (LIB) is a model selection algorithm designed for recovering GW signals that are poorly or un-modeled and estimating the parameters of the sources [142, 209, 203]. LIB is template based algorithm assuming signal waveforms are sine-Gaussian that depend on 9 parameters including sky position [212]. For signals that cannot be perfectly described by this waveform such as CBC signals, the localization performance will be suboptimal.

The reconstruction of the parameters of a GW candidate with LIB is based on Bayesian inference and MCMC approach with nested sampling [142]. LIB assumes that the signal is a sine-Gaussian waveform. The results are 9 posterior distributions for the parameters on which the sine-Gaussian waveform depends [212]. Unlike cWB, LIB is usually run as a follow-up of pre-selected times. Although there are some degree of flexibility and trade-off between computational cost and sensitivity, both the latency and computational cost are higher for LIB with typical latency from hours to days, for example, it took 14 hours for LIB to generate a sky map for GW150914 [190].

2.2.4 LALInference

LALInference [142] uses MCMC methods with different sampling algorithms to estimate the posterior distribution of interesting parameters of a GW event. LALInference is very similar to LIB in that they share most of their libraries [209]. But LALInference filters detector data using a parameterized CBC waveform that allows the considerations of the spins of the components in a CBC. Detector calibration uncertainties are also considered in LALInference [190, 142]. It is therefore the most accurate parameter estimation algorithm regarding CBC signals among all algorithms discussed in this section. The sky localization from LALInference is usually considered to be final and authoritative because of its accuracy [190]. However, it is also the most time consuming method due to the high dimensionality involved in the calculation. The runtime of LALInference for a CBC signal can be half a day or even longer.

2.3 Electromagnetic counterparts

Many GW sources are expected to emit both gravitationally and electromagnetically [7]. For example, NSs, CCSNe and CBCs containing at least one NS are expected to be sources of both GWs and EM waves. The possible EM signatures of these GW sources are expected to cover a wide range of the entire EM spectrum from gamma-ray to radio. Different EM counterparts of a GW trigger provide different information on the astrophysical origin.

However, not all GWs will be accompanied by EM emission. For example, not all BBH mergers are expected to emit EM waves. Supermassive BBH merger may produce an EM afterglow by the gas surrounding the binary after the two BHs merge. Such an activity could also generate a quasar [213]. However, for stellar mass BBH mergers, it is still not confirmed that they will be accompanied by EM counterparts although many groups have explored possible scenarios in which EM signatures of BBH mergers are generated [214, 215, 216, 217, 218, 219, 220, 221]. In this section, we will briefly explain the types of EM counterparts that can be expected from BNS merger events. Although neutrino is not EM radiation, we also provide a brief discussion since it is an expected important radiation from BNS mergers.

2.3.1 Gamma-Ray Burst

GRBs are intense and energetic transient astronomical phenomena lasting for a short duration with photon at energy level of $\lesssim$ Mev. There are two classes of GRBs defined by their durations and spectral hardness (short-hard and long-soft) [222]. We will refer to these two classes of GRBs using only their durations, namely, short GRB and long GRB respectively. Short GRBs last $\lesssim 2$ sec and release total energy $\lesssim 10^{49}$ erg [223, 224, 225]. The other class of GRB, known as long GRB, is observed to last for $\sim 2- \sim 100$ seconds and release energy at the level of 10^{51} erg [226, 227, 228]. In general for GRBs, it should be kept in mind that although the 2 second separation cut is convenient and sufficient for the purpose of statistical study, there are observed long GRBs with duration less than 2 sec and short GRB longer than 2 sec [229, 230]. We will restrict the discussion to short GRBs.

The major breakthrough in the study of the origin of short GRBs came in 2005 from the discoveries of the afterglows following short GRBs [231]. The detections of the afterglows in 2005 revolutionized the understanding of short GRBs by providing valuable information on the localization of the sources, the progenitor environment, the host galaxies and the scale of energies [232, 233, 234, 224, 235, 236]. The observations of the afterglows then helped confirm short GRBs to be cosmological events.

The progenitors of short GRBs were long considered to be the mergers of compact binaries consisting of at least one NS [237, 238, 239, 240]. As shown in Figure 2.2, the merger of two NSs or a NS with a BH powers and generates prompt short GRB emission via a jet fed by the accretion of material that remains around the BH formed after the merger [240, 238, 239]. After the prompt emission, there would be X-ray, optical and radio afterglows lasting for hours to days.

Short GRBs within the reach of aLIGO and AdVirgo will be easily detectable with gamma-ray satellites if the viewing angle is less than half the opening angle of the beams [206, 241]. They are considered the most useful EM counterpart of BNS merger and neutron star black hole (NSBH) merger in confirming their cosmological origin [206]. However, the redshift distribution of the detected short GRBs suggests that short GRBs rarely happen within the BNS range of aLIGO and AdVirgo [206].

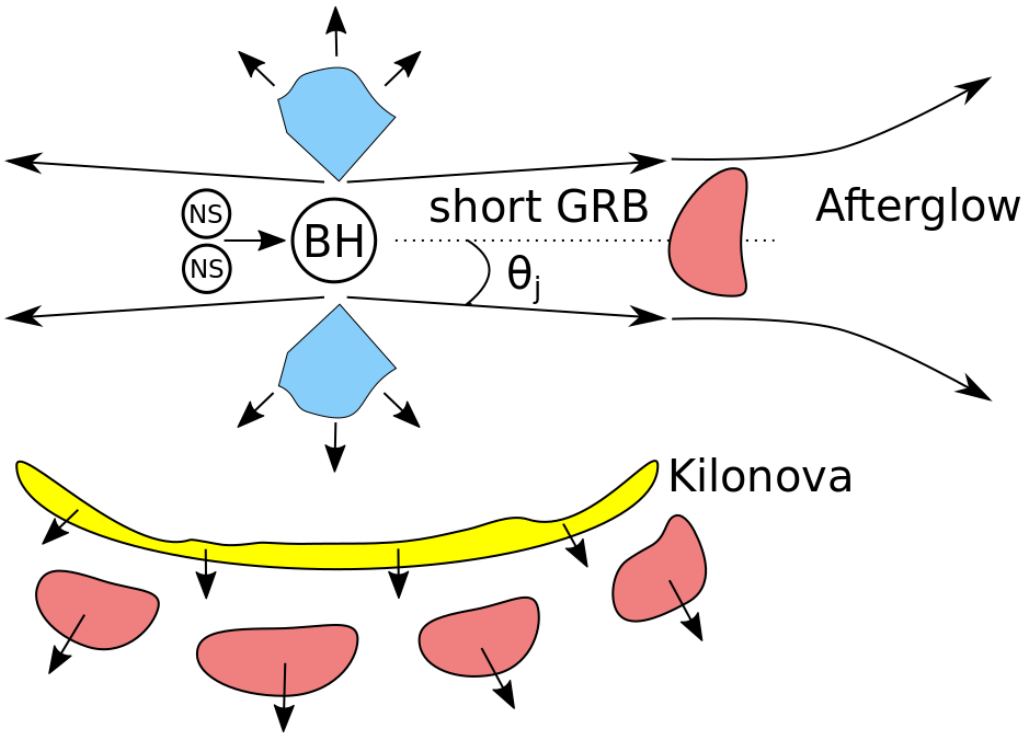

Figure 2.2: Diagram showing the possible EM counterparts associated with a BNS merger. After two NSs collide into each other, there will be an accretion disk (blue) around the newly formed BH. The accretion powers the prompt short GRB emission lasting ≤ 2 seconds, whose opening angle is denoted by θ_j. The interaction between the jet and the surrounding medium (red) results in afterglow emission in the optical and radio band. There will also be an isotropic transient known as kilonova or macronova in the optical and infrared band powered by the radioactive decay as well as α and β decay on a time scale of days to weeks. Diagram based on [206].

In addition, the opening angle of short GRB jets is usually narrow making them difficult to detect.

On the 17th of August, 2017, the detection of a short GRB, later referred to as GRB 170817A, was announced by *Fermi*-GBM [242, 243, 166]. The spectral energy of this short GRB at its peak is near the low end of the distribution of known short GRBs [244, 166]. About 6 minutes later, a BNS merger candidate was identified in low latency based on the analysis of the data from LIGO Hanford. The merger time of this event was estimated to be less than 2 seconds before GRB 170817A [136]. Such a temporal coincidence between the merger and the short GRB contributed to the release of a GCN report of an one detector GW trigger [196]. Prior to this, single-detector GW triggers was never released in low latency [136]. The later analysis of the data from the two aLIGO detectors and AdVirgo confirmed a significant signal consistent with a BNS merger with combined network SNR of 32.4 [136, 245]. The release of the GCN reports by *Fermi*-GBM and LIGO and AdVirgo cause the INTEGRAL to searched its data and results in a detection of GRB 170817A [246]. The difference in the arrival times of the short GRB at these two GRB observatories allowed localization of the source via triangulation. The position constraint from INTEGRAL and *Fermi*-GBM on the sky position will be important for future events that are less well-localized by GW detectors. The detection of the short GRB indicates that at least some short GRBs are indeed associated with BNS mergers [136].

2.3.2 Kilonova

Kilonova, also known as macronova, is an approximately isotropic quasi-thermal transient that produces optical and infrared emission [247, 248, 249, 250, 251, 252, 253, 254]. As indicated in Figure 2.2, it was thought that kilonova originates from the hot neutron-rich matter ejected from BNS mergers and NSBH mergers. This ejection triggers a rapid neutron capture process known as r-process nucleosynthesis, which takes place in the ejected material that is unbound from the remnant accretion disk [255, 256]. The r-process will only last for a few seconds. However, the radioactive decay of the heavy elements synthesized during the r-process through nuclear fission as well as α and β decay will last much longer [250]. The decay is able to sustain the high temperature of the ejecta and powers the kilonovae.

Theoretical calculation using nuclear physics suggested that kilonovae can be $\sim$1000 times brighter than a nova (peak luminosity $L \sim 10^{41}$ erg/s) and thus kilonova acquired its name [250, 206, 257]. In addition, calculations including the opacity of the r-process elements [252, 258, 259] indicate that a kilonova maintains its peak luminosity for days to weeks. Within the BNS range of aLIGO and AdVirgo, kilonovae should be bright enough to be detectable to telescopes such as the Large Synoptic Survey Telescope (LSST) ([241], also see Chapter 5).

Compared to other astrophysical transients, the quasi-thermal spectra of kilonovae are relatively unique. This feature allows kilonova to be distinguished from other

contaminating sources [206]. In addition, kilonova as an EM counterpart is more likely to accompany every BNS than other possible EM signatures of BNS such as short GRB as only small quantity of neutron-rich material ejected from the merger is required to produce the emission [206]. Because of these features, the approximately isotropic nature, and their detectability, it has been argued that kilonovae are the preferred EM counterparts for GW signals from BNS and NSBH mergers in obtaining information on the host galaxy and redshift of BNS mergers [247, 206, 260].

There were a few detections of kilonovae that were associated with GRB, such as GRB130603B [260, 261] and GRB060614 [262, 263] and GRB050709 [264]. In addition, after the observation of GW170817 by aLIGO and AdVirgo and that of GRB170817 by the *Fermi*-GBM, a series of EM follow-up observations has been launched, and a kilonova was observed in ultraviolet, optical, near-infrared wavelength confirming the association of kilonova with BNS merger and short GRB [159, 160, 161, 162, 163].

GW170817 was localised to be in the southern sky, and set in early evening as seen in the northen hemipshere. As such, it began to be inaccessible to the majority of the telescopes in the northern hemisphere after the early evening. Therefore, the first EM follow-up observations with ground-based telescope started with the One-Meter, Two-Hemisphere team approximately 10 hours later [265]. With the Swope telescope located at Las Campanas Observatory in Chile, the team detected a bright optical transient in i-band in the galaxy NGC4993. This transient is later designated SSS17a/AT 2017gfo [159]. Within an hour, the same transient was also detected by five other teams including the Dark Energy Camera [266, 160], the Visible and Infrared Survey Telescope for Astronomy [267], Las Cumbres Observatory [268, 163], the Distance Less Than 40 Mpc survey (with the transient designated DL17ck) [269, 161] and MASTER [270, 162]. Many other teams also carried out independent searches including the Rapid Eye Mount [271], Swift UVOT/XRT [272] and Gemini-South [273].

These discoveries from the optical to near-infrared constituted part of the motivations for follow-up observations that target ultraviolet, optical and infrared wavelengths of the EM spectrum [136]. Over the next two weeks, ground based telescopes and space observatories carried out follow-up observations in ultraviolet, optical, and infrared wavelengths of the detected transient. From 11.6 - 15.3 hours after the binary merger, further follow-up observations have been initiated by Magellan-Clay and Magellan-Baade telescopes [274, 275], the Rapid Eye Mount [276], the Gemini South FLAMINGO2 instrument [277, 273] and the Swift satellite [278, 277, 279]. These observations in different bands from ultraviolet to near-infrared placed different constraints on the properties of the transient at the early stage. For example, the observation of the Rapid Eye Mount and the Gemini South FLAMINGO2 instrument constrained the optical to near-infrared color of the transient at early stage [277, 273], while the ultraviolet observation by the Swift satellite constrained the effective temperature [279, 272]. Further monitoring of the evolution of the transient

in ultraviolet wavelength was carried out by the Swift satellite and the Hubble Space Telescope [279, 280, 281, 277]. In the next two days, the evolution of these wavelengths of the transient revealed a fast dimming of the ultraviolet-blue emission and a rise of the infrared emission, which started to fade after one week approximately [136]. Many other groups of astronomers have participated in the follow-up observations of this transient. For a full list, readers are referred to [136].

The photometric observations and measurements revealed that the transient had a fast decline in the optical to infrared bands (i.e., g, i, z, y, w bands), by 0.6 mag per day and 1 mag per day in blue, although there was initially a rise in w-band [281, 282, 163, 283, 284, 285, 165, 286]. However, it was reported in the near-infrared a more slow fading or even a brightness plateau was observed in the Ks band [287, 288, 289].

On the other hand, the observation of the spectrograph of the transient performed shortly after the first image also suggested the transient was unusual [290, 291] and showed that the transient was not consistent with young supernova [292, 293, 294, 295, 296, 297]. Continued observation of the spectrograph by other teams confirmed the discovery [277, 294, 274, 298, 291, 299]. These spectrum discoveries as well as others obtained by other teams also indicated that a fast cooling and the absence of elements abundant in ejecta from supernovae [294, 292, 300, 301]. ESO-VLT/X-shooter spectra taken over 2 weeks covering a wavelength range 320nm - 2480nm showed signatures of radioactive decay from elements produced from r-process nucleosynthesis [302, 300]. In addition, features consistent with production of lanthanides within the ejecta were identified with the Hubble Space Telescope [281, 303, 304, 167, 305]. The evolution of the spectral energy distribution, the broad spectral features and the fading in brightness suggested that the detected transient had properties similar to models of kilonova [250, 251, 253, 306, 307, 308, 309, 310, 311, 312]. The observations of the kilonova in ultraviolet, optical and infrared wavelengths as well as the delayed X-ray and radio counterpart allowed the determination of their associations with BNS mergers. A plot showing some of the representative spectra is displayed in Figure 2.3.

2.3.3 Gamma-ray Burst Afterglows

The interaction of the jet of a GRB with surrounding medium will result in X-ray, optical and radio emission known as afterglow emission (see Figure 2.2). Observing the afterglow of a short GRB can provide useful physical information of the event. For example, afterglow in the X-ray spectrum is useful in constraining the ejecta geometry, the energy output, the sky location and the system orientation of the GRB with respect to the line of sight of the observer [136]. On the other hand, the evolution of radio afterglow emission not only provide information on the explosion energetics but also the merger environment. Observations of the afterglows will also help determine the redshift of the host galaxy [229] as well as constrain proposed

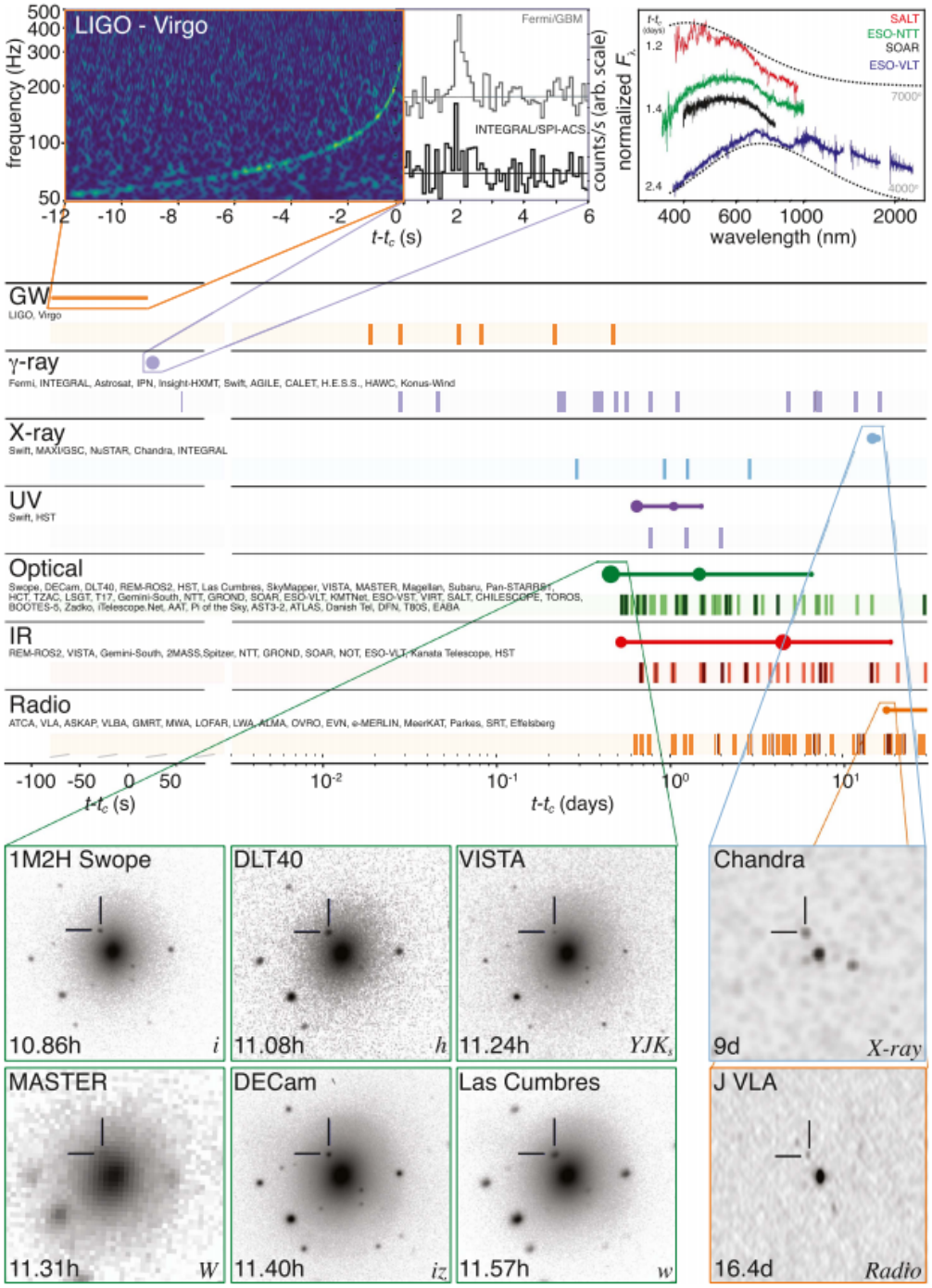

Figure 2.3: A plot showing the timeline of the discoveries of the BNS merger GW170817, the short GRB, the optical and radio afterglow, and the optical/infrared transient. The axis in the bottom shows the time that observations took place relative to the time of the GW event t_c. The shaded dashes indicate the times at which the GCN reports were released. The names of the instruments and observing partners are shown below the observing spectra. The insets show pictures of the first detections; the top row: 1. the combined spectrogram of the signals received by the two detectors of aLIGO; 2. the light curves of the short GRB observed by *Fermi*-GBM and INTEGRAL; 3. spectra information taken with the SALT, ESO-NTT, the SOAR 4 m telescope, and ESO-VLT-XShooter [292, 294, 300, 301]. The bottom shows: 1. the initial observations of SSS17a/AT 2017gfo; 2. the first X-ray and radio detections of the source by Chandra and JVLA. The solid horizontal lines indicate when the source was detectable to at least one telescope. Reproduced from [136]. For more details readers are referred to [136].

models of emission [313, 314, 315, 316, 317].

It is possible for an observer to observe an afterglow with or without an associated short GRB depending on whether the initial burst is aligned with the observer's line of sight [318]. If the burst is not aligned, the afterglow of a short GRB associated with a BNS merger will peak at a later time with a lower luminosity [206]. Another reason can be that the associated GRB is not within the sky coverage of gamma-ray satellites at the time the GRB happens. In the case where an associated GRB is absent, an afterglow is known as orphan afterglow and may provide a bright EM counterpart of the GW. It is suggested that the afterglow emission will peak at optical wavelengths for days after the merger, the emission will then become isotropic with a peak at radio wavelengths in weeks - months after the merger [206, 168, 319]. The actual detectability of afterglow depends on the properties of the circumburst environment. The narrow opening angle of X-ray and optical afterglows makes them challenging to detect. Although radio afterglows are relatively isotropic, their detections require very sensitive instruments due to their insufficient brightness indicating rare detection of radio afterglow as an EM counterpart [206].

Regarding the observation of the X-ray afterglows associated with the GRB 170817A, many groups carried out searches and reported the discovery of the X-ray counterpart at the position of the detected kilonova (see Section 2.3.2) 9 days after the merger [320, 305], which was confirmed to exist 15 days after the merger by Chandra [320, 136]. The detection of an X-ray source with position consistent with the host galaxy NGC4993 in the near vicinity of the detected optical/infrared transient was also reported by Margutti et al [321].

The non detection of X-ray source during earlier times after merger placed upper limits on the flux of possible X-ray counterpart source at those epochs [322, 323, 324, 279, 272, 325, 246]. Approximately 16 days after the merger, the detection of the radio counterpart was achieved [326]. Further searches for the radio counterpart covering multiple frequency bands were carried out by many groups [327, 328, 160, 329, 330, 331, 332, 333, 334, 335, 336, 337, 338].

2.3.4 Neutrino emission

Neutrino emission is generated by cataclysmic events such as CCSNe, both long and short GRBs, soft gamma-ray repeaters and magnetars [339, 340, 341, 342, 343, 344, 345, 346, 347, 229], when radiation and matter inside and around astrophysical sources interact with shock-accelerated protons and nuclei.

Neutrinos have the advantages of being able to escape from dense and deep environment and propagating at a speed close to the speed of light through magnetic fields and matter without being altered [348]. The information provided by neutrino detection of a GW source is complementary to that of GW in that neutrinos can trace the interactions between accelerated protons or heavier nuclei and matter or radiation in and around the source while GW carries information of the dynamics

related to the bulk motion of the source [340]. In general, neutrinos are expected to provide valuable information about the physical processes happening in astrophysical engines. For example, if neutrino emission is detected to arrive earlier than GW, it could signal that the GWs are not connected to the activity onset of the central engine [340]. Observing high energy neutrinos can also help understand the mechanism of relativistic outflow dissipation and hadronic content of the source [349].

A BNS merger can emit high energy neutrino emissions (e.g. from MeV to PeV) if a hyper-massive neutron star is formed after the merger [340, 256, 350, 351, 239, 240, 352, 353, 354, 355]. The total energy radiated in neutrinos, the duration as well as the luminosity are determined by a number of the properties of the BNS merger such as the thermodynamical conditions in, the evolution and structure of, the merger, as well as the merger product [350].

Searches for neutrino emission associated with GW170817 were initiated and carried out by IceCube [356], ANTARES [357] and the Surface detector of the Pierre Auger Observatory [358] over a $\pm$500s temporal window centered at the merger [359, 360, 361, 362, 363]. These neutrinos observatories also conducted extended searches for neutrinos within a period of 14 days. No significant neutrino candidates were found [364].

In the scenario of a CCSN, GWs and neutrinos are expected to carry with them information from the core of CCSNe on physical parameters such as rotation, magnetic field and degree of non-axisymmetry and the mechanism that drives the explosions [340]. The time delay between the arrival times of the emission from a CCSN and the associated neutrino pulse is expected to be only differed by a fraction of a second. This means both the detection of GWs and the neutrinos from a CCSN will serve as an early warning for the optical signal that will rise in several hours later [168]. If only the neutrino burst is observed, the on-source window the order of minutes or seconds can be defined for the search of associated GW from CCSNe in detector data.

2.4 Follow-Up Observations for GW150914 and GW151226

The first direct detection of GWs, designated as GW150914, was from a merger of two black holes of $36M_{\odot}$ and $29M_{\odot}$ respectively to form a black hole of $62M_{\odot}$ [130]. After the detection of this event was made by the two LIGO detectors, preliminary information about this event such as the estimate of the merger time, significance and two prompt sky maps produced using Omicron+LALInferenceBurst (oLIB) and cWB were shared with 63 teams of EM astronomers [212]. Omicron is a software algorithm used to detect and characterize transient event is data of gravitational detectors [365]. Sky map generated by BAYESTAR and LALInference were not shared until the end of the observing run. The prompt BAYESTAR was not available at the time of the detection because the detectors were not configured for CBC signals. The sky

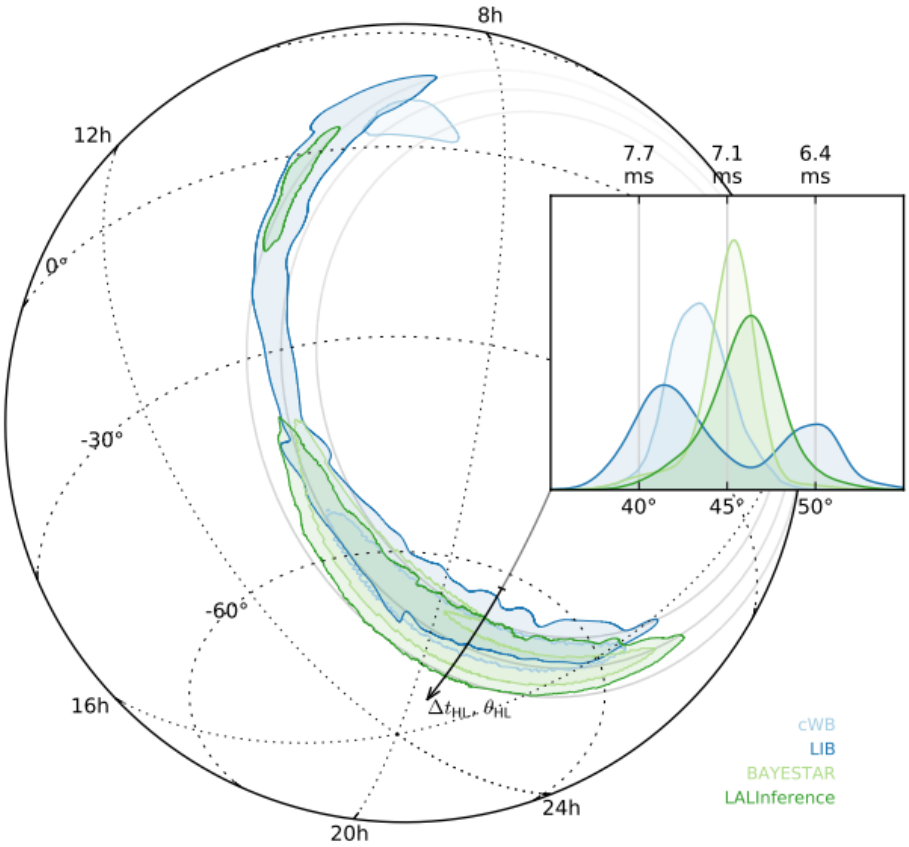

Figure 2.4: An illustration of the sky location reconstruction for GW150914 with different localization algorithms. Different localization algorithms generate sky maps using different methods based on different assumptions resulting in different accuracies and runtime. The four sky maps agree with each other qualitatively. Reproduced from [190].

location reconstruction of the event with these four algorithms is shown in Figure 2.4. As is seen in the figure, the sky localizations with different algorithms were generally qualitatively consistent. The event was localized to a board, long region in the sky of 630 deg^2 at 90% [130].

25 teams of EM partners with access to ground-based and space-based instruments covering a wide range of EM spectrum including gamma-ray, X-ray, optical, near-infrared and radio responded to the GW alerts [190]. Different teams employed different strategies in terms of searching the sky localization error for possible EM counterparts. For example, many facilities tiled the sky localization error using the prompt sky maps sent to them, while a few others focused on local and nearby galaxies based on the thoughts that GW150914 might be an event of BNS merger or that of a CCSN [366].

Due to the vast localization error associated with this event, the coverage of the localization area was not complete in many frequencies. The participating optical facilities together were only able to tile $\sim 50\%$ of the localization error computed using oLIB [190]. Among all the participating teams, only the INTEGRAL SPI-ACS was able to cover the entire 90% area in the energy range from $0.75-1$ MeV [367]. In addition, the assumption that the GW event was a BNS or NSBH event, for which the detectable range was less than that of GW150914, limited the depth reached by these instruments [190]. A few candidate counterparts were found in the optical band, but they were later identified to be supernovae, dwarf novae and active galactic nucleus. No EM counterpart candidates could be conclusively proven to be associated with the event.

Three months later, aLIGO and AdVirgo observed another BBH merger later designated as GW151226. The event was initially localized to ~ 1400 deg^2 at 90% credible level due to the weaker amplitudes of this event compared to GW150914 [131]. In total, 31 EM partners responded to the event alert[1]. The follow-up observation campaign for this event started roughly 1 day later the detection. Similarly, A number of candidate counterparts were detected in the optical band and later identified to be either supernova, dwarf novae or active galactic nucleus.

The majority of the detected GW events so far are BBH mergers, for which there has been little expectation that they will be accompanied by EM counterparts. Nonetheless, the EM follow-up observation campaigns launched for these events still have positive outcomes [190]. First, these campaigns demonstrated that the participating EM partners were capable of tiling the large associated sky localization error with their facilities, identifying counterpart candidates and characterizing photometric and spectroscopic features of candidates within just a matter of days after the event. In addition, the EM follow-up observations of these events are important in placing flux upper limit on any possible EM counterparts that may be generated in any scenarios [190, 136].

[1] http://gcn.gsfc.nasa.gov/gcn3_archive.html

Chapter 3

Optimization of Electromagnetic Follow-up Observation

Given the scientific benefits of a joint detection of the gravitational and EM emission of the same source (see Chapter 2), efforts should be put into observing the associated EM counterparts of a GW trigger. However, in many cases, it is expected that detecting GW associated EM counterparts is not a trivial task. The large localization error of a GW trigger and the detectability of the counterparts cause the detections of these objects challenging and may demand long exposure times even for powerful telescopes [241]. Although prompt localization algorithms (see Section 2.2) can provide quick guidance on the probable locations of the GW source, large localization errors imply that telescopes may not be able to completely search the 90% credible region before the EM counterparts become too faint to detect. For example, the brightness of kilonovae may peak at 1 day after the merger and then start fading [206] as was the case for the kilonova associated with GW170817 [167]. It has been proposed that the excellent sensitivity of future telescopes may alleviate the situation. For example, the infrared sensitivity of the planned James Webb Space Telescope (JWST) may enable detections with short exposure times, thus compensating for its small FOV compared to the localization error [368]. The use of galaxy catalogs may also provide prior information on the direction of an event [369, 370, 371, 241, 372, 373, 374, 375]. Nonetheless, even with JWST and galaxy catalogs, the observation time can still span an entire night, which may make target-of-opportunity BNS merger observations less attractive.

Considering that current and future EM telescopes will be subject to limited observational resources, we might ask how can we maximize the detection probability of a GW triggered EM signature. In this chapter, we describe an algorithm that we developed to answer this question, and here we present the results of a proof-of-concept demonstration applied to four different telescopes including

Subaru-HyperSuprimeCam (HSC)[1] [376] CTIO-Dark Energy Camera (DEC)[2] [377], Pan-Starrs 1[3] [378], Palomar Transient Factory (PTF) [379], and one space mission Einstein Probe (EP) for three different simulated GW events. HSC is a collaboration project between National Astronomical Observatory of Japan, University of Tokyo and several other institutes in Japan, Taiwan and Princeton. HSC is located in Hawaii and saw its first light in 2012. DEC is a international collaboration of more than 120 scientists from 15 institutes. It is mounted on the Blanco 4-m telescope at Cerro Tololo Inter-American Observatory in Chile and saw its first light in 2012. Pan-Starrs 1 is also located in Hawaii. Similar to the above telescopes, this project involves several universities and institute including the University of Hawaii Institute for Astronomy and Massachusetts Institute of Technology. The operation of it started in 2008. PTF is located in San Diego and started its operation in 2009.

This algorithm takes as inputs GW sky localization information, and returns a guidance strategy for time allocation and telescope pointing for a given EM telescope. In the most part of this chapter, we restrict the discussion to kilonovae for ground-based telescopes since as discussed in Chapter 2, kilonovae have been suggested to be the most favorable EM counterpart for GW signals from BNS and NSBH mergers among many other potential EM counterparts of GW events [247, 206, 260]. We also further restrict the discussion to kilonovae from BNS mergers and leave the discussion of kilonova from NSBH for future study. This is in part due to the fact that our chosen GW data set from [205] contains only BNS mergers. However, we remind the readers that there is no theoretical restriction preventing us from applying our algorithm using other EM counterpart models and neither is it restricted to using only GW sky maps from CBC events. In addition, in Section 3.4, we consider possible X-ray afterglow from magnetar as an intermediate product of a BNS merger as the target counterpart for EP. Other methods for improving the detection probability by finding observing fields exist such as that presented in [380, 381]. However, the former mostly considers fixed field locations and is concerned with telescopes with large FOV. The latter primarily focuses on the setting and rising of the Sun to be the only constraining factors of the coverage of the GW sky localization error region. It has been shown in [381] that observing fields with pre-defined locations may cover slightly more GW probability than methods allowing the fields to move freely on the sky if the telescopes are to observe $\geqslant O(10)$ fields. These methods could be potentially utilized to improve our method. However, in reality, given the peak luminosity of kilonovae, their likely distances and the amount of available observation time, most telescopes will only be able to observe a few fields if required to reach the depth necessary to capture kilonovae as EM counterparts. In addition, unlike the aforementioned studies, our method distinguishes itself by considering optimization of the time allocation given to the observing fields. This chapter is organized as follows: the methodology is

[1] http://www.subarutelescope.org/Observing/Instruments/HSC/
[2] http://www.ctio.noao.edu/noao/node/1033
[3] http://pan-starrs.ifa.hawaii.edu

introduced in Section 3.1 and we describe the implementation in Section 3.2. The results for one of the three simulated events obtained with the algorithm are given in Sections 3.3 and 3.4 along with a discussion in 3.5. The rest of the results is presented in Appendix A. The possible future directions of this work are provided in Section 3.6, and our conclusions are presented in Section 3.7.

In this work, we consider scenarios consistent with only two or three operating GW detectors. For such a network the sky location estimate for a GW event can cover a large fraction of the sky ($\sim$100 deg^2 [205]), posing a significant challenge to telescopes with FOVs of order $\sim$1 deg^2 trying to find counterpart signals in the EM spectrum (For larger detector networks it has been shown that the size of GW sky localization error regions can be reduced considerably [151, 382, 241, 89, 383].).

3.1 Optimisation Methodology

As a proof-of-concept of the EM follow-up method, here we have chosen to focus on kilonovae as the counterpart signatures. We have also adopted some simplifications which will be relaxed in future studies.

We assume that the available observation time is short compared to the luminosity variation timescale of a kilonova. This is validated by the fact that kilonova's luminosity variation timescale is estimated to be $\sim$days to a week, which is longer than a reasonable continuous EM observation. This approximation allows us to assume that a kilonova has constant luminosity during the observation period. We also only consider the use of R-band luminosity information, however the method presented can be extended to other regions of the EM spectrum. We note that kilonovae are predicted to have higher peak luminosities in the i-band but we do not consider the i-band in this study for two reasons, 1) although kilonovae luminosity indeed peaks higher at i-band, the difference is not dramatic, 2) SDSS survey for science indicates that the sky brightness is one magnitude brighter in i-band than in R-band, counteracting the increase in the peak luminosity of kilonovae in i-band [384]. In reality, identifying a target EM counterpart requires tracking the object's light curves, leading to several observations of the same point in the sky over several days. However, in this work we deal with the problem of detection, rather than identification. We consider only single observations and calculate optimized pointing directions and durations for a constrained total observation length and constant luminosity. Subsequent observations for the purpose of identifying variation within a field can be achieved by repeating our proposed observing strategy at some later time.

In general, GW events could be localized to $\gtrsim$100 deg^2, which is much larger than a typical EM telescope's FOV ($\lesssim$1 deg^2). We therefore do not consider the telescope's rotation around its own axis, hence throughout this work, reference to single telescope pointing implies a rectangular Charge-coupled device (CCD) image with edges parallel to lines of longitude and circles of latitude.

We also assume that the prior information from a GW trigger can be approximated

as having independent sky location and distance probability distributions. Generally, this may not be the case, however, our mathematical treatment can be greatly simplified under this assumption. We note that the sky maps available for our chosen dataset (discussed in Sec. 3.2) naturally lend themselves to this approximation since no distance information was computed as part of the rapid sky localization study reported in [385][4]. The final assumption is that the EM telescope can see every direction regardless of the location of the Sun, Moon, and the horizon. The issue of optimization of EM follow-up observations under the time-critical constraints such as those imposed by a source dipping below the horizon is explored in [381].

3.1.1 Bayesian Framework

We use $D_{\rm EM}$ to denote the successful detection of an EM counterpart. The probability of this occurring depends on the size of the selected telescope's FOV ω, the observed sky locations(α, δ), and the exposure time τ. The posterior probability of successful detection is then given by

$$P(D_{\rm EM}|\omega, \tau, I) = \int_{N^*}^{\infty} dN \; p(N|\omega, \alpha, \delta, \tau, I). \tag{3.1}$$

Here, I is prior information that includes the selected telescope's parameters, such as its photon collecting area A, filter and CCD efficiency. For a particular observation the number of photons N collected by the telescope is

$$N = 10^{\frac{25-m}{2.5}} \times (\tau A)\,, \tag{3.2}$$

where m is the apparent magnitude of the observed source. The threshold count N^* is the criterion for detection determined by the SNR threshold, background noise and the selected telescope's sensitivity. The value of N^* is given by Eq. 3.2 with input values of m and τ corresponding to the selected telescope's detection threshold (see Table 3.1[5]). The constant 10^{10} in Eq. 3.2 is the number of photons per second at $m = 0$. In practice, the value of N^* should also account for the change in background light accumulated for different choices of observation time τ, however, for simplicity we ignore this effect in this work. Since the number of photons expected from a target EM counterpart depends on its absolute magnitude M, distance R from the telescope, and how likely that the GW event is located within the field being observed, Eq. 3.1 can be expanded such that

$$P(D_{\rm EM}|\omega, \tau, I) = \int_{N^*}^{\infty} dN \int dM \int dR \times$$
$$\int_{\omega} d\alpha \, d\delta \; p(N|M, R, \tau, I) p(M|I) p(\alpha, \delta, R|I). \tag{3.3}$$

[4]The rapid sky localization algorithm BAYESTAR has since been updated to also provide rapid distance posteriors [386].

[5]We focus our discussion on ground-based telescope in this section. Discussion on EP will be presented in Section 3.4.

Table 3.1: Telescope parameters

Telescope	Aperture (m)	FOV (deg^2)	Exposure (s)	Sensitivity (5-σ mag in R-band)	N^*/A (m^{-2})
DEC	4.0	3.0	50	23.7	162.0
HSC	8.2	1.13[6]	30	24.5	46.5
Pan-Starrs	1.8	7.1	60	22.0	930.5
PTF	1.2	7.0	60	20.6	3378.3
LSST	6.7	9.6	15	24.5	23.26

The quantity $P(N|M, R, \tau, I)$ is the probability of receiving N photons from a source, given its absolute magnitude M, distance R, and observation time τ, and is described by a Poisson distribution. Since we assume that the prior distribution on the distance to the target EM counterpart is statistically independent of the prior distribution on its sky location, Eq. 3.3 can be written as

$$P(D_{\rm EM}|\omega, \tau, I) = P_{\rm GW}(\omega) \times P_{\rm EM}(\tau) \tag{3.4}$$

where,

$$P_{\rm GW}(\omega) = \int_{\omega} p(\alpha, \delta|I) d\alpha\, d\delta, \tag{3.5a}$$

$$P_{\rm EM}(\tau) = \int dM \int dR \int_{N^*}^{\infty} dN\, p(N|M, R, \tau, I) p(R|I) p(M|I). \tag{3.5b}$$

It should be noted that the GW sky localization information used for this work has been marginalized over distance, meaning that the GW information represents a 2D error region projected onto the sky. However, as a reasonable approximation, the marginalized (and therefore missing) low-latency distance uncertainty can be approximated by a Gaussian distribution [142, 386]. Hence we assume a Gaussian prior with mean = 200Mpc and standard deviation = 60Mpc for the distance. We note that in more general cases, specifically for GW events with low SNR this Gaussian approximation becomes invalid. In principle any form of positional information can be incorporated into our analysis and therefore our method can be adapted to include more realistic GW distance information. It is also possible that further constraints from galaxy catalogs can also be incorporated into our method [372].

We assume the least informative prior on peak luminosity such that $p(L|I) \propto L^{-\frac{1}{2}}$. It then follows that the prior on peak magnitude is given by

$$p(M|I) \propto 10^{-\frac{M}{5}} \tag{3.6}$$

[6]The full HSC FOV is 1.77 deg^2 but $\sim$ 20% is used for calibration purposes.

where we assume M has a prior range of $(-13, -8)$ as defined by the peak magnitudes of the models in [252].

The probability of EM detection as defined in Eq. 3.1 considers only one observing field. Given the size of a GW sky localization error region, and the typical size of an EM telescope's FOV, the number of fields needed to be considered is >1. If an error region enclosing 90% of the GW probability covers $S\,\mathrm{deg}^2$ and the EM telescope FOV is $w\,\mathrm{deg}^2$, the maximum number n of fields[7] required to cover the error region at 90% can be estimated as $n \lesssim S/\omega$.

One might assume that observing as many fields as possible is optimal but we will show that telescope time is better spent by observing k fields where k lies in the range $[1, n]$. This occurs when it becomes more beneficial to observe a particular field for longer than observing a new field.

For a given total observation time T, we are free to choose which fields we observe and the observation time allocated to each field. We represent these quantities by the vectors $\{\omega^{(k)}\}$ and $\{\tau^{(k)}\}$ respectively where k is the total number of chosen fields. Maximizing the detection probability of a kilonova amounts to finding the values of these vectors and the value of k which maximizes:

$$\begin{aligned} P(D_{\mathrm{EM}}|k) &\equiv P(D_{\mathrm{EM}}|\{\omega^{(k)}\}, \{\tau^{(k)}\}, I) \\ &\equiv \sum_{i=1}^{k\leq n} P(D_{\mathrm{EM}}|\omega_i^{(k)}, \tau_i^{(k)}, I). \end{aligned} \tag{3.7}$$

The choices of $\{\tau^{(k)}\}$ are subject to the constraint that

$$kT_0 + \sum_{i=1}^{k} \tau_i^{(k)} = T, \tag{3.8}$$

where T_0 represents the time required to slew between telescope pointings and/or perform CCD readout, and is equal to max(slew time, CCD readout time). We treat T_0 as independent of the angular distance between pointings.

The expression we have for kilonova detection probability (Eq. 3.7) as a function of the number of observed fields depends on our choice of field location and observation time within each field. Given a number of fields k we begin choosing fields with a greedy algorithm, which will be described in section 3.2. Once the k fields have been chosen, they are represented by $\{\omega^{(k)}\}$ and Eq. 3.7 is maximized over the parameter vector $\{\tau^{(k)}\}$ to obtain the optimal kilonova detection probability. This is then repeated for each k in the range $[1, n]$ to find the optimal number of observed fields k.

[7] In practice, n can be slightly larger due to overlapping fields.

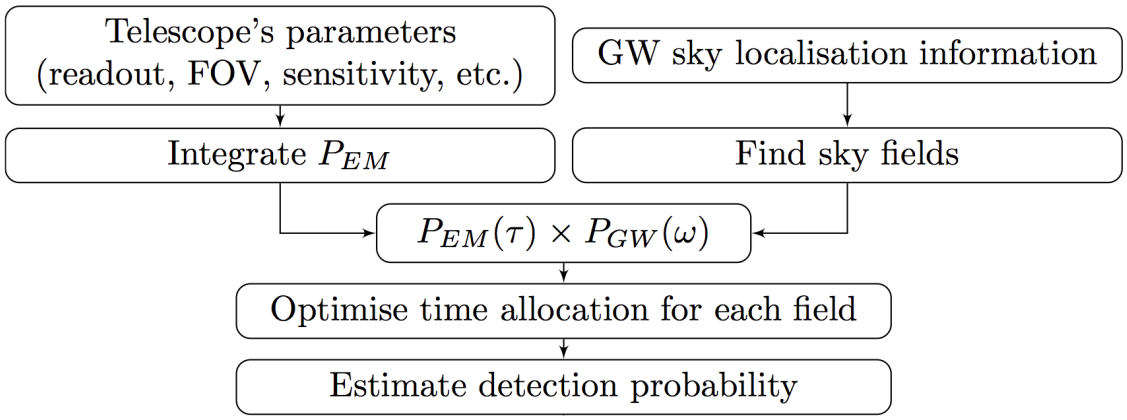

Figure 3.1: The process for generating an optimized observing strategy. Our algorithm takes two inputs: the GW sky localization information and a set of telescope parameters. After integrating over the number of received photons N, the source distance R, and the source absolute magnitude M, the algorithm returns the probability of detection of an EM kilonova signal $P_{\rm EM}$ as a function of the field observation time τ. In parallel, for each choice of the total number of observed fields k, the algorithm selects the fields using a greedy algorithm. Based on the enclosed GW probability within each field the corresponding optimized observation times are computed using a Lagrange Multiplier approach. The total EM detection probability is then output for each choice of k.

3.2 Implementation

In this section we describe the processes for applying the GW sky localization information and generating the optimal observing strategy. The flow chart in Figure 3.1 is a visual representation of this process.

As shown in Figure 3.1, we require information regarding the sky position of the GW source which we obtain from the BAYESTAR algorithm [207] (other algorithms for low latency GW sky localization exist such as that proposed by [387]). This algorithm outputs GW sky localization information using a HEALPix[8] coverage of the sky. Each HEALPix point corresponds to a value of the GW probability and represents an equal area of the sky. BAYESTAR can rapidly (in ∼10s) generate event location information and has been shown in [205] to closely match results from more computationally intensive off-line Bayesian inference methods [142]. The simulated GW events used in this work are from BNS systems and taken directly from the data set used in [205].

In this section, we consider follow-up observations using four telescopes (HSC, DEC, Pan-Starrs, and PTF) for three simulated representative GW events (see

[8] http://healpix.sourceforge.net

Table 3.2) which are studied assuming three total observation times $T = 2, 4, 6$ hrs. For any telescope, GW event and total observation time, the first stage of our procedure is to calculate the maximum number of fields n required to cover the sky area enclosed by the 90% probability contour of the GW sky region.

In order to identify the possible observing fields for a given GW event, the greedy algorithm identifies the least number of HEALPix locations on the sky whose sum of GW probability is equal to the desired confidence level (in our case 90%). Then, assuming that each of those points represents the center of an observing field we compute the sum of GW probability from each HEALPix point whose center lies within each of those fields. The field returning the maximum sum of the GW probability among those fields will be the first field. Subsequent fields are found by the same procedure, with the HEALPix points in the previous fields ignored. The summed probability within each field is an accurate approximation to the quantity $P_{\rm GW}(w)$ as defined in Eq. 3.5a. The n selected fields are labeled in the order with which they are chosen and hence their label indicates their rank in terms of enclosed GW probability. Therefore the first $k \leq n$ fields represent our optimized choice of the values of $\{\omega^{(k)}\}$ in Eq. 3.7.

As shown in Eqns. 3.4, 3.5b and 3.7, the detection probability achieved by observing k selected fields can be expressed as the sum of the product of the EM and GW probabilities in each field. For each value of k in the range $[1, n]$ we apply a Lagrange Multiplier to find the solution for the values $\{\tau^{(k)}\}$ that maximizes the detection probability given by Eq. 3.7. This is subject to the constraints defined in Eq. 3.8 and the value of k that returns the highest detection probability is identified as the optimal solution. The analysis therefore guides us as to which subset of fields should be observed with the selected telescope and how much time should be allocated to each of those selected fields given the total observation time constraint.

3.3 Results: Ground Based Telescopes

In this section we present the results of our algorithm using our four example telescopes applied to simulated GW event follow-up observations. These events are taken from the dataset used in [205] and are designated with the IDs 28700, 19296 and 18694. The error regions for these events each cover $\sim$300 deg^2, $\sim$100 deg^2, and $\sim$30 deg^2 respectively and details of these events are presented in Table 3.2. We will present the results for event 28700 in this section and the rest in Appendix A. But the discussions in this section, and Sections 3.4 and 3.5 will include all the results for a more complete picture. These events were chosen to represent the potential variation in sky localization ability of a global advanced detector network. We highlight that the actual injected distances for our chosen events are 51 Mpc, 27 Mpc and 12 Mpc respectively, while for our analysis we have assumed a distance of 200 Mpc for each event. However, the validity of this work is not undermined. The injected events were originally simulated assuming a 2 detector aLIGO First Observational Run configuration. Our

Table 3.2: Simulated GW event parameters.

Event ID[1]	SNR	90% Region (deg^2)	Chirp Mass ($M_\odot$)
28700	16.8	302	1.33
19296	24.3	103	1.28
18694	24.0	28.2	1.31

analysis assumes a 2(3) detector design sensitivity aLIGO configuration. The SNR and sky localization for an event at 200 Mpc in the latter configuration is comparable (to within factors of ∼few) to events at a few tens Mpc for the former configuration.

Figures 3.2 and 3.3 shows the optimized tiling of observing fields obtained using the greedy algorithm approach. For each telescope we show sky maps of the GW probability overlaid with the 90% coverage tiling choices for the three representative GW events (see Figures A.1, A.2, A.3 and A.4 for event 19296 and 18694). The FOVs of the telescopes range from 1.13 deg^2 to 7.1 deg^2 and as such the required number and location of tilings differ accordingly. The largest and smallest number of observation tilings are 230 and 7 for the largest GW error region (ID 28700) using HSC and for the smallest error region (ID 18694) using either Pan-Starrs or PTF, respectively.

Each of the event maps are the result of an analysis assuming only 2 GW detectors. Without a third detector the sky location of an event is restricted to a thin band of locations consistent with the single time delay measurement between detectors. This degeneracy is partially broken with the inclusion of antenna response information resulting in extended arc structures. The third event that we consider (ID 18694) has sufficient SNR and suitable orientation with respect to the detector network that even with 2 detectors the sky region is well localized and is only partially extended. We consider this event to be approximately representative of sky maps obtained from a 3 detector network. We also note that given the imperfect duty factors of both the initial and advanced detectors it is highly likely that future detections will be made whilst one or more detectors are offline. We therefore use the first 2 example events (ID 28700 and 19296) as simultaneously representative of such a 2-detector scenario and of the potential situation in which a third detector is significantly less sensitive than the other two.

Figures 3.4, 3.5 and 3.6 display the results of the simulated EM follow-up observations for the event labeled 28700 (see Figures A.5, A.6 and A.7 for event 19296, Figures A.8, A.9 and A.10 for event 18694). The assumed total observation times are 6 hrs, 4 hrs and 2 hrs for Figures 3.4, 3.5 and 3.6 respectively. The plots on the top of the figures show the optimized detection probability $P(D_{\rm EM}|k)$ as a function of the total observed number of fields k. The plots on the bottom of the figures display the optimal time allocations corresponding to the value of k returning the highest detection probability (indicated by a circular marker in the detection probability plots on

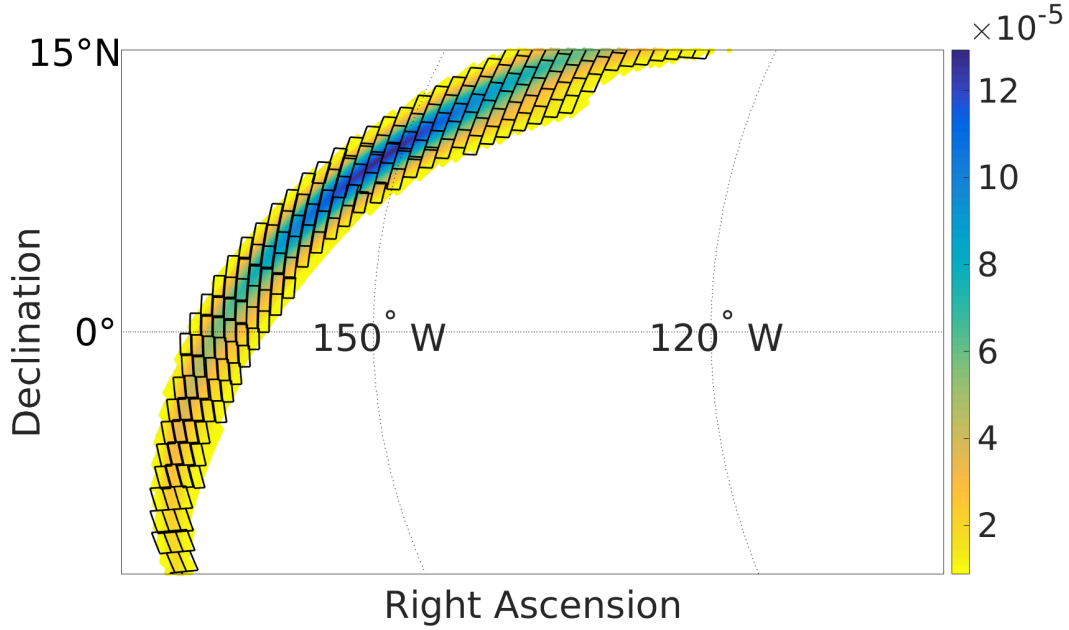

(a)

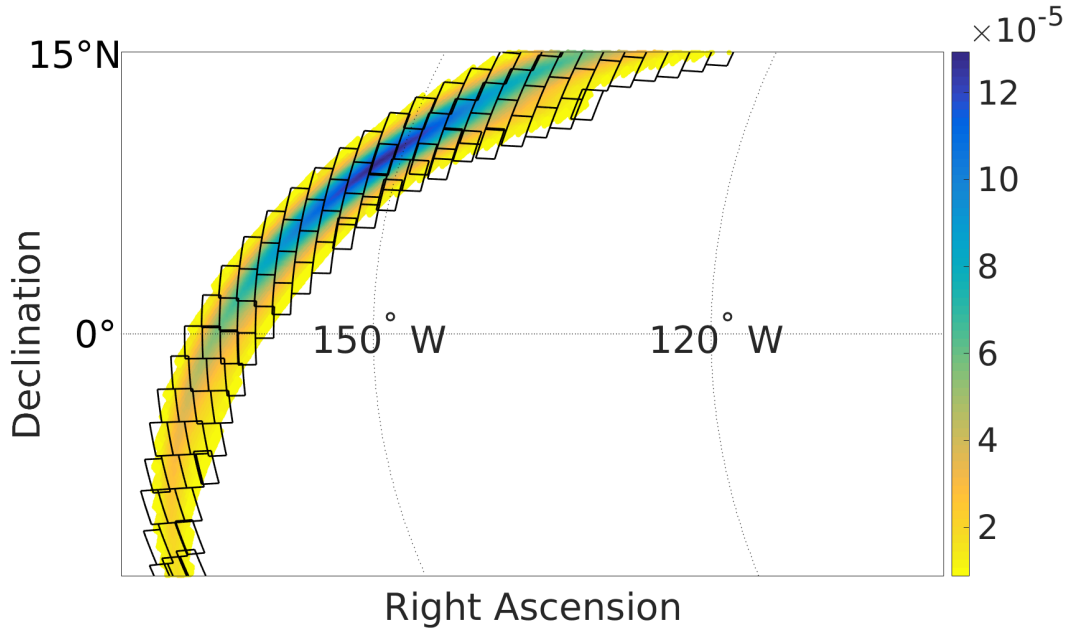

(b)

Figure 3.2: The optimized locations of the observing fields covering 90% of the GW probability for telescopes and for the simulated GW event 28700. The upper plot corresponds to HSC and the lower plot DEC. In each plot the GW sky error is shown as a shaded region with the color bar indicating the value of posterior probability density.

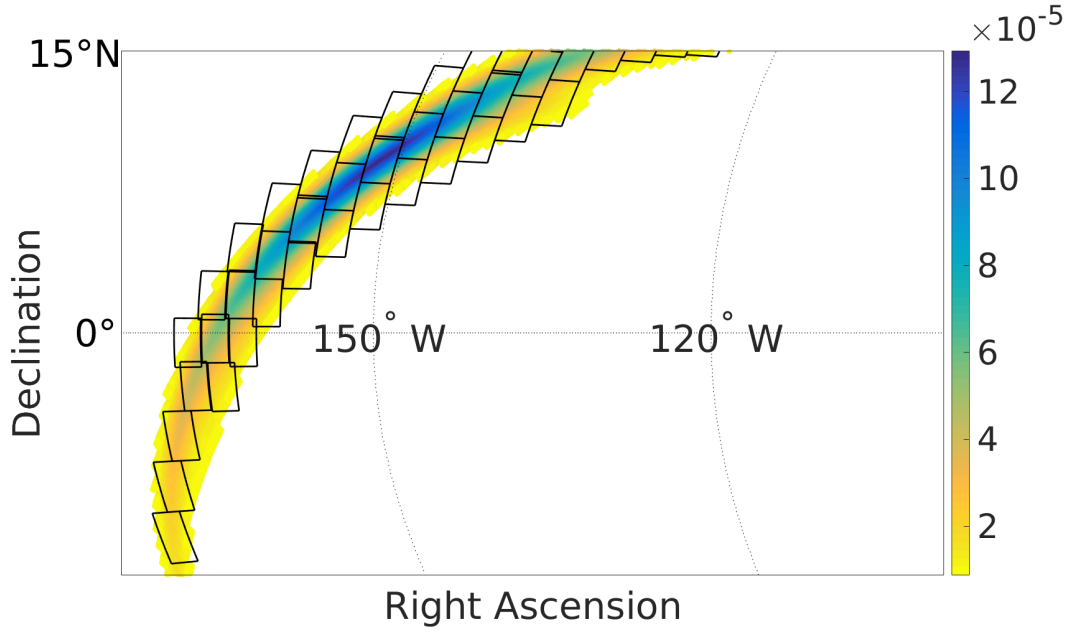

(a)

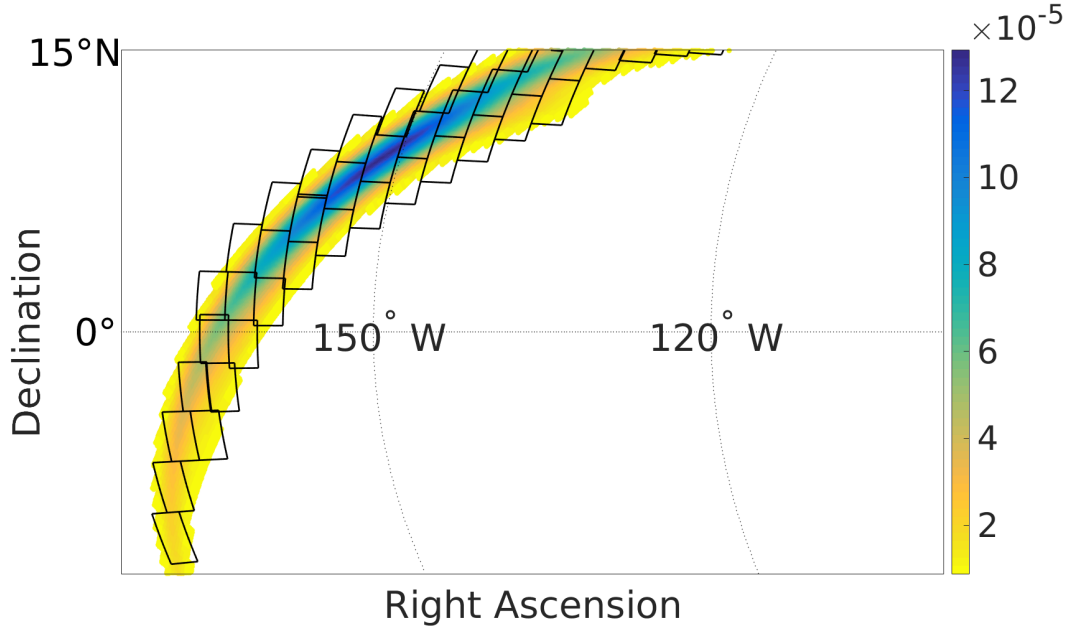

(b)

Figure 3.3: The same as Figure 3.2 but for Pan-Starrs(top) and PTF(bottom).

the top of the figures). The indices refer to the labels assigned to the fields when being chosen by the greedy algorithm.

We highlight the asymptotic behavior of the detection probability curves in Figures 3.4, 3.5 and 3.6 (as well as Figures A.5, A.6, A.7, A.8, A.9 and A.10). This is due to a particular feature of our algorithm and is explained as follows. As the number of fields are increased we approach an optimal value k^* where to observe an addition field with any finite observation time would actually reduce the detection probability. This occurs where the gains from an additional field are outweighed by the losses incurred by reducing the lengths of the observations of the other fields. In this case, for a given value of k above the optimal value the optimal choice is to allocate $\tau = 0$ to all fields with index greater than k^*. If we know that we will allocate no time to these fields then we also have no need to slew to them or to readout from the CCD. Hence the optimal time allocations and also detection probability for values of $k > k^*$ remains constant at the maximum value.

As a comparison, we introduce a second observing strategy for time allocation in which all the fields are observed with equal time. We call this method the equal time strategy. For each value of k, subject to the total observation time constraints and slew/readout time, the time allocated to each field is given by $T/k - T_0$. The values of $P(D_{\rm EM}|k)$ obtained using this strategy are plotted as dashed lines in the plots on the top of Figures 3.4, 3.5 and 3.6 and the corresponding figures in Appendix A. The time allocations corresponding to the peaks of the dashed lines are plotted as flat lines (constant equal values) in the plots on the bottom of the figures. The resultant maximal probabilities and corresponding optimal number of fields for both time allocation strategies are given in Table 3.3 [9] for all simulated events. We also indicate the relative gains in detection probability obtained using our fully optimized (Lagrange multiplier) approach relative to the equal time strategy.

In Figure 3.7 (Figures A.11 and A.12 for the other two simulated GW events) we provide an insight into the detection potential of future telescopes and those not included in our analysis. We have computed the detection probability $P(D_{EM}|k)$ and corresponding optimal number of fields k as a function of arbitrary FOV and telescope sensitivity. We define this sensitivity via the quantity N^*/A, the number of photons per m^2 required for detection (see Eq. 3.2). For this general case we consider only a 6 hr total observation of each of the 3 simulated events. For reference we include the 4 telescopes already considered plus the proposed LSST [388] plotted with points indicating their locations in the FOV, telescope sensitivity plane. The relevant parameters for all telescopes included are given in Table 3.1.

[9] This table is for total observation time equal to 6hrs. For total observation time equal to 4 and 2hrs, please refer to Tables A.1 and A.2 respectively.

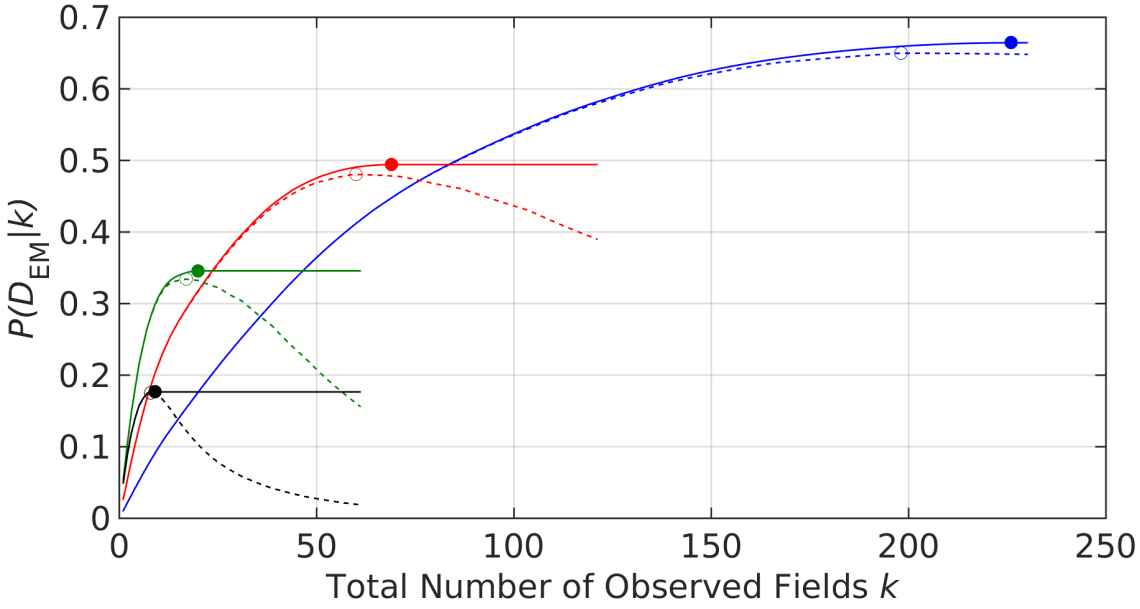

(a)

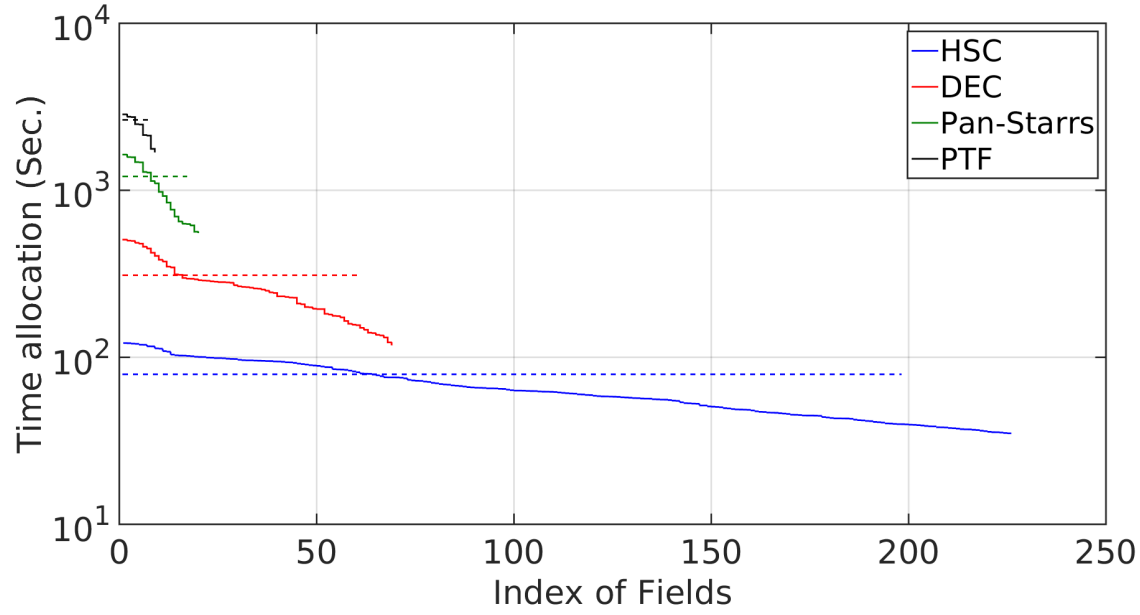

(b)

Figure 3.4: The results of simulated EM follow-up observations for the $\sim$300 deg^2 GW event (ID 28700). We show the optimized EM detection probability as a function of the number of observing fields (top) and the allocated observing times for the optimal number of fields (bottom). The total observation time is 6 hrs. The 4 solid curves in each plot correspond to the optimal time allocation strategy applied to each of the 4 telescopes. The dashed lines show results for the equal time strategy. The solid markers and the circles indicate the number of observing fields at which the maximum detection probability is achieved using the optimal time allocation strategy and the equal time strategy respectively.

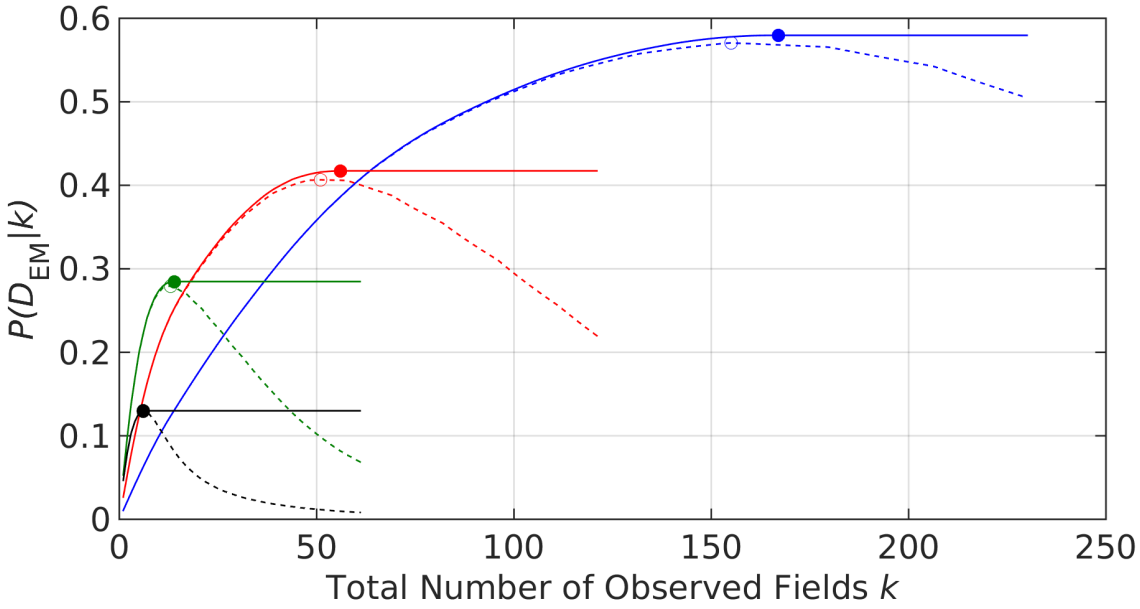

(a)

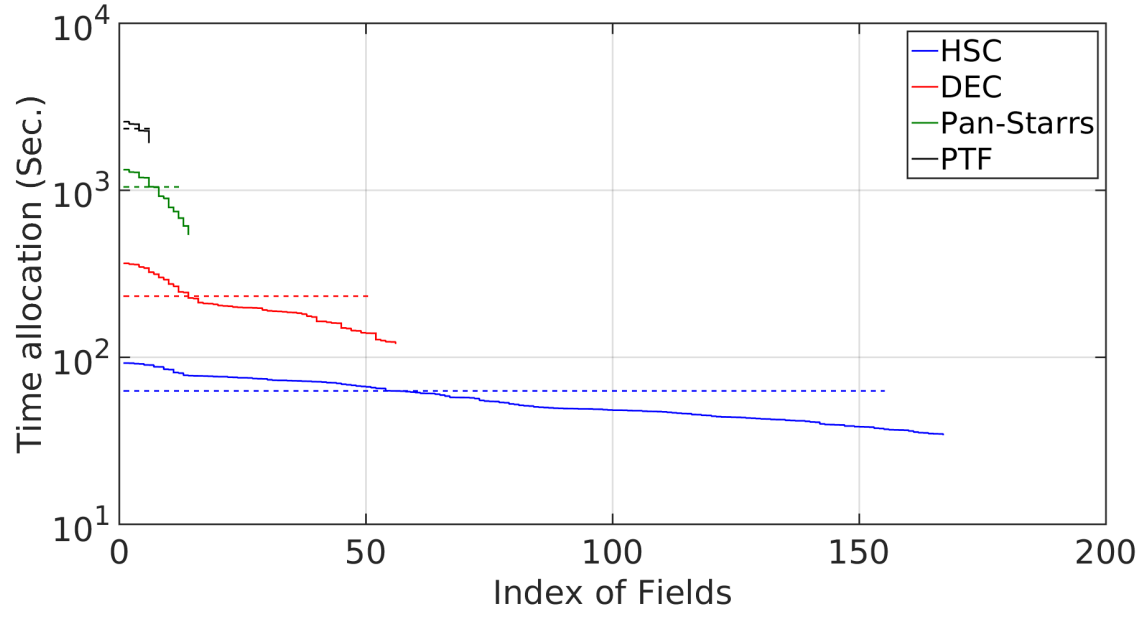

(b)

Figure 3.5: The same as Figure 3.4 but the total observation time is 4 hrs.

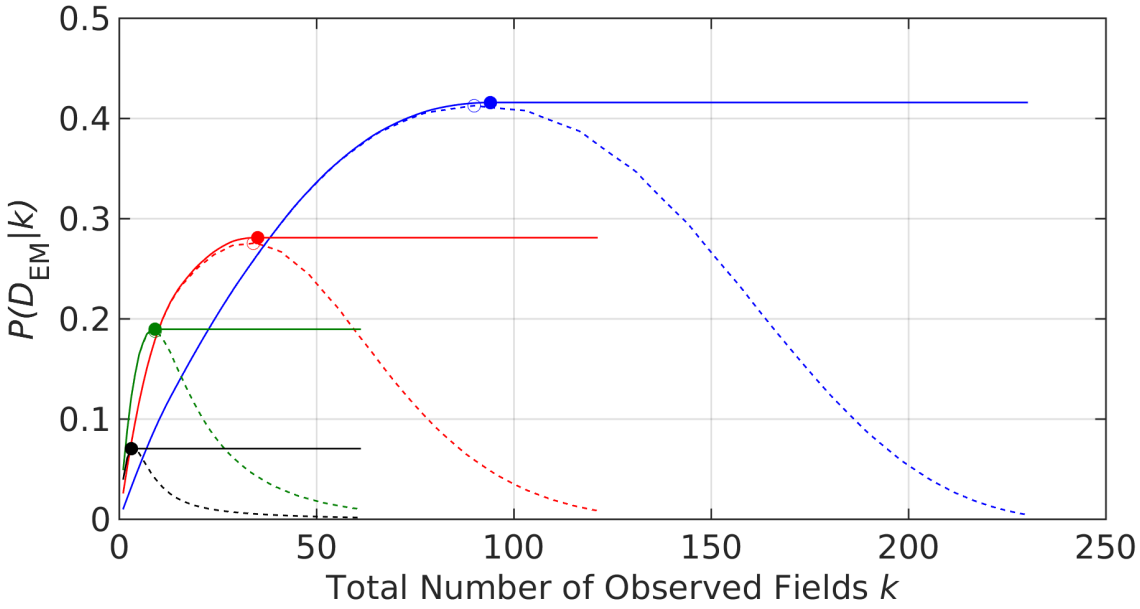

(a)

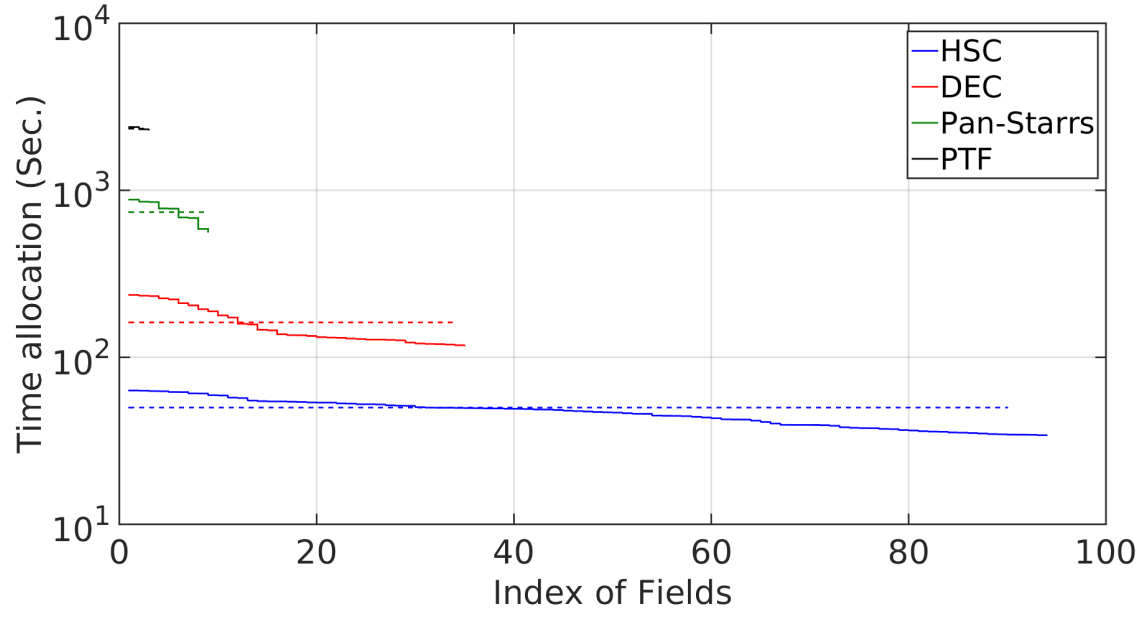

(b)

Figure 3.6: The same as Figure 3.4 but the total observation time is 2 hrs.

Table 3.3: The EM detection probability using both the optimal and equal time strategies

Telescope	Event ID	Strategy	EM detection probability Optimal number of fields 6 hrs		Relative Gain
HSC	28700	LM[10]	66.4%	(226)	1.4%
		ET[11]	65.0%	(198)	
	19296	LM	78.1%	(106)	1.1%
		ET	77.0%	(103)	
	18694	LM	93.7%	(47)	0.8%
		ET	92.9%	(47)	
DEC	28700	LM	49.4%	(69)	1.4%
		ET	48.0%	(60)	
	19296	LM	71.5%	(50)	4.3%
		ET	67.2%	(39)	
	18694	LM	85.3%	(16)	2.3%
		ET	83.0%	(16)	
Pan-Starrs	28700	LM	34.6%	(20)	1.2%
		ET	33.4%	(17)	
	19296	LM	57.4%	(12)	1.5%
		ET	55.9%	(11)	
	18694	LM	77.2%	(7)	4.0%
		ET	73.2%	(6)	
PTF	28700	LM	17.7%	(9)	0.2%
		ET	17.5%	(8)	
	19296	LM	34.1%	(7)	0.3%
		ET	33.8%	(7)	
	18694	LM	56.9%	(4)	0.8%
		ET	56.1%	(3)	

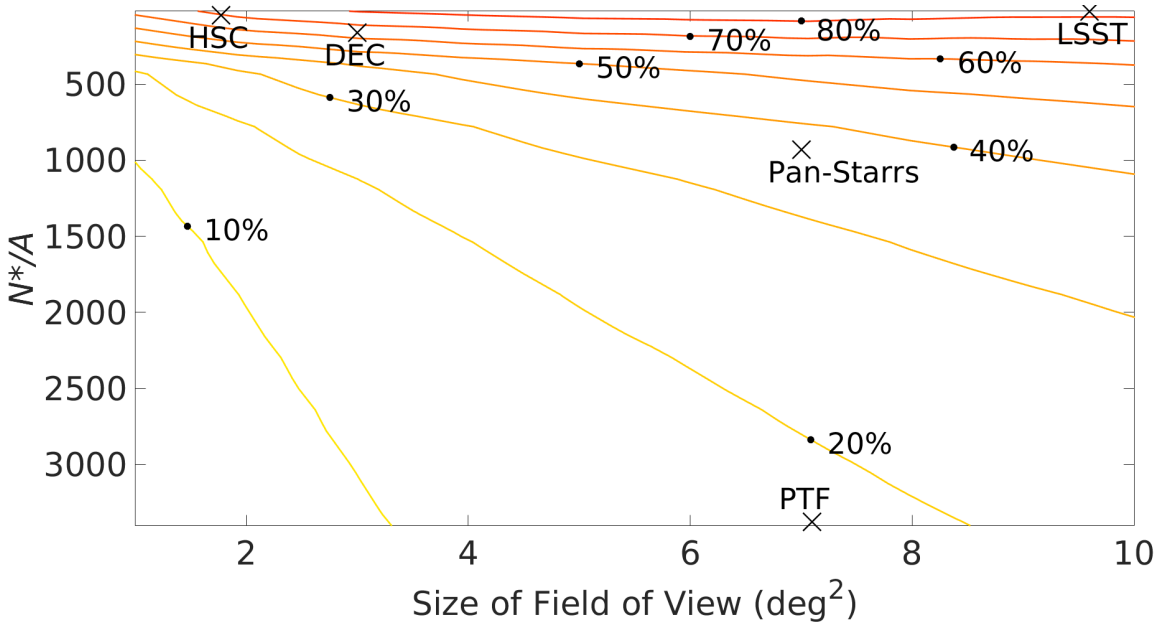

(a)

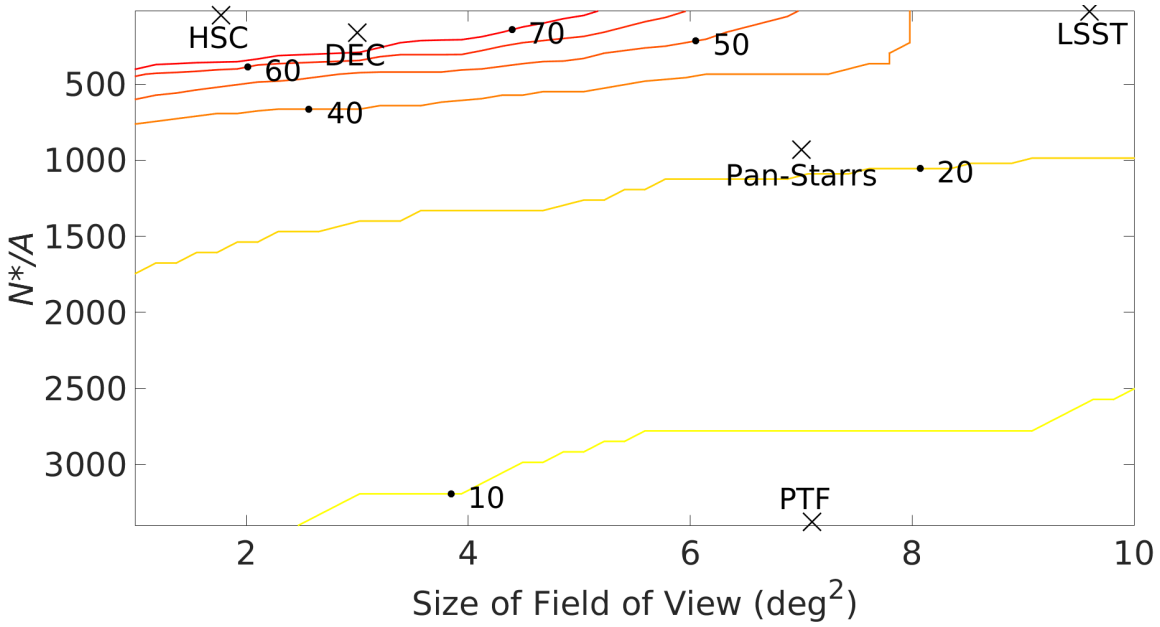

(b)

Figure 3.7: Contours of EM follow-up performance of kilonovae as a function of the size of telescope FOV and sensitivity assuming a 6 hr total observation. The results are for simulated GW event 28700, $\sim$300 deg^2. We plot contours of equal detection probability (top) and the corresponding optimal number of observing fields (bottom). Overlaid for reference on all plots are the locations of the telescopes considered in this work (including the proposed LSST).

3.4 Results: Einstein Probe

In this section, we introduce EP, and discuss the application of the algorithm to the design of it for observing BNS associated EM counterparts in the X-ray spectrum. EP is a space mission proposed by the Chinese Academy of Sciences Institute and Tsinghua University in 2002 [389]. This mission is dedicated to the discovery of astrophysical X-ray transient sources of which the energy of photons fall within the range 0.5 - 4 keV (the bandpass for EP), and to the study of the physics associated with these phenomena [389]. The primary target sources for EP include GRBs, active galactic nuclei, supernova shock breakouts and stellar coronal flares [389].

EP is still in its design stage. The current design is that EP will be equipped with two telescopes for different purposes. The first telescope will be built with a FOV as large as $60^\circ \times 60^\circ$ for wide field survey, called Wide-field X-ray Telescope (WXT) [389]. This telescope will make use of the novel Micro-Pore Optics configuration [390], which allows for a focusing gain ~ 2000 and a large FOV instrument that is light in weight. The sensitivity of the telescope is $\sim 10^{-11}$erg s^{-1} cm^{-2} [389].

The other telescope is a narrow-field telescope with a FOV of $1^\circ \times 1^\circ$, called Follow-up X-ray Telescope (FXT). It is mounted at the center of the WXT [389]. The smaller FOV and higher sensitivity ($\sim 3 \times 10^{-12}$erg s^{-1} cm^{-2}) of the telescope allow the telescope to focus incoming X-rays and perform follow-up observations of any sources detected with the WXT [389].

It is suggested that if the two NSs of a BNS merger are not too massive, the intermediate product of the merger could be still below the maximum mass allowed for a rapidly spinning NS [391]. Such a massive NS would survive for milliseconds and launch a wind that is approximately isotropic. The dissipation of the wind would then power an X-ray afterglow with a duration of 10^3-10^4s [391]. The isotropy of the X-ray emission would increase its detectability and could be detectable source to EP [389].

However, EP is an instrument on board a satellite and although it has some ability to slew, it cannot observe a source continuously for a long period of time [389]. As the satellite orbits the earth, an area in the sky will come in field and move out of field (private communication with Weimin Yuan). This may limit the ability of EP to confidently detect a source. One way to solve this problem is to increase the sensitivities of both the WXT and FXT, while maintaining the large FOV. However, the mission is funded on a relatively low budget [389] and there is an inevitable trade-off between the size of the FOV and the sensitivity.

To investigate different combinations of the size of FOV and the sensitivity of EP for the detections of BNS associated X-ray emission under the physical constraints on observation, we apply the optimization algorithm described above and carried out a simulation. To reflect the constraints on manipulation and observation, we take several modifications in the computation. First, we assume the total observation time is equal to 1000 seconds. When computing how many photons from a source

will be received by the EP, we assume average energy for each photon received which is defined by the bandpass,

$$\bar{\mathrm{E}} = \frac{1}{2}(\mathrm{E_{max}} + \mathrm{E_{min}}), \tag{3.9}$$

where $\bar{\mathrm{E}}$ is the average energy of a photon. $\mathrm{E_{max}}$ and $\mathrm{E_{min}}$ are the maximum and minimum energy of a photon within the bandpass range respectively. The number of photons received can then be defined as

$$\mathrm{n_p} \sim \frac{\mathrm{L_{peak}}}{\bar{\mathrm{E}}}, \tag{3.10}$$

where $\mathrm{n_p}$ is the number of photons from a source received by EP and $\mathrm{L_{peak}}$ the peak luminosity of the X-ray afterglow. In addition, we focus on the best scenario in which EP happens to be in a position in its orbit for it to observe the afterglow when the event happens. This may seem an oversimplification. However, as we focus on the optimal design of the telescopes rather than the actual detection probability, such a simplification allows to test the design of EP directly. Again, we employ the Bayesian framework described in Section 3.1.1. Here, we employ a conservative range from 10^{40} to 10^{44}erg/s for the peak luminosity of the X-ray afterglow [391]. For distance, we employ the same Gaussian distribution for distance as we stated in Section 3.1.1 (mean equal to 200Mpc and a standard deviation equal to 60Mpc).

Similar to what we have done in Figure 3.7, we computed the detection probability $P(D_{EM}|k)$ and corresponding optimal number of fields k as a function of arbitrary FOV and sensitivity of EP. The FOV and sensitivity here are referred to as the FOV and the sensitivity of the WXT since FXT only performs follow-up observations of the sources detected with WXT. The size of the WXT's FOV in this simulation is within the range from 100 - 3600 deg^2 and the sensitivity is between $\sim 10^{-11}$erg s^{-1} cm^{-2} and $\sim 10^{-12}$erg s^{-1} cm^{-2}. Again, we use the same events as we did for ground-based telescopes. We present the results for event 28700 in a manner similar to Figure 3.8, and the results for events 19296 and 18694 in Figures A.13 and A.14 in Appendix A.

3.5 Discussion

The behavior of the detection probability as a function of the number of observed fields (as shown in Figures 3.4, 3.5, 3.6, A.5, A.6, A.7, A.8, A.9 and A.10) shows that the 2 time allocation strategies produce similar detection probabilities. In all cases the optimized approach gives marginally greater probability. As listed in Table 3.3 for observation time equal to 6 hrs (Table A.1 and Table A.2 for 4 hrs and 2 hrs respectively), we see that for the particular cases examined in this work the fully optimal approach leads to a typical gain of a few percent in detection probability over the equal time strategy. The biggest gains of $\sim 5\%$ are obtained for the DEC telescope. These relatively modest gains suggest that spreading observation time equally is close to optimal at the optimal number of observing fields k^*. We also

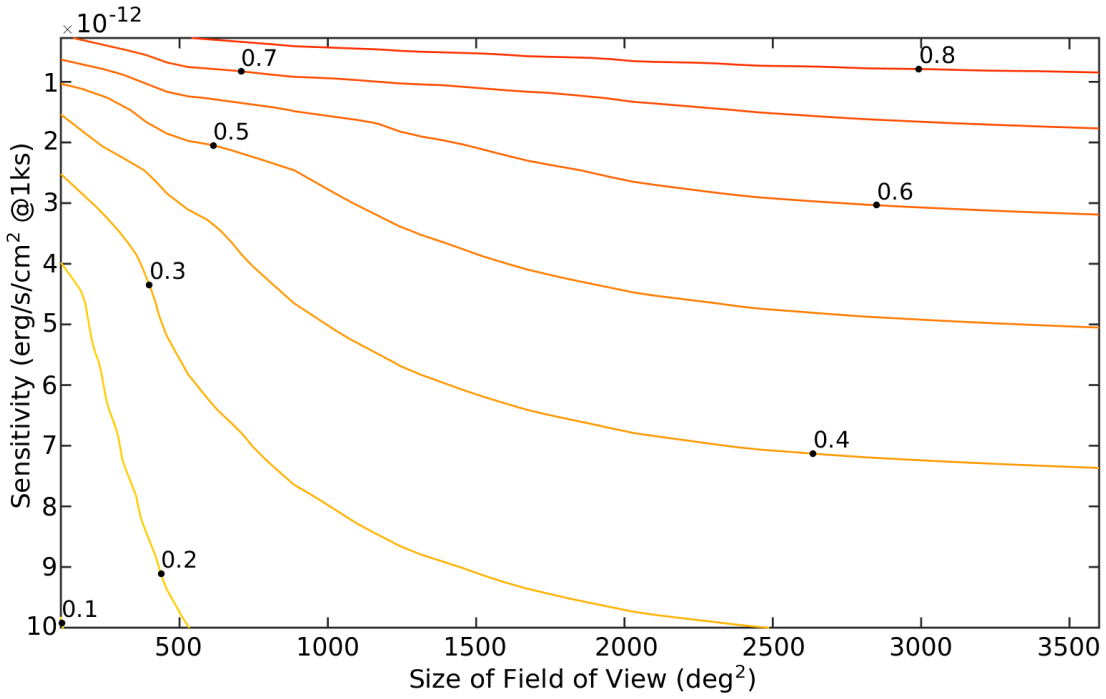

(a)

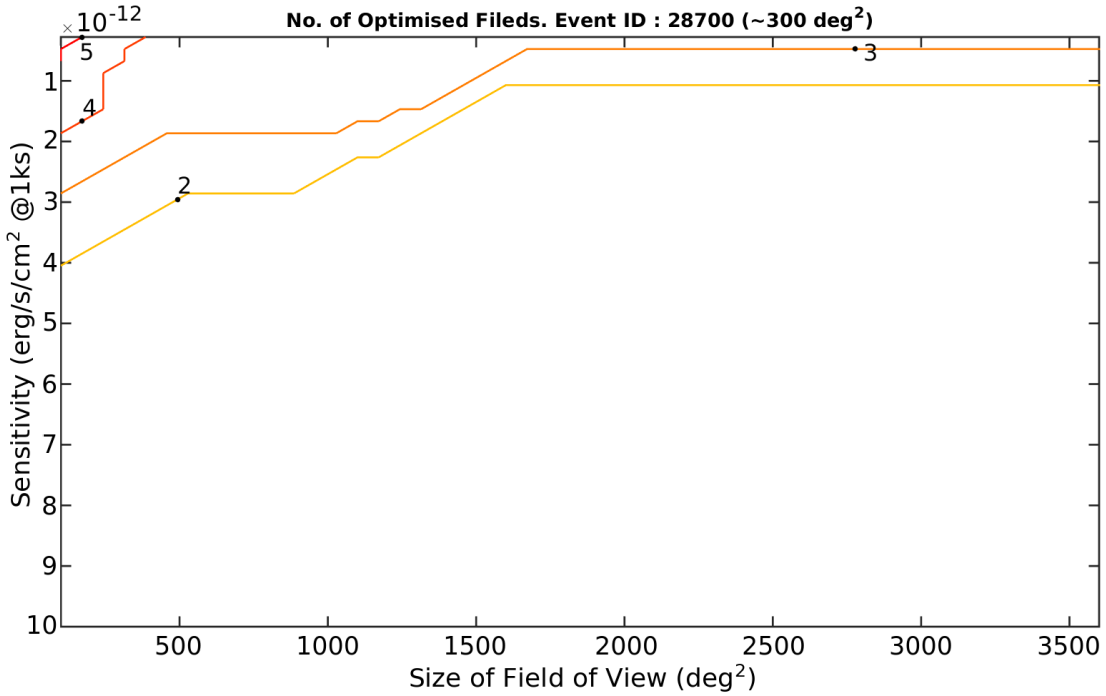

(b)

Figure 3.8: Contours of EM follow-up performance of X-ray afterglows associated with intermediate magnetar from BNS merger as a function of the size of the FOV of EP and the sensitivity of the WXT. The total observation time is assumed to be 1000s. The simulated GW event is event 28700 ($\sim$300 deg^2). In the top panel, we plot contours of equal detection probability, and in the bottom panel the corresponding optimal number of observing fields (right).

note that the number of fields at which the peak detection probability is achieved is similar for both strategies but always marginally lower for the equal time approach.

Both strategies clearly indicate that with a given telescope, there exits a number of fields at which the probability of a successful EM follow-up is maximized for a given GW event and a fixed amount of total observation time. In other words, exploring more or fewer fields than necessary will result in a decrease in detection probability. Although one would expect the probability of a successful EM follow-up first increases with the number of fields observed, a drop occurs if so many fields are observed that only observations of short exposure time in some or all of the observed fields are allowed, given that the observation time is fixed. This trade-off between exploring new fields and achieving increased depth within fields is broadly consistent with [241]. Overall, for the same event, the peak detection probabilities increase as the total observation time increases. For the same telescope, the detection probability increases as the size of error region decreases. This is expected since smaller error regions mean that a telescope requires fewer fields to cover that region at a given confidence. By examining the curves of detection probability in Figures 3.4, 3.5 and 3.6, it can be seen that an increase in the total observation time shifts the position of the peak to larger numbers of fields, but does not change the general shape of the function. This trend is also seen for the other two events.

The time allocations shown in the plots on the bottom of Figures 3.4, 3.5 and 3.6 are those computed for the optimal number of fields for event 28700 (or Figures A.5, A.6 and A.7 and Figures A.8, A.9 and A.10 for event 19296 and 18694 respectively). In all cases our optimal strategy ensures that proportionally more time will be assigned to those fields containing the greater fraction of GW probability (the lower index fields). In general the range in observation times per field spans $\sim$ 1 order of magnitude for a given optimized observation. A surprising feature of these distributions is that the optimal time allocations can therefore differ by factors of a few per field with respect to the equal time distribution. However, both distributions result in very similar detection probabilities. Recently, [392] have produced an analytic result for the distribution of observing times under a number of simplifying assumptions including a uniform prior on peak luminosity. They recommend that the time spent per field should be proportional to the prior GW probability in each field to the 2/3 power. We find that our numerical results are broadly consistent with this result but highlight again that the relative gains in detection probability are quite insensitive to the time allocation distribution.

Figure 3.7 shows our results for event 28700 from another perspective, namely the optimal performance of any existing or future telescope of arbitrary sensitivity and FOV (results for event 19296 and event 18694 are shown in Figure A.11 and Figure A.12). As mentioned in Sec. 3.1 our treatment of the detection threshold criterion N^* is simplified and hence these results should be treated as illustrative rather than definitive. However, as might be expected, a telescope with poor sensitivity and small FOV will be unlikely to detect an EM counterpart unless the GW event is

particularly well localized.

That LSST should explore more fields than PTF for these GW events may seem slightly confusing at first glance as LSST's FOV is larger than PTF's. This is because LSST is far more sensitive than PTF and can therefore explore as many fields as needed to cover the entire error region. In comparison PTF has to spend a considerable fraction of its total observation time on each of its observed fields, which results in PTF being only able to observe a limited number of fields.

In general, the EM detection probabilities achieved are more sensitive to the telescope parameters for events with smaller error regions. For example, imagine that a telescope with a $2\,\mathrm{deg}^2$ FOV and a R-band limiting magnitude of 20.3 in 30 sec ($N^*/A = 2273$) needed to raise the detection probability $P(D_{\mathrm{EM}}|k)$ by 10%. For event 18694, where the size of the 90% credible region is $\sim 30\,\mathrm{deg}^2$, it could either increase its FOV by a factor of ≈ 2, or reduce its limiting magnitude to ≈ 21.0 in 30 s. However, if the 90% credible region is $\sim 300\mathrm{deg}^2$ as for event 28700, it would have to either further increase its FOV by a factor of ≈ 2.5 or enhance its limiting magnitude to ≈ 21.5 in 30 sec to have the same factor of improvement.

In addition, the fact that at high sensitivity the contours in Figure 3.7 appear to be almost flat indicates that as the size of the GW error region becomes larger, the FOV of a telescope has negligible impact on the detection probability $P(D_{EM}|\omega)$. For the design of future EM telescopes performing follow-up observations of GW events there will likely be a trade-off between sensitivity and FOV. This result implies that for GW triggers with relatively large error regions, sensitivity, rather than FOV, is the dominant factor determining EM follow-up success. However, we remind the reader that this result is based on particular choices of source and corresponding prior on the source luminosity (see Eq. 3.6). Different choices may have different impacts on the outcome of our method.

For EP (Figures 3.8, A.13 and A.14), the results suggest that even with the smallest size of FOV in this simulation, the WXT would be able to cover the 90% credible regions of the events with a small number of fields ($\mathcal{O}(1)$). It is therefore not surprising that the detection probability is largely determined by the sensitivity of the WXT. In fact, depending on whether the 90% credible region is comparable (i.e. event 28700 and 19296) to or smaller (i.e. 18694) than the size of the WXT's FOV, the detection probability is either largely or solely determined by the sensitivity of the WXT. This indicates that the sensitivity of the WXT is a more dominant factor than the size of FOV for detecting the X-ray counterpart with EP.

3.6 Future Work

This work considers source sky error regions based solely on the information obtained from low latency GW sky localization [207]. One may also include galaxy catalogs to further constrain source locations within our existing Bayesian approach. In this work, the GW source distance was assumed to be statistically independent of its

sky location. In the future we plan to use more realistic distance information [375] therefore enhancing the effectiveness of our follow-up optimization strategy.

Moreover, since telescopes are distributed at various latitudes and longitudes on the Earth, different telescopes are able to see different parts of the sky at different times. As has been studied by [381] we would include the effect of observation prioritization when considering the diurnal cycle and for instances where GW sky error regions may pass below the horizon during a follow-up observation. Depending on the type of telescope considered we would also incorporate factors such as the obscuration of the source by the Sun and/or moon.

In this work, we ask the question of detecting kilonovae rather than identifying and characterizing them. The task of source identification is more demanding and will require the ability to differentiate our desired sources from contaminating backgrounds such as SNe and M-dwarf flares. One way to accomplish this is to perform multiple observations of the same fields. In this case a tentative detection is followed by an observation of the candidate for a period of time until the source's light curve allows it to be classified as a kilonova or contaminating noise [393, 241]. As mentioned in Sec. 3.1, simply repeating our proposed observations would enable the identification of variable objects for deeper follow-ups. However, a more involved procedure could incorporate light-curve information into our strategy therefore jointly optimizing the pointings used in both the detection and identification stages. This more complex strategy is left for future implementation.

3.7 Conclusion

In summary, we have demonstrated a proof-of-concept method for quantifying and maximizing the probability of a successful EM follow-up of a candidate GW event. We have applied this method to kilonovae counterpart for ground-based telescopes. We have shown that there exists an optimal number of fields on which time should be spent, and that observing more or fewer fields will result in a decrease in the detection probability. This analysis has been based on the assumptions of a static telescope with unconstrained pointings, a kilonova source at constant peak luminosity and the independence of statistical uncertainty between the distance and the GW trigger sky location.

Our approach takes as inputs the GW sky localization information, and the selected telescope's characteristics. The method selects the observed field locations with a greedy algorithm and then uses Lagrange Multipliers to compute the time allocation for those fields based on maximizing the detection probability. For ground-based telescopes, we have tested the algorithm by optimizing the EM follow-up observations of the HSC, DEC, Pan-Starrs, and PTF telescopes for three simulated GW events. By comparing the results of our methods with the results of equally dividing the observation time amongst the observed fields, we have shown that both strategies return similar results, with our method producing marginally larger detection probabilities.

In addition, we have provided estimates for the EM follow-up performance of a general telescope of arbitrary sensitivity and FOV. These results indicate that in terms of telescope design, the likelihood of its success in the follow-up of kilonova signals is approximately independent of the FOV for reasonably sensitive telescopes.

We also applied the algorithm to the design of EP for the detection of X-ray afterglow. To reflect the constraint on the maneuver, the analysis of EP has been done with the assumption that the total observation time is 1000s. We found that for EP and for the three simulated GW events, the detection probability is largely determined by the sensitivity of the WXT given that the size of FOV is comparable to the 90% credible region. Although we considered kilonovae and X-ray afterglow, we emphasize that this method is versatile and applicable to any EM counterpart model.

To extend this work, it may be helpful to consider including constraints from galaxy catalogs on source location. Also, the assumptions that the kilonova luminosity is constant during the observation period, more realistic treatment of the source distance, and consideration of the dynamics of the telescope with respect to the source should also be investigated. Finally, the inclusion of multiple observations of the same fields should be implemented to help distinguish kilonovae from contaminating sources.

Acknowledgements

We thank our colleagues Xilong Fan, who provided insight and expertise that greatly assisted the research. We also thank Keiichi Maeda, Tomoki Morokuma, Hsin-Yu Chen, and Daniel Holz for assistance and comments that hugely improved the manuscript. This research is supported by The Scottish Universities Physics Alliance and Science and Technology Facilities Council. C. M. is supported by a Glasgow University Lord Kelvin Adam Smith Fellowship and the Science and Technology Research Council (STFC) grant No. ST/ L000946/1.

Chapter 4

Localization of Compact Binary Coalescences

As discussed in Section 2.2, one key factor to the success of EM follow-up observations triggered by GW events, or that of identifying the host galaxy, is the localization of the GW source. GW interferometric detectors' performances are usually relatively poor when it comes to localizing sources of GWs. This has improved when VIRGO joined the observing runs in 2017 [134, 135] and will continue to do so after KAGRA and LIGO India joining the observing runs in later years. However, with 2G detectors, the observation of EM counterparts and the identification of host galaxies may remain a challenge difficult to achieve for sources at large distances. This is because a GW source observed at a larger distance will also have a larger associated localization error on the sky. For EM follow-up observations, larger distances also mean that telescopes will need to observe for longer to reach the sensitivity required to detect the counterparts [241]. This may lead to the same result stated in Chapter 3 that the telescopes may be unable to scan the whole 90% credible region before the EM counterpart fades below the detectable threshold.

Third generation detectors such as the ET and CE can bring significant improvements in GW source localization. Third generation detectors with enhanced sensitivity across the frequency band accessible to ground-based detectors will be able to detect GWs from BBH and BNS sources located at distances far beyond the horizon of 2G detectors. In particular, the improved sensitivity below 10Hz of these detectors will distinguish them from 2G detectors, as this allows for an extended duration of in-band observation of the signal. Depending on the distance, signals from BNS can be traced back up to hours or days before merger.

The long in-band duration of a signal will introduce several effects. Firstly, it allows the detector to accumulate SNR over a significantly longer period of time. As mentioned, one of the difficulties in EM follow-up observations of BNS merger triggers at large distance will be the time available to scan the 90% credible region associated with the BNS trigger before the EM counterpart becomes too faint. If the

SNR of a BNS trigger can be accumulated to a statistically significant level *prior* to the merger, prompt detection alerts could be made possible – thus increasing the probability of detecting the EM signature of the trigger [394]. The long duration also enables the detector to observe the source from different positions and directions as the earth rotates. This effect is important in localizing the source of GWs as it results in the time-dependency of the antenna pattern. The GW will also be Doppler shifted as the detector moves relative to the source as it rotates with the Earth's spin. The long duration of a signal thus requires the consideration of the earth's rotation when estimating the localization error.

In the literature, most studies of localization errors of GWs from CBCs are based on the assumption that the duration of the signal is short enough that the rotation of the earth is negligible [150, 151, 387]. This is justifiable for the reason that the in-band durations of the signals in those studies are only seconds to minutes in length. More recently, [395] considers localization of short transient signals from BNS mergers with a network of both second and third generation detectors. In addition, there has been work considering the long in-band duration and the rotation of the earth [396]. In this latter work the authors have modeled the GW signal using the stationary phase approximation – essentially the leading-order term in an expansion in powers of the small quantity that is the ratio of the radiation-reaction time scale and the orbital period.

In this chapter, we take into account the earth's rotation and, using a FM approach, estimate the localization of GWs from BNS sources observed by the ET and CE individually and as a network. We perform a series of tests to estimate the localization capabilities of these detectors for BNSs at 40, 200, 400, 800 and 1600Mpc and for a population of BNS sources that are distributed uniformly in the comoving volume. The configurations of third generation detectors that we consider for the ET and CE in this chapter are discussed in Section 1.3.4. As the exact geographic locations at which the detectors will be built are still unknown, in this chapter, the location adopted for the ET is (Longitude, Latitude) = (10.4°, 43.7°), and for CE is (−119.41°, 46.45°). We then investigate the feasibility of "early-warning" detection by setting requirements on localization error and accumulated SNR before merger for an alert to be released. For third generation detectors, we focus our analysis on BNSs where the in-band duration of their signals can be days' long, and thus the effect of earth's rotation is important.

Although the possibility that BBH mergers will be accompanied by EM emission is not completely ruled out, there is little expectation that there would be EM signatures of these events (see Chapter 2). Measuring the redshift of BBH mergers, therefore, relies on the identification of the host galaxies. If the localization error of a BBH merger is too large for its host galaxy to be confidently identified, investigation of cosmology using the BBH merger will be difficult or the statistics will be ambiguous. However, there are two reasons that BBH mergers can still be a useful tool to strongly constrain cosmology: first, BBH mergers are more massive than NSBH and BNS

mergers, and so they are detectable to a larger distance. Second, recent population synthesis models predict that BBH mergers will be the most numerous among CBC events [397, 398]. It is therefore reasonable to expect that observations of CBC events will be dominated by BBH mergers. If the localizations of these BBH mergers are well enough, a population of BBH mergers can still be used to establish robust statistics of cosmology [172]. In the end of this chapter, we will investigate the localization of BBH mergers with networks consisting of 2G detectors and detectors proposed by [90].

This chapter is structured as follows: the methodology for computing the localization of BNS mergers with third generation detectors is presented in Section 4.2. The results and simulations are presented in Section 4.3 together with a discussion. We will discuss the localization of BBH mergers with extended networks of detectors in Section 4.4. We then provide our conclusions in Section 4.5.

It needs pointing out that since the noise curve for the ET used in this chapter is for a single interferometer with opening angle equal to 90%, which is therefore roughly 15% better than a single interferometer with opening angle equal to 60% [102]. The estimate shown in this chapter is expected to be slightly more optimistic than the reality.

4.1 Duration of Binary Neutron Star Signals

As mentioned in Section 1.3.4, third generation detectors (i.e. ET and CE) will have improved sensitivity throughout the frequency band relevant to ground-based detectors (i.e. 1Hz - 2000Hz). Different relative improvements in sensitivity as a function of frequency can lead to different impacts on the sky localization capability. Better sensitivity in the medium to high frequency band can effectively increase the SNR for a GW event and thus reduce the localization error. On the other hand, improvement in the low frequency band might not increase the SNR as much, but it will substantially extend the in-band duration of the signal from the order of seconds/minutes to the order of hours/days.

By replacing the starting frequency f_s with the low frequency cut-off of the detector in Eq.1.7, one can obtain the approximate in-band duration of a signal from a given compact binary system in a detector. As indicated in Figure 1.3, for BNS systems, if the detector's low frequency cut-off is reduced to 2Hz, the in-band duration of the signal will be close to 1 day, and will be more than 5 days if the low frequency cut-off is 1Hz. This is substantially longer than the in-band duration for aLIGO and Advanced VIRGO, where the low frequency cut-off is 10Hz. The in-band duration of BBH signals are expected to be shorter. For the ET with low cut-off frequency at 1Hz, $10M_\odot - 10M_\odot$ BBH signals will last for ~ 5 hours.

Such a long duration allows the detector to observe the signal along the detector's trajectory on earth as the earth rotates, and therefore makes the detector's response explicitly time-dependent. To illustrate this time-dependence, in Figures 4.1 and 4.2

two source sky locations are selected and the change over 5 days of the ET and CE detector response to sources at those locations is shown.

4.2 Methodology

Using the FM, we aim to provide a lower bound on source sky position error for GW sources and examine the feasibility of early warning. The FM is briefly discussed in Section 1.6.3. Here, we will recapitulate the definition of the FM. We then extend the expression to be applicable to situation where the rotation of the earth is considered.

For an incoming GW, the strain observed by the I^{th} detector can be expressed as $h_I(\boldsymbol{\theta}, t)$ in the time domain. It is a linear combination of the wave's two polarizations $h_+(\boldsymbol{\theta}, t)$, $h_\times(\boldsymbol{\theta}, t)$ and the detector response $F_I^+(\theta, \phi, \psi, t)$, $F_I^\times(\theta, \phi, \psi, t)$ as,

$$h_I(\boldsymbol{\theta}, t) = F_I^+(\theta, \phi, \psi, t)h_+(\boldsymbol{\theta}, t) + F_I^\times(\theta, \phi, \psi, t)h_\times(\boldsymbol{\theta}, t), \tag{4.1}$$

where the vector $\boldsymbol{\theta}$ represents the unknown signal parameters: sky position, distance, time of arrival at the center of the earth, binary masses, initial phase of the wave when it arrives at the center of the earth, inclination angle and polarization angle. The time at the detector is denoted by t which is equal to the arrival time t_0 of the incoming wave at the center of the earth, plus the time τ required for the wave to travel from the center of the earth to the detector, given by

$$\tau = \frac{\mathbf{n} \cdot \mathbf{r}}{c}, \tag{4.2}$$

where $\mathbf{n}$ is the GW propagation direction and $\mathbf{r}$ is the location vector of the detector relative to the center of the Earth. The Fourier transform of $h_I(\boldsymbol{\theta}, t)$ is then defined as

$$\tilde{h}_I(\boldsymbol{\theta}, f) = \int_t^{t+\Delta t} h_I(\boldsymbol{\theta}, t) e^{-2i\pi ft} \mathrm{d}t, \tag{4.3}$$

where Δt refers to the duration of $h_I(\boldsymbol{\theta}, t)$. The start and the end of $h_I(\boldsymbol{\theta}, t)$ are denoted by t and $t + \Delta t$. The mathematical definition of the FM, as defined in Eq. 1.31, is given by

$$\Gamma_{ij} = \sum_{I=1}^{N} 2 \int_0^\infty \frac{\frac{\partial \tilde{h}_I^*(\boldsymbol{\theta}, f)}{\partial \theta_i} \frac{\partial \tilde{h}_I(\boldsymbol{\theta}, f)}{\partial \theta_j} + \frac{\partial \tilde{h}_I^*(\boldsymbol{\theta}, f)}{\partial \theta_j} \frac{\partial \tilde{h}_I(\boldsymbol{\theta}, f)}{\partial \theta_i}}{S_I(f)} \mathrm{d}f. \tag{4.4}$$

where $\partial \tilde{h}(\boldsymbol{\theta}, f)/\partial \theta_i$ is the partial derivative of $\tilde{h}(\boldsymbol{\theta}, f)$ with respect to the i^{th} unknown parameter θ_i. The power spectrum density of the I^{th} detector is denoted by $S_I(f)$. We also sum over the number of detectors, or in the case of the ET, over the number of individual interferometers. The optimal SNR, ρ, of the incoming GW can be expressed as

$$\rho^2 = 4 \int_0^\infty \frac{|\tilde{h}_I(\boldsymbol{\theta}, f)|^2}{S_I(f)} \mathrm{d}f. \tag{4.5}$$

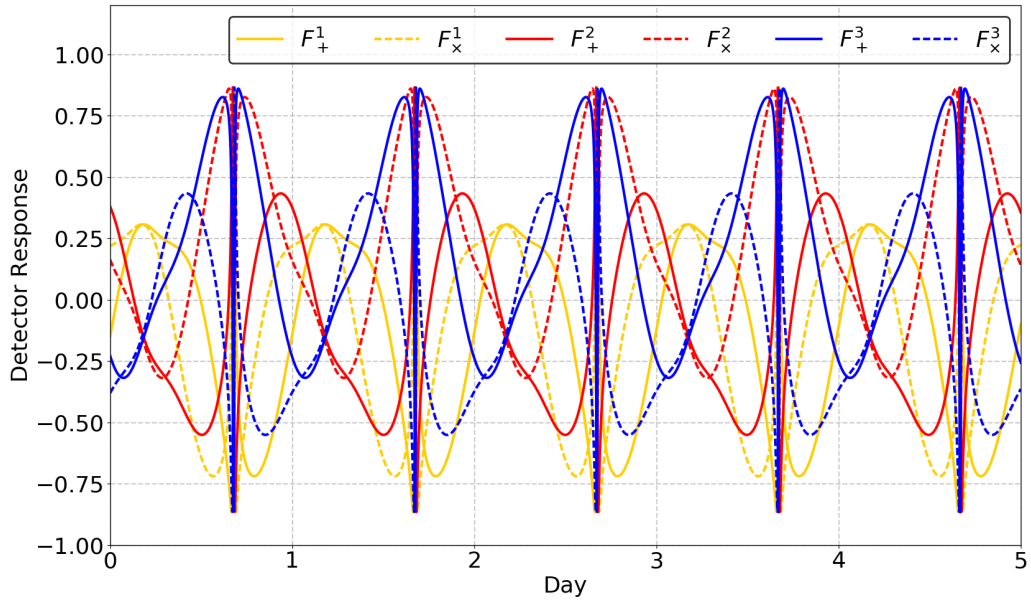

(a)

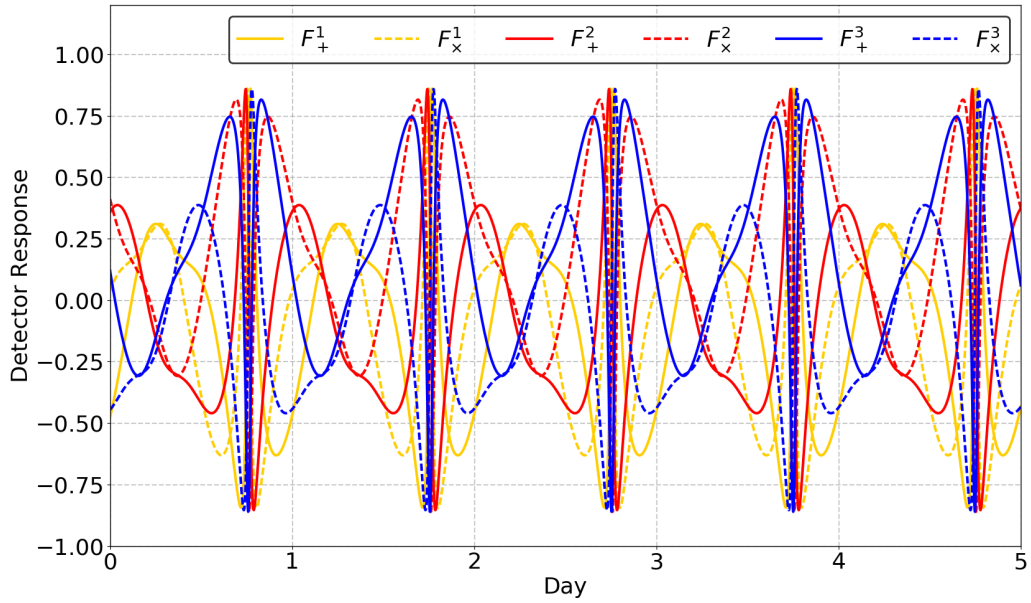

(b)

Figure 4.1: The time-dependency of ET's detector response to GWs with a polarization angle equal to $\pi/8$ coming from two example locations in the sky over the course of 5 days. Panel a shows the detector response to a source located at (α, δ) = $(0°, 45°)$ and panel b shows that to a source at (α, δ) = $(30°, 60°)$, where α and δ are right ascension and declination of the source. In the legend in panel a and b, the superscript $k = (1, 2, 3)$ indicates the k^{th} interferometer of the ET.

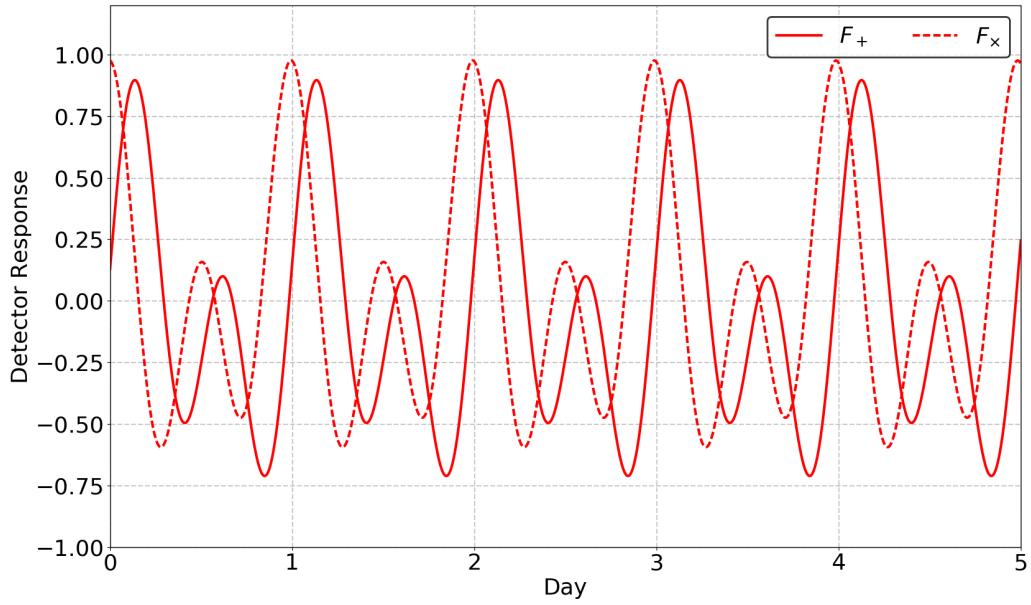

(a)

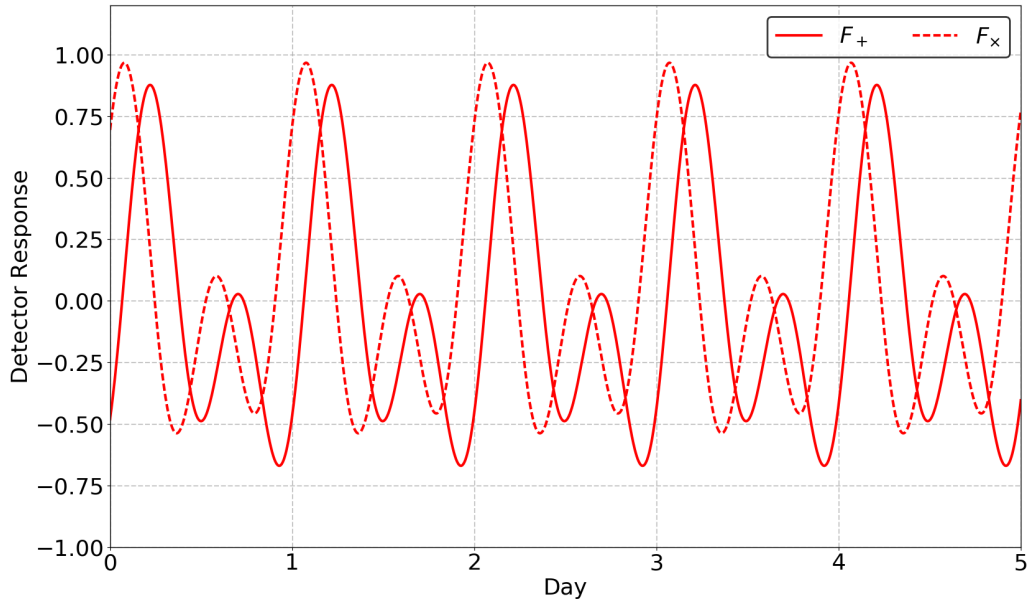

(b)

Figure 4.2: The same as Figure 4.1 but showing the time-dependency of CE's detector response.

In this work, we construct the FM for the following unknown parameters: right ascension, α; declination, δ; arrival time, t_0, at the center of the earth; the log of the distance, $\log_{10} d$; polarization angle, ψ; the log of the total binary masses, $\log_{10} M$; the cosine of the inclination angle, $\cos\iota$; the symmetric mass ratio, $\eta = M_1 \times M_2/M^2$, of the masses of the two bodies in the binary; the initial phase, ϕ_0, of the wave when it arrives at the center of the earth. Specifically, the equatorial coordinates α and δ of a source are related to θ and ϕ in Eqs. 1.11 and 1.13 by rotation matrices once detector location and the time of observation are specified.

When computing the GW localization error for a source at a particular sky location, we divide the entire wave into pieces, each of which is 100 seconds long – with the final piece ≤ 100 seconds depending on the specific in-band duration of the signal. The total number of pieces $N_{\rm p}$ is then equal to $\tau_{\rm c}/100$, rounded towards positive infinity. For each piece of the wave, we employ the formalism described above to compute the FM Γ^k_{ij} and the optimal SNR ρ^k. The superscript k indicates the $k^{\rm th}$ piece of the wave. The final FM $\Gamma^{\rm f}_{ij}$ is then

$$\Gamma^{\rm f}_{ij} = \sum_{k=1}^{N_p} \Gamma^k_{ij}, \tag{4.6}$$

where we sum over the FM contributions from each piece of the waveform, and the superscript f indicates the resultant FM. The matrix inverse of the FM then gives the covariance matrix of the unknown parameters as

$$\mathrm{cov}_{ij} = \Gamma^{-1}_{ij}, \tag{4.7}$$

from which the localization error is extracted using

$$\Delta\Omega = 2\pi\sqrt{\lambda_\alpha \lambda_\delta}\cos\delta, \tag{4.8}$$

where $\Delta\Omega$ is the localization uncertainty, λ_α and λ_δ are the eigenvalues of the matrix cov_{ij} corresponding to the α and δ of the source respectively. The following expression can be used to convert $\Delta\Omega$ to any desired confidence level,

$$\Delta\Omega_p = -2\log(1-p)\Delta\Omega, \tag{4.9}$$

where p is a value between 0 and 1 indicating the confidence level. Similarly, the accumulated SNR is given by

$$(\rho^f)^2 = \sum_{k=1}^{N_p} (\rho^k)^2. \tag{4.10}$$

4.3 Results of Simulation and Discussion

4.3.1 Localization

To test the localization capabilities of third generation detectors, we have simulated GW signals from $1.4M_{\odot}$-$1.4M_{\odot}$ BNS sources at distances of 40, 200, 400, 800, and 1600Mpc. The masses are defined in the local frame, i.e. $M_{\rm Local}$, which is related to the observed masses $M_{\rm Obs}$ by

$$M_{\rm Obs} = M_{\rm Local}(1+z), \tag{4.11}$$

we use z to denote redshift. All the masses defined earlier and in Figure 1.3 refer to the observed masses $M_{\rm Obs}$. The inclination angle ι, polarization angle ψ and the sky position (α, δ) are randomized. For each specific distance, we have simulated 500 BNS signals. To determine whether a source is detectable, we have employed different SNR cuts for each network configuration. For networks with more than one interferometer such as the ET or the ET and CE, we have applied an SNR requirement similar to that in [151]. A detection is achieved if the network SNR is larger than or equal to 12 and the SNRs in at least two interferometers are no less than 5.5. For a network with only one interferometer, namely, CE, we require that the accumulated SNR is no less than 12 to claim a detection [1]. The results of the simulations are presented as cumulative distributions in Figures 4.3 and 4.4.

For BNSs at 40Mpc using only the ET, 50% of the detectable sources can be localized with 90% confidence to within $2.0\,\mathrm{deg}^2$, and 90% of the detectable sources to within $7.5\,\mathrm{deg}^2$. For the best localized 10% of sources, the 90% credible region is within $0.2\,\mathrm{deg}^2$ and these correspond to the best located and orientated sources. For BNSs at 200Mpc, 50% and 90% of the detectable sources can be localized with 90% confidence to within $42\,\mathrm{deg}^2$ and $183\,\mathrm{deg}^2$ respectively. Assuming EM follow-up observations are achievable for sources that are localized to within $100\,\mathrm{deg}^2$, this indicates 100% (74%) of the detectable sources at 40Mpc (200Mpc), suggesting many opportunities for joint EM observations provided by the ET for BNSs within 200Mpc.

For sources located at 400Mpc, the upper limit of the size of 90% credible region increases to $187\,\mathrm{deg}^2$ ($812\,\mathrm{deg}^2$) for the best localized 50% (90%) of the detectable sources. This still leaves 36% of the detectable sources localized to within $100\,\mathrm{deg}^2$ with 90% confidence. For sources located at larger distances, i.e. 800Mpc and 1600Mpc, the upper limit of the size of 90% credible regions for the best localized 50% (90%) of the detectable sources increases substantially to $764\,\mathrm{deg}^2$ ($3485\,\mathrm{deg}^2$) and $3994\,\mathrm{deg}^2$ ($1.7\times10^4\,\mathrm{deg}^2$) respectively. Moreover, only 11% and 5% of the detectable sources can be localized to within $100\,\mathrm{deg}^2$. This is because the amplitude of the signals from sources at greater distances will be weaker. Also, the observed $M_{\rm Obs}$ as defined in Eq. 4.11 will be larger, meaning that the in-band duration will be

[1] We require a single detector to achieve SNR ≥ 12 for a detection for consistency. The results shown here for a single detector may therefore be more pessimistic than the reality.

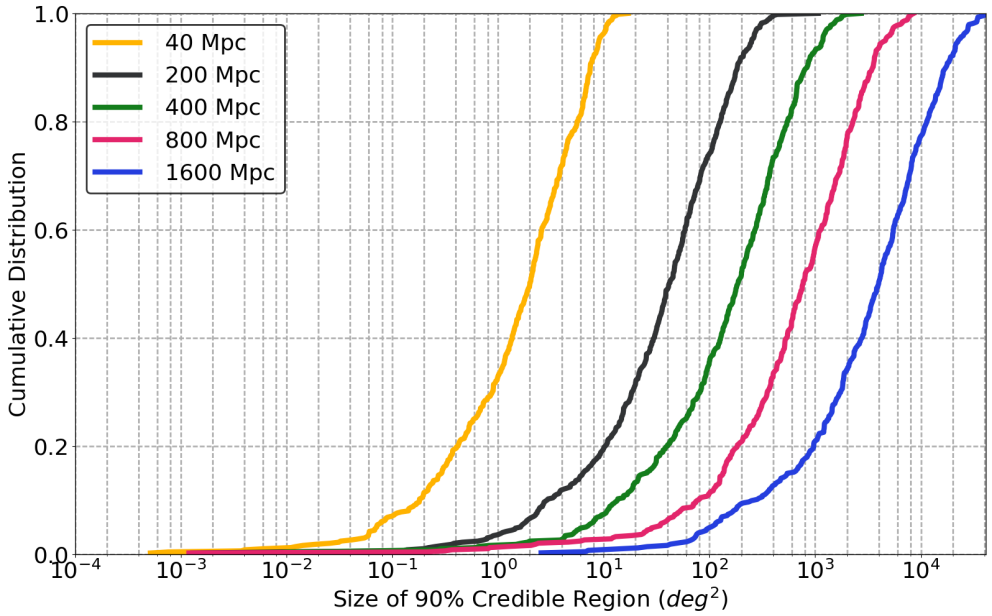

(a)

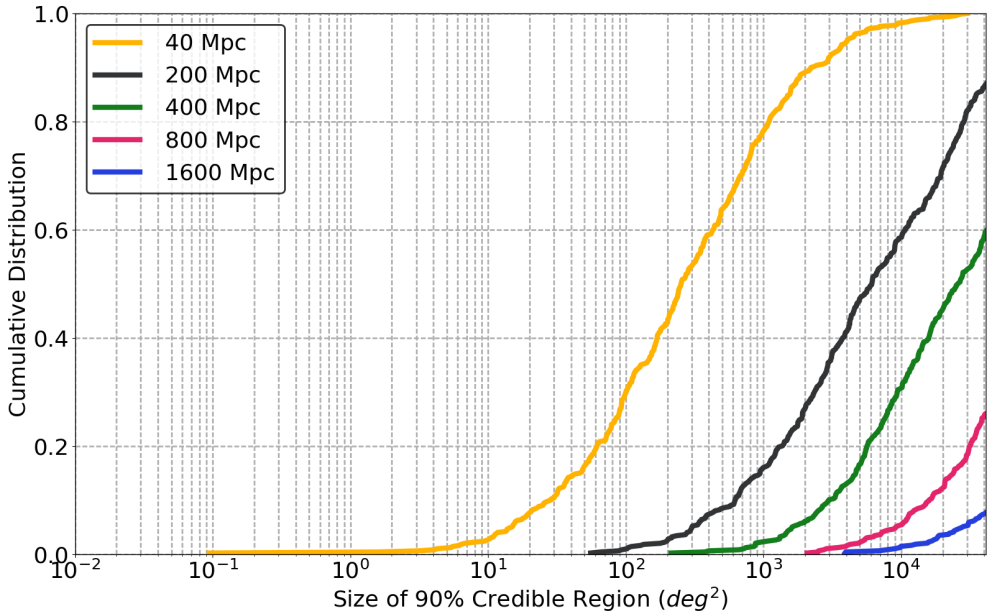

(b)

Figure 4.3: The cumulative distribution of the size of 90% credible regions for sources at fixed distances. The x-axes show the size of the 90% credible region and the upper limit of the x-axes corresponds to the size of the whole sky. The yellow, black, green, red, and blue lines represent BNS sources at 40, 200, 400, 800, and 1600Mpc respectively. Panel a and b show the results for the ET and CE respectively.

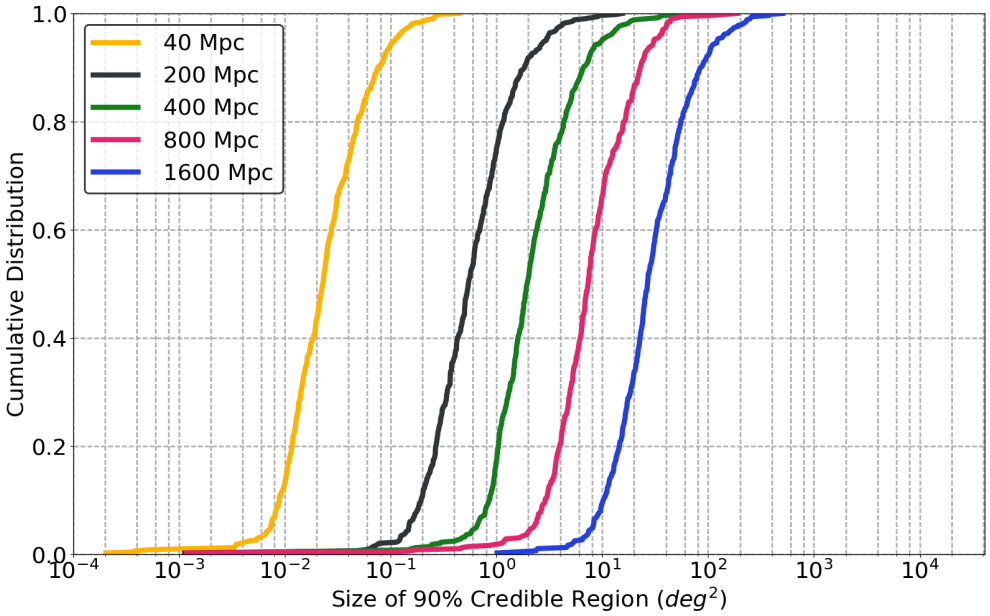

Figure 4.4: The same as Figure 4.3 but for the ET and CE as a network.

shorter. This suggests that localization of a BNS at such distances by the ET alone will still be poor and EM follow-up observations will remain a challenge if the ET is the only operating detector.

Since the sensitivity of CE at low frequencies is limited, the in-band durations of the signals are shorter than that in the ET. As shall be seen later, the time-dependent modulation of detector response is the main factor contributing to improved localization. Consequently, the localization of a BNS by CE alone is worse. For example, 50% (90%) of the detectable BNSs at 40Mpc can be localized to only within 252 $\deg^2$ (2212 $\deg^2$), a factor of ~ 126 and ~ 295 larger than using only the ET. Only 30% of the detectable sources can be localized to within 100 $\deg^2$ with 90% confidence. For sources at distances $\geq$ 400Mpc, the upper limits of localization error for the best localized 50% and 90% are larger than the whole sky. This means that for some sources, despite accumulating enough SNR to claim a detection, no localization information is available.

Combining the ET and CE together as a network greatly improves the localization since it vastly increases the geographical baseline of the network. This greatly improves triangulation between the detectors in the network and will take advantage of the high frequency, high SNR components of the waveform, i.e., the final seconds. This will complement the localization information gained from the long duration and changing antenna patterns. All sources within 200Mpc are localized to within 30 $\deg^2$ with 90% confidence. Importantly, at 40Mpc and 200Mpc, the 90% credible region upper limit for the best localized 90% of the detectable sources are only $\mathcal{O}(10^{-2})$ $\deg^2$ and $\mathcal{O}(1)$ $\deg^2$ respectively. For the detectable sources at 1600Mpc, there are still

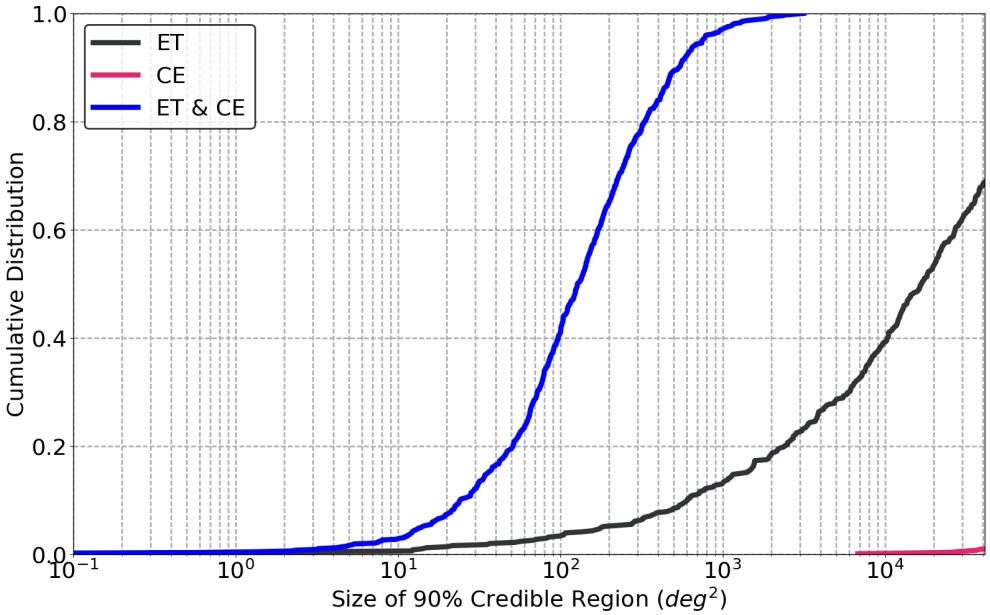

Figure 4.5: The cumulative distribution of the size of 90% credible regions in the sky, for detectable BNS sources uniformly distributed in comoving volume, observed by the ET and CE both individually and as a network. The upper limit of the x-axis corresponds to the size of the entire sky.

92% localized to within $100\,\mathrm{deg}^2$ with 90% confidence. This shows a great promise for BNS multi-messenger astronomy even at relatively large cosmological distances.

To present a more general picture, we have also simulated the localization of a population of BNS that are distributed uniformly in the comoving volume. The results are presented in Figure 4.5 as cumulative distributions. Using the ET alone, the farthest detectable source is at $z = 1.7$. Of the detectable sources, 50% can be localized to within $\sim 1.7 \times 10^4\,\mathrm{deg}^2$ with 90% confidence. The cumulative distribution for the ET reaches 68% when the value at the x-axis is the size of the entire sky – i.e. this indicates that for up to 32% of the detectable sources, essentially no localization information is available. For CE, the situation is worse. The farthest detectable source is located at $z = 4.9$, but only $\sim 2\%$ of the detectable sources will have any localization information available. Again, a network with the ET and CE can bring a huge improvement to the localization performance. For example, compared to using the ET only, the upper limit of the 90% credible region for the best localized 90% of the detectable sources has been reduced by a factor > 100 to $123\,\mathrm{deg}^2$. The fraction of detectable sources that can be localized to within $100\,\mathrm{deg}^2$ with 90% confidence has increased by more than 10 times to 43%. Interestingly, the farthest detectable source with a network of the ET and CE is located at $z = 2.2$. This is because for a network of more than one interferometer, we require an SNR ≥ 5.5 in at least two of the interferometers, besides also requiring a network SNR ≥ 12. For sources located

Table 4.1: Statistical Summary of Results

Network	d (Mpc)	n	50% ($\deg^2$)	90% ($\deg^2$)	≤ 100 ($\deg^2$)	≤ 30 ($\deg^2$)
ET	40	500	2	8	100%	100%
	200		42	183	74%	40%
	400		187	837	36%	16%
	800		764	3485	11%	5%
	1600		3994	1.7×10^4	5%	2%
	Uniform [1]	3000	1.7×10^4	> Sky	3%	2%
CE	40	500	252	2212	30%	10%
	200		6118	> Sky	1%	0%
	400		2.6×10^4	> Sky	0%	0%
	800		> Sky	> Sky	0%	0%
	1600		> Sky	> Sky	0%	0%
	Uniform [1]	5000	> Sky	> Sky	0%	0%
ET & CE	40	500	2×10^{-2}	8×10^{-2}	100%	100%
	200		5×10^{-1}	1.8	100%	100%
	400		2	7	100%	99%
	800		7	23	99%	94%
	1600		27	85	92%	55%
	Uniform [1]	5000	128	538	41%	12%

[1] Uniformly distributed in the comoving volume.

A brief statistical summary of our results for sky localization. In the first row, we use d to denote distance and n the number of injections. The third and the fourth columns indicate the upper limit of the size of 90% credible regions for the best localized 50% and 90% of the detectable sources. The fifth column shows the percentage of the detectable sources that can be localized to within $100\,\deg^2$ with 90% confidence, and the last column the percentage within $30\,\deg^2$ with 90% confidence.

at $z > 2.2$, only the CE is able to accumulate enough SNR – leading to a failure to meet the detection criterion.

A summary of the results is given in Table 4.1. Given the success of the EM follow-up observations of GW170817, where the localization error at 90% confidence is $28\,\deg^2$ [135], also presented in the table is a column showing the percentage of detectable sources that can be localized to within $30\,\deg^2$ with 90% confidence.

Although the discussion in this chapter is restricted to localization error, the application of the FM is not. We therefore present the estimate of other parameters of detected BNS mergers as derived from the FM (i.e., luminosity distance $d_{\rm L}$, inclination ι and polarization ϕ angles) in Appendix B.

[0] LM: Lagrange multiplier

[1] ET: Equal time strategy

4.3.2 Early Warning

In the era of third generation detectors, due to the extended in-band duration of detectable signals, it is possible that signals will accumulate SNR such that the trigger may be considered significant before the merger occurs. In this section we investigate the feasibility of issuing early warnings prior to binary coalescence. We assume that if the SNR for a GW event can be accumulated before merger, up to a level that satisfies the detection requirement as defined in Section 4.3.1, the event will be deemed significant. As the purpose of releasing an early warning is to increase the chance of successful EM follow-up observation, releasing an alert too early may result in a localization error too large to carry out any meaningful follow-ups. We therefore require two criteria to be met before an alert can be released. Firstly, the signal has to satisfy the SNR requirement for detection and secondly, the 90% credible region has to be no larger than $100\,\mathrm{deg}^2$ at the moment the alert is sent. The latter requirement is chosen to be consistent with the sky coverage of the EM follow-up campaign for the first detected GW event GW150914 by optical telescopes with $\lesssim 10\mathrm{deg}^2$ fields of view [190]. This is also consistent with the number of fields these telescopes are able to observe in an hours-long observation targeting kilonovae associated with BNS mergers [1]. We will refer to these two requirements as early warning criteria in the remaining of this chapter. As early warning is mostly made possible due to the improvement in the sensitivity in the low frequency band, we focus our analysis on the ET, and the ET and CE as a network. The BNS systems are distributed at specific distances and uniformly in the comoving volume as discussed before.

We present the results for the ET in Figures 4.6, 4.7 and 4.8 and the ET and CE operating together as a network in Figures 4.9, 4.10 and 4.11. These histograms show the distribution of the fraction of detectable events as a function of the time before merger at which the events meet the early warning criteria.

Using the ET, all the signals at 40Mpc meet the early warning criteria between 1 and 20 hours before merger, with the mode of the distribution at $\sim$ 5 hours. At 200Mpc, 58% of the detectable signals have accumulated enough SNR for early warning between 1 to 6 hours prior to merger. This represents a significant advantage that can be provided by the ET in EM follow-up observations for sources within 200Mpc. As the distance increases, the fraction of detectable sources that meet the early warning criteria continues to drop. Of the detectable sources at 400Mpc, only $\sim$ 27% can meet the early warning criteria and the fraction further drops to $\sim$ 9% and $\sim$ 3% for sources at 800Mpc and 1600Mpc respectively. Moreover, at 1600Mpc, the times prior to merger when the signals meet the early warning criteria drop to $\leq$ 50 minutes.

As would be expected, an additional third generation detector will improve the performance significantly and provide much improved early warning capability. In Figures 4.9, 4.10 and 4.11, it can be seen that for distances $\geq$ 200Mpc and $\leq$ 1600Mpc, the distributions of early warning times have become noticeably skewed to larger times compared to using only the ET. This suggests that a network of the ET and CE

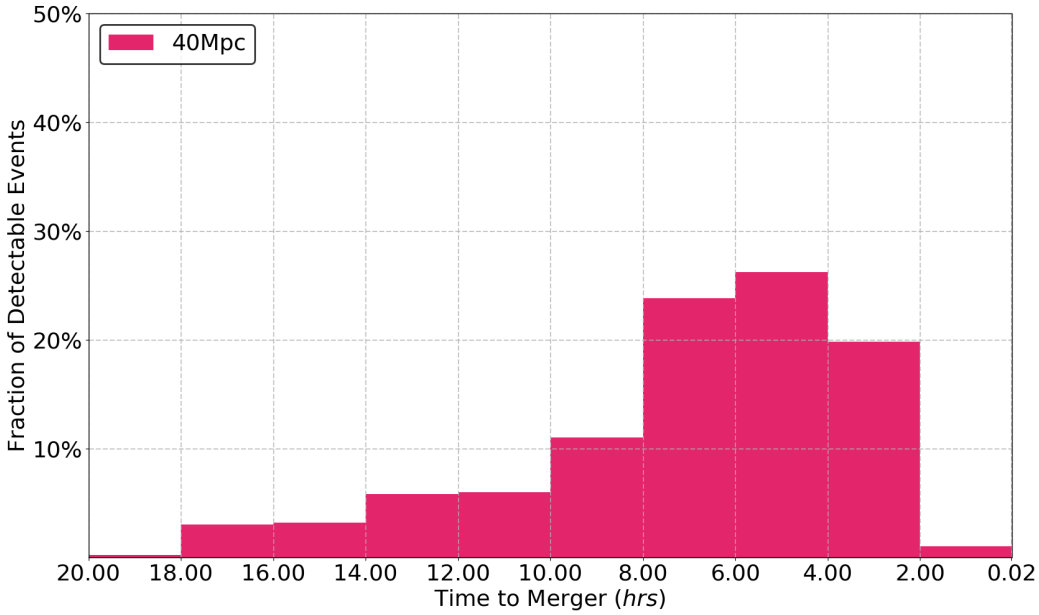

(a)

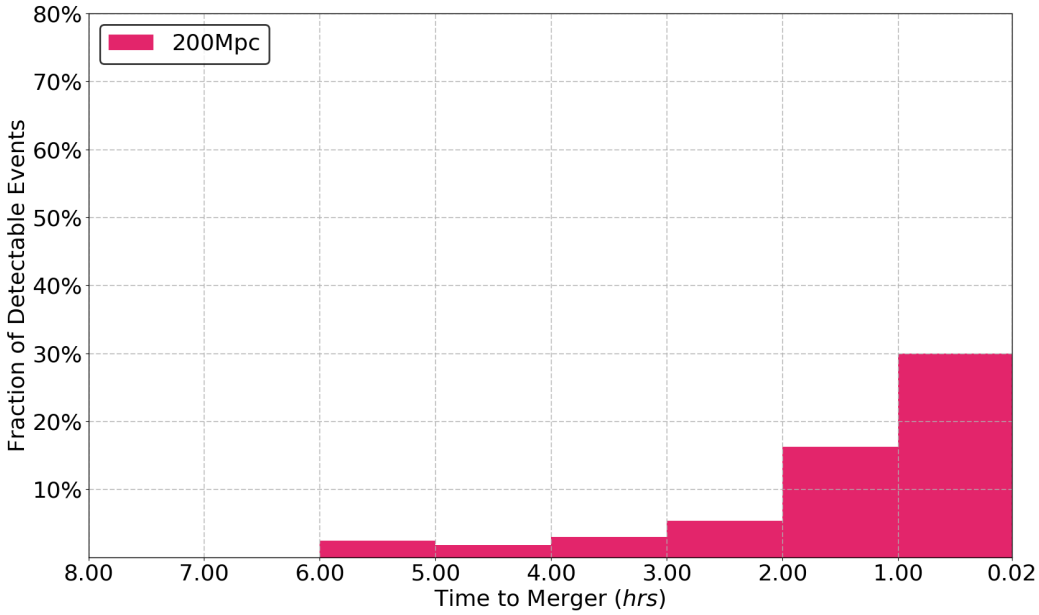

(b)

Figure 4.6: Histograms of the fraction of detectable events that achieve the early warning criteria. Panel a and b are for events at 40 and 200Mpc respectively. The x-axes indicate the time to merger when the signal meets the early warning criteria. The y-axes indicate the fraction of detectable events that achieve these early warning criteria. Note that at distances $\geq$ 400Mpc (Figures 4.7 and 4.8), since a large fraction of the times until merger will fall within 1 hour, for greater clarity the scale of the axes varies from panel to panel. Only those signals which achieve the early warning criteria at least 100 seconds prior to merger will be counted.

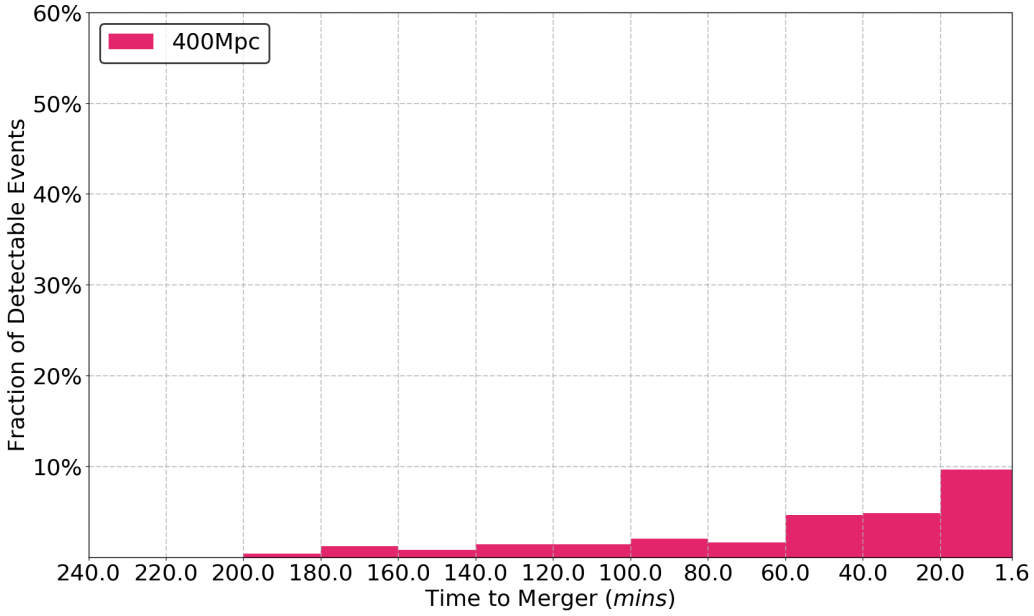

(a)

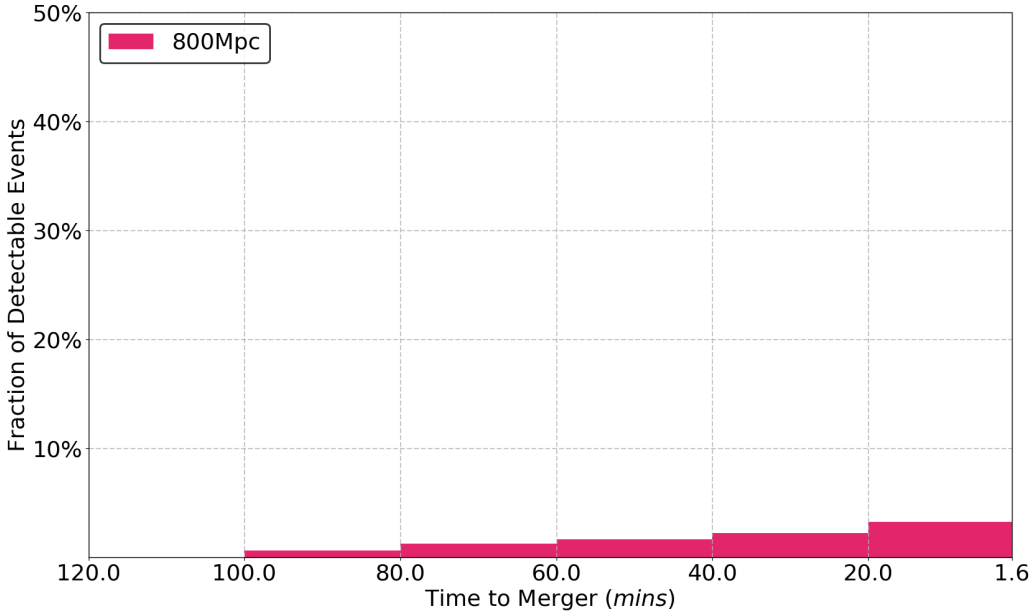

(b)

Figure 4.7: The same as Figure 4.6 but for different distances. Panel a and b are for events at 400Mpc and 800Mpc.

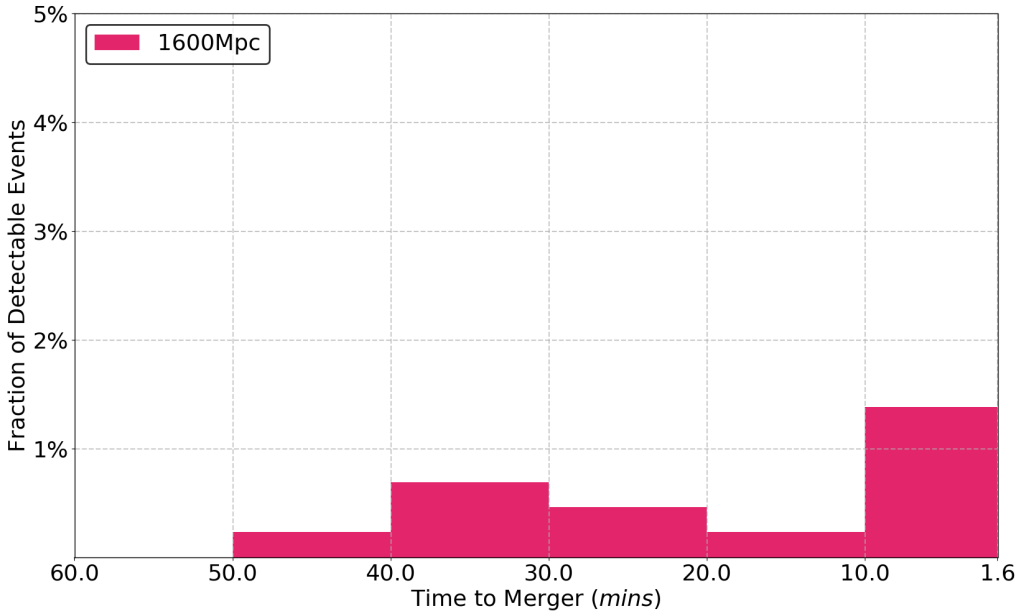

Figure 4.8: The same as Figure 4.6 but for events at 1600Mpc.

detectors will provide better early warning capability for sources at relatively large distance. For example, the fractions of the detectable sources at 400Mpc, 800Mpc and 1600Mpc that can meet the early warning criteria are 98%, 51% and 5% respectively. At 40Mpc, since using only the ET all the sources will have already met the early warning criteria at a time when the frequency of the signal is still relatively low, an additional detector of CE does not alter the distribution significantly. At 1600Mpc, the result may seem to suggest that a network of the ET and CE does not perform much better than using the ET alone. However, this is because a network of the ET and CE will be able to detect sources that are undetectable to the ET alone. These sources will not contribute much to the number of events that meet the early warning criteria but will contribute to the number of detectable events.

Finally, to provide a more general picture, we present in Figure 4.12 the results for a population of BNS distributed uniformly in comoving volume. In line with the results shown in the previous sections, a network of the ET and CE will increase the number of events that meet the early warning criteria. With the ET alone, $\sim 2\%$ of detectable sources can have their alerts released prior to merger. This ratio is $\sim 4\%$ after CE joining the observation. However, the reason for the small increase in the fraction is because a network of the ET and CE will be able to detect sources that are undetectable to the ET alone, and sources located at greater distances. In Table 4.2, we present a summary of the results in terms of early warning.

As discussed, modulations of the Doppler effect and time-dependent detector responses are the two main consequences that will be seen in long in-band duration signals. Zhao and Wen, 2017 [396] has tested thoroughly the difference in local-

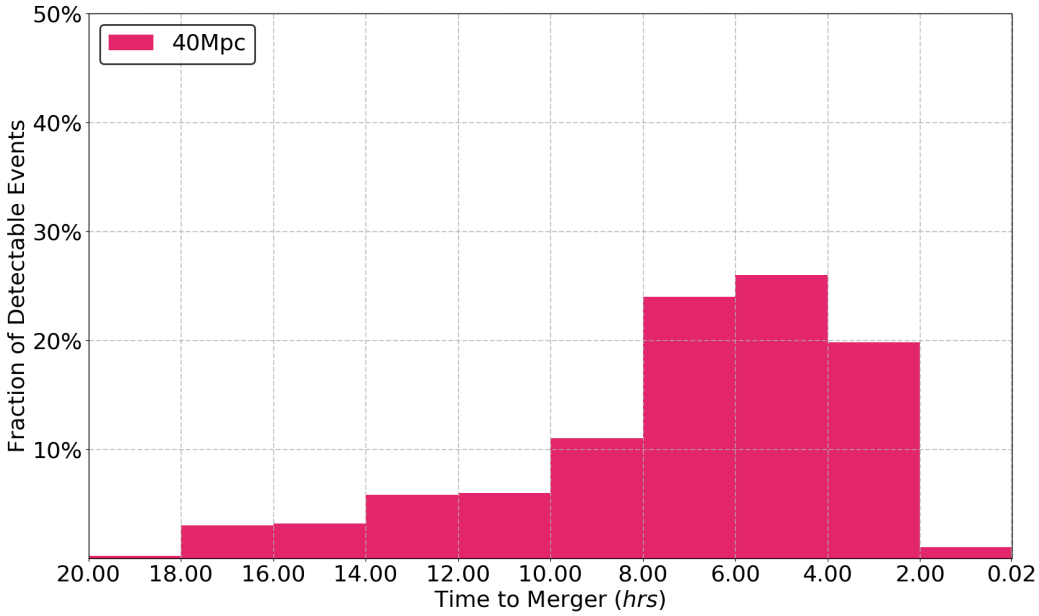

(a)

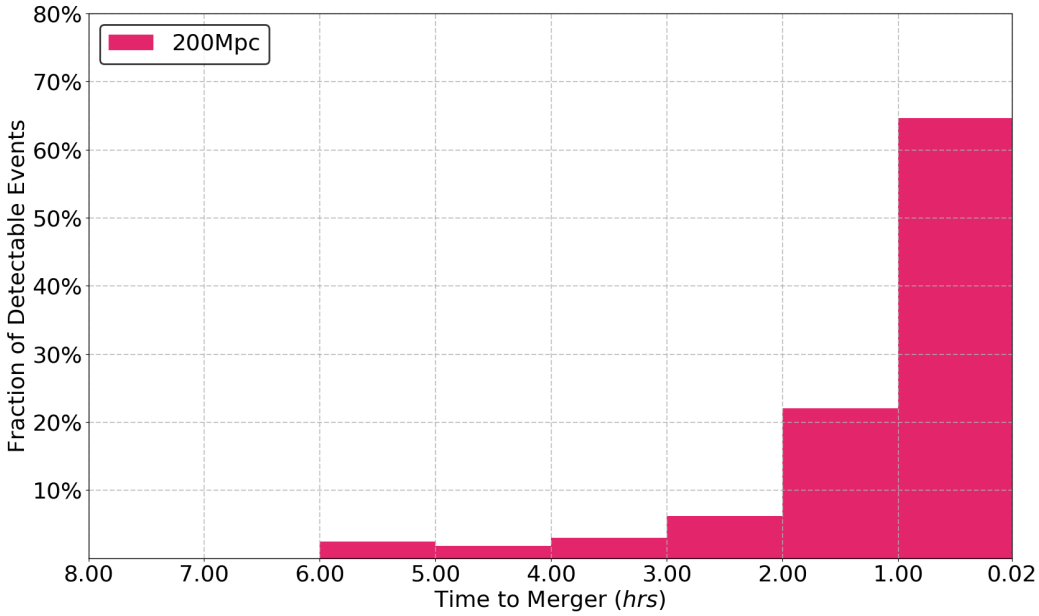

(b)

Figure 4.9: The same as Figure 4.6 but using the ET and CE as a network. Panel a and b are for events at 40Mpc and 200Mpc. The scale of the panels is the same as is shown in Figure 4.6 to allow a convenient comparison.

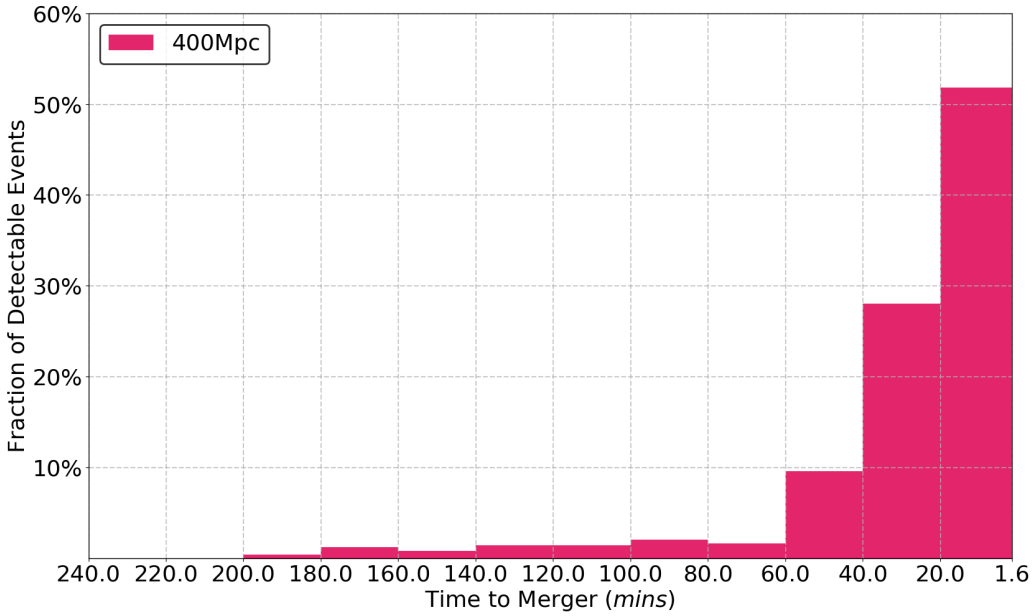

(a)

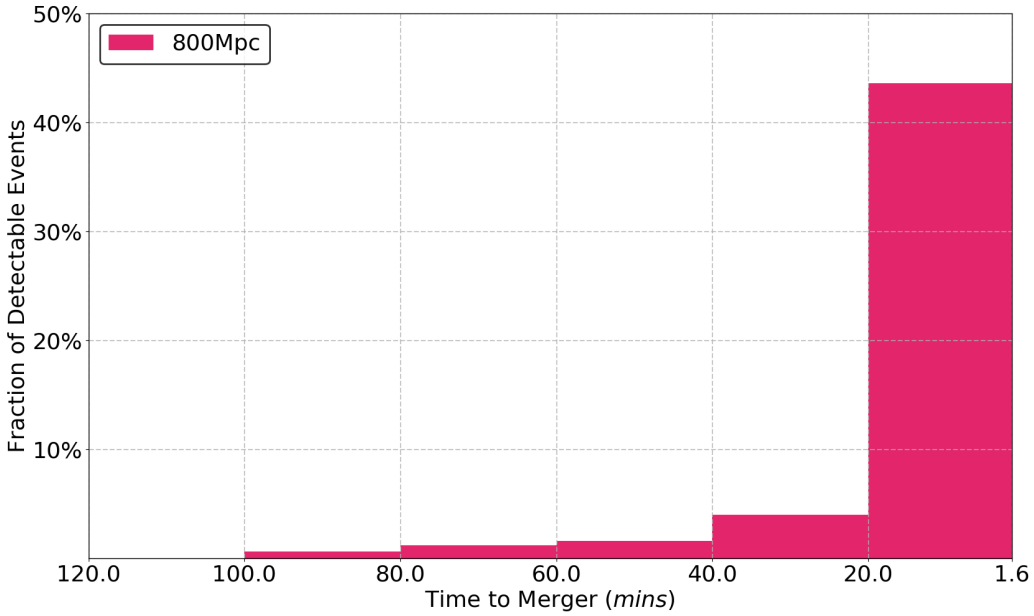

(b)

Figure 4.10: The same as Figure 4.7 but using the ET and CE as a network. Panel a and b are for events at 400Mpc and 800Mpc. The scale of the panels are the same as is shown in Figure 4.7 to allow a convenient comparison.

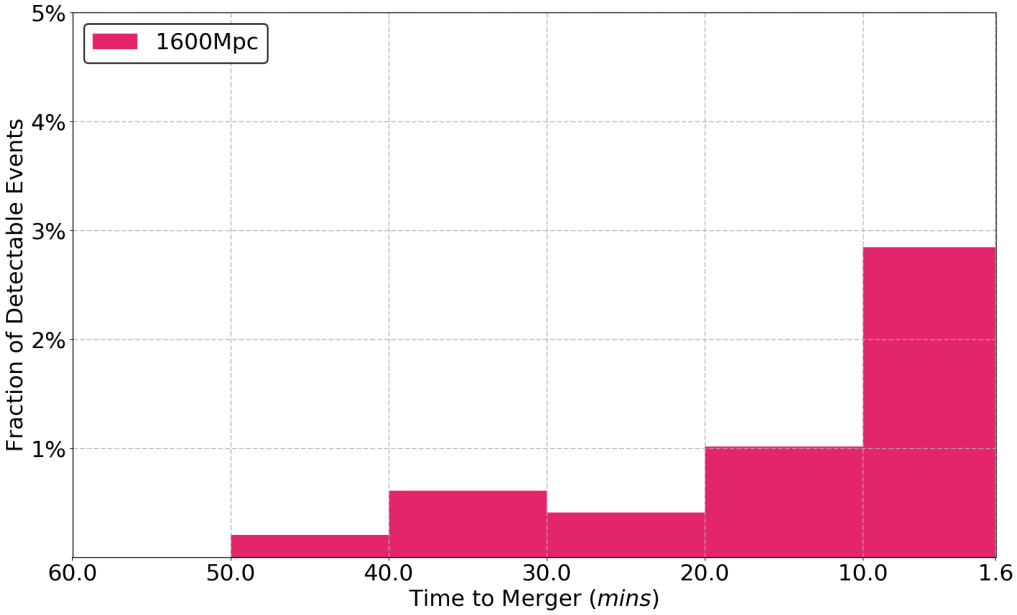

Figure 4.11: The same as Figure 4.8 but using the ET and CE as a network. The events are at 1600Mpc. The scale of the panels are the same as is shown in Figure 4.8 to allow a convenient comparison.

Table 4.2: Statistical Summary of Results For Early Warning

Network	d (Mpc)	n	100 sec	0.5 hrs	2 hrs	5 hrs	10 hrs
ET	40	500	100%	100%	99%	66%	18%
	200		58%	39%	13%	2%	0%
	400		28%	16%	4%	0%	0%
	800		9%	4%	0%	0%	0%
	1600		3%	1%	0%	0%	0%
	Uniform [1]	3000	2%	1%	0%	0%	0%
ET & CE	40	500	100%	100%	99%	66%	18%
	200		100%	74%	13.4%	2%	0%
	400		98%	27%	4%	0%	0%
	800		51%	4%	0%	0%	0%
	1600		5%	1%	0%	0%	0%
	Uniform [1]	5000	4%	1%	0%	0%	0%

[1] Uniformly distributed in the comoving volume.

A brief statistical summary of the results for early warning. In the first row, we again use d to denote distance and n the number of injections. The third to the seventh columns indicate the fraction of detectable events that meet the early warning criteria within the corresponding times.

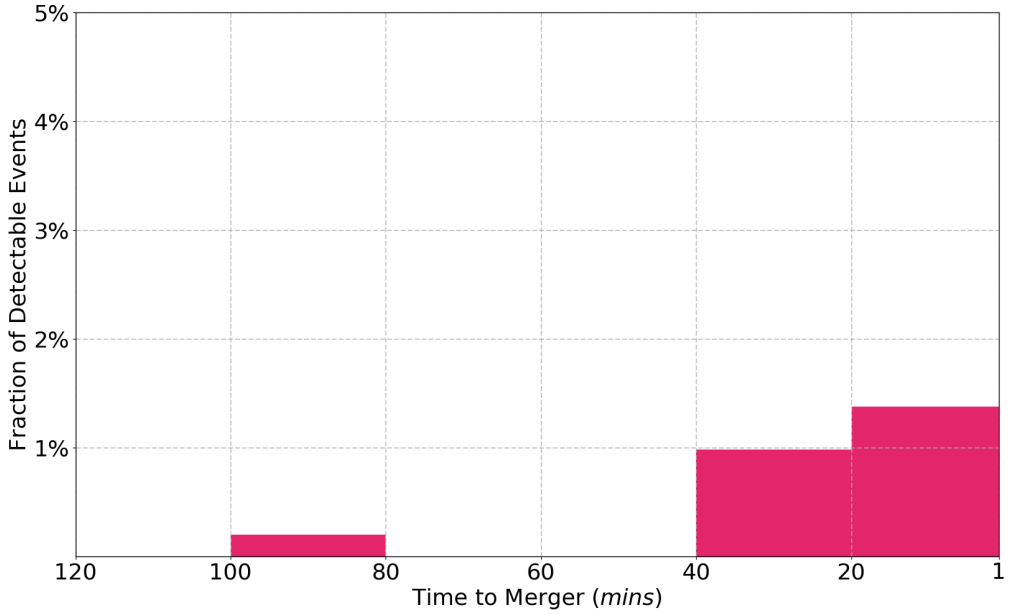

(a)

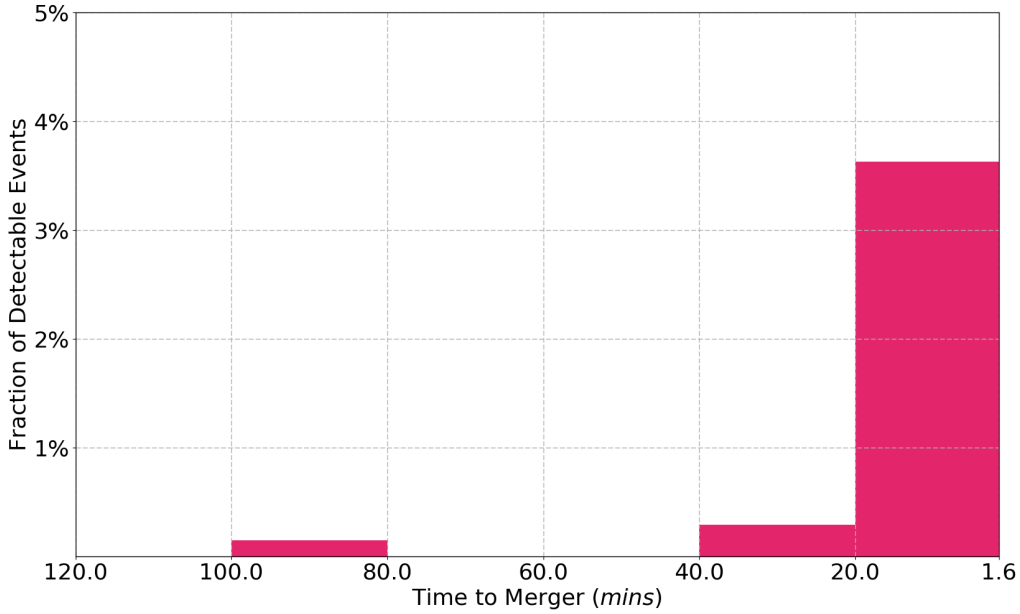

(b)

Figure 4.12: Histograms showing the fraction of detectable events that meet the early warning criteria as a function of time to merger for a population of BNS sources distributed uniformly in comoving volume. Panel a shows the results for the ET and panel b for the ET and CE as a network.

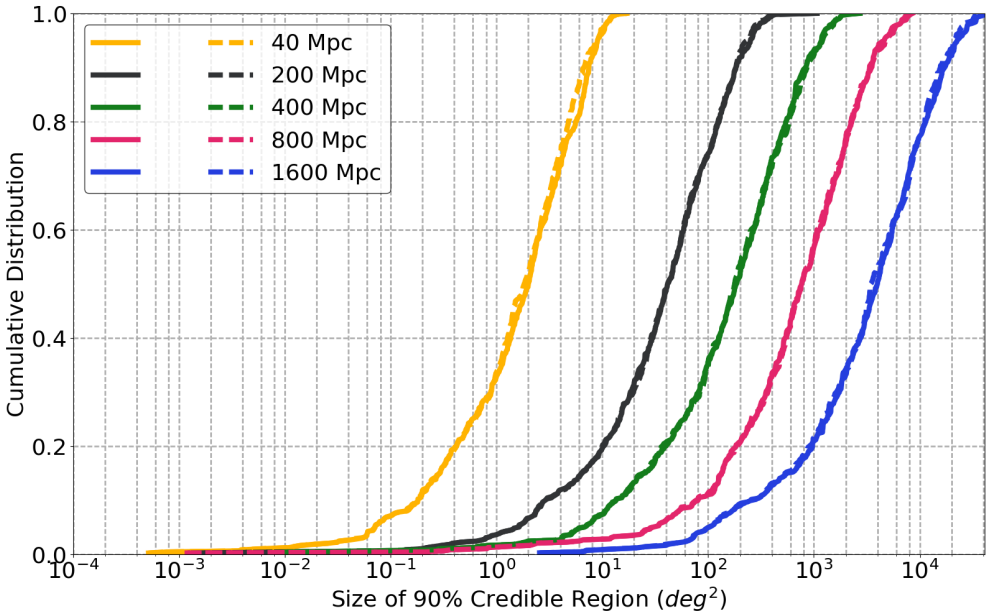

Figure 4.13: The cumulative distribution of the size of 90% credible regions for sources at fixed distances, with and without the Doppler shift effect. The x-axis shows the size of the 90% credible region and the upper limit of the x-axis corresponds to the size of the whole sky. The yellow, black, green, red, and blue lines represent BNS sources at 40, 200, 400, 800, and 1600Mpc respectively. The solid lines and the dashed lines show the results with and without including the Doppler shift of the waves respectively.

izations with or without including the time-dependencies of these two effects, for networks of third generation detectors. However, it is still not clear which of these two factors has a more important role in terms of localizing BNS mergers. We here investigate the relative importance of these two factors.

To test this, we repeat the simulations for the ET shown in Section 4.3.1. While we still enable a time-dependent detector response, we fix the time delay between the center of the earth and the ET at the beginning of the signals. This is because turning on and off the Doppler shift should allow us to see more easily its importance. The results are shown in Figure 4.13. It can be seen that at all distances, the cumulative distributions are almost identical, with only marginal discrepancy. This suggests that the Doppler effect is not important and the modulation of the detector response is the main cause of improved sky localization.

4.3.3 Calibration Errors

Previous studies have dealt with calibration errors in the context of second generation detectors [147, 399, 400, 401]. We present here a brief discussion of the impact of

calibration errors on localization for third generation detectors. It is recognized that bias in the output of a detector can be introduced by errors in its calibration – i.e., differences between the actual response function and the measured response function of the detector. These differences can then affect the noise and cause amplitude errors and timing errors in the GW strain used for analysis. Inference on the location of the source of a GW from the output strain can therefore be biased.

Amplitude errors will affect the localization by introducing a bias in the measurement of distance, inclination and polarization angles. With 2G detectors, these parameters cannot be measured precisely. For example, the uncertainty on distance can be $\sim 40\%$ for an event with SNR ~ 8 [399]. Therefore, systematic errors caused by amplitude uncertainties are not expected to be dominant. However, the fractional uncertainty on distance of a GW from BNS is inversely proportional to SNR. It is conceivable that when the ET and CE are operational, higher SNR and the extended in-band duration will increase the accuracy with which these parameters can be determined. The amplitude error-induced bias may therefore be comparable to the uncertainty on the measurement of the parameters. Moreover, we assumed in this work that the actual value of the detector response will agree with the theoretical calculation. As shown in Figure 4.13, the time evolution of the detector response is crucial for localization of BNS mergers with third generation detectors. Any uncertainty in the amplitude of the waves or the detector response will certainly affect that. As a result, the inference without accounting for these errors may systematically shift the probable locations of the source away from its true location. Amplitude errors are therefore expected to have a larger effect in parameter estimation for third generation detectors and need to be quantified.

Localization can also be affected by timing errors of a signal through timing triangulation. The accuracy with which the arrival time of a signal is determined is inversely proportional to the SNR of a wave cycle at the frequencies at which the detectors are most sensitive. For advanced detectors, such as aLIGO and Advanced VIRGO, this happens at ~ 100Hz giving a timing accuracy $\mathcal{O}(10^{-3})$ seconds. Timing errors (i.e., the errors intrinsic to timing when the data sample is taken) therefore would have to be comparable to a millisecond in order to be significant. However, as third generation detectors will have improved sensitivity, the SNRs for a fraction of detectable sources will therefore be high enough that timing error may be significant. It is therefore necessary to quantify timing errors for third generation detectors.

4.4 Binary Black Holes with Extended Networks of Detectors

Provided they are at distances close to the earth, events of BBH mergers are expected to register at advanced detectors with relatively high SNR and be relatively well localized with three or more detectors. Unfortunately, the majority of the detectable

BBH mergers will be at cosmological distances with random orientation. The localization of these events may still be of the order $\mathcal{O}(10^2)\,\mathrm{deg}^2$ or $\mathcal{O}(10^3)\,\mathrm{deg}^2$ if only the advanced detectors are operative [402]. With more detectors in a network, especially if the detectors are with large geographical separations (the baseline), localization of BBH can be expected to improve. In this section, we focus on the estimate of the localization error of BBH mergers with extended networks consisting of 2G detectors and the detectors proposed by [90].

For BBH signals, if detector's sensitivity in the low frequency range (1Hz - 10Hz) is limited, only the near-merger inspiral and merger signal will be detectable to the detector. Such a signal will have an in-band duration much shorter than that described in previous sections (see Figure 1.3). For such signals, the rotation of the earth (thus the time-dependency of antenna pattern) is negligible. As mentioned, localization is mainly achieved via timing triangulation, although in practice, information such as the phases and polarizations of the waves can also help improve the localization [202, 203, 204].

Localization based on timing triangulation is determined by the number of detectors in a network and the baseline between the detectors as well as the distance, direction and the orientation of the source [147, 151]. As one would expect, longer baseline means larger difference in the arrival times at the detectors and thus better localization for the same source. For a network with 3 detectors, the following equation gives an approximation of the localization error [202],

$$\Delta\Omega = \frac{2c^2\Delta\tau_{12}\Delta\tau_{13}}{A\cos\theta}, \tag{4.12}$$

where c is the speed of light, A the area formed by the detectors, Δ_{12} and Δ_{13} are the uncertainty in the time delays between pair of detectors with the subscripts indicating the detectors. In the literature, two different FM approaches to derive a lower bound on the uncertainty of the sky position of GW sources with 2G detectors have been proposed, namely [151] and [149]. We show the comparison between these two FM approaches for estimating the localization error of face-on BNS mergers in Appendix C. In the remaining of this section, we will describe and employ an analytical form of the FM outlined in [149] to derive a lower bound on the uncertainty of the sky position of BBH mergers.

4.4.1 Analytical Expression of the Fisher Matrix

We will now present the analytical expression of the FM and the relevant equations. Readers interested in the full derivation of the expression are referred to [149]. The analytical expression described here is only applicable to signal of short duration where the rotation of the earth is negligible. For consistency, in this section, we still use upper case letter $I,\ J,\ K$ to indicate detectors and lower case letter $i,\ j,\ k$ the position of the element in the FM or the unknown parameters themselves (similar to

Section 4.2). The Fisher Matrix can be expressed as,

$$\Gamma_{ij} = \sum_{I,\ J} \triangle_{IJ} \frac{\partial \tau_I}{\partial n_i} \frac{\partial \tau_J}{\partial n_j}, \tag{4.13}$$

where τ is the time required for the wave to travel from the center of the earth to the detector as defined in Eq. 4.2. For generality, in this section, we denote the sky coordinates of the sources as n_i and n_j without referring to a specific coordinate system. $\frac{\partial \tau_I}{\partial n_i}$ indicates the partial derivative of the signal arrival time at the I^{th} detector with respect to sky coordinate n_i. $\triangle_{IJ}$ on the right hand side is defined as

$$\triangle_{IJ} = 4\pi^2 \left(\langle f\tilde{h}_I | f\tilde{h}_J \rangle \delta_{IJ} - \sum_{k,\ l} \langle f\tilde{h}_I | \frac{\partial \tilde{h}_I}{\partial \lambda_k} \rangle \mathbf{B}^{-1}_{kl} \langle \frac{\partial \tilde{h}_J}{\partial \lambda_l} | f\tilde{h}_J \rangle \right), \tag{4.14}$$

where λ_k is the k^{th} unknown parameter and the k^{th} element of the vector $\boldsymbol{\lambda}$. The number of the elements in the vector is equal to the number of the unknown parameters. These unknown parameters can be the mass, distance or inclination angle of the system. $\tilde{h}$ is the Fourier transform of the detector data h as defined in Eq. 4.3. The matrix $\mathbf{B}$ can be expressed as,

$$\mathbf{B} = \langle \frac{\partial \tilde{\mathbf{h}}}{\partial \boldsymbol{\lambda}} | \frac{\partial \tilde{\mathbf{h}}}{\partial \boldsymbol{\lambda}} \rangle. \tag{4.15}$$

$\mathbf{h}$ is a vector defined as,

$$\mathbf{h} = \left[\ \tilde{h}_1(f), \quad \tilde{h}_2(f), \quad \cdots, \quad \tilde{h}_{N_d}(f) \ \right]. \tag{4.16}$$

The $\langle | \rangle$ indicates inner product, which is given by,

$$\langle a | b \rangle = 2 \int_{-\infty}^{+\infty} \mathrm{d}f a^{\dagger} b, \tag{4.17}$$

The symbol † indicates the transpose and the complex conjugate of the vector. The analytical expressions in [149] and described above (i.e. Eqs. 4.13, 4.14 and 4.15) are applicable to more general situations (i.e. parameters such as distance, masses and orientation of the system are unknown). However, as in this section, we focus on a simplified situation where the time of arrival of the signal is the only unknown parameter in addition to the sky coordinates of the sources, $\boldsymbol{\lambda}$ is a one element vector, of which the element is the time of arrival. Hence, $\triangle_{IJ}$ is simply the following:

$$\triangle_{IJ} = 4\pi^2 \left(\int_{-\infty}^{\infty} \mathrm{d}f |\tilde{h}_I|^2 f^2 - \frac{2 \int_{-\infty}^{\infty} \mathrm{d}f |\tilde{h}_I|^2 f^2 \times \int_{-\infty}^{\infty} \mathrm{d}f |\tilde{h}_J|^2 f^2}{\sum_K \int_{-\infty}^{\infty} \mathrm{d}f |\tilde{h}_K|^2 f^2} \right),$$

which leads to the following result:

$$\Gamma_{ij} = 4\pi^2 \Bigg(\sum_{I}^{K} \int_{-\infty}^{\infty} \mathrm{d}f |\tilde{h}_I|^2 f^2 \frac{\partial \tau_I}{\partial n_i} \frac{\partial \tau_I}{\partial n_j} \tag{4.18}$$

$$- \frac{2 \sum_{J}^{N} \frac{\partial \tau_J}{\partial n_i} \int_{-\infty}^{\infty} \mathrm{d}f |\tilde{h}_J|^2 f^2 \times \sum_{K}^{N} \frac{\partial \tau_K}{\partial n_j} \int_{-\infty}^{\infty} \mathrm{d}f |\tilde{h}_K|^2 f^2}{\sum_{L}^{N} \int_{-\infty}^{\infty} \mathrm{d}f |\tilde{h}_L|^2 f^2} \Bigg). \tag{4.19}$$

4.4.2 Localization of Binary Black Holes

As mentioned in Section 1.3.4, to bridge the gap in time between second and third generation detectors, two detectors designed with more advanced technologies than 2G detectors are proposed to be built in Australia and China. We will refer to any detectors designed with the technologies proposed in [90] as Blair et al detectors plus their locations, e.g., Blair et al A or Blair et al C for such a detector in Australia or in China respectively. For these detectors and 2G detectors, the sensitivity in the low frequency range (1Hz - 10Hz) is limited (see Figure 1.7). As a result, the in-band duration of the signals of BBH will only be of the order $\mathcal{O}(10^2)$s at most (see Figure 1.3). Therefore, the formalism described above is applicable.

Using the above formalism, we estimate the localization error of BBH mergers with a network of 2G and Blair et al detectors. The BBHs are either $30\mathrm{M}_\odot - 30\mathrm{M}_\odot$ or $10\mathrm{M}_\odot - 10\mathrm{M}_\odot$ (observed masses in Eq. 4.11). The $30\mathrm{M}_\odot - 30\mathrm{M}_\odot$ are distributed at different specific distances such as 400, 800, 1600 and 3200Mpc. For $10\mathrm{M}_\odot - 10\mathrm{M}_\odot$, we fix the distance at 400Mpc. All BBH mergers will have randomized sky locations (α and δ), and orientation (ϕ and ι). We employ the same SNR cut as described in Section 4.3.1. The detectors simulated for in this section are listed in Table 4.3, of which different combinations are the networks assumed in this section. The results are shown in Figures 4.14, 4.15 and 4.16.

It can be seen that for both $30\mathrm{M}_\odot - 30\mathrm{M}_\odot$ and $10\mathrm{M}_\odot - 10\mathrm{M}_\odot$ BBH mergers at 400Mpc, the localization provided by a network of LHVJIAC as estimated using the FM is accurate. The best localized 50% and 90% of the detectable $30\mathrm{M}_\odot - 30\mathrm{M}_\odot$ BBH mergers at 400Mpc can be localized to within $0.2\,\mathrm{deg}^2$ and $0.7\,\mathrm{deg}^2$ respectively. With the same network for $10\mathrm{M}_\odot - 10\mathrm{M}_\odot$ BBH mergers at 400Mpc, the localization errors of the detectable sources are only $\mathcal{O}(1)\,\mathrm{deg}^2$ for the best localized 90% of the detectable sources.

For $30\mathrm{M}_\odot - 30\mathrm{M}_\odot$ BBH mergers at larger distances such as 800, 1600 and 3200Mpc, the localization errors for the majority of the sources are still relatively small on the sky. However, given their distances, a small region on the sky would contain a large number of galaxies making it difficult to associate the sources with their host galaxies confidently. For example, at 800Mpc, assuming 30% relative distance error and an r limiting magnitude of 17 , an area of $0.4\,\mathrm{deg}^2$ would contain $\sim$ 100 galaxies [4]

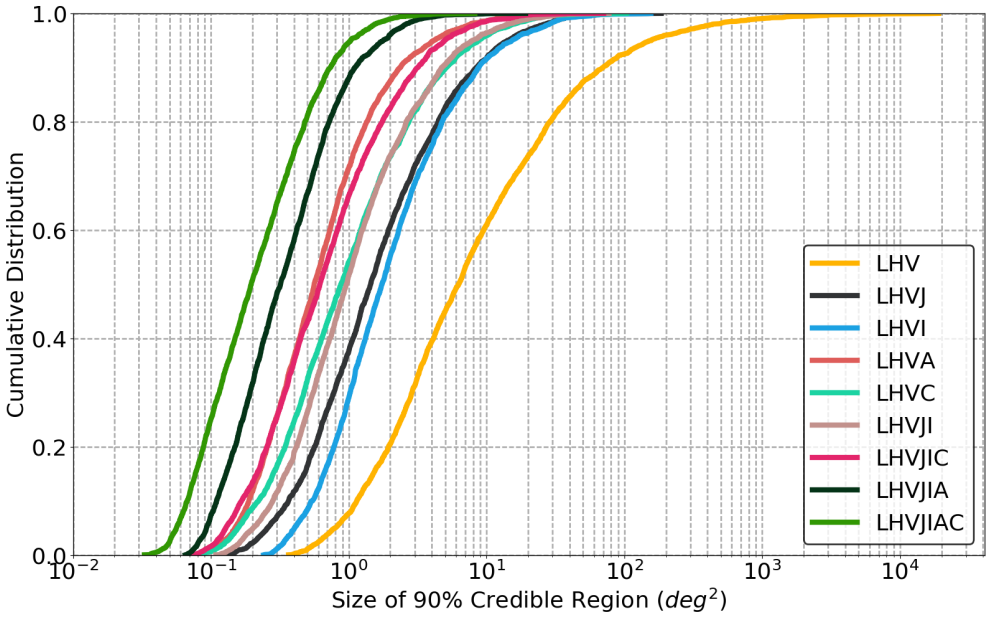

(a)

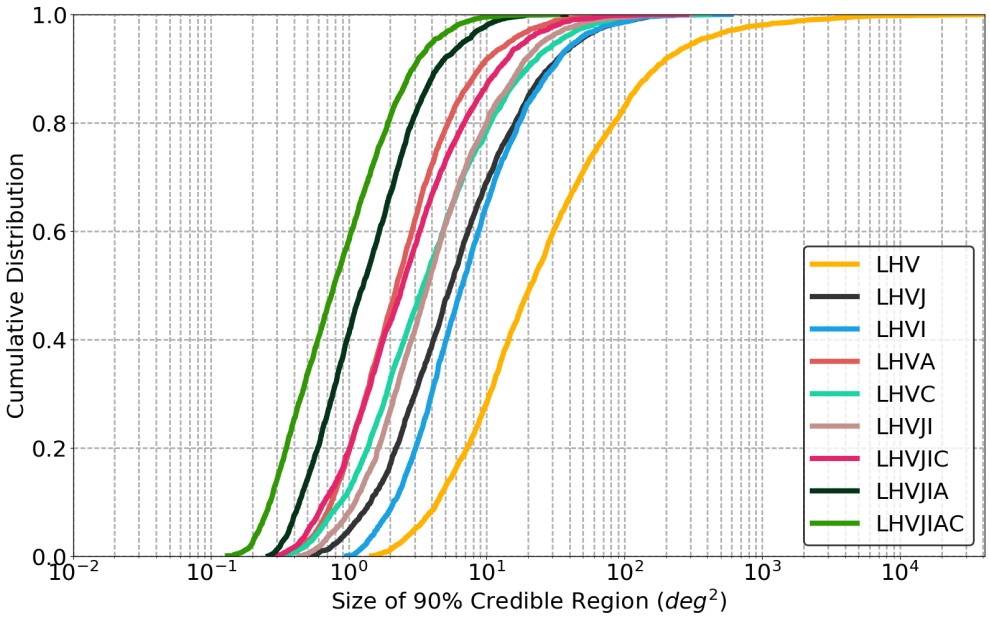

(b)

Figure 4.14: The cumulative distribution of the size of 90% credible regions for $30M_{\odot} - 30M_{\odot}$ BBH mergers at fixed distances. The x-axes show the size of the 90% credible region and the upper limit of the x-axes corresponds to the size of the whole sky. Panel a and b show BBH mergers at 400Mpc and 800Mpc respectively. In the legend, L, H, V, J, I, A and C are acronyms referring to different detectors specified in Table 4.3.

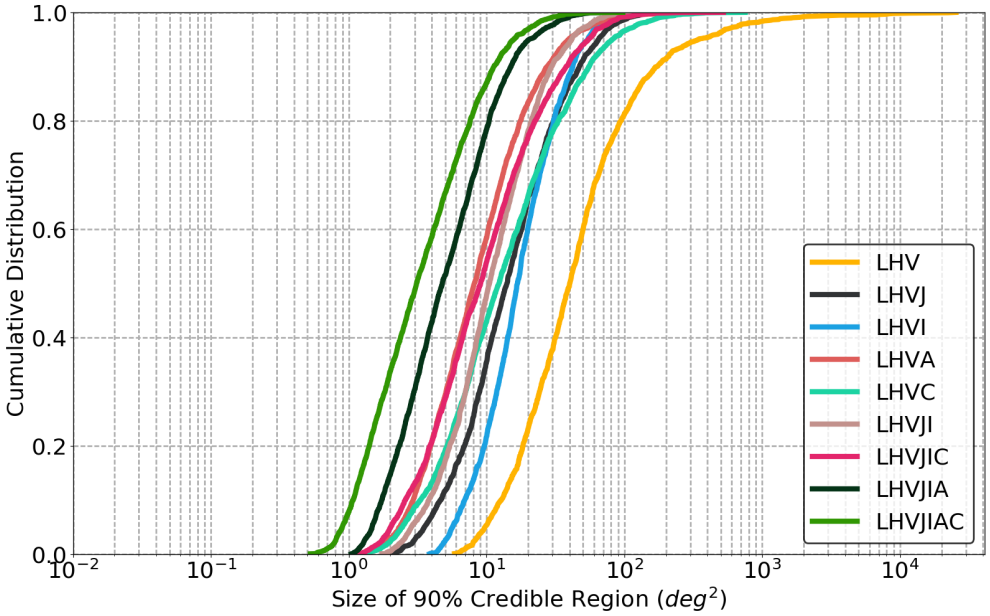

(a)

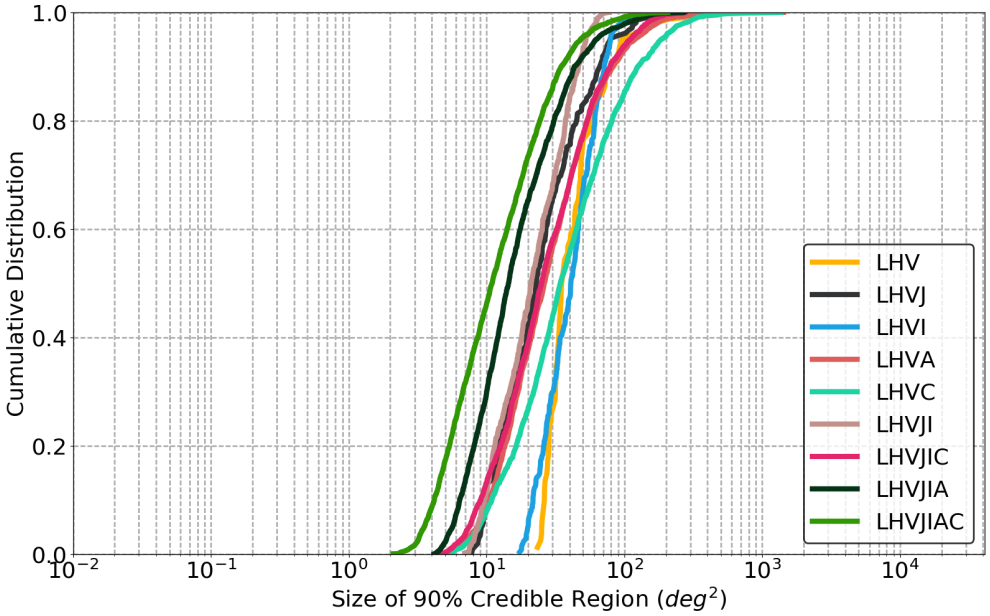

(b)

Figure 4.15: The same as Figure 4.14 but for different distances. Panel a and b show $30M_{\odot} - 30M_{\odot}$ BBH mergers at 1600Mpc and 3200Mpc respectively.

Table 4.3: Detectors

Detector	Sensitivity	Acronym
aLIGO Hanford	LIGO Design Sensitivity	H
aLIGO Livingston	LIGO Design Sensitivity	L
AdVirgo	VIRGO Design Sensitivity	V
KAGRA	KAGRA Design Sensitivity	J
aLIGO India	LIGO Design Sensitivity	I
Blair et al A	Blair et al	A
Blair et al C	Blair et al	C

The detectors that we simulate for in this section. All detectors are at their respective design sensitivities as shown in Figure 1.7.

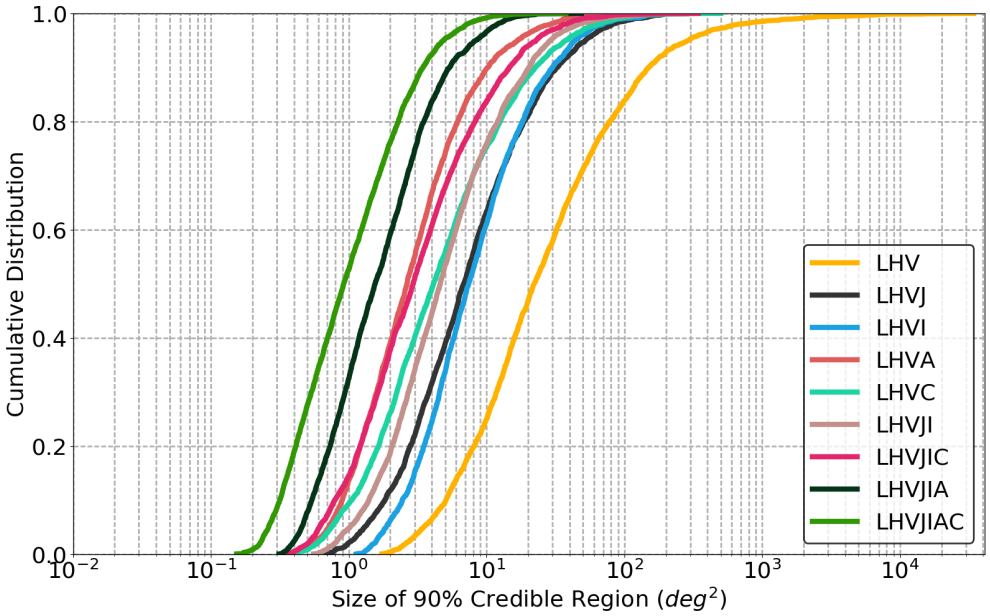

Figure 4.16: The cumulative distribution of the size of 90% credible regions for $10M_{\odot} - 10M_{\odot}$ BBH mergers at 400Mpc. The x-axes show the size of the 90% credible region and the upper limit of the x-axes corresponds to the size of the whole sky. In the legend, L, H, V, J, I, A and C are acronyms referring to different detectors specified in Table 4.3.

Table 4.4: Statistical summary

Network	30 - 30 BBH Distance (Mpc)								10 - 10 BBH	
	400		800		1600		3200		400	
	50%	90%	50%	90%	50%	90%	50%	90%	50%	90%
LHV	6.3	69.5	21.0	168.0	40.1	172.6	34.9	84.2	20.1	150.1
LHVJ	1.4	8.4	5.5	28.1	14.1	47.1	23.1	66.2	6.8	32.6
LHVI	1.7	8.7	6.7	30.0	16.8	42.2	40.1	71.5	7.4	29.9
LHVA	0.6	2.4	2.2	8.9	8.2	27.6	26.2	82.6	2.6	10.2
LHVC	0.9	5.1	3.5	20.0	12.3	55.2	34.2	125.2	4.1	22.5
LHVJI	1.0	4.7	3.7	17.4	10.5	29.6	21.0	46.3	4.6	20.3
LHVJIC	0.6	3.2	2.5	12.2	9.0	37.8	25.1	78.7	2.9	14.6
LHVJIA	0.3	1.1	1.3	4.3	4.8	15.0	14.4	43.3	1.6	5.4
LHVJIAC	0.2	0.7	0.7	2.9	3.1	11.3	10.9	34.9	1.0	3.4

In the table, the columns indicate the upper limit of the 90% credible region for the best localized 50% and 90% of the detectable sources with different networks.

(Since in this section, we focus on localization error rather than the estimate of the number of galaxies within the localization error, interested readers are referred to [4] for further discussion). Interestingly, for $30M_{\odot} - 30M_{\odot}$ BBH mergers at 400 - 3200 Mpc, the cumulative distributions of the 90% credible regions are shifted towards the right without changing the shape of distance except for the network of LHV. This indicates that the localization error is roughly inversely proportional to the SNRs. For the network of LHV, the network SNRs for a fraction of the events drop below the detectable threshold and therefore result in a different distribution. Statistical summary for BBH mergers at other distances with other networks are displayed in Table 4.4.

4.5 Conclusion

The ET and CE are two currently proposed third generation detectors. Due to the huge improvement in the sensitivity in the frequency band below 10Hz, the in-band durations of the GWs detected from BNS mergers will be hours or even days long. Therefore the Earth's rotation will become important, leading to several effects that become relevant for such long in-band duration signals. The long in-band duration allows us to observe the signal from different positions along the detector trajectory as the earth rotates. This in turn leads to a time-dependent detector response during the signal and also causes the wave to be Doppler modulated.

Using the FM and taking the earth's rotation into consideration, we have esti-

mated the localization capabilities of the ET and CE individually and as a network for BNS sources at distances equal to 40, 200, 400, 800 and 1600Mpc and for a population of BNS sources that is distributed uniformly in comoving volume. We have found that for BNS at 40 and 200Mpc, the ET alone will be able to localize most of the signals to within $100\,\mathrm{deg}^2$ with 90% confidence. If we assume EM follow up observation is achievable for BNS whose associated 90% credible region is $\leq 100\,\mathrm{deg}^2$, this means the ET alone will be able to provide support for multi-messenger astronomy for BNS mergers within 200Mpc. However, for distances $\geq$ 400Mpc, localization from the ET alone will still be poor. This is consistent with the localization performance for a population of BNS distributed uniformly in comoving volume. Of the detectable sources, only $\sim 32\%$ can be localized with 90% to within a region less than the size of the whole sky.

Combining the ET and CE can dramatically boost the performance in localization. Almost all the sources within 1600Mpc can be localized to within $100\,\mathrm{deg}^2$ with 90% confidence. In particular, the upper limit of the 90% credible region for the best localized 90% of the detectable sources at 40 and 200 Mpc has reduced by $\sim$ 100 times compared to using only the ET. Similar or greater improvements are seen for sources at greater distances. For a population of BNS uniformly distributed in the comoving volume, the improvement is equally impressive. The upper limit of the 90% credible region for the best localized 90% of the detectable sources as derived from the FM shrinks from an area larger than the entire sky to $\sim 500\,\mathrm{deg}^2$.

Regarding the ability to send event alerts prior to merger, the trend is similar. Using the ET alone, alerts for most BNSs within 200Mpc can be sent a few hours prior to merger, while for BNSs at $\geq$ 400Mpc, a large fraction of sources do not meet our early warning criteria. Those which do meet the criteria do so at a time relatively close to merger ($\mathcal{O}(10) - \mathcal{O}(10^2)$ minutes). A network with both the ET and CE substantially increases the number of signals at distances $\geq$ 400Mpc that meet the early warning criteria. This highlights the desirability and potential of such a network for BNS at relatively large distances. By turning on and off the Doppler effect in the simulation, we also established that the modulation of detector responses during the in-band duration is the main cause for improved localization.

In addition, we estimated the localization error of $30\mathrm{M}_\odot$ - $30\mathrm{M}_\odot$ BBH mergers at 400, 800, 1600 and 3200Mpc and $10\mathrm{M}_\odot$ - $10\mathrm{M}_\odot$ at 400Mpc with 2G detectors and two Blair et al detectors in Australia and China. With LHVJIAC as a network, the best localized 90% of the detectable $30\mathrm{M}_\odot$ - $30\mathrm{M}_\odot$ and $10\mathrm{M}_\odot$ - $10\mathrm{M}_\odot$ BBH mergers at distances $\leq$ 400Mpc can be localized to within $\mathcal{O}(10^{-1})\,\mathrm{deg}^2$ and $\mathcal{O}(1)\,\mathrm{deg}^2$ with 90% confidence. For $30\mathrm{M}_\odot$ - $30\mathrm{M}_\odot$ BBH mergers, the results suggest that the 90% localization error is inversely proportional to the SNR. As a consequence, the cumulative distribution of the 90% credible region will shift to the right for larger distance. An exception is the network of LHV, where the SNRs for a fraction of events will drop below the SNR threshold.

ACKNOWLEDGEMENTS

We are grateful to Prof. Yanbei Chen for his help with the methodology of the paper, and to Prof. Steve Fairhurst for his constructive comments on the paper. We are thankful to Dr. Xilong Fan and Teng Zhang for constructive discussions of this work. We are also grateful for computational resources provided by Cardiff University, and we are funded by an STFC grant supporting UK Involvement in the Operation of Advanced LIGO. This research is supported by The Scottish Universities Physics Alliance and Science and Technology Facilities Council. I.S.H., C.M. and M.H. are supported by the Science and Technology Research Council (grant No. ST/L000946/1)

Chapter 5

Electromagnetic Follow-Up Observation of Binary Neutron Stars with the Large Synoptic Survey Telescope

The LSST is a telescope currently being constructed in Cerror Pachón, Chile and is anticipated to see its first light in $\sim$ 2019 [403, 388, 404]. The LSST has a unique design in which the telescope will be a three-mirror system consisting of a primary mirror, a secondary mirror and a tertiary mirror, of which the diameters are 8m, 3.4m and 5m respectively [388]. In addition, the LSST will have a FOV as wide as 9.6 deg^2, which is considered to be large even among telescopes with similar size of primary mirrors ($\sim$ 8m-class) [388, 404]. The camera has 6 filters in total covering wavelength from 320 nm to 1080 nm ($u,\ g,\ r,\ i,\ z,\ y$), and can carries any 5 of them simultaneously. If needed, the change of a filter requires 2 minutes [388, 404]. Because of the large size of the primary mirror and the FOV, the LSST can provide fast cadence coverage of the sky in optical bands that reach faint magnitudes [388]. In a single visit ($\sim$ 30 seconds), it can reach magnitudes of 23.7, 24.9, 24.4, 24.0, 24.5 and 22.6 in $u,\ g,\ r,\ i,\ z$ and y bands respectively (5σ, point source) [403].

Indeed, the excellent multi-band sensitivity of LSST will enable much shorter exposure time for the detections of the EM counterparts associated with GW sources than most existing telescopes observing in the same bands. The large FOV of LSST is also helpful for tiling the sky location estimate of GW events. The capabilities of the LSST as a telescope enable it to be a promising telescope in multi-messenger astronomy with GWs. For example, the authors of [241] have shown that for BNS mergers, with GW detector networks consisting of aLIGO, AdVirgo and/or KAGRA, LSST will detect the associated kilonovae in a 2 hrs observation campaign if the kilonovae are not much fainter than $M = -11$ in the r band. It is suggested [241] that for BNS and NSBH mergers localized with a network of 3 advanced detectors, LSST

will be able to detect all the associated kilonovae out to $\sim$ 700Mpc and $\sim$ 1200Mpc respectively if the absolute magnitude of the kilonovae are at least -14. Even if the kilonovae are as faint as magnitudes equal to -11, LSST will still capture most of them to the same distances.

The GW detectors that are anticipated to be operational concurrently with LSST are LIGO A+ (both Hanford and Livingston), aLIGO India, AdVirgo, and KAGRA. with these detectors forming a global network, the localization for BNS mergers within the horizon of the advanced detectors can be expected to be improved. However, for sources at larger distances, the localization may still be poor. Larger distances also suggest that longer exposure is necessary for the detection of their associated EM counterparts. These factors can extend the time needed for EM follow-up observations of BNS mergers even with LSST.

In this chapter, we ask a question regarding EM follow-up observations that is different from the one we tackled in Chapter 3 - given a detected BNS merger event, how long will an observation campaign have to be for LSST to detect the kilonova associated with the BNS merger as an EM counterpart? To answer this question, we utilize the data for the GW170817 kilonova from the Open Kilonova Catalog[1]. Assuming a simple procedure for EM follow-up observations of BNS merger events, we will then investigate and quantify the time LSST will require to complete the procedure. We focus our attention on networks and detectors expected to operate within the same time frame as LSST such as LIGO A+, aLIGO India, AdVirgo, and KAGRA. We also include the analysis for two Blair et al detectors in Australia and China.

This chapter is structured as follows. In Section 5.1, we present the GW170817 kilonova luminosity data that we use in this chapter. The methodology is given in Section 5.2. The simulation and the results will be presented in Section 5.3 along with a discussion pf the results. In Section 5.4, we discuss possible extensions to this work, which will be followed by a summary in Section 5.5.

5.1 Kilonova Light Curves

The GW170817 kilonova as the first detected BNS associated kilonova has given many physical insights into, and confirmed many predictions related to, the phenomena. One of these is in the evolution of the luminosity of the transient.

For the purpose of this study, we employ the luminosity curves for the GW170817 kilonova gathered in the Open Kilonova Catalog. We compile the luminosity data for the GW170817 kilonova using a procedure similar to that in [405]. We focus on data in u, g, r, i, z and y band from [161, 163, 167, 406, 407, 281, 408, 298, 409, 277, 302, 305, 410, 300, 411]. Only data points with reported errors no larger than 0.35 in magnitude will be considered. We then take the average of the data collected at

[1] http://www.kilonova.space

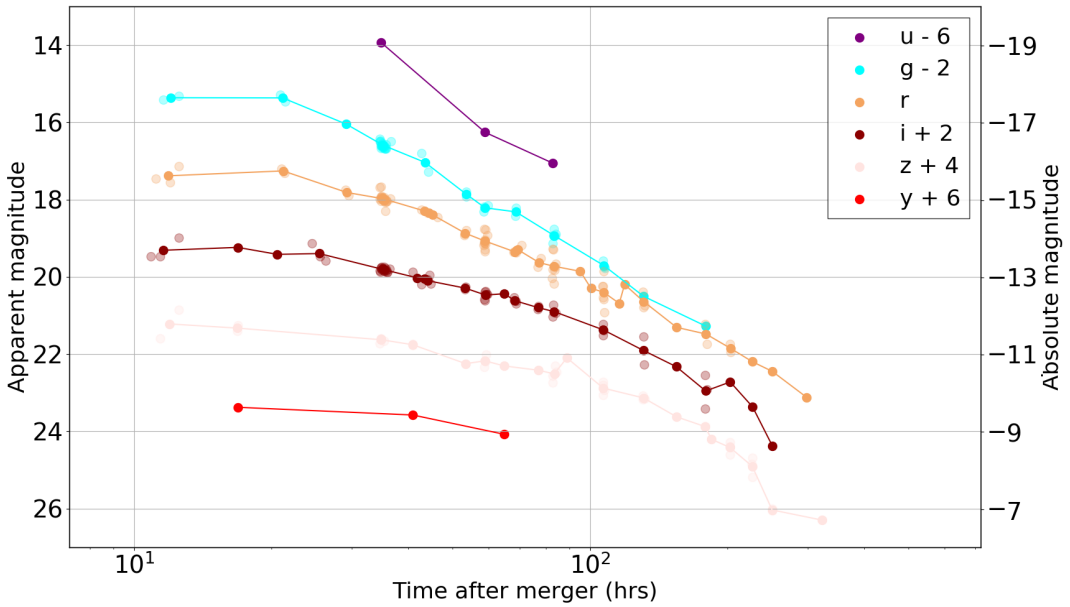

Figure 5.1: The light curves of the GW170817 kilonova in u, g, r, i, z and y band with offset indicated in the legend. The left y-axis shows the data in apparent data, and the right y-axis shows absolute magnitude. The semi-transparent points indicate the original data from [161, 163, 167, 406, 407, 281, 408, 298, 409, 277, 302, 305, 410, 300, 411], the solid points show the average of the data taken within 0.1 days of each other. This data was retrieved from the Open Kilonova Catalog.

observation times within less than 0.1 day of each other. The resultant light curves are shown in Figure 5.1. The original data are represented in apparent magnitude, so we present the absolute magnitudes on the right y-axis of Figure 5.1, given by

$$M_{\mathrm{GW},x} = m - 5\log_{10} d_{\mathrm{L}} + 5, \tag{5.1}$$

where m is the apparent magnitude and d_{L} is the luminosity distance. Specifically, we use 40Mpc for the d_{L} of the GW170817 kilonova, and $M_{\mathrm{GW},x}$ to denote the absolute magnitude of the GW170817 kilonova in the x band, where x can be either u, g, r, i, z or y. Although later in Section 5.2, we will define a procedure for follow-up observation with LSST which mostly concerns the sensitivity in the i and z bands, we still present the light curves of the GW170817 kilonova in u, g, r, i, z and y bands for completeness as LSST will also operate in these bands.

However, we note that although the discovery and observations of the GW170817 kilonova place constraints on kilonova luminosity models, there are currently many uncertainties on the mechanism for the ejection material, the opacity and the properties of kilonova emission components such as the mass, the velocity, radioactivity and the composition. In fact, many models in the literature predict different luminosities. In general, the GW170817 kilonova is consistent with the emission from a mildly rel-

ativistic expanding ejecta heated by energy released from radioactive element heavier than the iron group [163, 281, 408, 311, 412]. Therefore, the analysis and the results shown in later sections will be applicable to the extent that the light curves of the GW170817 kilonova are representative of kilonovae as a population.

5.2 Methodology

In Chapter 3, we were faced with the problem of optimizing follow-up observations targeting kilonovae associated with BNS mergers and given limited observational resources such as observation time and limited telescope sensitivity. In this chapter, we are interested in how long a follow-up observation campaign has to be for LSST to follow up a BNS merger event. This indicates we are more interested in how much time is required to achieve a detection instead of the estimate of the detection probability. Therefore, we will employ the formalism in [403] to compute the observation time needed for LSST to achieve a 5σ depth for a point source.

Given an observation time $\tau_{\rm obs}$, the 5σ depth $m_{5\sigma}$ can be determined using the following,

$$m_{5\sigma}(\tau_{\rm obs}) = C_m + 0.5(m_{\rm sky} - 21) + 2.5\log_{10}\frac{0.7}{\theta} + 1.25\log_{10}\frac{\tau_{\rm obs}}{\tau_{\rm fid}} - k_m(X-1), \quad (5.2)$$

where C_m is a constant depending on the sensitivity of the instrument and the overall instrument throughput. The observing conditions are described by the sky brightness $m_{\rm sky}$ in AB mag/arcsec^2, the seeing θ, atmospheric extinction coefficient k_m and the airmass X. The values of these parameters are published in [403] and are also presented in Table 5.1. The parameter $\tau_{\rm fid}$ refers to the fiducial exposure time for LSST, which is 30s (i.e. the exposure time for two single exposures, each of which is 15s). Eq. 5.2 may become invalid when the observation time is much longer than the fiducial observation time for LSST, i.e., $\tau_{\rm obs} \gg \tau_{\rm fid}$. For such an observation, the following correction term needs to be added to C_m,

$$\Delta C_m(\tau_{\rm obs}) = \Delta C_m^{\infty} - 1.25\log_{10}\left(1 + \frac{10^{(0.8\Delta C_m^{\infty})} - 1}{\tau_{\rm obs}/\tau_{\rm fid}}\right), \quad (5.3)$$

where ΔC_m^{∞} is the loss of depth due to instrumental noise, of which the values are given in Table 5.1. In all cases except for the u band, the correction is negligible.

In Eqs. 5.2 and 5.3, given the values of $m_{\rm sky}$, θ, $\tau_{\rm fid}$, k_m, X and ΔC_m^{∞}, the 5σ depth $m_{5\sigma}$ is a function of LSST observation time $\tau_{\rm obs}$. The 5σ depth for a point source in different bands as a function of observation time $\tau_{\rm obs}$ is plotted in Figure 5.2. By manipulating Eqs. 5.2 and 5.3, it is possible to obtain the observation time $\tau_{{\rm obs},5\sigma}$ as a function of 5σ depth in AB magnitude for a point source (e.g. the apparent magnitude of a kilonova), given by,

$$\tau_{{\rm obs},5\sigma}(m_{5\sigma}) = m_{5\sigma}^{-1}(\tau_{{\rm obs},5\sigma}). \quad (5.4)$$

Table 5.1: Values of the parameters used in Eq. 5.2 and Eq. 5.3

Band	u	g	r	i	z	y
$m_{\rm sky}$	22.9	22.3	21.2	20.5	19.6	18.6
θ	0.77	0.73	0.70	0.67	0.65	0.63
k_m	0.451	0.163	0.087	0.065	0.043	0.138
C_m	22.92	24.29	24.33	24.20	24.07	23.69
$m_{5\sigma}$	23.68	24.89	24.43	24.00	24.45	22.60
ΔC_m^{∞}	0.67	0.21	0.11	0.08	0.05	0.04
X			1.2			

From the top to the bottom:
$m_{\rm sky}$: the expected median zenith sky brightness.
θ: the seeing in arcsec.
k_m: atmospheric extinction coefficient.
C_m: a band-dependent constant describing the sensitivity of the instrument. C_m depends on the overall instrument throughput.
$m_{5\sigma}$: the 5σ depth for point source for an exposure of 30 seconds.
ΔC_m^{∞}: instrumental noise caused loss of depth.
X: airmass.
All the values listed are taken from [403].

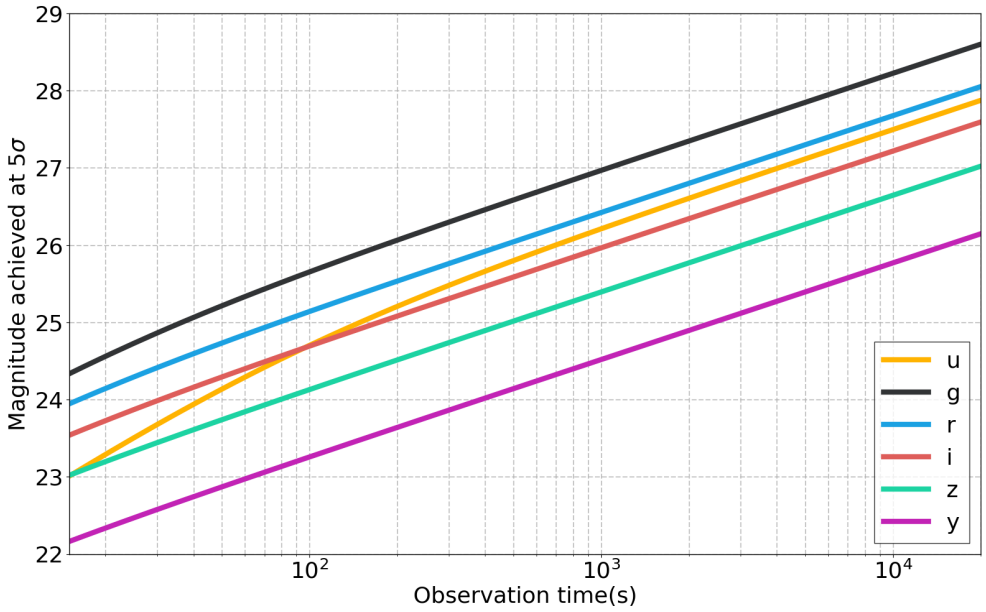

Figure 5.2: Depth as a function of observation time $\tau_{\rm obs}$ in different LSST bands. The values of $m_{\rm sky}$, θ, τ_{fid}, k_m, and X for different bands are given in Table 5.1. The yellow, black, blue, red, green and purple lines represent depth in u, g, r, i, z and y bands respectively.

For $\tau_{\rm obs,5\sigma}(m_{5\sigma}) < 30$s, we set the values of $\tau_{\rm obs,5\sigma}(m_{5\sigma})$ to be 30s as this is the fiducial minimum observation time of LSST.

For each BNS merger event simulated in this chapter, there will be an associated uncertainty on the estimate of the distance. We derive the 90% upper limit uncertainty on distance using the FM, which we denote as $\Delta d_{\rm L}$. We then use the following equation to compute the lower limit on the apparent magnitude of the associated kilonova in the x band,

$$m_x = M_{{\rm GW},x} + 5\log_{10}(d_{\rm L} + \Delta d_{\rm L}) - 5, \tag{5.5}$$

where m_x is the apparent magnitude of the kilonova at $d_{\rm L} + \Delta d_{\rm L}$ in x band and $d_{\rm L}$ the true distance of the source. Using Eqs. 5.4 and 5.5, we can compute the observation time $\tau_{\rm obs,5\sigma}(m_x)$ required for the detection of a kilonova of apparent magnitude m_x, provided that the kilonova is in the observation field.

For a GW event, we use the FM approach described in Section 4.2 to estimate the localization error. Assuming a GW event is localized to an area of S on the sky with 90% confidence by a network of GW detectors, covering the localization error would usually require n fields for a telescope with FOV equal to ω, where n is given by

$$n \leq \frac{S}{\omega}. \tag{5.6}$$

Therefore, the total observation time $\tau^{90\%}_{\mathrm{obs},5\sigma}$ required to cover the 90% credible region as well as achieving m_x is given by

$$\tau^{90\%}_{\mathrm{obs},5\sigma}(m_x) \leq n[\tau_{\mathrm{obs},5\sigma}(m_x) + T_0], \tag{5.7}$$

where T_0 is the time required for the telescope to readout from the CCD and to slew, which we assume to be 2s and 5s respectively for LSST [388, 404]. When the 90% localization error region requires only 1 field to cover, the slew time will be zero meaning there is no need to slew. In this chapter, in order to allow for a conservative estimate of $\tau^{90\%}_{\mathrm{obs},5\sigma}$, we take the equal sign in Eqs. 5.6 and 5.7.

To estimate the time a follow-up observation campaign of a BNS merger with LSST will need, we need to define a procedure with which the follow-up observation will be performed. The procedure defined here will be similar to the strategy DEC took for GW170817 [160]. We assume that in total, LSST will need three observations to identify the associated kilonova within the localization error region. The first observation will commence 11 hrs after the merger. The second observation will take place 24 hrs after the first observation. These two observations will cover the 90% credible region and reach the magnitude in both i and z bands given in Figure 5.1 at the corresponding epoch. The third observation will occur 14 days after the first observation, and will reach the same depth achieved in the first observation. The data taken with the third observation plays the role of an image template for image subtraction in practice, as at this time, the kilonova is expected to have already faded below the depth achieved with the third observation.

We then further assume two extreme scenarios. In the first scenario, we assume that only 1 potential candidate is detected within the 90% credible region on the sky after the first and second observations so that LSST needs to only observe one field in the third observation. The second scenario is the exact opposite in which there is at least one potential candidate in each of the observed fields so that the third observation will need to follow up on each of those observed fields. Therefore, the total time τ_{tot} for the follow-up observation campaign is given by

$$\tau_{\mathrm{tot}} = \tau_{\mathrm{tot},2} + \begin{cases} \max[\tau_{\mathrm{obs},5\sigma}(m_i^{11}), \tau_{\mathrm{obs},5\sigma}(m_z^{11})], & \text{first scenario} \\ n \times \max[\tau^{90\%}_{\mathrm{obs},5\sigma}(m_i^{11}), \tau^{90\%}_{\mathrm{obs},5\sigma}(m_z^{11})], & \text{second scenario} \end{cases} \tag{5.8}$$

In the above equation, $\tau_{\mathrm{tot},2}$ refers to the sum of the time for the two observations that occur in 11 hours and 35 hours after merger and is defined as

$$\tau_{\mathrm{tot},2} = n \times \max[\tau^{90\%}_{\mathrm{obs},5\sigma}(m_i^{11}) + \tau^{90\%}_{\mathrm{obs},5\sigma}(m_i^{35}), \tau^{90\%}_{\mathrm{obs},5\sigma}(m_z^{11}) + \tau^{90\%}_{\mathrm{obs},5\sigma}(m_z^{35})], \tag{5.9}$$

where n refers to the number of fields given by Eq. 5.6. The superscript h of m_x^{h} indicates the apparent magnitude of the kilonova at h hours after merger. In the second term on the right hand side, although the 3rd observation happens 14 days after the 1st observation, we use the term m_x^{11} because that is the depth required by the procedure for EM follow-up observations. We will further assume that LSST will be able to perform this procedure of follow-up observation regardless of the sky location of the BNS merger.

5.3 Results of Simulation and Discussion

For this study, we simulate $1.4M_\odot - 1.4M_\odot$ BNS mergers which are located at 200, 400 and 800Mpc. Similar to Chapter 4, the masses are defined in the source frame. The sky locations are randomly drawn from a uniform distribution in right ascension α and the sine of declination δ. Polarization angles ϕ are also drawn from a uniform distribution from 0 - 2π, and inclination angles ι from a uniform distribution on the cosine of ι. However, we exclude face-on sources for two reasons (i.e. $\iota \leq 18^\circ$ or $\iota \geq 162^\circ$) . First, for these sources, short GRBs as an EM counterpart might be present. The fact that we do not consider short GRBs in this chapter and that the localization information from the detection of the associated gamma-ray bursts will change the analysis here implies that the analysis will likely be inapplicable to face-on sources with associated short GRB. Second, the polarization of GWs from more edge-on sources are better linearized than those from face-on sources. Therefore, the estimate of the uncertainty on distances of face-on sources from the FM would be unreliable. For a uniform distribution on the cosine of ι, this amounts to $\sim 4\%$ of the population, which should not alter the result significantly. For 200 and 400Mpc, we simulate 5×10^3 BNS mergers, but for 800Mpc, we simulate 5×10^4 due to the low detection rate with networks only consisting of detectors such as aLIGO A+, AdVirgo, LIGO India, and KAGRA (the simulated networks are listed in Table 5.2 and will be explained in the next paragraph). Since for network consisting more than one Blair et al detector, the detection horizon will extended, we also simulate 5×10^3 BNS mergers at 1600Mpc for this network.

In this chapter, we consider 7 networks of GW detectors. The networks of detectors considered are given in Table 5.2. For the remaining of this chapter, we will refer to these networks using the notations in the first column in Table 5.2. For instance, the network of H+ L+ V will be referred to as Network 1. We again employ the SNR requirement defined in Section 4.3 to determine whether a source is detectable, i.e. for an event to be detectable, the network SNR has to be larger than or equal to 12, and no fewer than two detectors have an SNR larger than or equal to 5.5.

Using the FM and Eq. 5.8, we compute the value of $\tau_{\rm tot}$ for each of the detectable BNS merger events for the two scenarios defined by Eq. 5.8. We present the results for Network 1 - 4 in Figures 5.3, 5.4, 5.5 and 5.6. The results for Network 5 - 7 will be shown in Appendix D in Figures D.1, D.2 and D.3.

In Figures 5.3, it can be seen that for BNS mergers localized with Network 1, performing EM follow-up observations using the defined procedure with LSST will require observation time $\tau_{\rm tot} \leq 10^3$s for the majority of the detectable BNS mergers at all three distances, and $\leq 10^4$s for all detectable BNS mergers, which is a few hours. This is not surprising as the 90% credible regions, as shown in Figure 5.3(a), provided by this network for most detectable BNS mergers span $10\,{\rm deg}^2$ - $10^2\,{\rm deg}^2$ on the sky, which will require only ~ 1 to ~ 10 fields to tile. Only the events with 90% credible region $\sim 10^3\,{\rm deg}^2$ will require $\sim 10^4$s. In our simulation, this level of

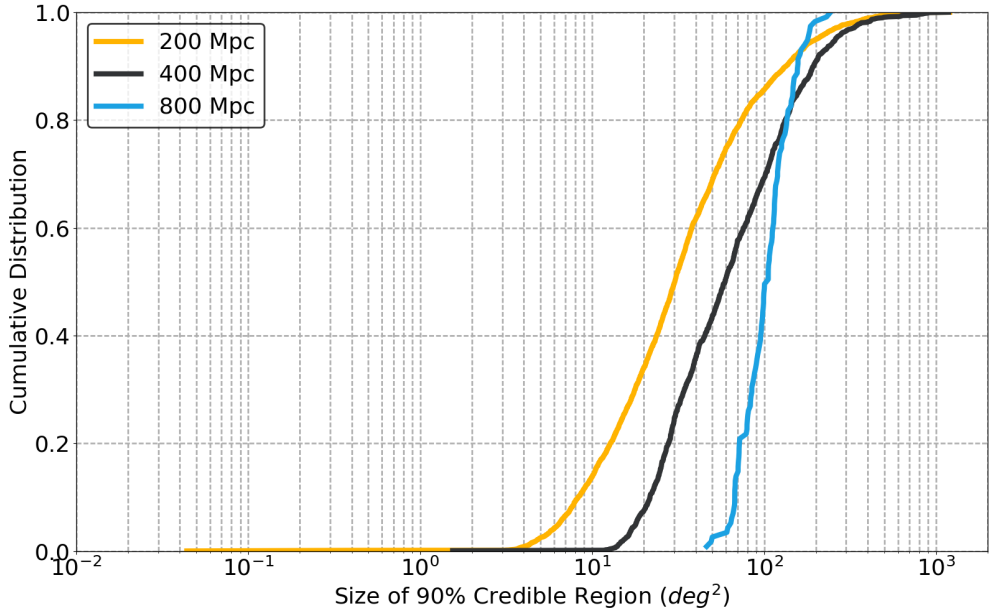

(a)

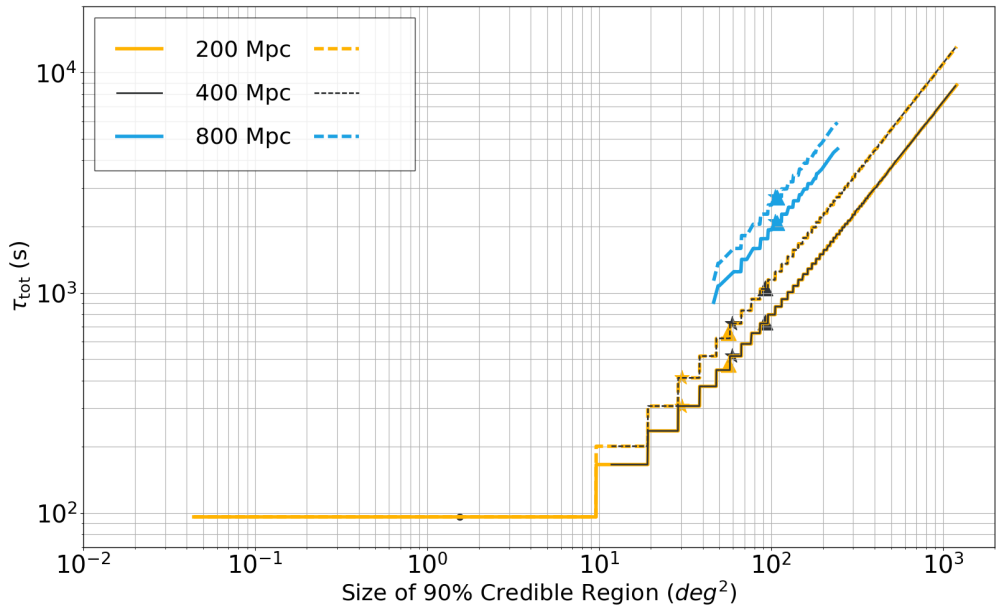

(b)

Figure 5.3: Plots showing the results for the simulation for Network 1 (H+ L+ V). The upper panel shows the cumulative distribution of the size of the 90% credible regions for detectable BNS mergers. The blue line shows a different shape compared to the other lines. This is because the SNR threshold has ensured that for sources at 800Mpc, only those at sky positions with detector response strong enough will be detectable, effectively excluding sources with large sky localization errors. The lower panel shows the values of $\tau_{\rm tot}$. The legends in the plots indicate the true distances of the sources. In the lower panel, the solid lines shows the values of $\tau_{\rm tot}$ for the first scenario, and the dashed lines show that for the second scenario, as indicated in Eq. 5.8. The black dot shows the best localized event at 400Mpc, of which the size of the corresponding the 90% credible region is at least 1 order of magnitude less than the rest of events at the same distance. If plotted as a line with the rest of the data, the line would produce misleading results for events that fall between the first best localized event and the second best localized event in the simulation. The stars and triangles indicate the median and the mean values of the $\tau_{\rm tot}$ respectively (i.e. excluding the data plotted as dots).

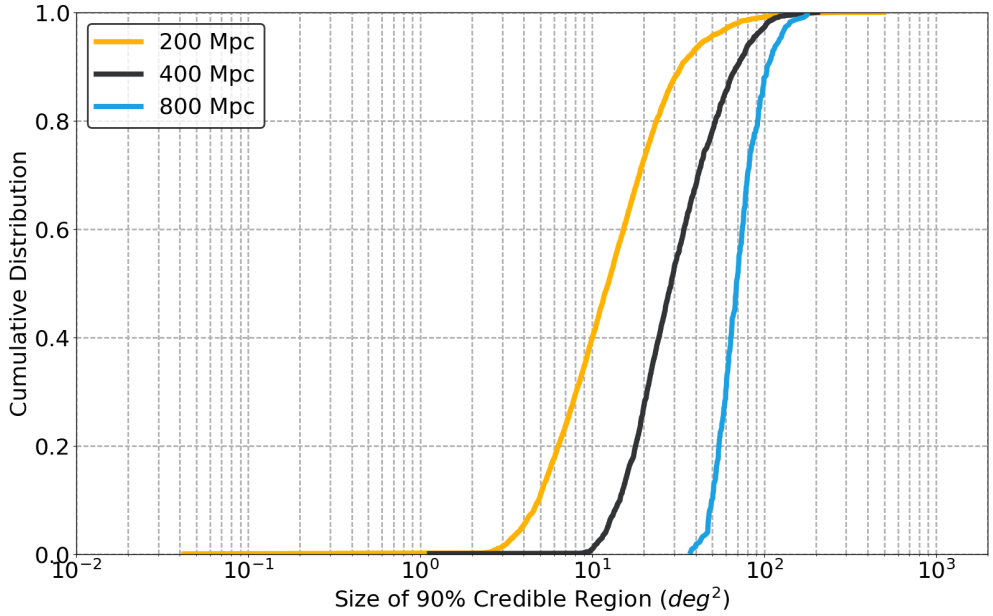

(a)

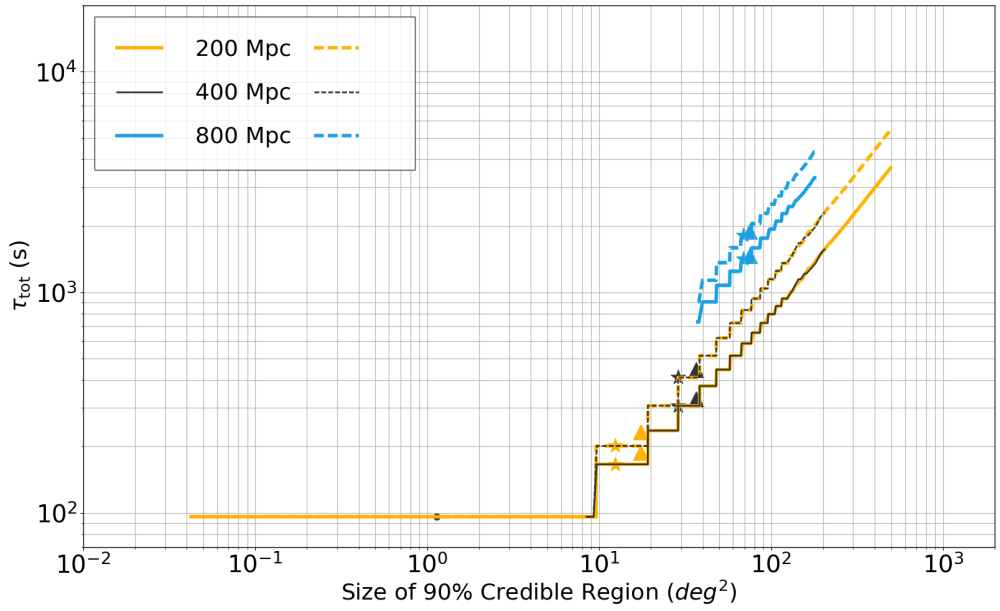

(b)

Figure 5.4: Similar to Figure 5.3. In this case, the network is Network 2 (H+ L+ V I).

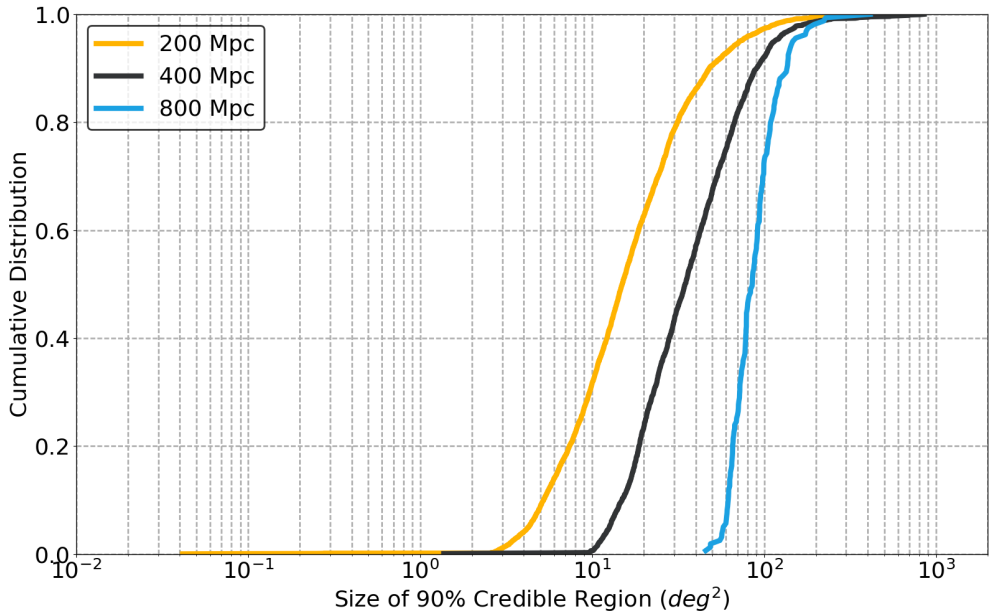

(a)

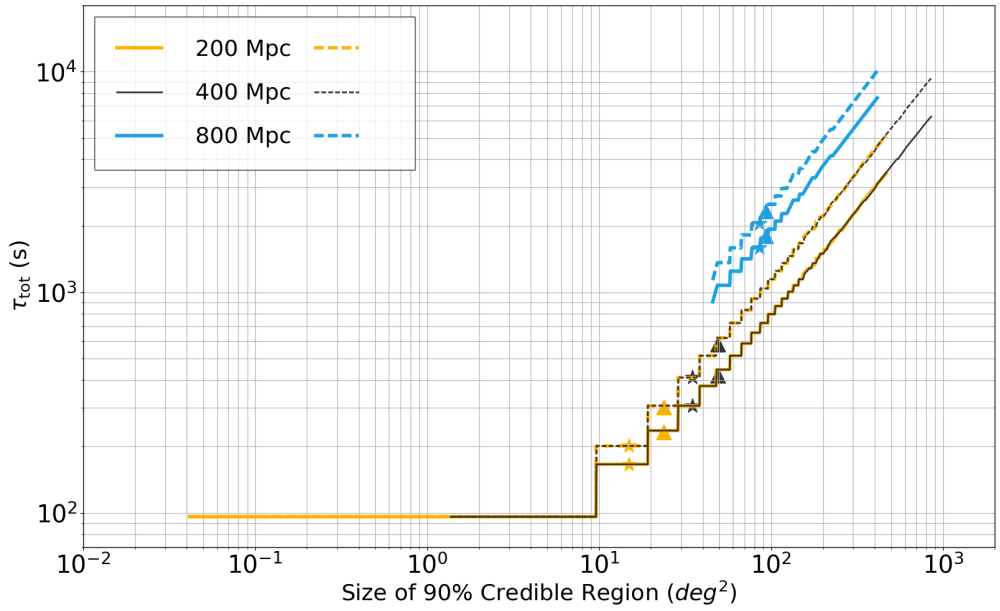

(b)

Figure 5.5: Similar to Figure 5.3. In this case, the network is Network 3 (H+ L+ V J).

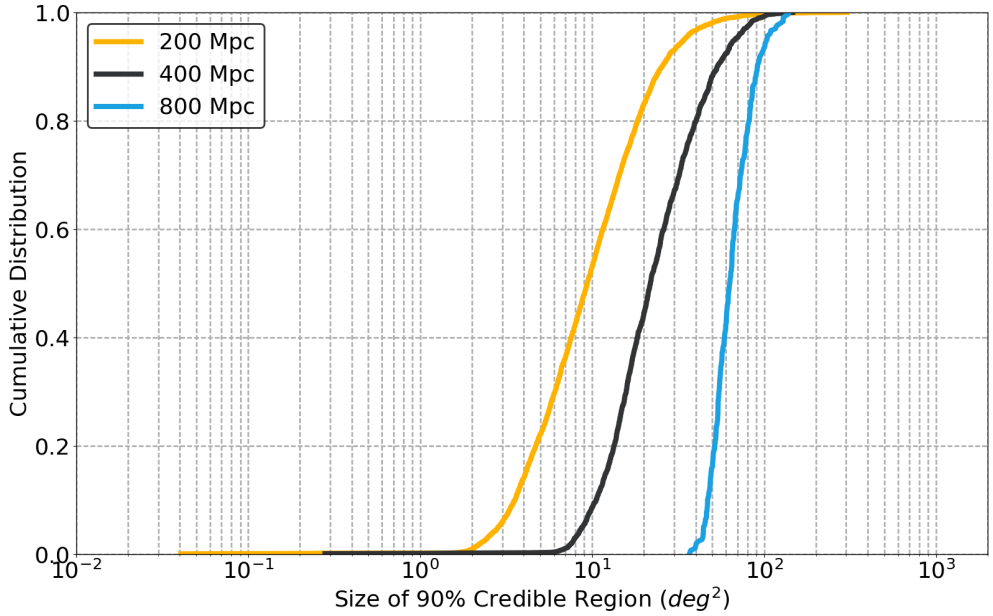

(a)

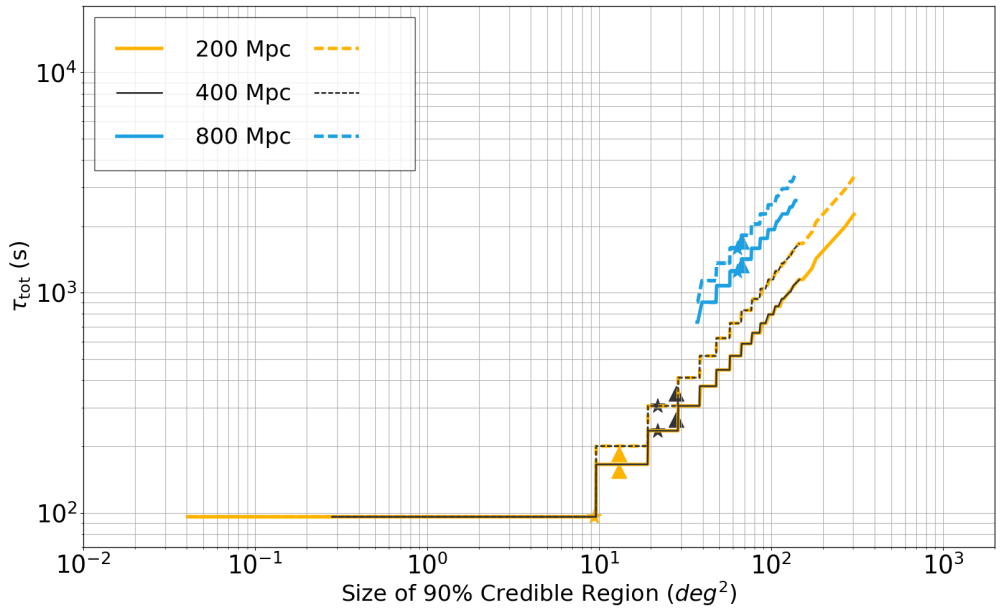

(b)

Figure 5.6: Similar to Figure 5.3. In this case, the network is Network 4 (H+ L+ V I J).

Table 5.2: Networks of GW detectors considered in this chapter.

	Network
Network 1	H+ L+ V
Network 2	H+ L+ V I
Network 3	H+ L+ V J
Network 4	H+ L+ V I J
Network 5	H+ L+ V I J C
Network 6	H+ L+ V I J A
Network 7	H+ L+ V I J A C

H+: LIGO Hanford at A+ sensitivity.
L+: LIGO Livingston at A+ sensitivity.
V : AdVirgo at the design sensitivity of VIRGO.
I : aLIGO at the design sensitivity of LIGO in India.
J : KAGRA at the design sensitivity of KAGRA.
C : A detector at Blair et al sensitivity in China.
A : A detector at Blair et al sensitivity in Australia.
All these noise curves are shown in Figure 1.7.

poor localization corresponds to 1 event for both 200Mpc and 400Mpc for the second scenario, and no event for 800Mpc. Interestingly, it can be seen that some events at 800 Mpc will require less observation time than lower distances. This is because for BNS mergers at 800Mpc, the SNR requirement for detection effectively requires detectable events to be positioned at locations with strong detector responses and favorable orientations.

In Figure 5.3(b), and other similar plots in this section, we use stars and triangles to represent the median and the mean values of the $\tau_{\rm tot}$ for sources at the corresponding distances respectively. The positions of the stars and triangles in relation to the overall distribution indicate how skewed the distributions are. In addition, we present a statistical summary of the results in Table 5.3 to indicate the fractions of events for which the values of $\tau_{\rm tot}$ is below a certain threshold for Network 1 - 4. A similar table for Network 5 - 7 is given in Table D.1. For BNS mergers at 200 and 400 Mpc with Network 1, the fraction of the detectable events with corresponding values of $\tau_{\rm tot} \leq 10^3$s is 89.0% and 77.1% for the first scenario respectively. Even for the second scenario, there are still 83.5% and 64.1% of the events requiring $\tau_{\rm tot}$ less than 10^3s. This represents a promising prospect for EM follow-up observations of BNS mergers with LSST detected with a network of the aLIGO detectors at A+ sensitivity and AdVirgo at the design sensitivity of AdVirgo.

Adding an extra detector of I or J or both I and J to the network helps improve the localization as shown in Figures 5.4(a), 5.5(a) and 5.6(a). This is also directly

reflected by the shorter observation time $\tau_{\rm tot}$ required, indicated by the positions of the means and medians shown in Figure 5.4(b), 5.5(b) and 5.6(b). Moreover, the fraction of events at 200 and 400Mpc with $\tau_{\rm tot} \leq 10^3$s has increased to $\geq 95\%$ for both scenarios. The only exception are BNS mergers at 400Mpc with Network 3 for the second scenario.

However, for BNS mergers at 800 Mpc, the majority of detectable BNS events will need $\geq 10^3$s to perform the defined procedure for EM follow-up observations. In our simulation, no events could be followed-up with $\tau_{\rm tot} \leq 10^2$s. This is because for sources at such a distance, the sensitivities of aLIGO India, AdVirgo and KAGRA are so weak that almost all localization information is provided by the two LIGO A+ detectors in the networks, preventing extremely well localized events (i.e. $S \leq 10\,{\rm deg}^2$). In addition, for BNS mergers at 800Mpc, LSST needs longer exposure lengths than the fiducial exposure time $\tau_{\rm fid}$ to reach the depth required, which in turn leads to an increase in the values of $\tau_{\rm tot}$.

The almost linear trend of the lines for BNS mergers at 200 and 400Mpc at large 90% credible region (i.e. $\leq 10^2{\rm deg}^2$ indicates that for these events, the time for EM follow-up observation is mostly spent on tiling the error regions, instead of achieving depth. In all plots, the lines at small 90% credible region have a linear trend that is constructed from a series of small step changes. This is because we require a minimal exposure of 30s. As a result, when the distance of a source is too close, the value of $\tau_{\rm tot}$ is dominantly determined by the size of the 90% credible region, even after taking into account the distance uncertainty $\Delta d_{\rm L}$ as derived from the FM. Consequently, for sources that can be localized within an area that requires the same number of fields, the values of $\tau_{\rm tot}$ will be identical. This means, for sources with the size of 90% credible regions that satisfy the following relation, their corresponding values of $\tau_{\rm tot}$ will be equal,

$$(n-1)\omega < S \leq n\omega. \tag{5.10}$$

When the size of the 90% credible region is increased to an extent where one extra field is needed to cover the 90% credible region, there will be a sudden jump in the value of $\tau_{\rm tot}$ which is similar to a step. However, as the number of fields becomes large, the extra time induced by one extra field will become relatively less significant. This explains why the lines transform to be a smooth line when the size of the 90% credible region becomes larger. The straightness of the lines in the log-log space also indicates a power law relationship between the size of the 90% credible region and the values of $\tau_{\rm tot}$. For larger distances such as 800Mpc, the values of $\tau_{\rm tot}$ are determined by the localization error, the distance and the distance uncertainty.

For a BNS merger, the total observation time $\tau_{\rm tot}$ is dependent on the distance of the source and its associated localization errors on the sky. Networks of larger numbers of detectors with improved sensitivity will improve the localizations and thus allow LSST to tile the sky with fewer fields, but their extended horizon for BNS mergers will also entail longer exposure for source located further. Readers who are interested in how the result will change when more sensitive detectors are included in

Table 5.3: Statistical summary of EM follow-up observations of BNS mergers with LSST

Network	Scenario	Distance (Mpc) 200		400		800	
		$< 10^2$s	$< 10^3$s	$< 10^2$s	$< 10^3$s	$< 10^2$s	$< 10^3$s
Network 1	First	12.9%	89.0%	0.1%	77.1%	0.0%	0.9%
	Second	12.9%	83.5%	0.1%	64.1%	0.0%	0.0%
Network 2	First	38.0%	99.6%	0.4%	99.3%	0.0%	7.6%
	Second	38.0%	98.8%	0.4%	95.0%	0.0%	0.9%
Network 3	First	29.7%	98.5%	0.2%	95.9%	0.0%	0.6%
	Second	29.7%	96.3%	0.2%	88.9%	0.0%	0.0%
Network 4	First	51.3%	99.9%	7.5%	99.7%	0.0%	11.5%
	Second	51.3%	99.6%	7.5%	98.5%	0.0%	0.7%

The statistical summary of the results for the simulations for Network 1 - 4. The networks are defined in Table 5.2. The first and second scenarios are the scenarios defined by Eq 5.8. The 3rd, 5th and the 7th columns shows the fractions of detectable events with $\tau_{\rm tot} \leq 10^2$s, and the 4rd, 6th and the 8th columns those with with $\tau_{\rm tot} \leq 10^3$s.

the networks are referred to the Appendix D for the results for Network 5-7. For BNS mergers at 200, 400 and 800Mpc, the inclusion of two Blair et al detectors further reduces the size of the 90% credible regions, which further shorten the time to perform the defined EM follow-up observation. However, even though sources at 1600Mpc can still be less than $10^2\,\mathrm{deg}^2$, the large distance results in the values of $\tau_{\rm tot}$ close to or in the order of $\mathcal{O}(10^4)$.

5.4 Future work

In this chapter, we asked the question of how long the total observation time has to be for LSST to detect BNS associated kilonovae with luminosity curves similar to the GW170817 kilonova. As we stated in Section 5.1, there are currently many uncertainties on the evolution of the luminosities of kilonovae. In practice, it is possible to detect kilonovae with properties and light curves that are different from the GW170817 kilonova. Different light curves and their evolution will result in different apparent magnitude in different observation epochs and thus different values and distributions of $\tau_{\rm tot}$. An approach to solve this problem is to generate a more general light curve for kilonovae by marginalizing over kilonovae model uncertainties. Repeating this work using such a model should produce more representative results.

5.5 Summary

In this work, we have investigated the prospects for EM follow-up observations of BNS mergers with LSST and detectors that are likely to be operative concurrently. The analysis include the LIGO detectors at A+ sensitivity, AdVirgo at design sensitivity, aLIGO India, KAGRA, and two Blair et al detectors in China and Australia (results for the two Blair et al detectors are presented in Appendix D). We computed the observation time $\tau_{\rm obs,5\sigma}$ required for LSST to achieve the depth required to detect BNS merger kilonovae with light curves similar to that of the GW170817 kilonova. We defined a procedure for EM follow-up observation for two different scenarios and derived the size of 90% credible regions and $\Delta d_{\rm L}$ using a FM approach. We then quantified the LSST observation time $\tau_{\rm tot}$ for BNS mergers at 200, 400 and 800Mpc observed with 7 different networks consisting of LIGO A+, AdVirgo, LIGO India, KAGRA and two Blair et al detectors.

We have found that using LSST and a network of the two aLIGO detectors at LIGO A+ sensitivity and AdVirgo at its design sensitivity, the prospect for EM follow-up observations of BNS mergers is promising. Our simulation suggested that EM follow-up observations with LSST should require $\leq 10^3$s for a large fraction of the events at 200Mpc and 400Mpc, and $\leq 10^4$s even including BNS mergers at 800Mpc.

Adding detectors such as aLIGO India and/or KAGRA reduces the values of $\tau_{\rm tot}$ by improving the localization. The improvement as seen in our simulation is obvious. The fraction of events at 200 and 400Mpc that require $\tau_{\rm tot} \leq 10^3$ has been increased to $\geq 95\%$ for Network 2 and 4 for both scenarios. Similar improvements are seen for Network 3.

We have also found that for BNS mergers at 200 and 400Mpc, the values of $\tau_{\rm tot}$ is largely determined by the size of the 90% credible region since the fiducial observation time for LSST will be long enough to achieve the necessary depth. For sources at further distances, i.e. 800Mpc, the values of $\tau_{\rm tot}$ are determined by the localization error, the distance and the distance uncertainty combined.

We note that this work is limited by how representative the GW170817 kilonova is for the population of kilonovae. To extend this work, considering more general kilonovae light curve models would be a natural extension to this work.

Chapter 6

Summary

The detections of GWs from CBCs with aLIGO and AdVirgo in the recent years have opened up a new window on the universe and marked the beginning of a new era in GW astronomy. The discovery of the first BNS mergers and its associated EM counterpart in wavelengths from gamma-ray to radio has turned a new page in the history of GW astronomy and multi-messenger astronomy. The network of advanced detectors is anticipated to observe GW signals from many more sources including CBCs, spinning NSs, CCSNe and sources that are currently un-modeled and unknown.

Many GW sources have expected EM signatures across the entire EM spectrum. CBCs consisting of at least one NS are an important source both for GW astronomy and multi-messenger astronomy. Their associated EM counterparts include short GRBs, X-ray and radio afterglows, and optical and infrared kilonovae. It is also possible for BNS mergers to have neutrino emission. As gravitational and EM emission will carry with them information that is complementary of their astrophysical origin, observing these sources both gravitationally and electromagnetically is important in understanding the physics that governs the emission mechanism and the progenitor's environment. GW170817 and the detected associated EM counterparts as the first source detected both in GWs and EM waves have confirmed the associations of BNS mergers and their EM counterparts, and provided insight in the physics that govern the generation of these signals. In addition, CCSNe are expected to be sources of GW and EM waves.

A challenge of detecting the EM counterparts of BNS merger events is the large localization errors on the sky. Although prompt localization algorithms such as those discussed in Chapter 2 are in place to facilitate follow up observations of GW events, the mismatch between the size of 90% credible region on the sky and the size of FOV of telescopes indicates that follow-up observations with existing facilities can still be a demanding task. In Chapter 3, we presented a proof-of-concept demonstration of an algorithm we developed to alleviate the situation. The algorithm takes as input a sky map of GW event, and the properties of a telescope such as its sensitivity and the

size of its FOV. Based on this information, the algorithm will generate a strategic observation plan that maximizes the detection probability by providing guidance on the locations of the observing fields and the corresponding observing times to each of the observing fields.

We applied the algorithm to four ground-based telescope including HSC, DEC, Pan-Starrs and PTF for three simulated GW events. The 90% credible region of the events range from $30\,\mathrm{deg}^2$ - $300\,\mathrm{deg}^2$. Using a greedy algorithm for optimizing the locations of the observing fields and Lagrange multiplier to allocate the observation times to each of the fields, we have shown that for each event, there exist a number of fields at which the detection probability of the target EM counterpart is maximized.

In addition, we also compared two strategies for allocating the observation times to each of the observing fields. We demonstrated that observing the fields with equal time can achieve a detection probability close to using Lagrange multiplier, while the latter always perform marginally better. By presenting our results from another prospective, we showed that if the size of the FOV is too small compared to the size of the 90% credible region, the detection probability will be largely determined by the sensitivity of the telescope.

We have also applied the algorithm to the design of a satellite mission known as EP for the three simulated GW events. We simulated the performance of EP for EM follow-up observations targeting an X-ray counterpart by computing the optimal number of observing fields and estimating the detection probability as a function of the size of FOV and the sensitivity under simplifying assumptions. We found that since the FOV of EP within the simulated range is comparable to the localization error of the simulated GW events, EP will be able to cover the error region of the simulated BNS events with $\mathcal{O}(1)$ observing fields, which leads to the sensitivity being the only dominant factor of the detection probability.

Localization is one of the key factors to the success of EM follow-up observation of GW events. We estimate the localization error of BNS mergers with third generation detectors such as the ET and CE in Chapter 4. Third generation detectors will have sensitivity improvement throughout the relevant frequency band for ground-based detectors compared to 2G detectors. The improvement in the low frequency band ($\leq$ 10Hz) is expected to increase the in-band duration of GW signals from BNS mergers from minutes to hours or days. The earth's rotation is therefore important in the estimates of the localization errors of the sources. This will cause the GWs received at the detectors Doppler shifted. The antenna pattern during the in-band duration of the GWs will also become explicitly time-dependent.

Using a FM approach, we studied the localization capability of the ET and CE individually and as a network for BNS mergers. The BNS mergers simulated are located at specific distances such as 40, 200, 400, 800 and 1600Mpc and as a population distributed uniformly in the comoving volume. We found that the ET alone can localize the majority of the BNS mergers within 200Mpc to within $\mathcal{O}(10^2)\,\mathrm{deg}^2$ with 90% confidence. This is promising for multi-messenger astronomy with GWs from

BNS mergers. For BNS mergers at larger distances such as 400, 800 and 1600Mpc, a network of the ET and CE can localization 100%, 99% and 92% of the detectable sources to within $\mathcal{O}(10^2)\,\mathrm{deg}^2$ with 90% confidence. We also showed that by turning off the Doppler effect, the localization improvement is mainly due to the time dependency of the antenna pattern.

Another emphasis of the work presented in Chapter 4 is on the prospect for early warning with the ET and CE. Early warning refers to the situations where the SNR of a CBC event is accumulated to a significant level prior to merger so that event alert can be released to boost the chance for EM follow-up observations. Hours or days long in-band duration of signals enabled by the improvement in sensitivity in the low frequency band increases the possibility of early warnings. By setting two requirements on the SNR and the localization error, we found that for BNS mergers within 200Mpc with the ET, a large fraction of the detectable sources can accumulate enough SNR to be considered significant a few hours prior to merger. Because of the relatively limited sensitivity of CE in the low frequency band, adding CE to the network does not alter significantly the results for sources at distance $\leq$ 200Mpc. However, a network of the ET and CE can significantly increase the fraction of events that satisfy the early warning requirement for BNS at larger distance. This emphasizes the importance and potential of a network of the ET and CE for BNS merger events at large distances.

For CBC signals with short duration (e.g. those detected with 2G detectors), we presented two FM approaches for estimating the localization error from the literature - Wen and Chen's approach and Fairhurst's approach. We applied the former to $10M_\odot$ - $10M_\odot$ BBH mergers at 400Mpc and $30M_\odot$ - $30M_\odot$ BBH mergers at 400, 800, 1600 and 3200Mpc with a network of 2G detectors and two Blair et al detectors in China and Australia. As expected, the localization improves as the number of detectors in a network increases, and as the sensitivities of the detectors in the network increase. We also found that for $30M_\odot$ - $30M_\odot$ BBH mergers, the 90% localization error is inversely proportional to the SNR. The only exception in the simulation is the network of aLIGO and AdVirgo for $30M_\odot$ - $30M_\odot$ BBH mergers at 3200Mpc where the increase in distance from 1600Mpc to 3200Mpc has caused the SNRs for a fraction of events to drop below the detectable threshold.

In chapter 5, we investigate the capabilities of LSST for performing EM follow up observations of BNS mergers detected with networks consisting of detector expected to be operational concurrently with the telescope. We first defined a simple procedure for EM follow-up observation of BNS mergers with LSST. Combined with the GW170817 kilonova data and the luminosity distance uncertainties from the FM for sources at 200, 400 and 800Mpc, we then computed the time required for LSST to complete the defined procedure under the assumption that all kilonovae will have luminosity similar to the GW170817 kilonova.

We found that for a network of the two aLIGO detectors at LIGO A+ sensitivity and AdVirgo at design sensitivity, at least 83.5% and 64.1% will require LSST

observation time only $\leq \mathcal{O}(10^3)$s to complete the defined EM follow-up observation procedure for BNS mergers at 200 and 400Mpc. If KAGRA and/or LIGO India are added to the network, improved localization will reduce the observation time. With a network consisting of H+ L+ V I J, the fraction of detectable events at 200 and 400Mpc that require $\tau_{\rm tot} \leq \mathcal{O}(10^3)$s has increased to $\geq 98\%$. The observation time is mostly spent on tiling the 90% credible region since an exposure of 30s (the fiducial minimum exposure time) with LSST is already enough to reach the necessary depth. This shows the desirability of LSST for multi-messenger astronomy with BNS mergers at similar distances. Due to the poor localization for and the increase in the distance of BNS mergers at 800Mpc and, only $\leq \mathcal{O}(10)\%$ can be followed-up with LSST observation time $\leq \mathcal{O}(10^3)$s.

Appendices

Appendix A

Appendix A

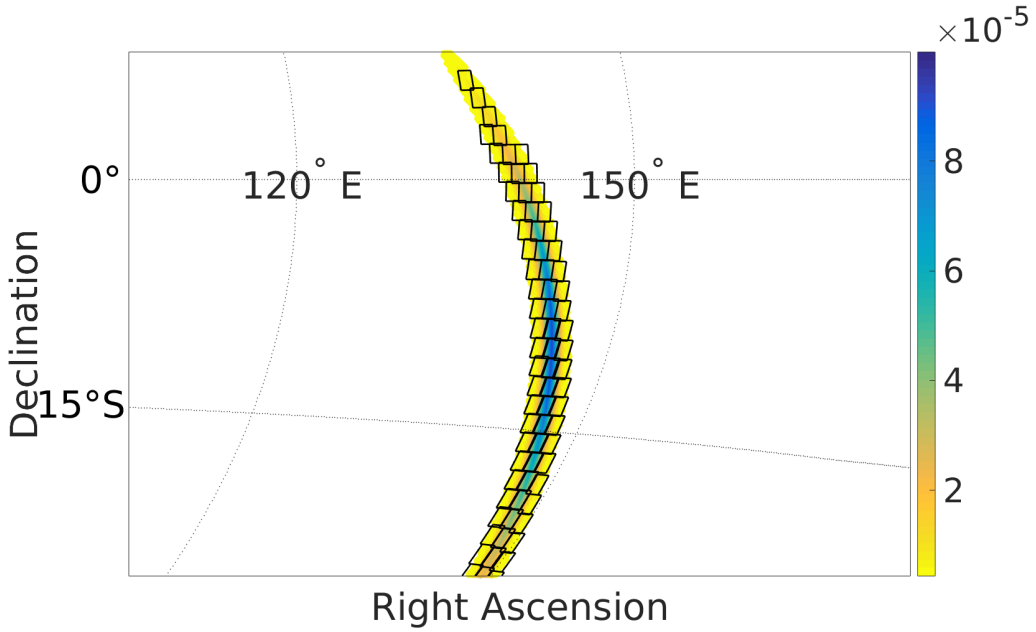

(a)

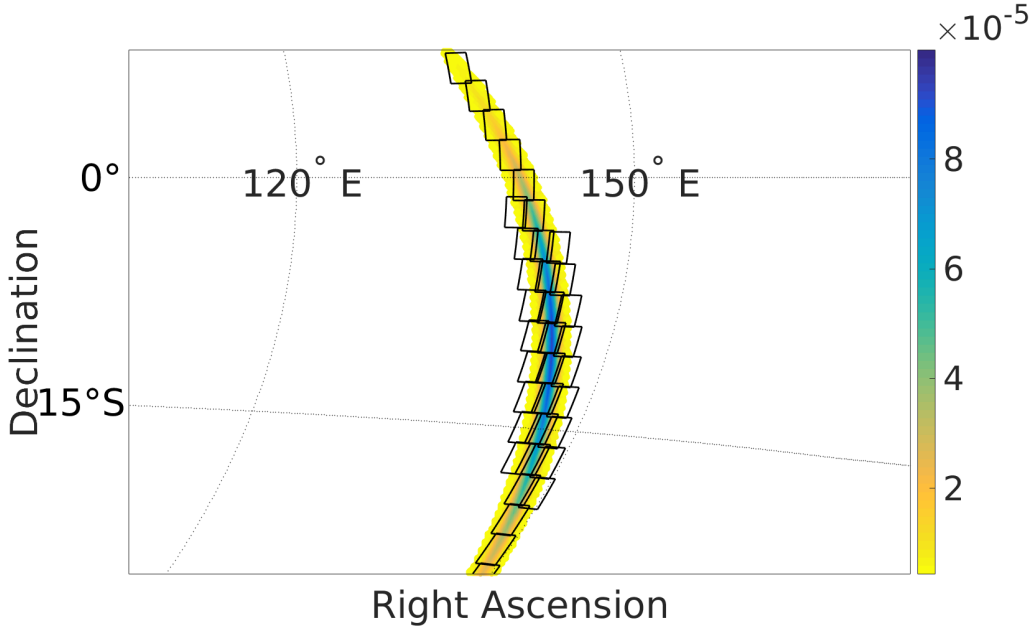

(b)

Figure A.1: The optimized locations of the observing fields covering 90% of the GW probability for telescopes and for simulated GW event 19296. The upper plot corresponds to HSC and the lower plot DEC. In each plot the GW sky error is shown as a shaded region with the color bar indicating the value of posterior probability density.

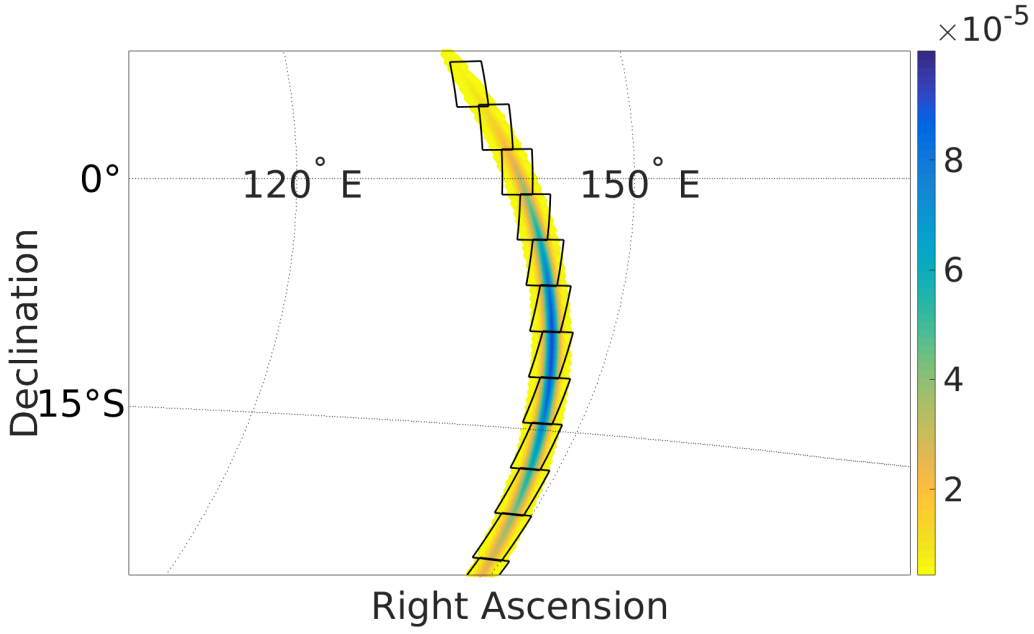

(a)

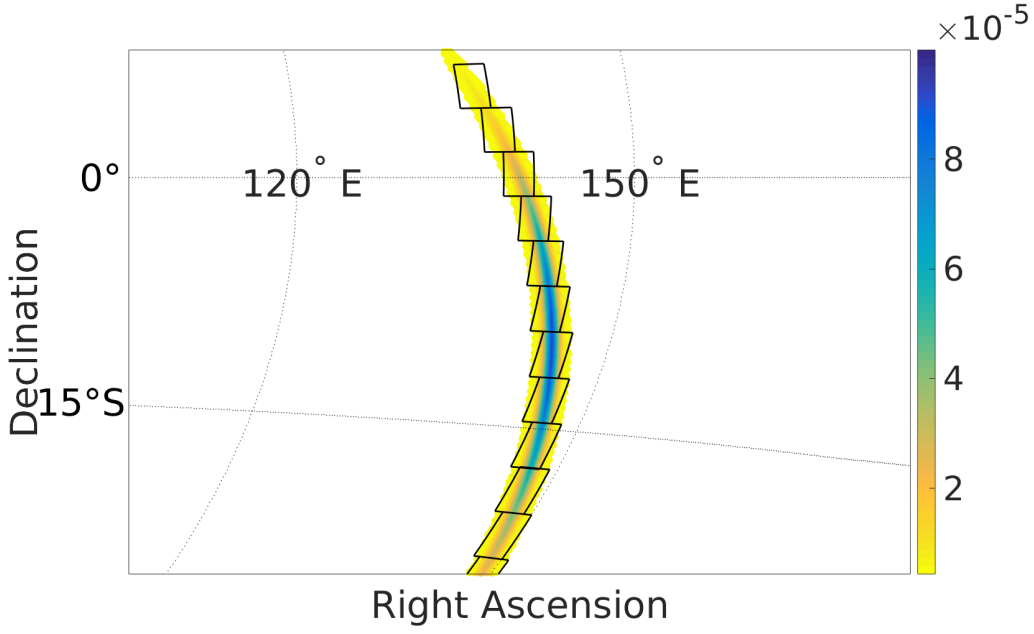

(b)

Figure A.2: The same as Figure A.1. In both plots, the GW sky error for simulated GW event 19296 is shown as a shaded region with the color bar indicating the value of posterior probability density. The upper plot corresponds to Pan-Starrs and the lower plot PTF.

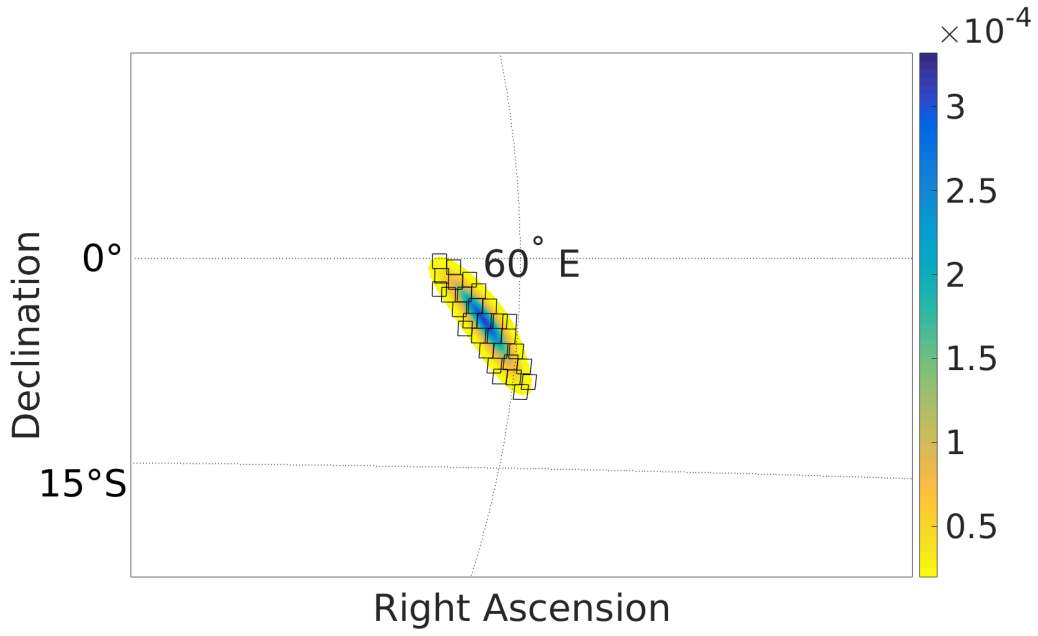

(a)

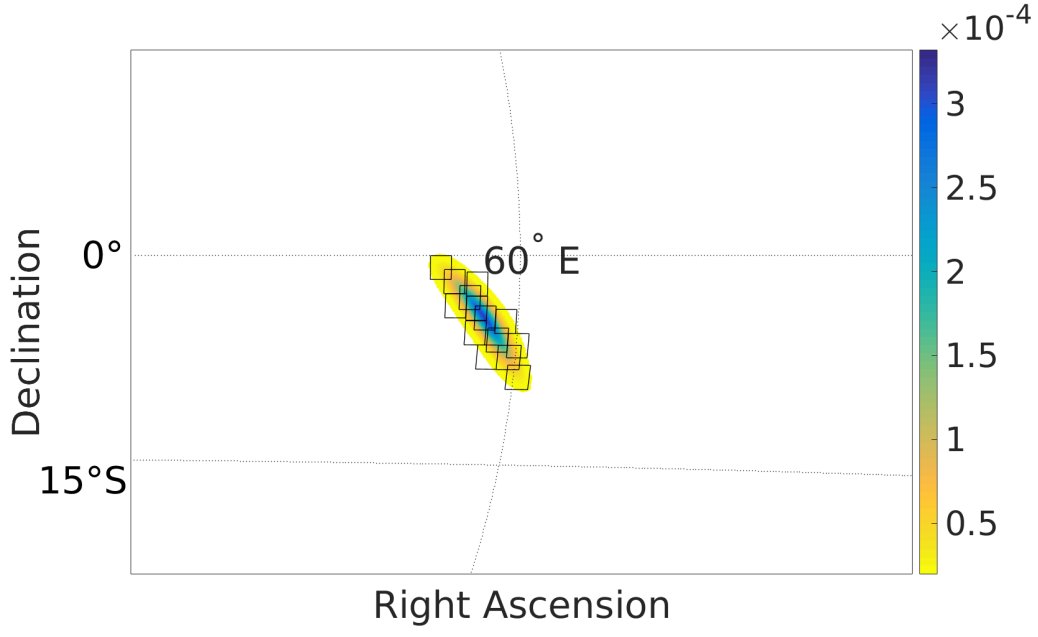

(b)

Figure A.3: The same as Figure A.1. In both plots, the GW sky error for simulated GW event 18694 is shown as a shaded region with the color bar indicating the value of posterior probability density. The upper plot corresponds to HSC and the lower plot DEC.

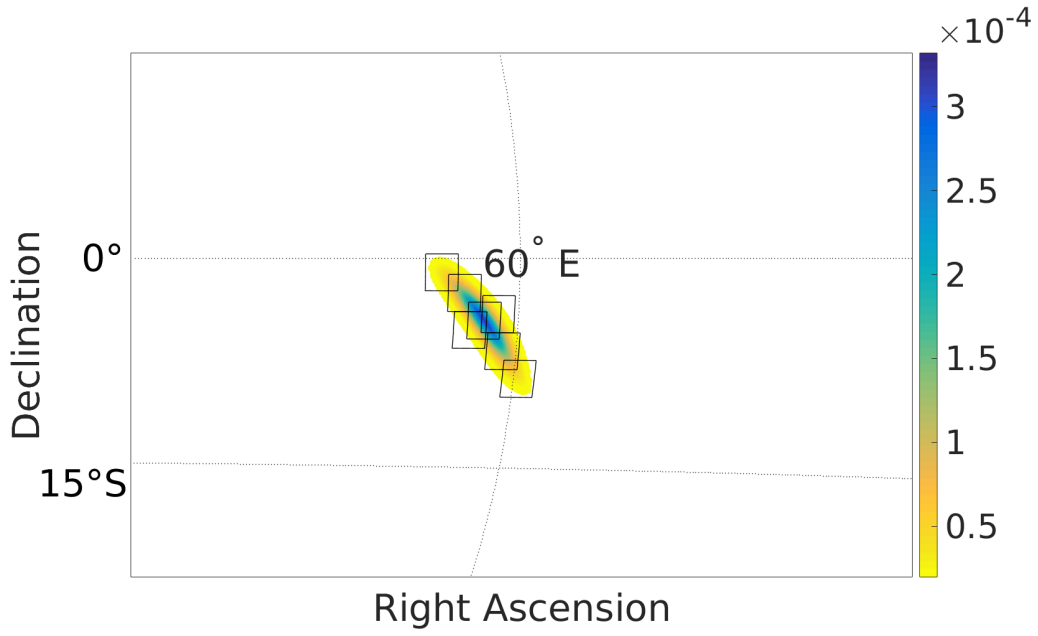

(a)

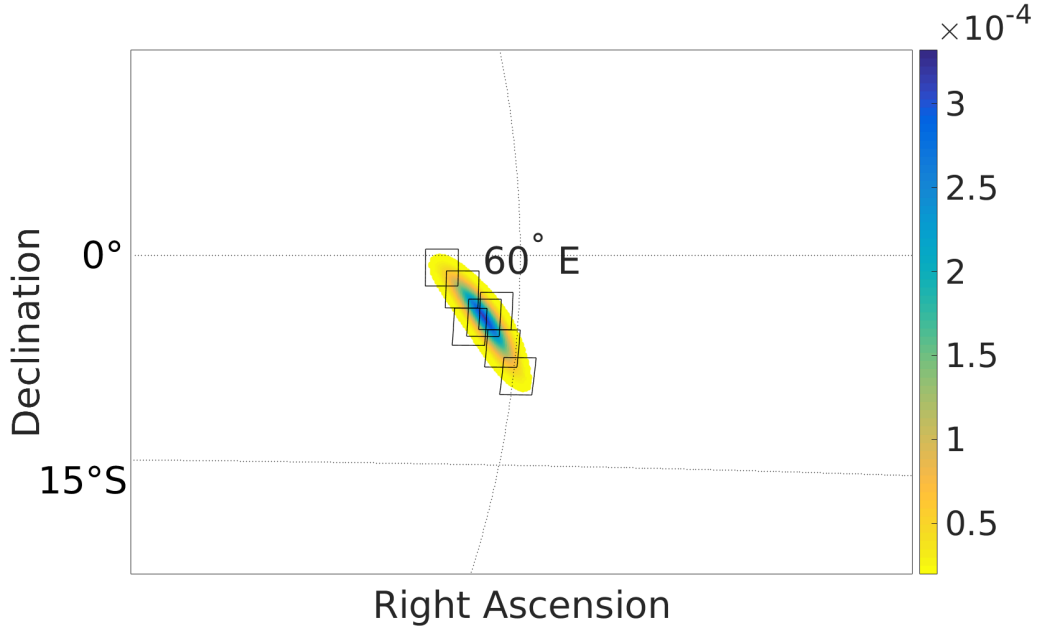

(b)

Figure A.4: The same as Figure A.1. In both plots, the GW sky error for simulated GW event 18694 is shown as a shaded region with the color bar indicating the value of posterior probability density. The upper plot corresponds to Pan-Starrs and the lower plot PTF.

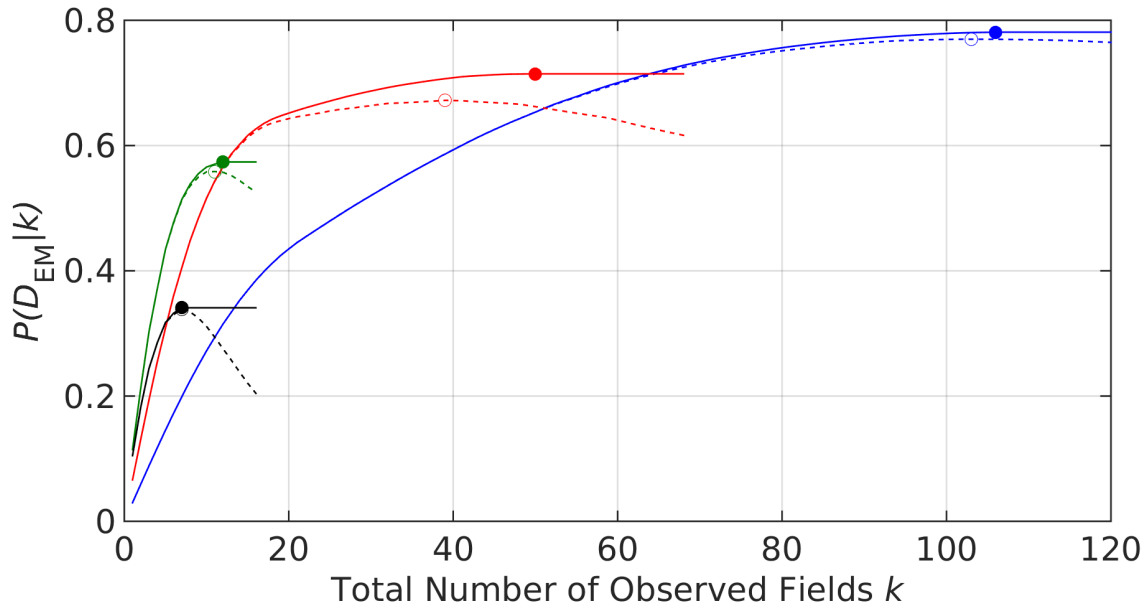

(a)

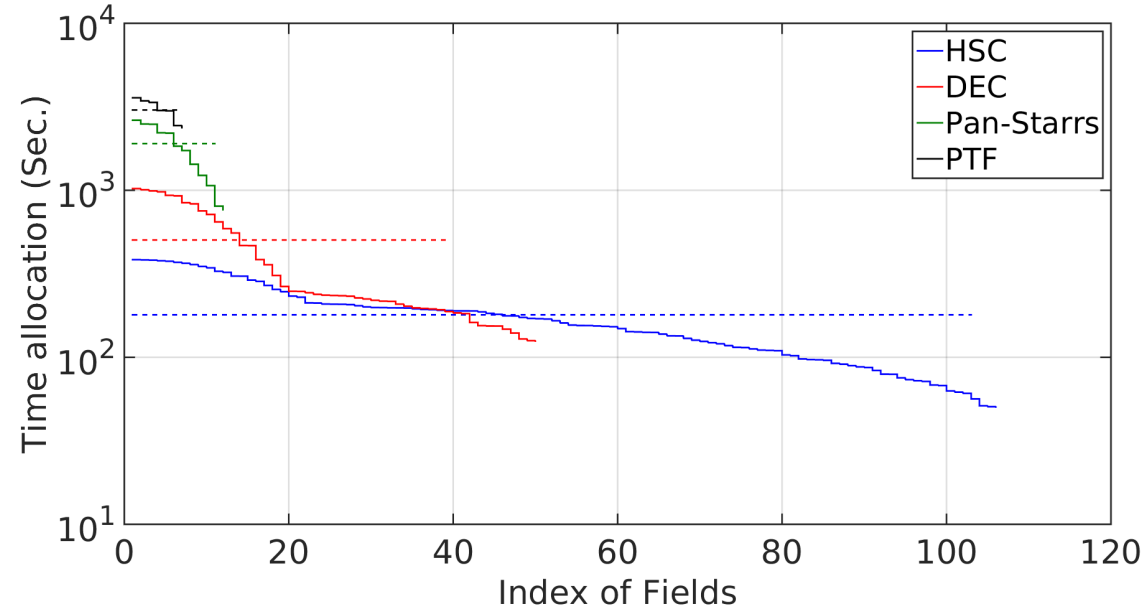

(b)

Figure A.5: The results of simulated EM follow-up observations for the $\sim$100 deg^2 GW event (ID 19296). We show the optimized EM detection probability as a function of the number of observing fields (top) and the allocated observing times for the optimal number of fields (bottom). The total observation time is 6 hrs. The 4 solid curves in each plot correspond to the optimal time allocation strategy applied to each of the 4 telescopes. The dashed lines show results for the equal time strategy. The solid markers and the circles indicate the number of observing fields at which the maximum detection probability is achieved using the optimal time allocation strategy and the equal time strategy respectively.

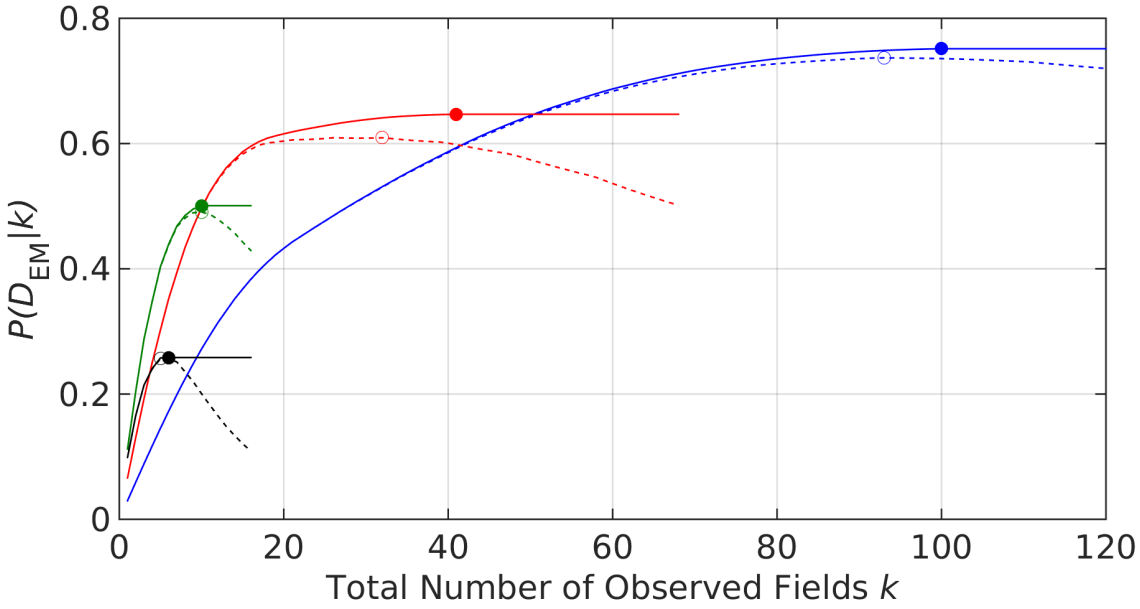

(a)

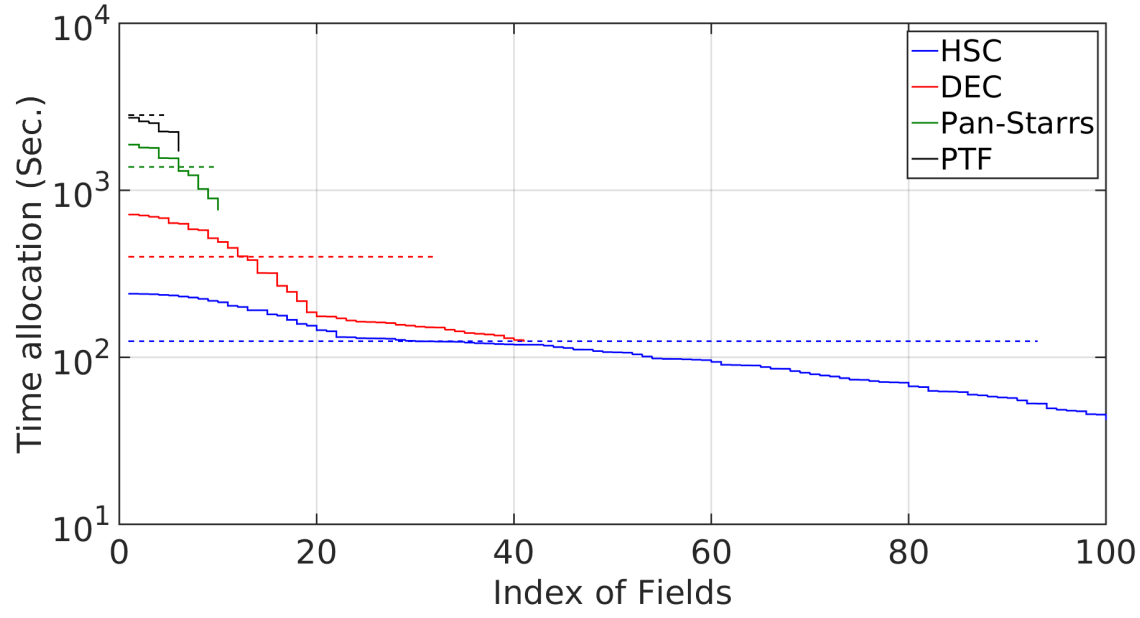

(b)

Figure A.6: The same as Figure A.5 but the total observation time is 4 hrs.

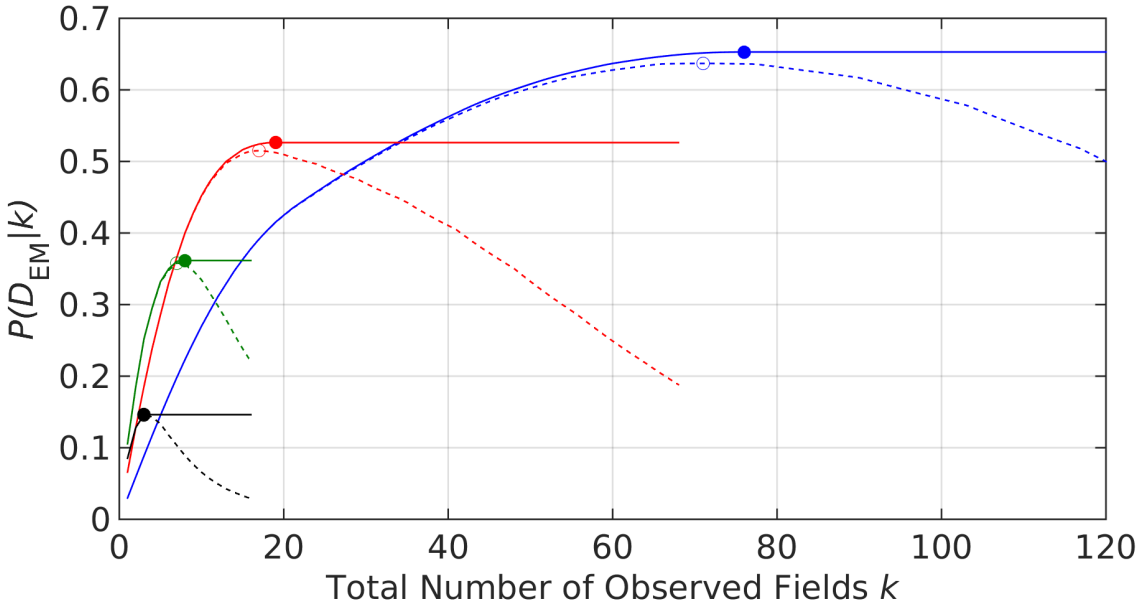

(a)

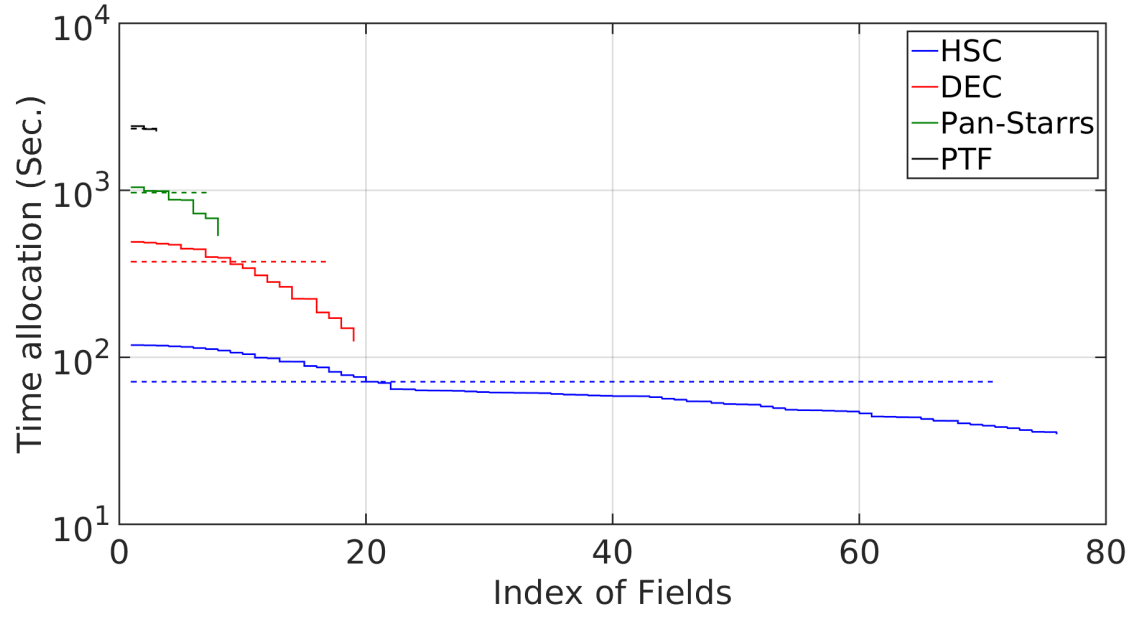

(b)

Figure A.7: The same as Figure A.5 but the total observation time is 2 hrs.

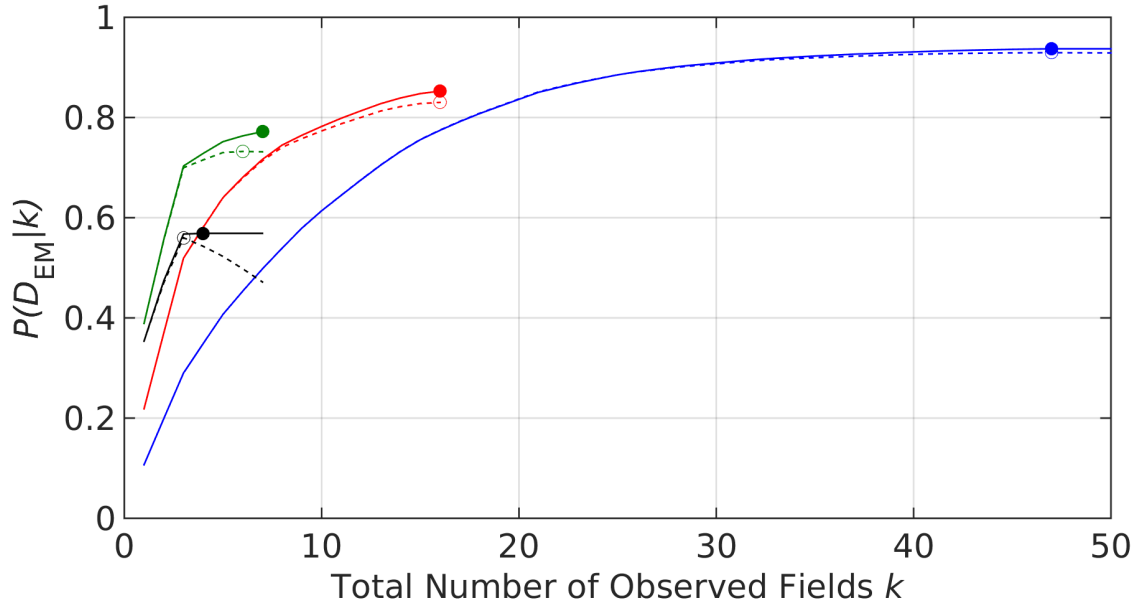

(a)

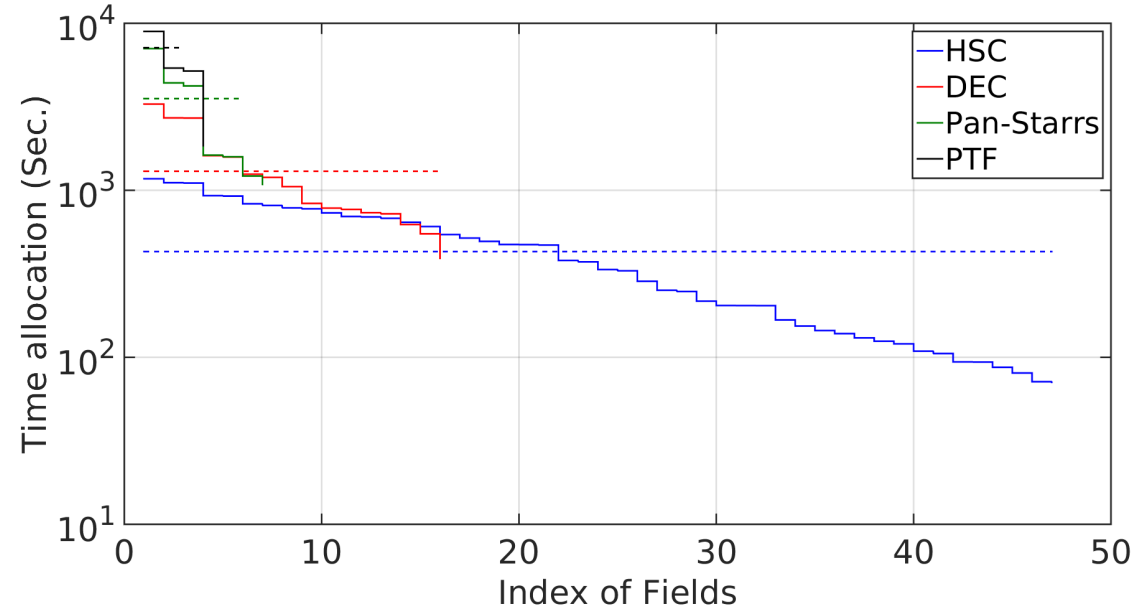

(b)

Figure A.8: The results of simulated EM follow-up observations for the $\sim$30 deg^2 GW event (ID 18694). We show the optimized EM detection probability as a function of the number of observing fields (top) and the allocated observing times for the optimal number of fields (bottom). The total observation time is 6 hrs. The 4 solid curves in each plot correspond to the optimal time allocation strategy applied to each of the 4 telescopes. The dashed lines show results for the equal time strategy. The solid markers and the circles indicate the number of observing fields at which the maximum detection probability is achieved using the optimal time allocation strategy and the equal time strategy respectively.

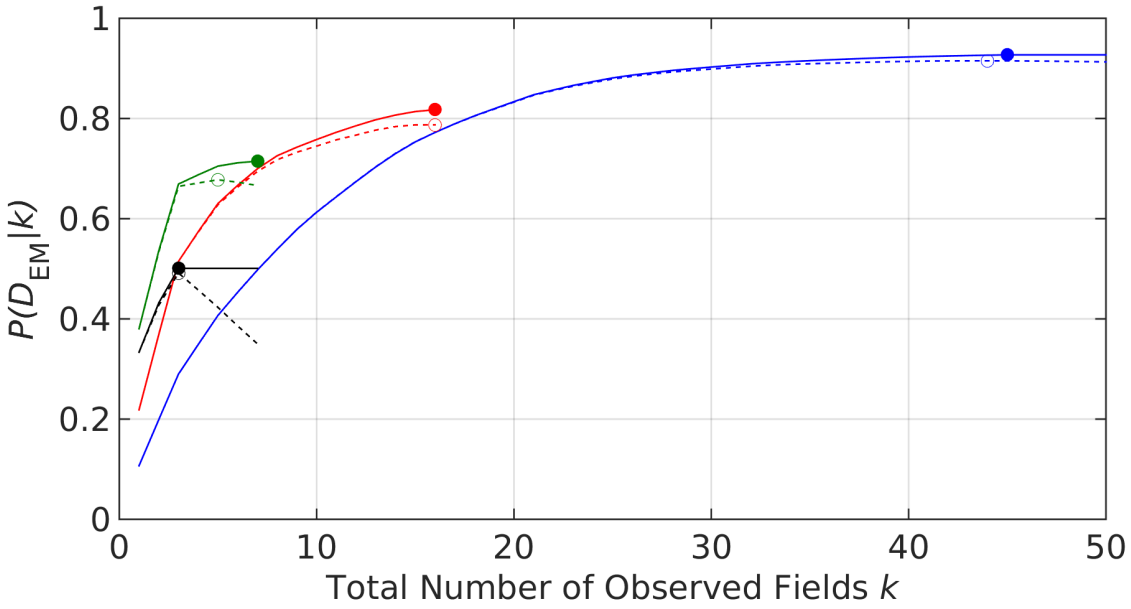

(a)

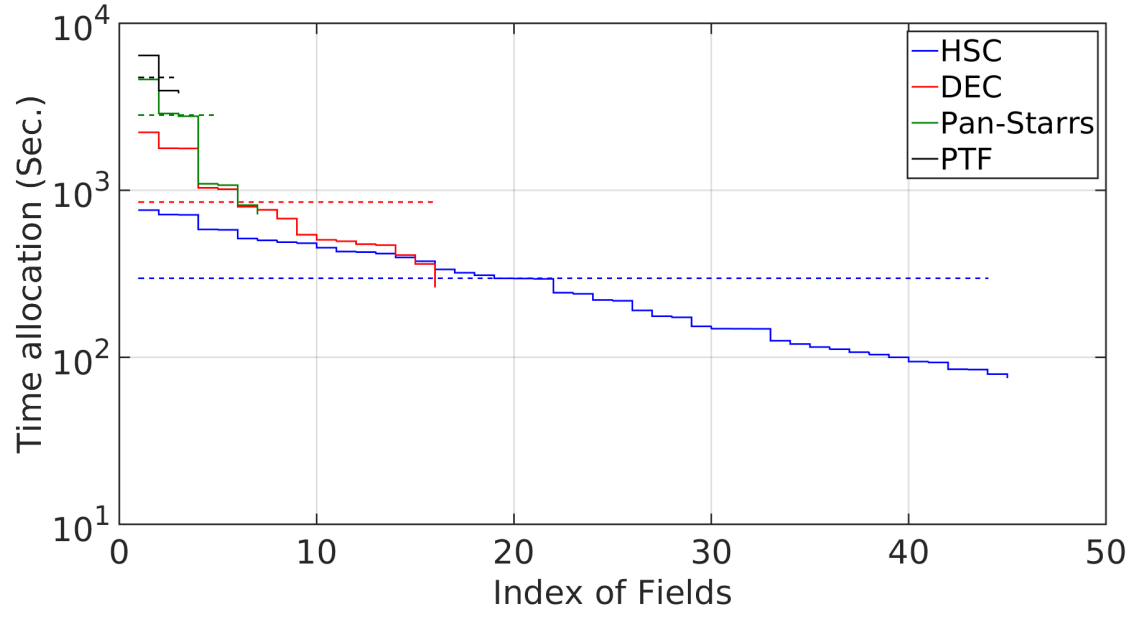

(b)

Figure A.9: The same as Figure A.5 but the total observation time is 4 hrs.

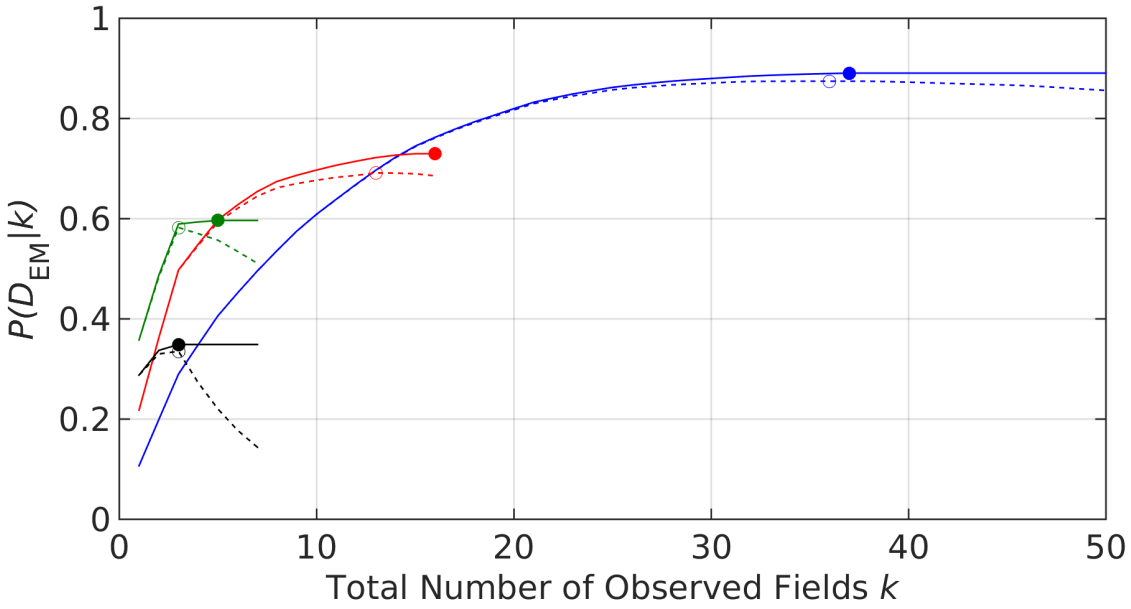

(a)

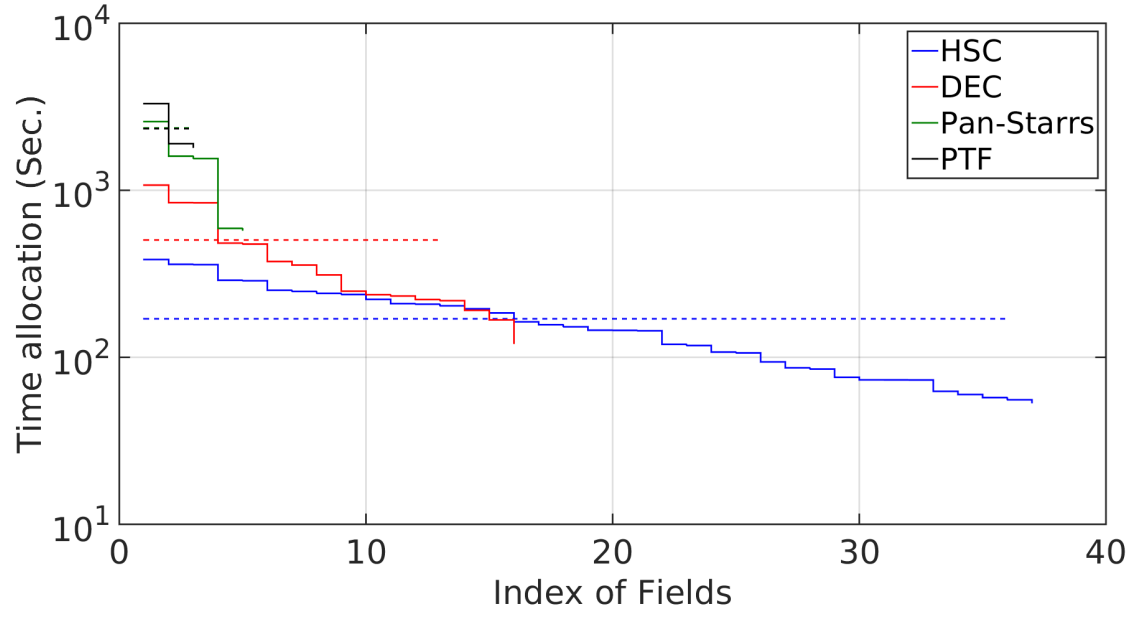

(b)

Figure A.10: The same as Figure A.8 but the total observation time is 2 hrs.

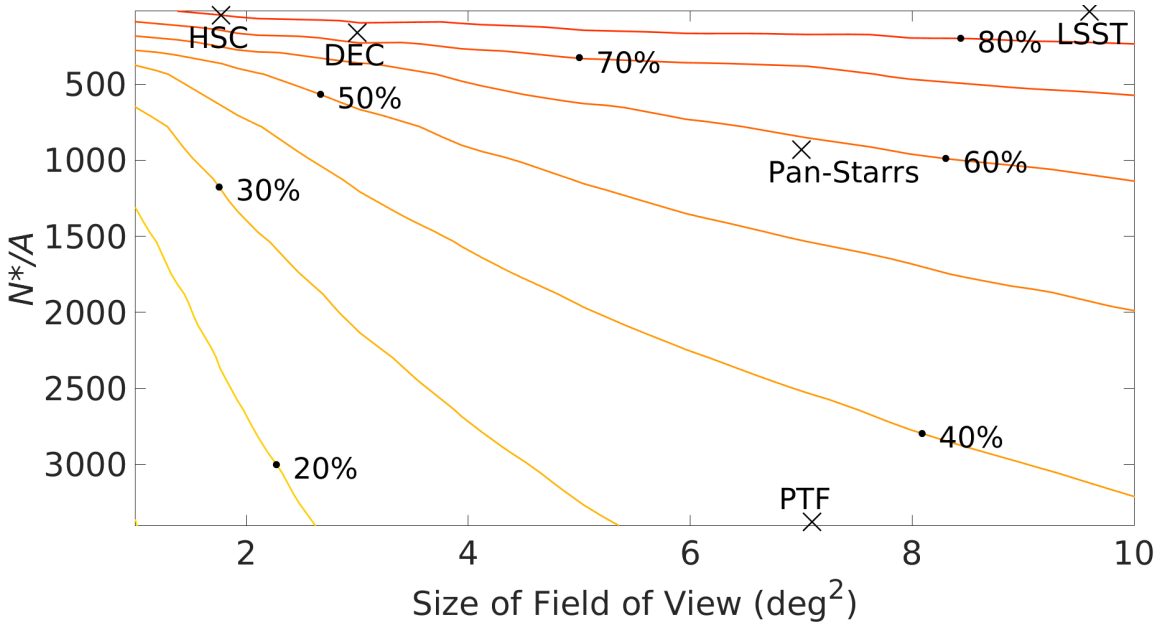

(a)

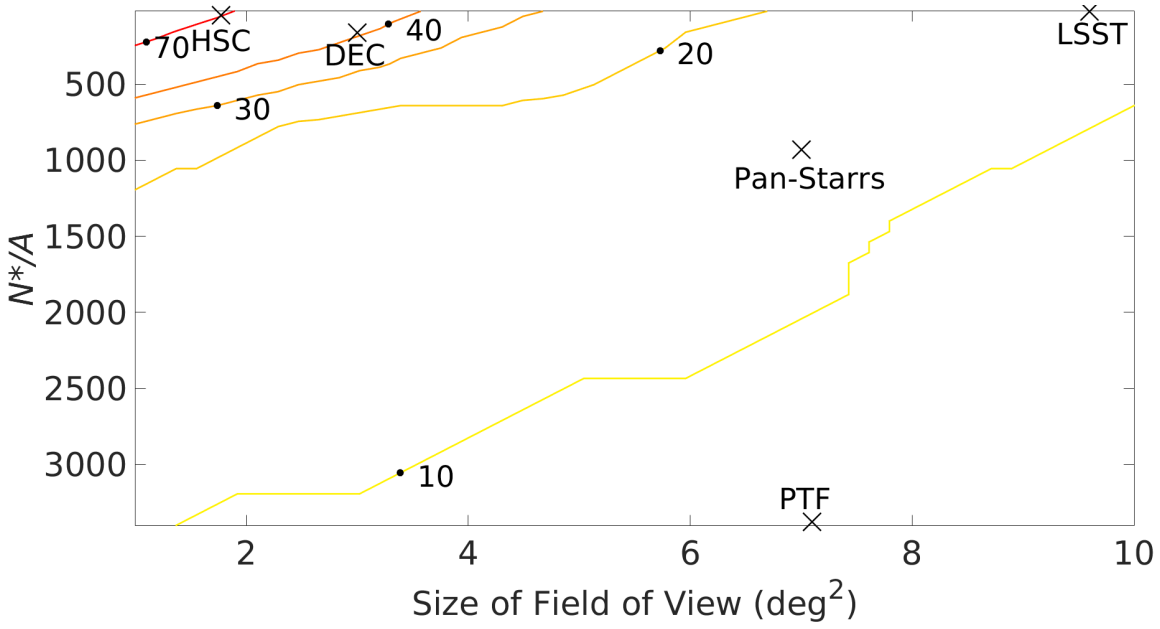

(b)

Figure A.11: Contours of EM follow-up performance of kilonovae as a function of the size of telescope FOV and sensitivity assuming a 6 hr total observation. The results are for simulated GW event 19296, $\sim$100 deg^2. We plot contours of equal detection probability (top) and the corresponding optimal number of observing fields (bottom). Overlayed for reference on all plots are the locations of the telescopes considered in this work (including the proposed LSST).

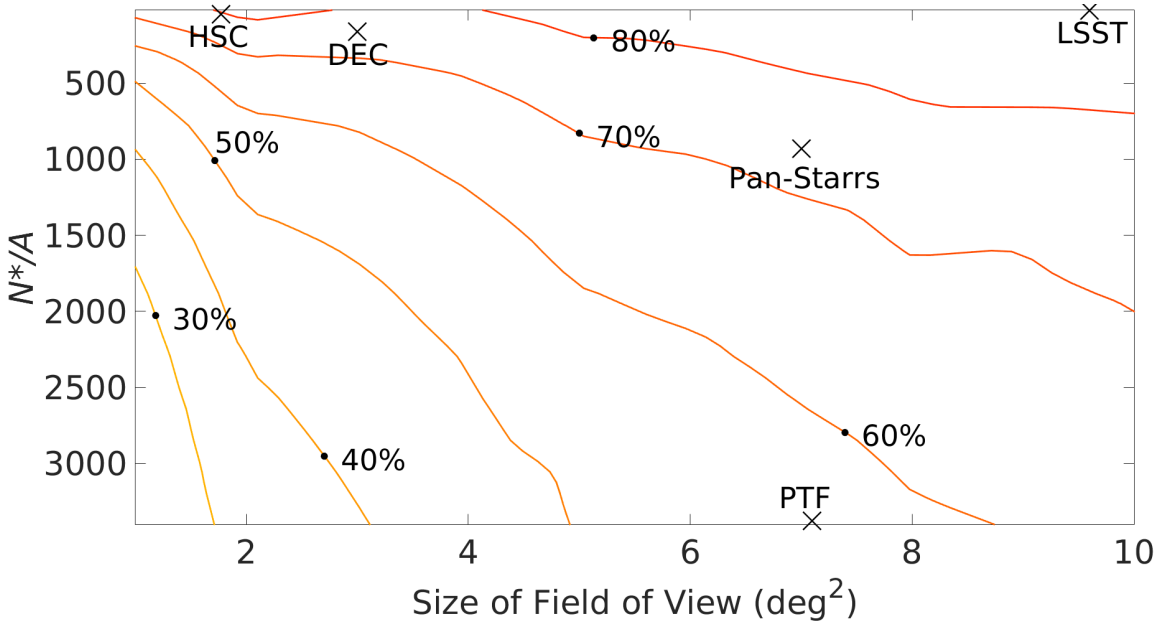

(a)

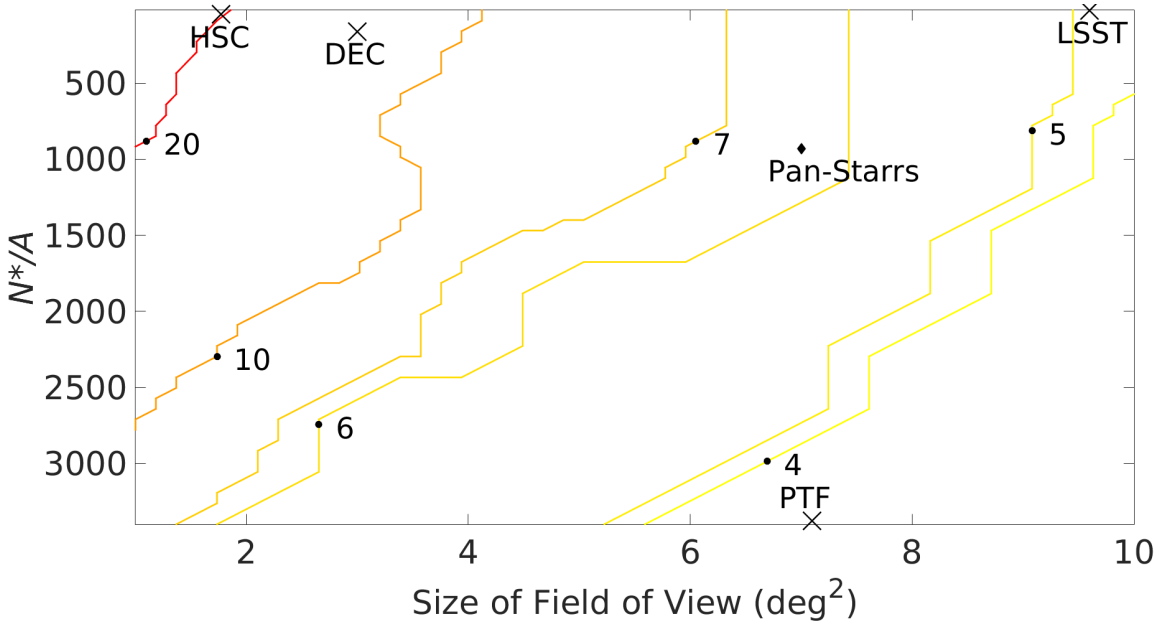

(b)

Figure A.12: The same as Figure A.11 but for simulated GW event 18694.

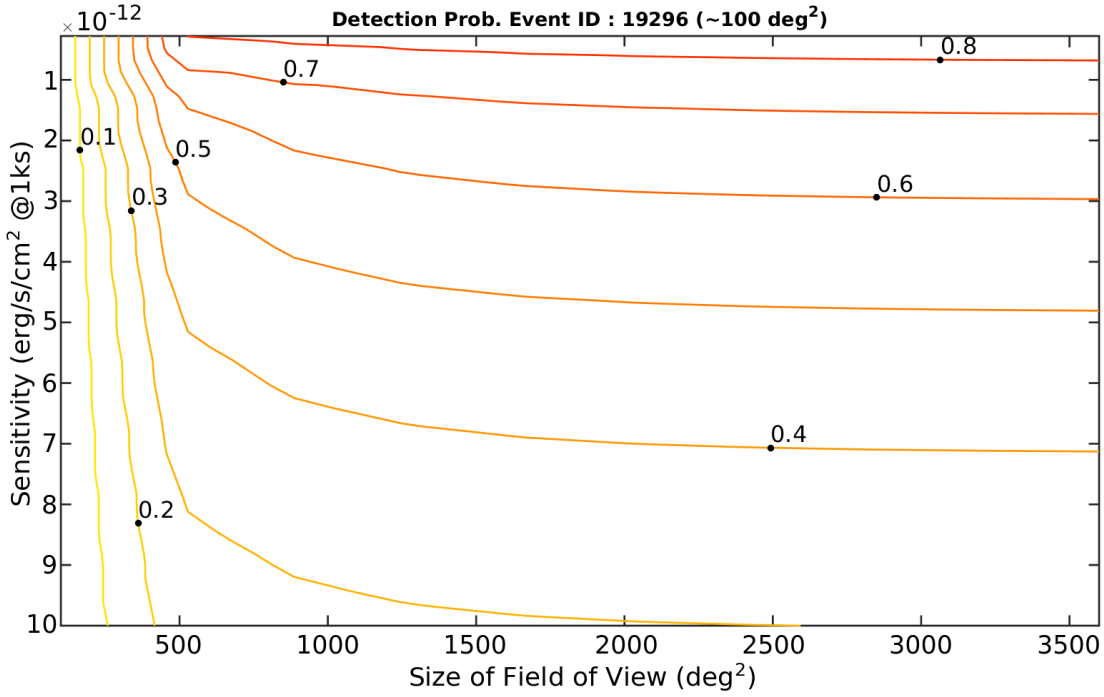

(a)

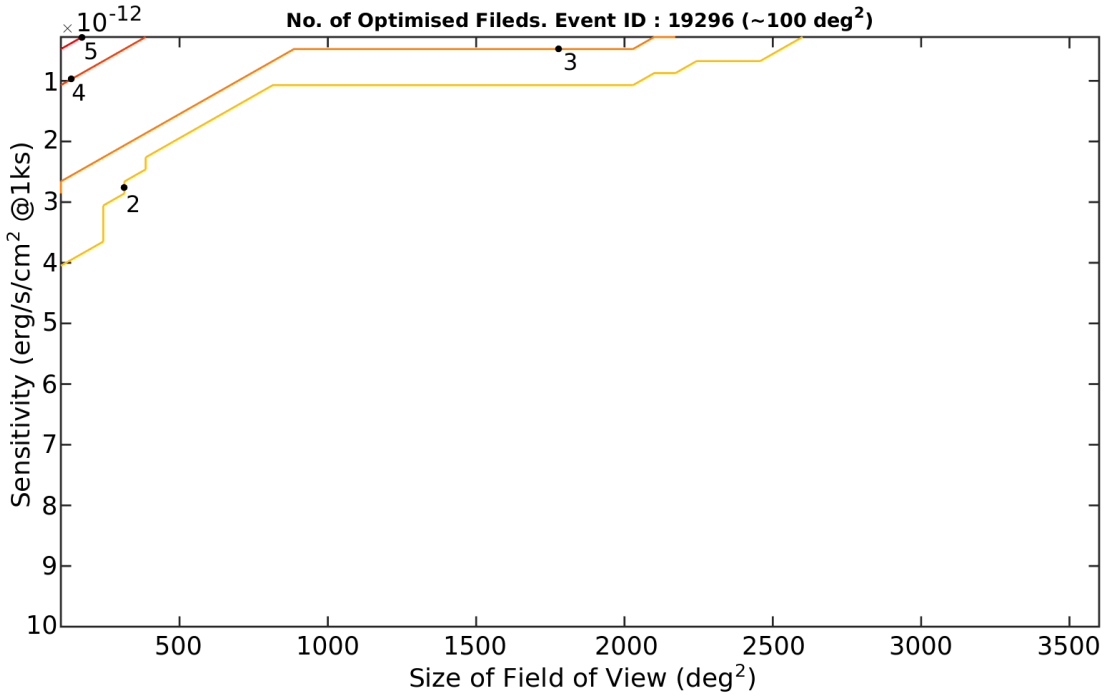

(b)

Figure A.13: Contours of EM follow-up performance of X-ray afterglows associated with intermediate magnetar from BNS merger as a function of the size of the FOV of EP and the sensitivity of the WXT. The total observation time is assumed to be 1000s. The simulated GW event is event 19296 ($\sim$100 deg^2). In the top panel, we plot contours of equal detection probability, and in the bottom panel the corresponding optimal number of observing fields (right).

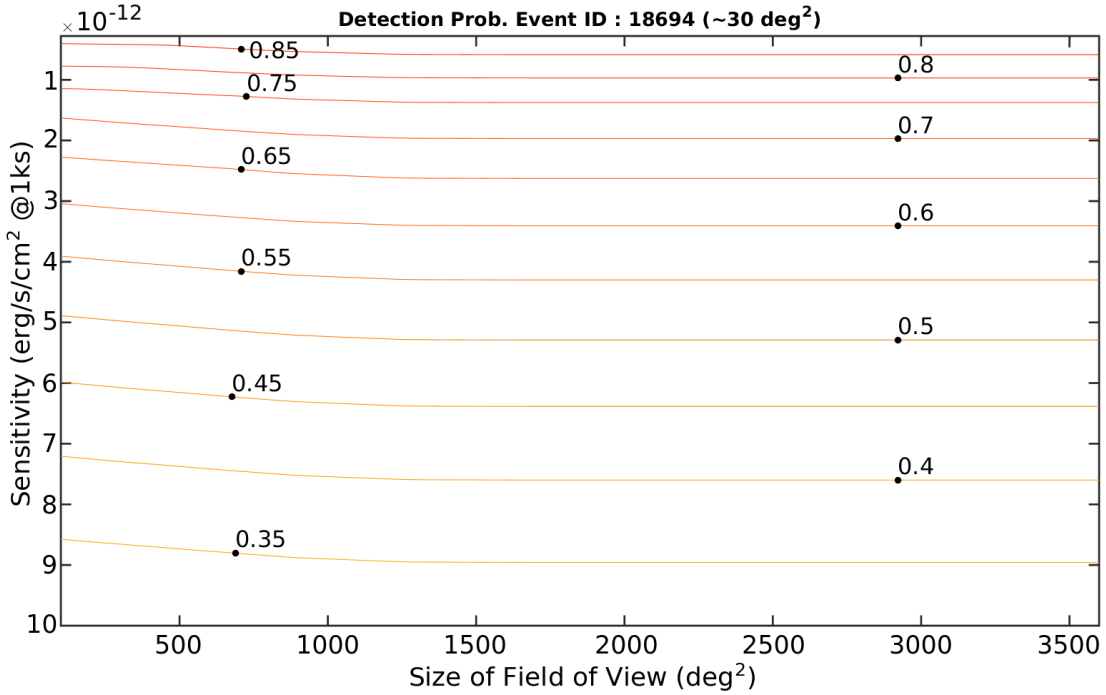

(a)

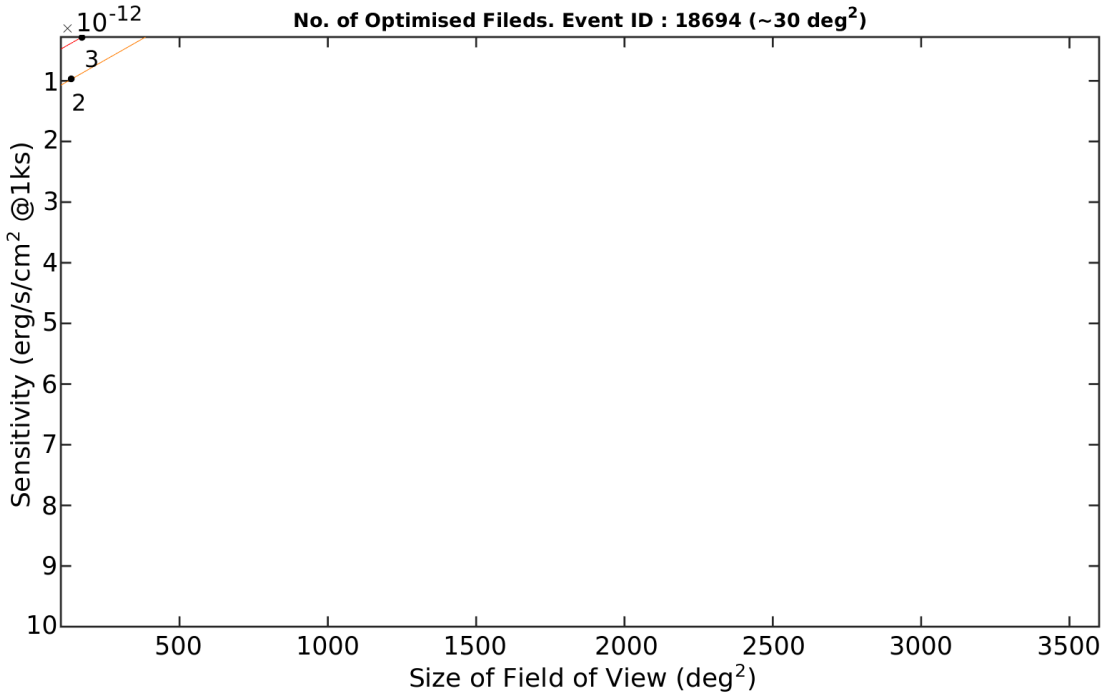

(b)

Figure A.14: The same as Figure A.13. But the simulated event is event 18694 ($\sim$30 deg^2).

Table A.1: The EM detection probability using both the optimal and equal time strategies

Telescope	Event ID	Strategy	EM detection probability Optimal number of fields 4 hrs		Relative Gain
HSC	28700	LM[1]	58.0%	(167)	1.0%
		ET[2]	57.0%	(155)	
	19296	LM	75.1%	(100)	1.4%
		ET	73.7%	(93)	
	18694	LM	92.7%	(45)	1.2%
		ET	91.5%	(44)	
DEC	28700	LM	41.7%	(56)	1.0%
		ET	40.7%	(51)	
	19296	LM	64.7%	(41)	3.8%
		ET	60.9%	(32)	
	18694	LM	81.7%	(16)	3.0%
		ET	78.7%	(16)	
Pan-Starrs	28700	LM	28.5%	(14)	0.5%
		ET	28.0%	(13)	
	19296	LM	50.1%	(10)	1.0%
		ET	49.1%	(10)	
	18694	LM	71.5%	(7)	3.7%
		ET	67.8%	(5)	
PTF	28700	LM	13.0%	(6)	0.1%
		ET	12.9%	(6)	
	19296	LM	25.8%	(6)	0.2%
		ET	25.6%	(5)	
	18694	LM	50.1%	(3)	0.9%
		ET	49.2%	(3)	

Table A.2: The EM detection probability using both the optimal and equal time strategies

Telescope	Event ID	Strategy	EM detection probability Optimal number of fields 2 hrs		Relative Gain
HSC	28700	LM[3]	41.6%	(94)	0.3%
		ET[4]	41.3%	(90)	
	19296	LM	65.3%	(76)	1.6%
		ET	63.7%	(71)	
	18694	LM	89.1%	(37)	1.7%
		ET	87.4%	(36)	
DEC	28700	LM	28.1%	(35)	0.5%
		ET	27.6%	(34)	
	19296	LM	52.6%	(19)	1.1%
		ET	51.5%	(17)	
	18694	LM	73.0%	(16)	3.9%
		ET	69.1%	(13)	
Pan-Starrs	28700	LM	19.0%	(9)	0.2%
		ET	18.8%	(9)	
	19296	LM	36.2%	(8)	0.4%
		ET	35.8%	(7)	
	18694	LM	59.7%	(5)	1.4%
		ET	58.3%	(3)	
PTF	28700	LM	7.1%	(3)	0.0%
		ET	7.1%	(3)	
	19296	LM	14.6%	(3)	0.0%
		ET	14.6%	(3)	
	18694	LM	34.9%	(3)	1.4%
		ET	33.5%	(3)	

Appendix B

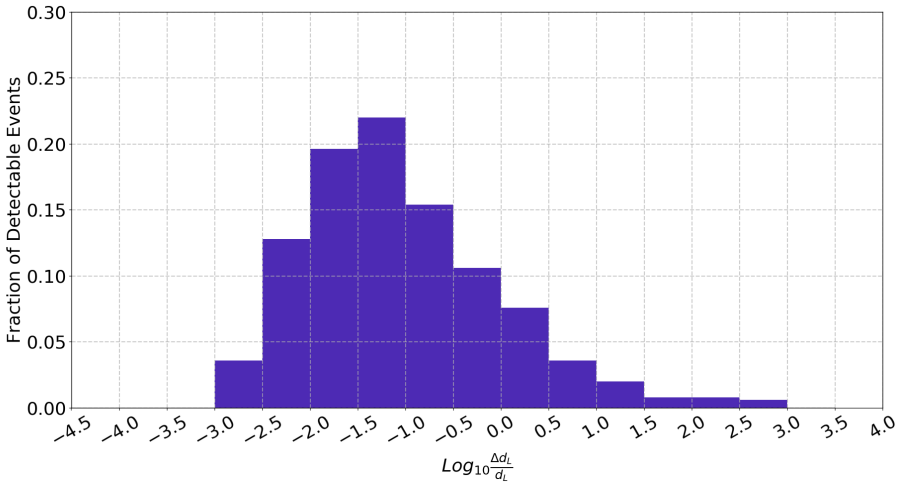

(a)

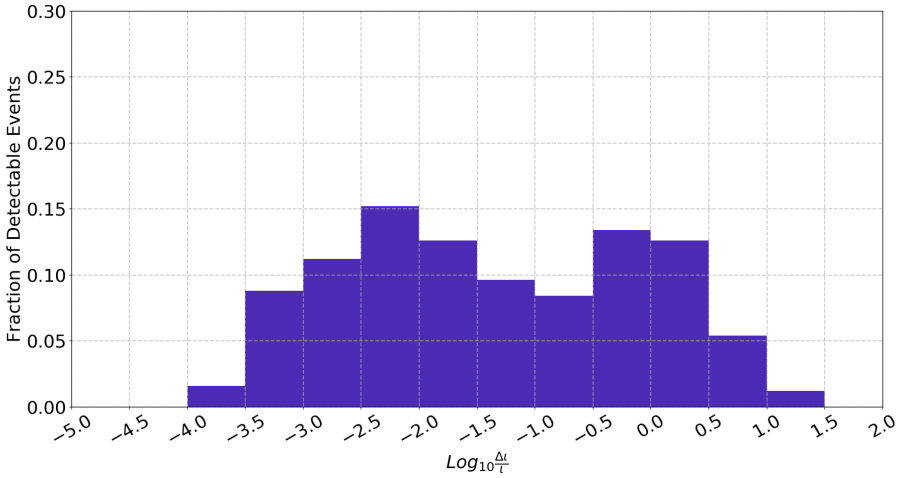

(b)

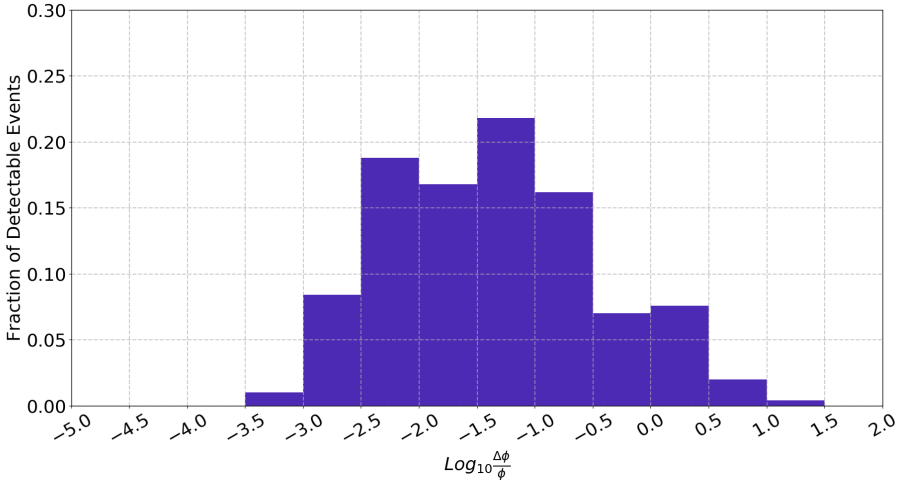

(c)

Figure B.1: The estimate of the 90% uncertainty on the parameters of the BNS merger at 40Mpc detected with the ET. From the top to the bottom: the log of the ratio of the 90% distance uncertainties to the true distances; the log of the ratio of the 90% inclination angle uncertainties to the true inclination angles; the log of the ratio of the 90% polarization angle uncertainties to the true polarization angles.

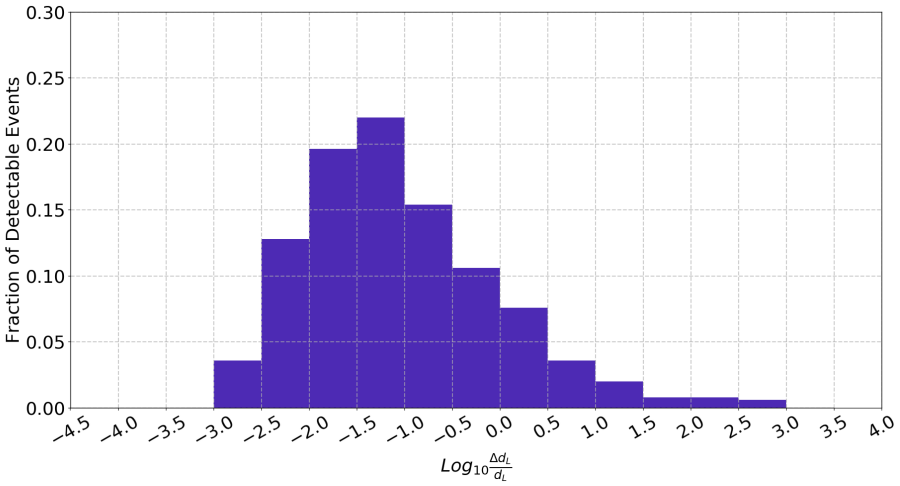

(a)

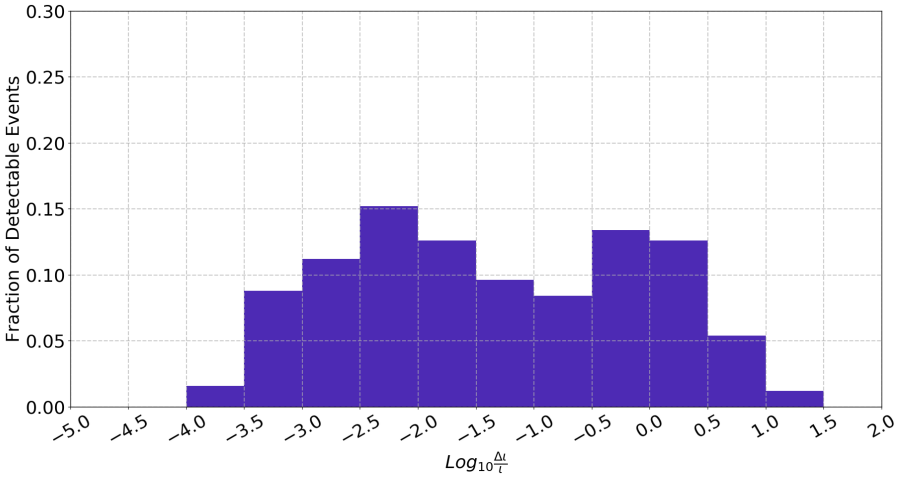

(b)

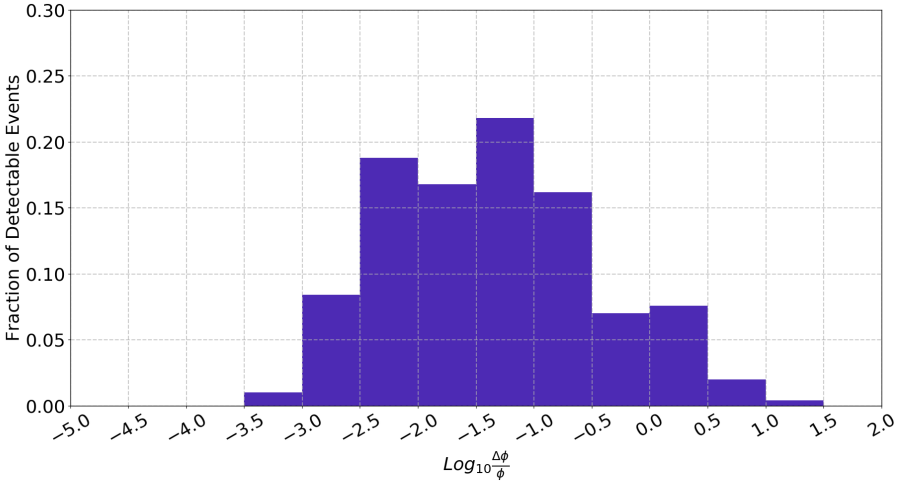

(c)

Figure B.2: Similar to Figure B.1. But the network is ET and CE.

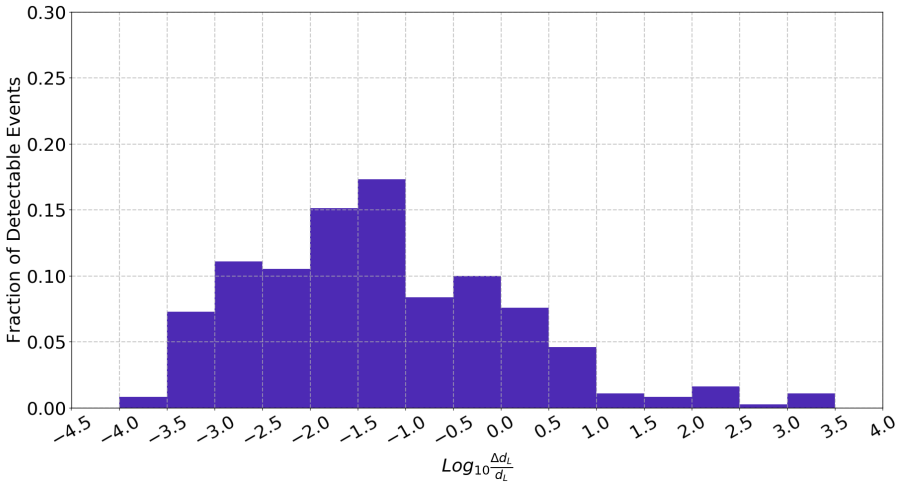

(a)

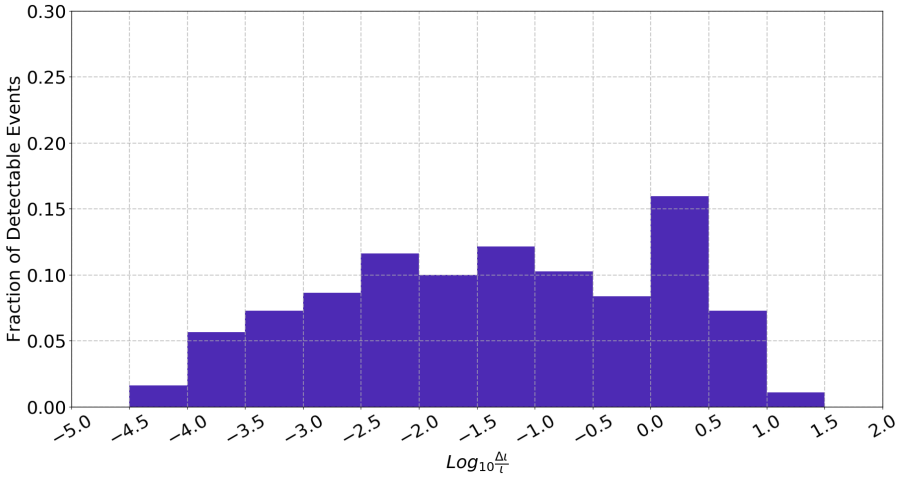

(b)

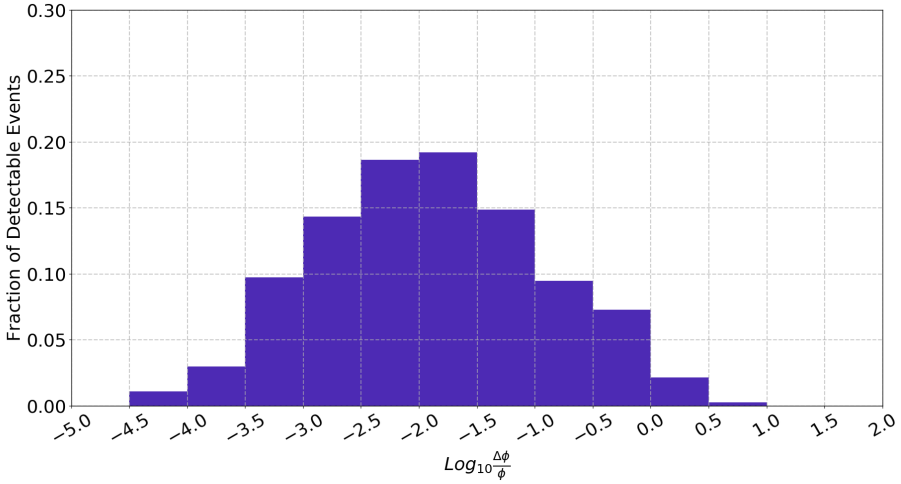

(c)

Figure B.3: The estimate of the 90% uncertainty on the parameters of the BNS merger at 200Mpc detected with the ET. From the top to the bottom: the log of the ratio of the 90% distance uncertainties to the true distances; the log of the ratio of the 90% inclination angle uncertainties to the true inclination angles; the log of the ratio of the 90% polarization angle uncertainties to the true polarization angles.

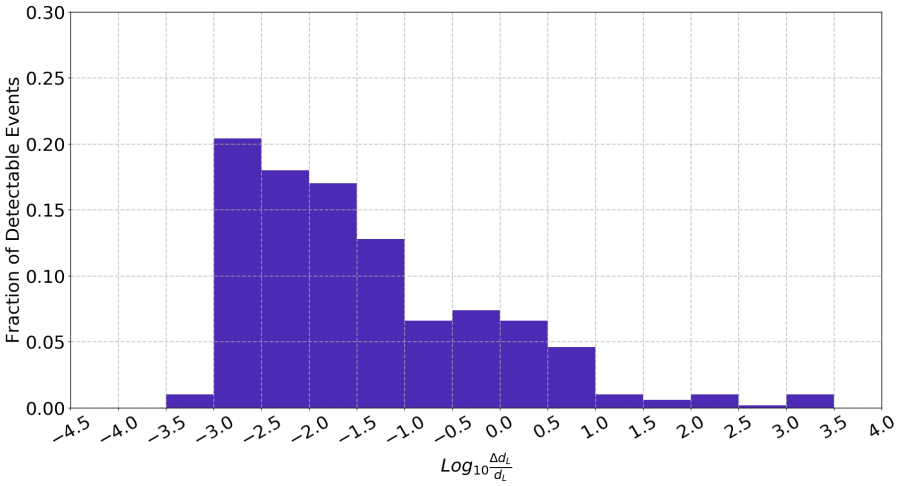

(a)

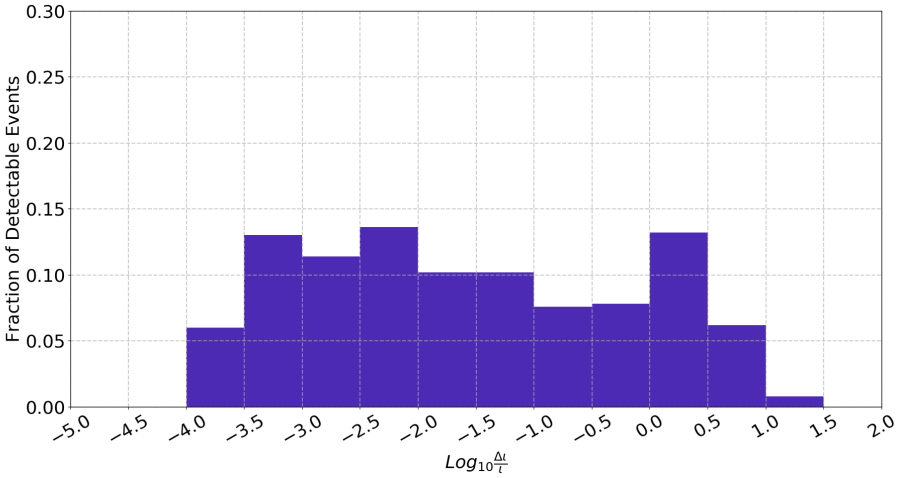

(b)

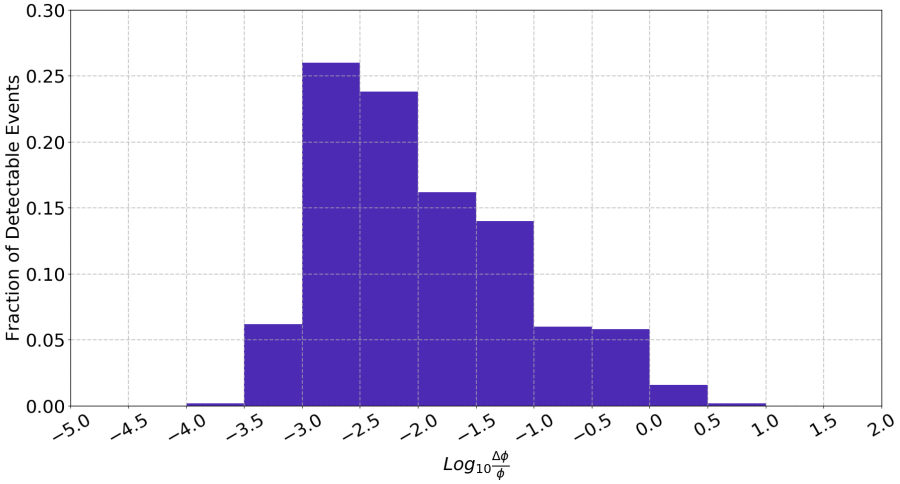

(c)

Figure B.4: Similar to Figure B.3. But the network is ET and CE.

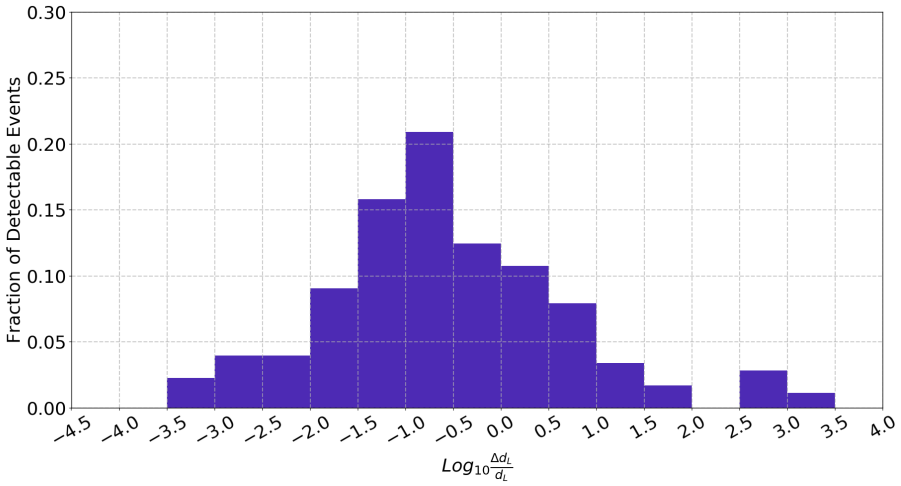

(a)

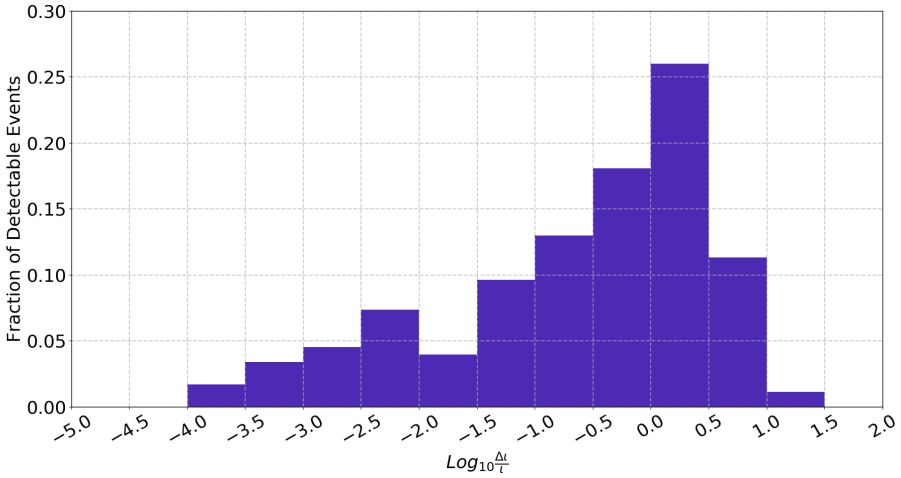

(b)

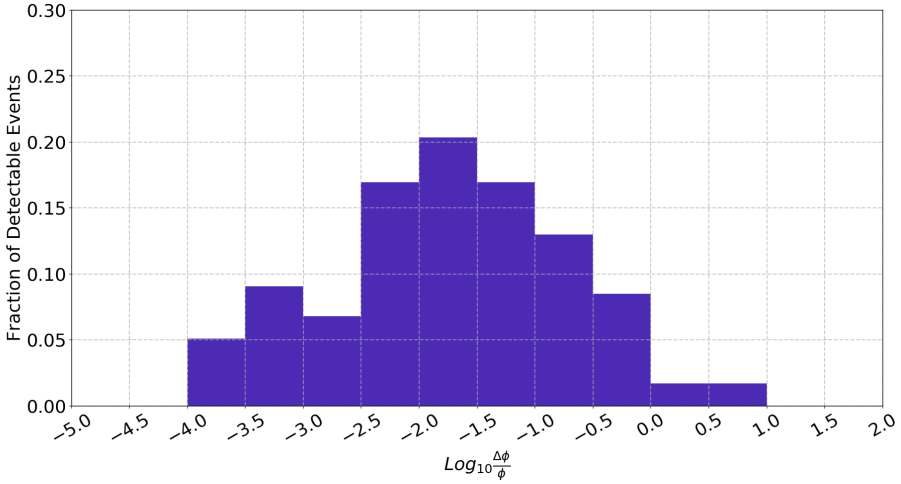

(c)

Figure B.5: The estimate of the 90% uncertainty on the parameters of the BNS merger at 400Mpc detected with ET. From the top to the bottom: the log of the ratio of the 90% distance uncertainties to the true distances; the log of the ratio of the 90% inclination angle uncertainties to the true inclination angles; the log of the ratio of the 90% polarization angle uncertainties to the true polarization angles.

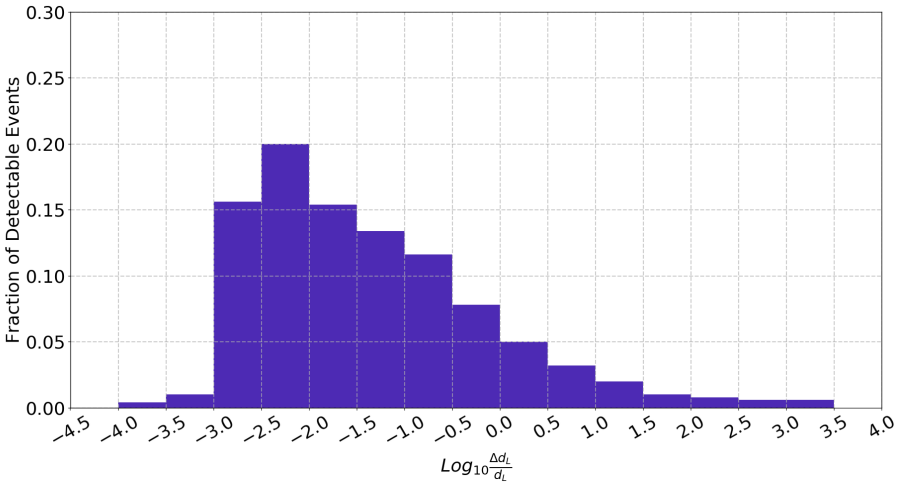

(a)

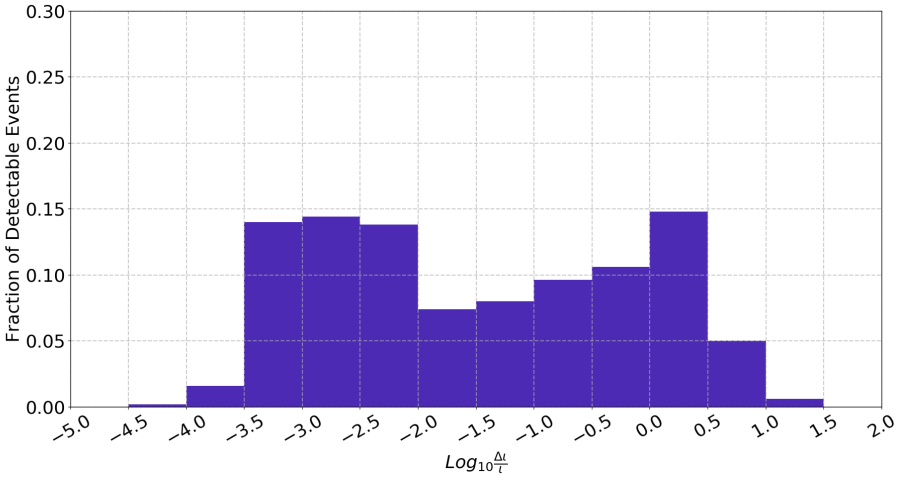

(b)

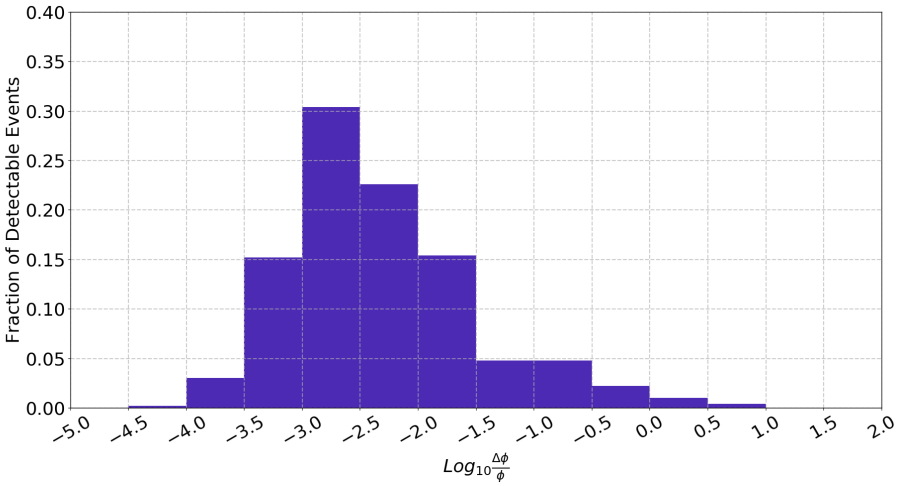

(c)

Figure B.6: Similar to Figure B.5. But the network is ET and CE.

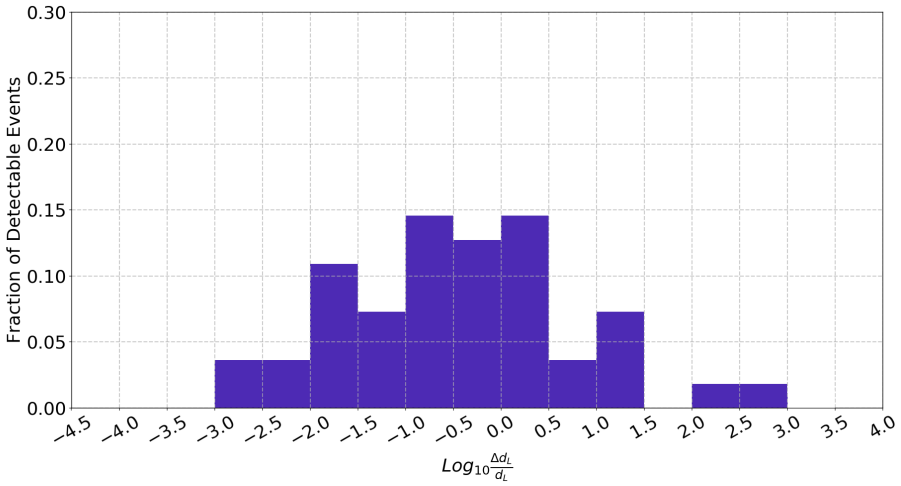

(a)

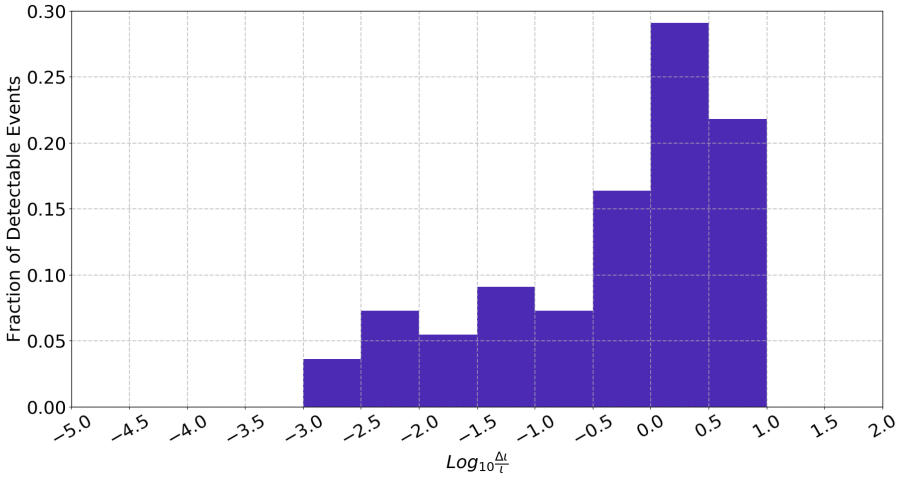

(b)

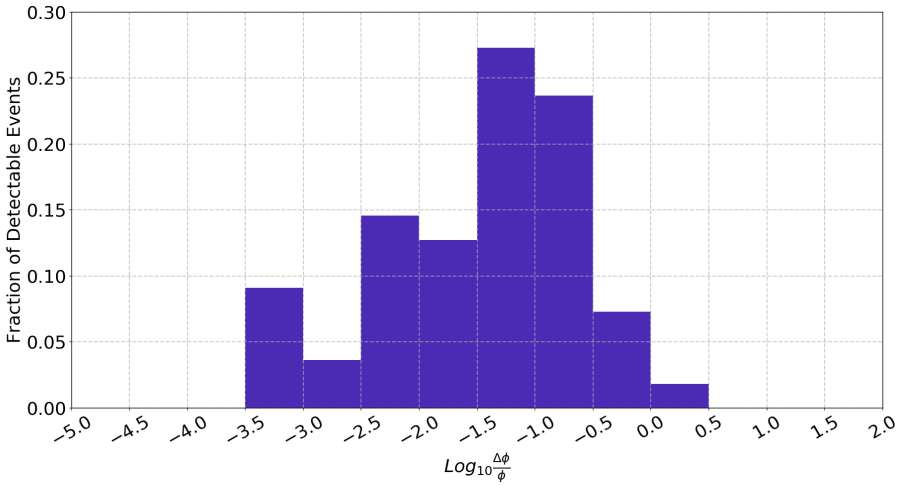

(c)

Figure B.7: The estimate of the 90% uncertainty on the parameters of the BNS merger at 800Mpc detected with ET. From the top to the bottom: the log of the ratio of the 90% distance uncertainties to the true distances; the log of the ratio of the 90% inclination angle uncertainties to the true inclination angles; the log of the ratio of the 90% polarization angle uncertainties to the true polarization angles.

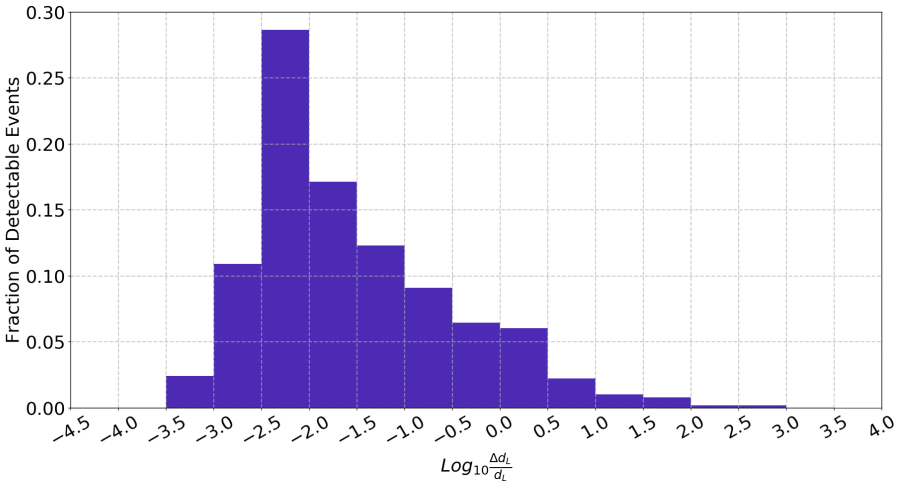

(a)

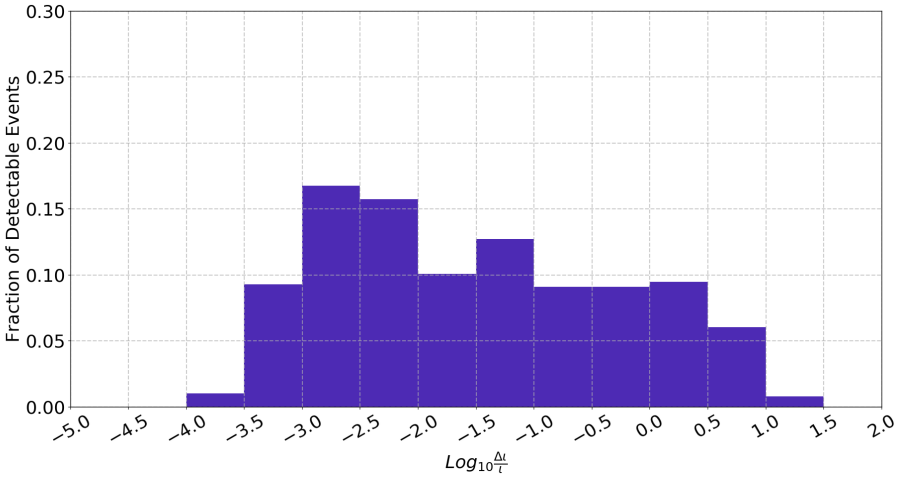

(b)

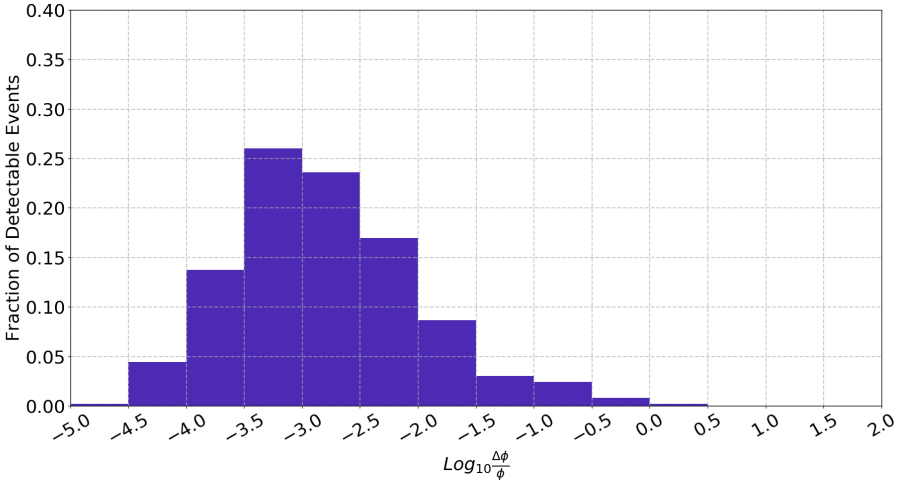

(c)

Figure B.8: Similar to Figure B.7. But the network is ET and CE.

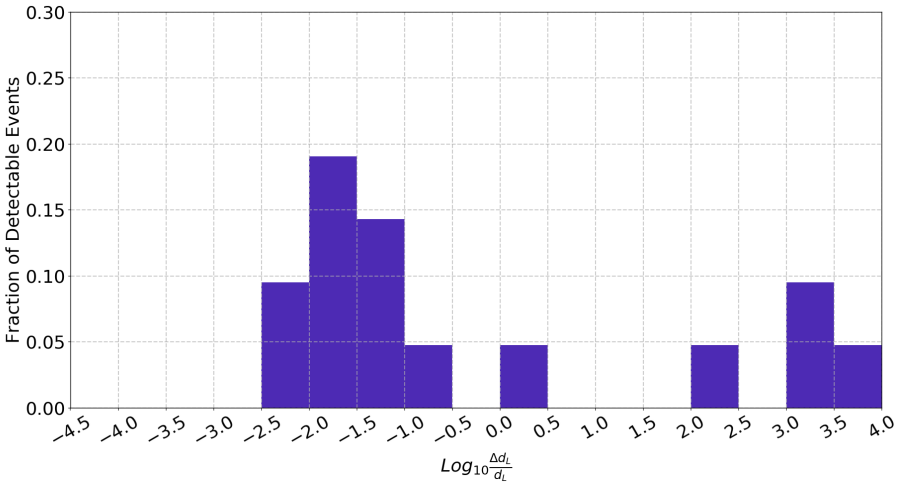

(a)

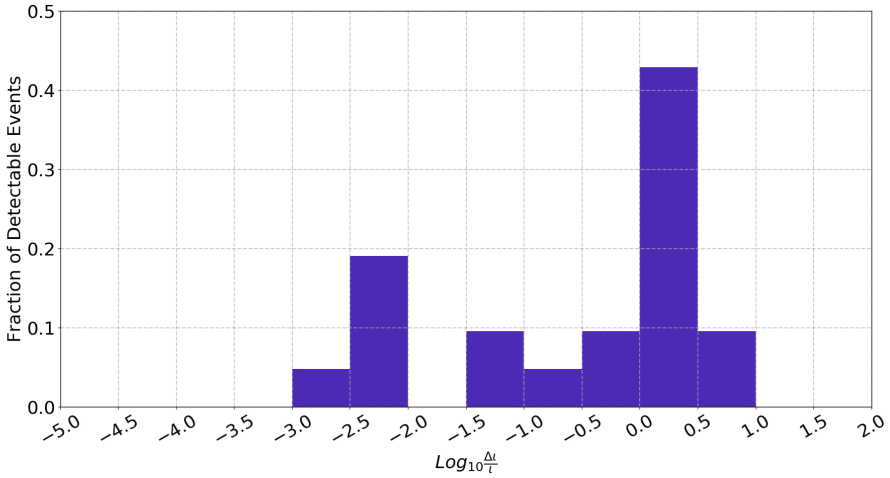

(b)

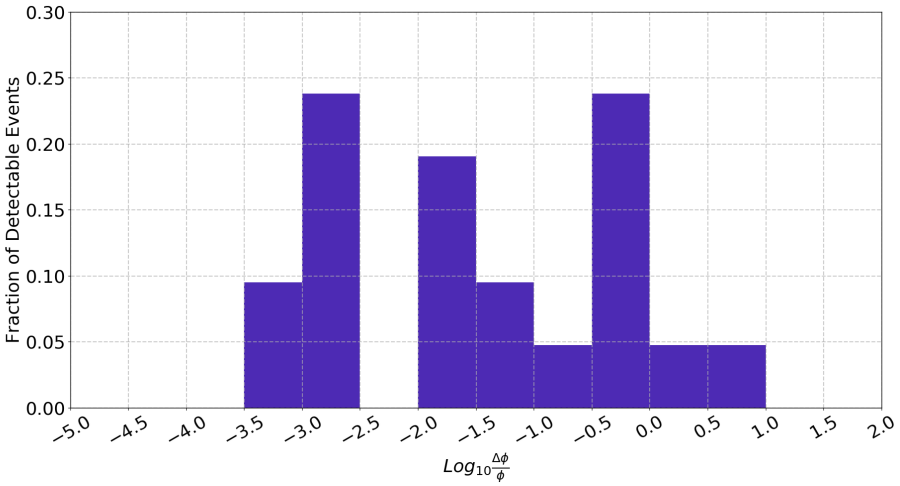

(c)

Figure B.9: The estimate of the 90% uncertainty on the parameters of the BNS merger at 1600Mpc detected with ET. From the top to the bottom: the log of the ratio of the 90% distance uncertainties to the true distances; the log of the ratio of the 90% inclination angle uncertainties to the true inclination angles; the log of the ratio of the 90% polarization angle uncertainties to the true polarization angles.

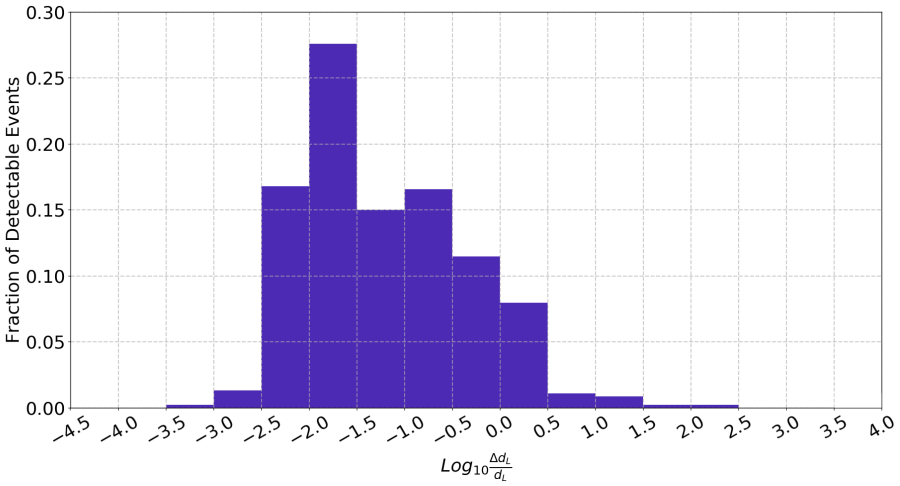

(a)

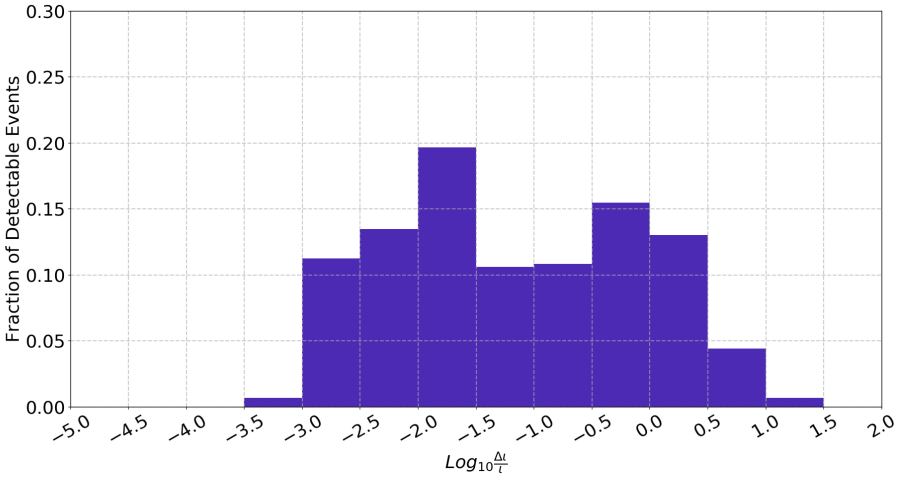

(b)

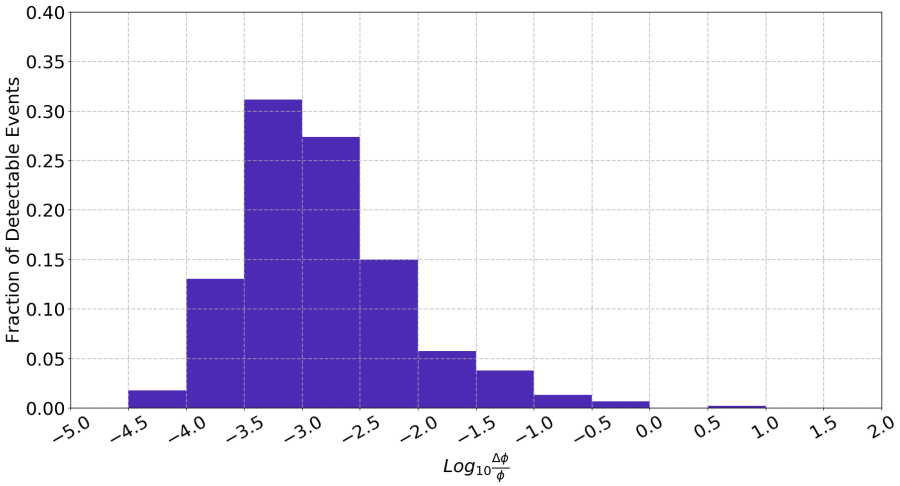

(c)

Figure B.10: Similar to Figure B.9. But the network is ET and CE.

Appendix C

In this section, we will attempt to compare two FM approaches for the estimate of localization error of BNS with a network of 2G detectors. The first approach is laid out in [149] and is already presented in Section 4.4.1. We will refer to this approach as Wen and Chen's approach. The second approach is developed and described in [151, 147] and will be referred to as Fairhurst's approach. This section will be a brief review of Fairhurst's approach. Only the relevant equations will be presented along with explanation. For full description or derivation of the expression, readers are referred to [151, 147].

C.1 Expression

Assuming a network of detectors is involved in localizing a GW signal, the actual arrival time of the signal at the I^{th} detector T_I can be expressed as

$$T_I = T_o - \tau_I = T_o - \frac{\mathbf{n} \cdot \mathbf{r}_I}{c}, \tag{C.1}$$

where T_o is the actual arrival time of the signal at the center of the earth. $\mathbf{n}$ and $\mathbf{r}$ are already defined in Eq. 4.2. Given the actual arrival times T_I, the distribution for the measured arrival time t_I in different detectors in the network can be written as,

$$p(t_I|T_I) = \prod_I \frac{1}{\sqrt{2\pi}\sigma_I} e^{[-\frac{(t_I - T_I)^2}{2\sigma_I^2}]}. \tag{C.2}$$

We can then use Bayes' theorem to derive the posterior distribution for the actual arrival times as a function of the measured arrival time as:

$$p(T_I|t_I) \propto p(T_I) e^{[-\frac{(t_I - T_I)^2}{2\sigma_I^2}]}, \tag{C.3}$$

where $p(T_I)$ is the prior distribution for the actual arrival times T_I. The measured arrival times of the GWs t_I and the measured location $\mathbf{n}_{\text{m}}$ of the source have a relation similar to that in Eq. C.1 which is given by

$$t_I = t_o - \frac{\mathbf{n}_{\text{m}} \cdot \mathbf{r}_I}{c}, \tag{C.4}$$

Using Eqs. C.1 and C.4, we can eliminate T_I and t_I in Eq. C.3 . One can then derive the distribution for the sky location $\mathbf{n}$ of a GW signal with a network of detectors by marginalizing over T_o.

$$p(\mathbf{n}|\mathbf{n}_{\rm m}) \propto p(\mathbf{n}) e^{-\frac{1}{2}(\mathbf{n}_{\rm m}-\mathbf{n})^T \mathbf{M} (\mathbf{n}_{\rm m}-\mathbf{n})}, \tag{C.5}$$

where Matrix $\mathbf{M}$ encodes the orientation and the size of the error region on the source's location and takes the following form

$$\mathbf{M} = \frac{1}{\sum_K \sigma_K^{-2}} \sum_{IJ} \frac{\mathbf{r}_{IJ}\mathbf{r}_{IJ}^T}{2\sigma_I^2\sigma_J^2}, \tag{C.6}$$

where $\mathbf{r}_{IJ}$ is the distance between the $I^{\rm th}$ detector and the $J^{\rm th}$ detector in the network. Since the localization depends on the difference in the arrival times between the detectors in a network, longer distance between detectors will give better localization performance. $\sigma_{I,J,K}$ is the timing uncertainty σ_t from a single detector with I, J, K indicating the detectors and is given by

$$\sigma_t = \frac{1}{2\pi\rho\sigma_f}. \tag{C.7}$$

where σ_f is the effective bandwidth of the detector with respect to the signal and ρ is the SNR of the signal defined in Eq. 4.5. The definition of σ_f is given by

$$\sigma_f^2 = \left(\frac{4}{\rho^2}\int_0^\infty {\rm d}f \frac{f^2|\tilde{h}(f)|^2}{S(f)}\right) - \left(\frac{4}{\rho^2}\int_0^\infty {\rm d}f \frac{f|\tilde{h}(f)|^2}{S(f)}\right)^2. \tag{C.8}$$

It can be seen from Eq. 4.5, the SNR of a signal is proportional to the amplitude of the signal ($|\tilde{h}(f)|$), which is inversely proportional to the distance of the source for close sources where cosmological effects are negligible. Therefore, assuming an SNR of 8 for an optimally located face-on BNS merger at a distance equal to 490Mpc for aLIGO, we use the following expression to scale the value of SNR for GW from an BNS merger detected by a detector at the design sensitivity of LIGO

$$\rho_{\rm aLIGO} = \sqrt{\left(\frac{490{\rm Mpc}\times 8}{d_L}\right)({F_+}^2 + {F_\times}^2)}, \tag{C.9}$$

where $d_{\rm L}$ is the luminosity distance of the BNS merger. Similarly, by assuming the SNR for an optimally located face-on BNS merger at 350Mpc is 8 for a detector at the design sensitivity of Virgo, we have

$$\rho_{\rm AdVirgo} = \sqrt{\left(\frac{350{\rm Mpc}\times 8}{d_L}\right)({F_+}^2 + {F_\times}^2)}. \tag{C.10}$$

In both equations, F_+ and $F_\times$ represent detector response, which are defined in 1.11. From Eq. C.6, we can see that for a given signal and a given network, the construction of the matrix $\mathbf{M}$ depends on the distances between the detectors $\mathbf{r}_{IJ}$ and the timing uncertainty from detectors σ_I. By diagonalizing the matrix $\mathbf{M}$, three orthogonal eigen directions and eigen values can be obtained. These eigen directions and eigen values describe ellipsoid of constant likelihood. Since the source is assumed to be located on the unit sphere, the ellipsoid will intersect the sphere to give an ellipse on the sphere as the localization error. To do that, the matrix $\mathbf{M}$ needs to be projected onto the direction orthogonal to $\mathbf{r}$ using the equation below:

$$\begin{aligned} \mathbf{P}(\mathbf{r}) &= \mathbf{I} - \mathbf{r}\mathbf{r}^T, \\ \mathbf{M}(\mathbf{r}) &= \mathbf{P}(\mathbf{r})\ \mathbf{M}\ \mathbf{P}(\mathbf{r}). \end{aligned} \tag{C.11}$$

Since after projection, the Matrix describes a 2-D probability distribution, one of the three eigenvalues of the matrix $\mathbf{M}(\mathbf{r})$ is equal to zero. The other two eigenvalues are the localization accuracies of the directions represented by the corresponding eigenvectors of the matrix $\mathbf{M}(\mathbf{r})$. The localization error region can be obtained using C.12,

$$\begin{aligned} \text{Area}(p) &\approx 2\pi\sigma_1\sigma_2[-\ln(1-p)], \\ \sigma_{1,2} &= \frac{1}{\lambda_{1,2}}, \end{aligned} \tag{C.12}$$

where p is the confidence level, and $\sigma_{1,2}$, which are different from σ_t defined above, are the inverse of the non zero eigenvalues $\lambda_{1,2}$.

C.2 Simulation

To compare the two FM approaches, we have simulated the localization of GW signals from BNS mergers distributed across the sky with 5 different networks. The networks simulated are given in Table C.1. Among the simulated detectors, H, L, J and A are at the design sensitivity of aLIGO while V are at the design sensitivity of AdVirgo. Note for this particular test, J or A only means that a detector as sensitive as aLIGO is located in Japan or Australia. It does not refer to any existing or proposed detectors in those places. They are not to be confused with the definition given in Section 4.4.2.

We will focus our comparison on face-on BNS mergers located at a distance equal to 160Mpc. Each body of the BNS mergers has a mass of 1.4 $M_\odot$. We use the formalism described above for Fairhurst's approach, and that described in Section 4.4.1 for Wen and Chen's approach. To determine whether a source is detectable, we again use the SNR cut described in Section 4.3. The results of the simulations for the first three networks in Table C.1 are displayed in Figure C.1 and the remaining networks in Figure C.2. If a source is not detectable, a cross will be marked at its location. The same row in Figure C.1 and C.2 shows the same network with the

Table C.1: Simulated Networks

Networks	Abbreviation
LIGO Hanford - LIGO Livingston - Virgo	HLV
LIGO Hanford - LIGO Livingston - Virgo - Japan	HLVJ
LIGO Hanford - LIGO Livingston - Japan - Australia	HLJA
LIGO Hanford - LIGO Livingston - Virgo - Australia	HLVA
LIGO Hanford - LIGO Livingston - Virgo - Australia - Japan	HLVAJ

one on the left showing the estimate from Fairhurst's approach, and the one on the right the estimate from Wen and Chen's approach. For clarity, ellipses obtained using Fairhurst's approach are in blue and those using Wen and Chen's approach are in red.

C.3 Discussion

It can be seen from Figure C.1 and Figure C.2, the estimate of the localization errors are pretty similar between the two approaches. The biggest discrepancy is seen in the biggest ellipses with network HLV. The biggest discrepancy occurs at sky positions to which the sensitivity of one or more detectors in the network is weak resulting in low SNR in one or more detectors. As discussed in Section 1.6.3, the FM assumes Gaussianity of the unknown parameter's distribution. This assumption holds only when the SNR is moderate or high enough. When the SNR at one or more detectors is so low that this assumption is no longer valid, the estimate from the FM will become too optimistic and therefore untrustworthy. For the rest of the ellipses in the plots, the estimates from both methods agree with each other.

The characterizing feature of Fairhurst's approach is that the construction of the FM relies on only a few parameters: the SNR of the signal from an optimally located and oriented BNS, the distance d_{L} to it, and the effective bandwidth σ_f of the detectors with respective to a signal. The effective bandwidth σ_f encapsulates the detectors' sensitive with respect to a signal. Since the computation of the effective bandwidth σ_f of the detectors in a network is just an integration as shown in Eq. C.8, once a source of which one wants to estimate the localization error is decided, the computation of the localization can be as simple as the computation of a few numbers making this approach relatively computationally cheap.

Wen and Chen's approach incorporates more general situations in the expression where the time of arrival of GW signals is not the only unknown parameter. It allows a straightforward relation between the localization error and the frequencies of a GW signal in the calculations. For example, if one changes the lower limit and the upper limit of the integrals in Eq. 4.18, it would be possible to observe the evolution of the FM with the information available and the effect of the information on our current

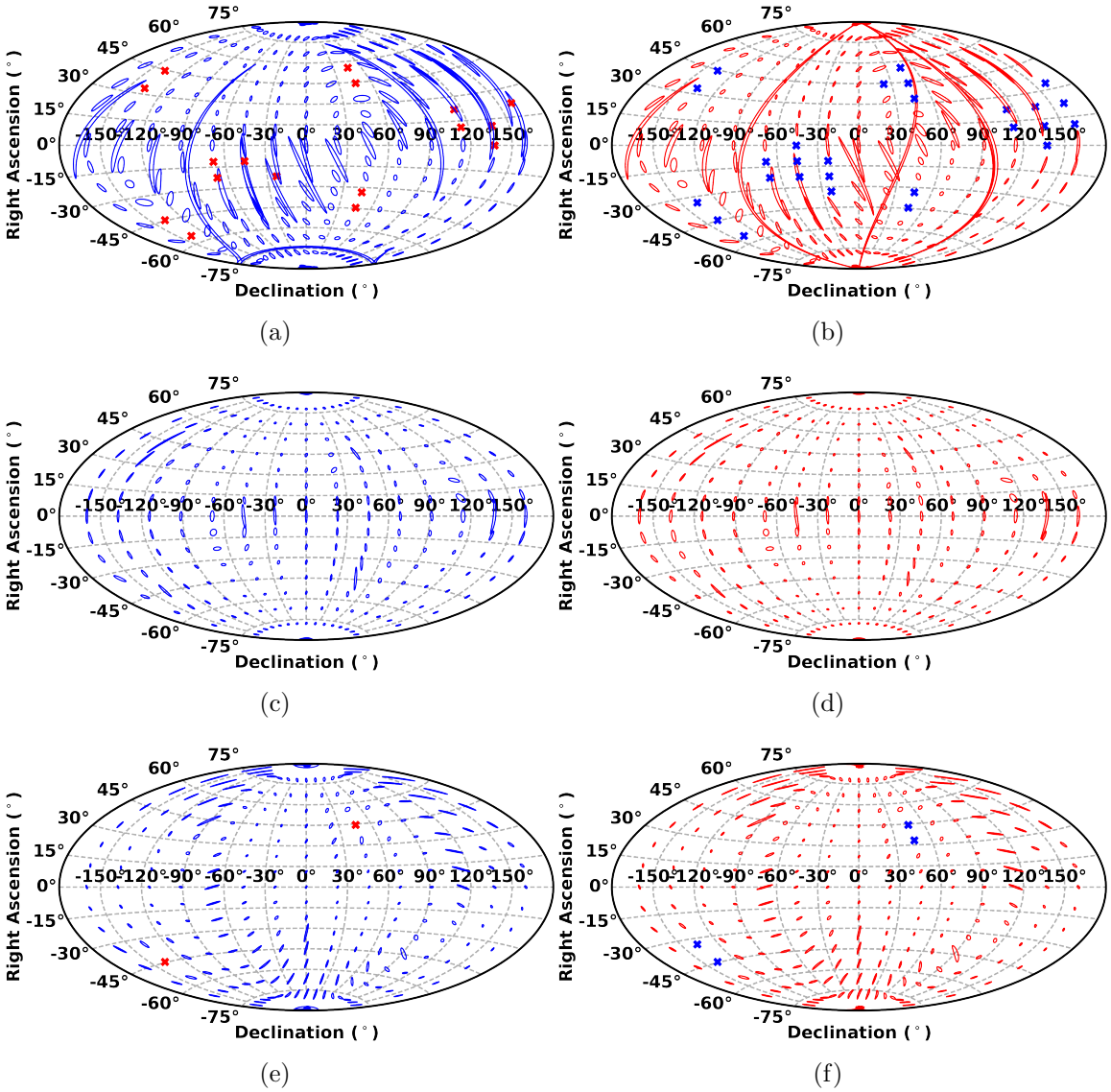

(a) (b)

(c) (d)

(e) (f)

Figure C.1: The comparison between the estimates of 90% localization error region using different Fisher Matrix approaches. The sources are assumed to be face-on $1.4M_{\odot}$ - $1.4M_{\odot}$ BNS mergers located at a distance equal to 160Mpc. The panels on the same row display the estimate of localization errors with the same networks: Panel (a) & (b) : HLV; Panel (c) & (d) HLVJ; Panel (e) & (f) AHJL. The crosses indicate that the sources at those positions are not detectable. The panels on the left show the localization errors estimated using Fairhurst's approach, and the sky maps on the right Wen and Chen's approach.

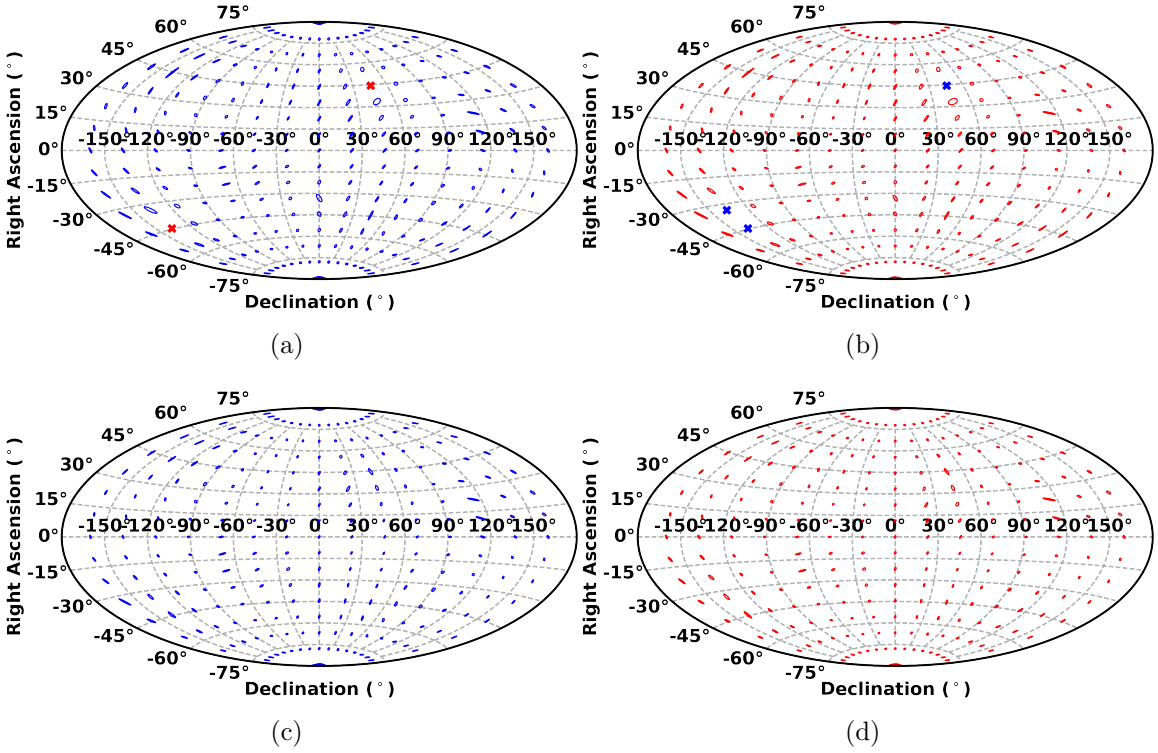

(a) (b)

(c) (d)

Figure C.2: The same as Figure C.1 but with different networks. Panel (a) & (b) : AHLV; Panel (c) & (d) AHJLV.

knowledge. However, including the evolution of the frequency of a GW may cause problems of computational resources, and thus reduce the speed of Wen and Chen's approach.

Appendix D

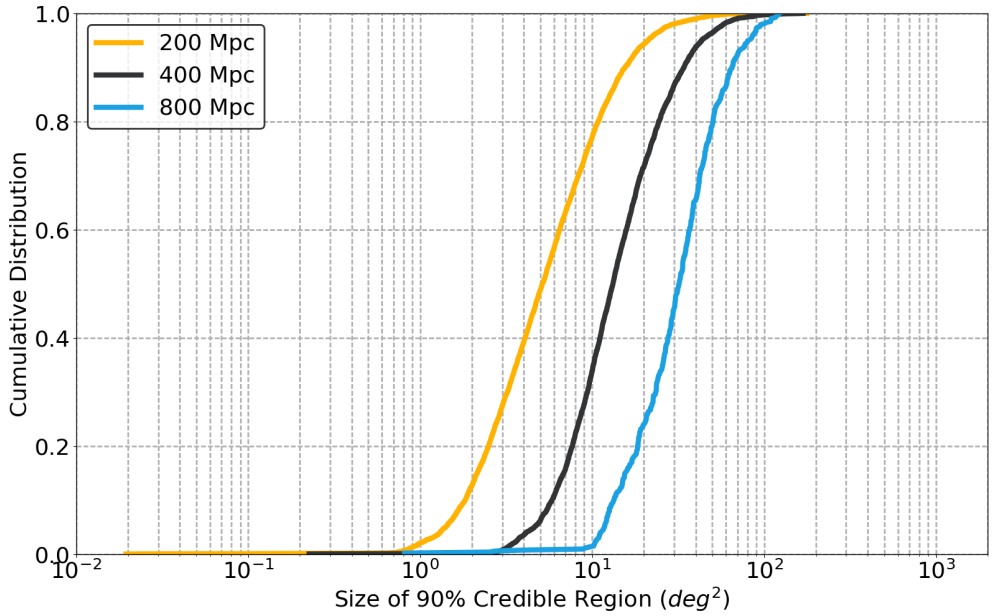

(a)

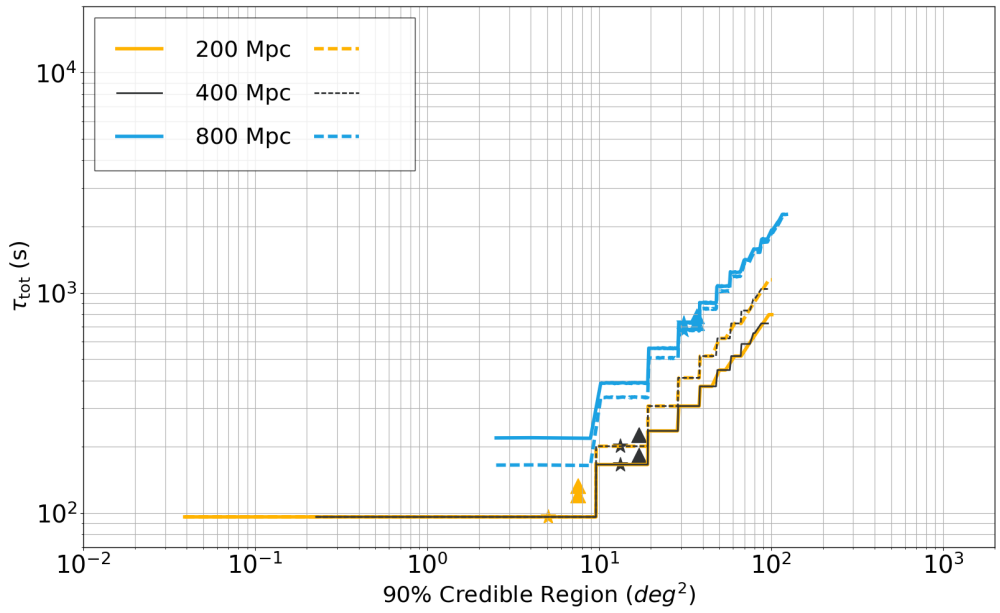

(b)

Figure D.1: Plots showing the results for the simulation for Network 5 (H+ L+ V I K C). The upper panel shows the cumulative distribution of the size of the 90% credible regions for detectable BNS mergers. The lower panel shows the values of $\tau_{\rm tot}$. The legends in the plots indicate the true distances of the sources. In the lower panel, the solid lines shows the values of $\tau_{\rm tot}$ for the first scenario, and the dashed lines show that for the second scenario, as indicated in Eq. 5.8. The stars and triangles indicate the median and the mean values of the $\tau_{\rm tot}$ respectively (i.e. excluding the data plotted as dots).

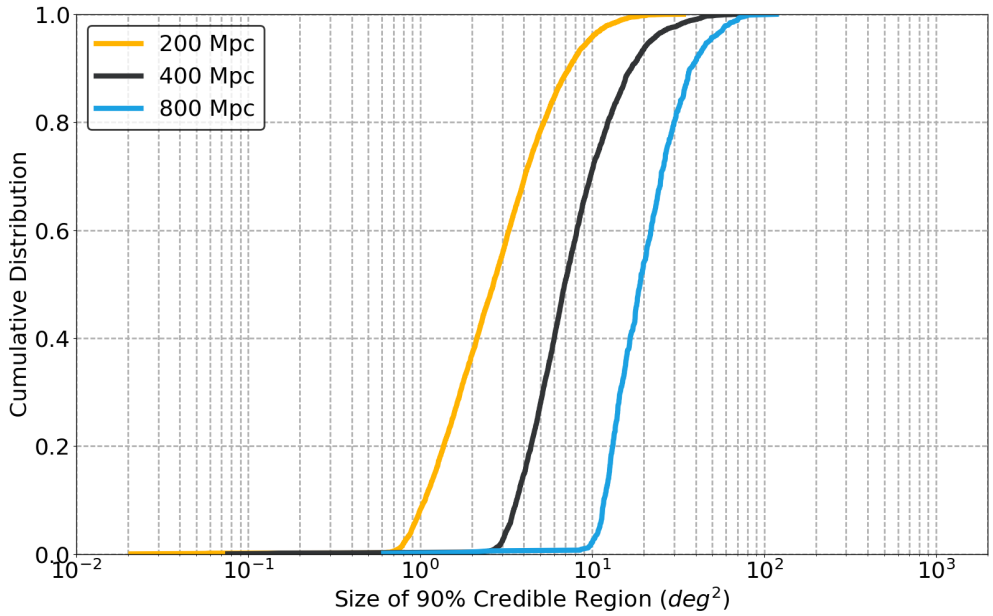

(a)

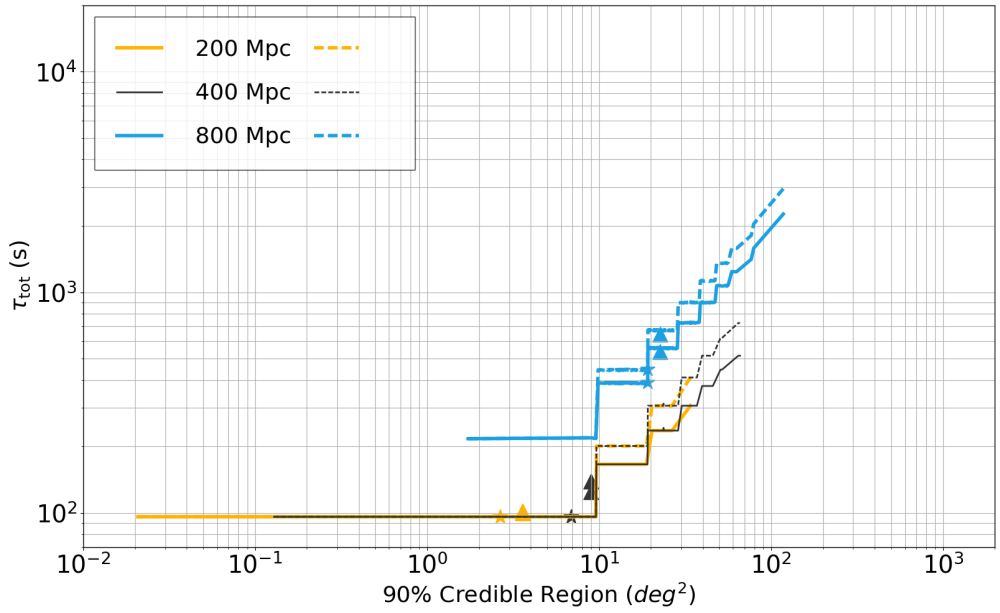

(b)

Figure D.2: Similar to Figure D.1. In this case, the network is Network 6 (H+ L+ V I K A).

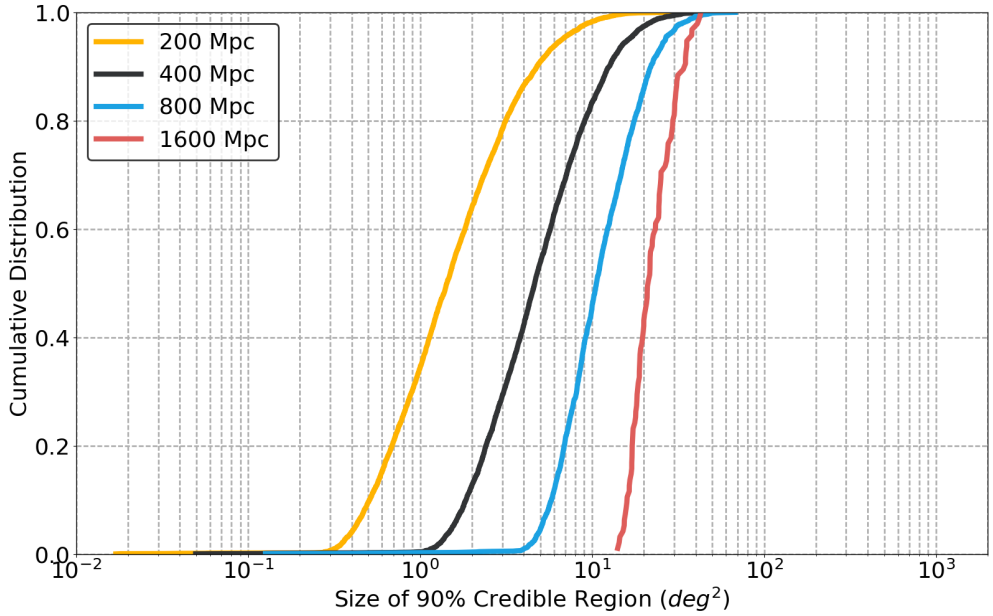

(a)

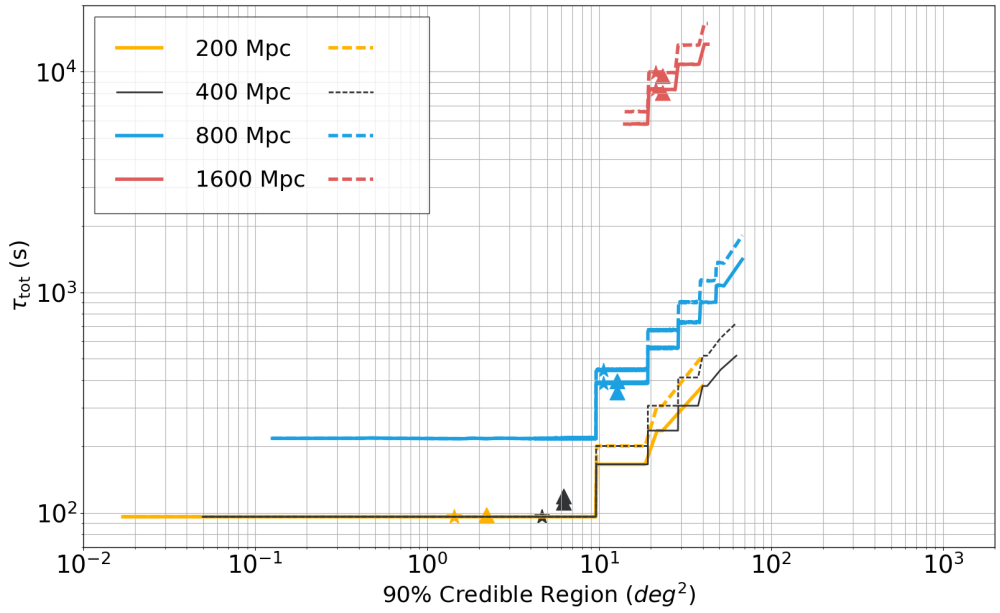

(b)

Figure D.3: Similar to Figure D.1. In this case, the network is Network 7 (H+ L+ V I K A C).

Table D.1: Statistical summary of EM follow-up observations of BNS mergers with LSST

Network	Scenario	Distance (Mpc) 200		400		800	
		$< 10^2$s	$< 10^3$s	$< 10^2$s	$< 10^3$s	$< 10^2$s	$< 10^3$s
Network 5	First	75.6%	99.9%	31.2%	99.8%	0.0%	77.3%
	Second	75.6%	99.9%	31.2%	99.4%	0.0%	63.2%
Network 6	First	95.2%	100.0%	68.9%	100.0%	0.0%	95.0%
	Second	95.2%	100.0%	68.9%	100.0%	0.0%	90.4%
Network 7	First	98.1%	100.0%	81.7%	100.0%	0.0%	99.7%
	Second	98.1%	100.0%	81.7%	100.0%	0.0%	98.9%

		1600Mpc	
		$< 10^2$s	$< 10^3$s
Network 7	First	0.0%	0.0%
	Second	0.0%	0.0%

A table similar to Table 5.3 showing the results for the simulations for Network 5 - 7.

Bibliography

[1] M. L. Chan, Y.-M. Hu, C. Messenger, M. Hendry, and I. S. Heng. Maximizing the Detection Probability of Kilonovae Associated with Gravitational Wave Observations. The Astrophysical Journal, 834:84, January 2017. (document), 4.3.2

[2] M. W. Coughlin, D. Tao, M. L. Chan, et al. Optimizing searches for electromagnetic counterparts of gravitational wave triggers. Monthly Notices of the Royal Astronomical Society, 478:692–702, July 2018. (document)

[3] M. L. Chan, C. Messenger, I. S. Heng, and M. Hendry. Binary neutron star mergers and third generation detectors: Localization and early warning. Physical Review D, 97(12):123014, June 2018. (document)

[4] E. J. Howell, M. L. Chan, Q. Chu, et al. Host galaxy identification for binary black hole mergers with long baseline gravitational wave detectors. Monthly Notices of the Royal Astronomical Society, 474:4385–4395, March 2018. (document), 4.4.2

[5] A. Einstein. Die Grundlage der allgemeinen Relativitätstheorie. Annalen der Physik, 354:769–822, 1916. 1.1

[6] Jolien DE Creighton and Warren G Anderson. Gravitational-wave physics and astronomy: an introduction to theory, experiment and data analysis. John Wiley & Sons, 2012. 1.1

[7] Bangalore Suryanarayana Sathyaprakash and Bernard F Schutz. Physics, astrophysics and cosmology with gravitational waves. Living Reviews in Relativity, 12(1):2, 2009. 1.1, 1.1, 1.2, 1.2.1, 1.2.1, 1.2.2, 1.2.2, 1.2.4, 2, 2.3

[8] Bernard Schutz. A first course in general relativity. Cambridge university press, 2009. 1.1

[9] Wm. R. Johnston. Gravitational wave-related images. http://www.johnstonsarchive.net/relativity/pictures.html. Accessed: 2018-01-25. 1.1

[10] R. A. Hulse and J. H. Taylor. Discovery of a pulsar in a binary system. The Astrophysical Journal Letters, 195:L51–L53, January 1975. 1.1

[11] J. M. Weisberg and J. H. Taylor. The Relativistic Binary Pulsar B1913+16: Thirty Years of Observations and Analysis. In F. A. Rasio and I. H. Stairs, editors, Binary

Radio Pulsars, volume 328 of Astronomical Society of the Pacific Conference Series, page 25, July 2005. 1.1, 1.1, 1.2

[12] Charles W Misner, Kip S Thorne, and John Archibald Wheeler. Gravitation. Princeton University Press, 2017. 1.2

[13] B. Kiziltan, A. Kottas, M. De Yoreo, and S. E. Thorsett. The Neutron Star Mass Distribution. The Astrophysical Journal, 778:66, November 2013. 1.2.1

[14] G. Ushomirsky, C. Cutler, and L. Bildsten. Deformations of accreting neutron star crusts and gravitational wave emission. Monthly Notices of the Royal Astronomical Society, 319:902–932, December 2000. 1.2.1

[15] B. P. Abbott, R. Abbott, T. D. Abbott, et al. First Search for Gravitational Waves from Known Pulsars with Advanced LIGO. The Astrophysical Journal, 839:12, April 2017. 1.2.1

[16] K. Riles. Recent searches for continuous gravitational waves. Modern Physics Letters A, 32:1730035–685, December 2017. 1.2.1

[17] N. Andersson, V. Ferrari, D. I. Jones, et al. Gravitational waves from neutron stars: promises and challenges. General Relativity and Gravitation, 43:409–436, February 2011. 1.2.1

[18] B. Abbott, R. Abbott, R. Adhikari, et al. Beating the Spin-Down Limit on Gravitational Wave Emission from the Crab Pulsar. The Astrophysical Journal Letters, 683:L45, August 2008. 1.2.1

[19] Keith Riles for the LIGO Scientific Collaboration and Virgo Collaboration. Searches for continuous gravitational waves with the LIGO and Virgo detector. ArXiv e-prints, October 2012. 1.2.1

[20] J. A. Faber and F. A. Rasio. Binary Neutron Star Mergers. Living Reviews in Relativity, 15:8, July 2012. 1.2.2

[21] B. S. Sathyaprakash. Gravitational Radiation - Observing the Dark and Dense Universe. ArXiv General Relativity and Quantum Cosmology e-prints, May 2004. 1.2.2, 1.2.2, 1.2.4, 1.4.4

[22] Massimo Bassan. Advanced Interferometers and the Search for Gravitational Waves: Lectures from the First VESF School on Advanced Detectors for Gravitational Waves, volume 404. Springer, 2014. 1.2.2

[23] J. Aasi, B. P. Abbott, R. Abbott, et al. The NINJA-2 project: detecting and characterizing gravitational waveforms modelled using numerical binary black hole simulations. Classical and Quantum Gravity, 31(11):115004, June 2014. 1.2.2

[24] Thomas W Baumgarte and Stuart L Shapiro. Numerical relativity: solving Einstein's equations on the computer. Cambridge University Press, 2010. 1.2.2

[25] C. Kalaghatgi, P. Ajith, and K. G. Arun. Template-space metric for searches for gravitational waves from the inspiral, merger, and ringdown of binary black holes. Physical Review D, 91(12):124042, June 2015. 1.2.2

[26] E. Barausse, A. Buonanno, S. A. Hughes, et al. Modeling multipolar gravitational-wave emission from small mass-ratio mergers. Physical Review D, 85(2):024046, January 2012. 1.2.2

[27] A. K. Mehta, C. K. Mishra, V. Varma, and P. Ajith. Accurate inspiral-merger-ringdown gravitational waveforms for nonspinning black-hole binaries including the effect of subdominant modes. Physical Review D, 96(12):124010, December 2017. 1.2.2

[28] P. Ajith, S. Babak, Y. Chen, et al. Template bank for gravitational waveforms from coalescing binary black holes: Nonspinning binaries. Physical Review D, 77(10):104017, May 2008. 1.2.2

[29] P. Ajith, M. Hannam, S. Husa, et al. Inspiral-Merger-Ringdown Waveforms for Black-Hole Binaries with Nonprecessing Spins. Physical Review Letters, 106(24):241101, June 2011. 1.2.2

[30] M. Hannam, P. Schmidt, A. Bohé, et al. Simple Model of Complete Precessing Black-Hole-Binary Gravitational Waveforms. Physical Review Letters, 113(15):151101, October 2014. 1.2.2

[31] S. Husa, S. Khan, M. Hannam, et al. Frequency-domain gravitational waves from nonprecessing black-hole binaries. I. New numerical waveforms and anatomy of the signal. Physical Review D, 93(4):044006, February 2016. 1.2.2

[32] P. Ajith, S. Babak, Y. Chen, et al. A phenomenological template family for black-hole coalescence waveforms. Classical and Quantum Gravity, 24:S689–S699, October 2007. 1.2.2

[33] P. Ajith. Gravitational-wave data analysis using binary black-hole waveforms. Classical and Quantum Gravity, 25(11):114033, June 2008. 1.2.2

[34] L. London, S. Khan, E. Fauchon-Jones, et al. First Higher-Multipole Model of Gravitational Waves from Spinning and Coalescing Black-Hole Binaries. Physical Review Letters, 120(16):161102, April 2018. 1.2.2

[35] J. S. Read, L. Baiotti, J. D. E. Creighton, et al. Matter effects on binary neutron star waveforms. Physical review D, 88(4):044042, August 2013. 1.2.2

[36] lalsimulation. https://lscsoft.docs.ligo.org/lalsuite/lalsimulation/index.html. Accessed: 2018-10-31. 1.4

[37] J. Aasi, B. P. Abbott, R. Abbott, et al. Search for gravitational radiation from intermediate mass black hole binaries in data from the second LIGO-Virgo joint science run. Physical Review D, 89(12):122003, June 2014. 1.2.3

[38] C. D. Ott, E. Abdikamalov, S. Gossan, et al. The Gravitational-Wave Signature of Core-Collapse Supernovae. In APS Meeting Abstracts, page Q10.007, April 2013. 1.2.3

[39] A. Heger, C. L. Fryer, S. E. Woosley, N. Langer, and D. H. Hartmann. How Massive Single Stars End Their Life. The Astrophysical Journal, 591:288–300, July 2003. 1.2.3

[40] B. P. Abbott, R. Abbott, T. D. Abbott, et al. First targeted search for gravitational-wave bursts from core-collapse supernovae in data of first-generation laser interferometer detectors. Physical Review D, 94(10):102001, November 2016. 1.2.3, 2

[41] S. E. Gossan, P. Sutton, A. Stuver, et al. Observing gravitational waves from core-collapse supernovae in the advanced detector era. Physical Review D, 93(4):042002, February 2016. 1.2.3

[42] G. A. Tammann, W. Loeffler, and A. Schroeder. The Galactic supernova rate. The Astrophysical Journal Supplement Series, 92:487–493, June 1994. 1.2.3

[43] E. Cappellaro, R. Evans, and M. Turatto. A new determination of supernova rates and a comparison with indicators for galactic star formation. Astronomy & Astrophysics, 351:459–466, November 1999. 1.2.3

[44] H.-T. Janka. Explosion Mechanisms of Core-Collapse Supernovae. Annual Review of Nuclear and Particle Science, 62:407–451, November 2012. 1.2.3

[45] H. Dimmelmeier, C. D. Ott, A. Marek, and H.-T. Janka. Gravitational wave burst signal from core collapse of rotating stars. Physical Review D, 78(6):064056, September 2008. 1.2.3

[46] E. Abdikamalov, S. Gossan, A. M. DeMaio, and C. D. Ott. Measuring the angular momentum distribution in core-collapse supernova progenitors with gravitational waves. Physical Review D, 90(4):044001, August 2014. 1.2.3

[47] S. Scheidegger, R. Käppeli, S. C. Whitehouse, T. Fischer, and M. Liebendörfer. The influence of model parameters on the prediction of gravitational wave signals from stellar core collapse. Astronomy & Astrophysics, 514:A51, May 2010. 1.2.3

[48] J. W. Murphy, C. D. Ott, and A. Burrows. A Model for Gravitational Wave Emission from Neutrino-Driven Core-Collapse Supernovae. The Astrophysical Journal, 707:1173–1190, December 2009. 1.2.3

[49] K. N. Yakunin, P. Marronetti, A. Mezzacappa, et al. Gravitational waves from core collapse supernovae. Classical and Quantum Gravity, 27(19):194005, October 2010. 1.2.3

[50] E. Müller, H.-T. Janka, and A. Wongwathanarat. Parametrized 3D models of neutrino-driven supernova explosions. Neutrino emission asymmetries and gravitational-wave signals. Astronomy & Astrophysics, 537:A63, January 2012. 1.2.3

[51] C. D. Ott, E. Abdikamalov, P. Mösta, et al. General-relativistic Simulations of Three-dimensional Core-collapse Supernovae. The Astrophysical Journal, 768:115, May 2013. 1.2.3

[52] I. S. Heng. Rotating stellar core-collapse waveform decomposition: a principal component analysis approach. Classical and Quantum Gravity, 26(10):105005, May 2009. 1.2.3

[53] J. Powell, S. E. Gossan, J. Logue, and I. S. Heng. Inferring the core-collapse supernova explosion mechanism with gravitational waves. Physical Review D, 94(12):123012, December 2016. 1.2.3

[54] T. Regimbau. The astrophysical gravitational wave stochastic background. Research in Astronomy and Astrophysics, 11:369–390, April 2011. 1.2.4

[55] B. P. Abbott, R. Abbott, T. D. Abbott, et al. Upper Limits on the Stochastic Gravitational-Wave Background from Advanced LIGO's First Observing Run. Physical Review Letters, 118(12):121101, March 2017. 1.2.4

[56] J. Weber. Detection and Generation of Gravitational Waves. Physical Review, 117:306–313, January 1960. 1.3, 1.3.1

[57] J. Weber. Gravitational Radiation. Physical Review Letters, 18:498–501, March 1967. 1.3

[58] J. Weber. Evidence for Discovery of Gravitational Radiation. Physical Review Letters, 22:1320–1324, June 1969. 1.3.1

[59] J. Weber. Anisotropy and Polarization in the Gravitational-Radiation Experiments. Physical Review Letters, 25:180–184, July 1970. 1.3.1

[60] James Hough and LIGO Scientific Collaboration. The search for gravitational waves. In AIP Conference Proceedings, volume 957, pages 93–98. AIP, 2007. 1.3.1

[61] RWP Drever, J Hough, R Bland, and GW Lessnoff. Search for short bursts of gravitational radiation. Nature, 246(5432):340, 1973. 1.3.1

[62] University of Rome La Sapienza. Rome gravitational wave group. http://www.roma1.infn.it/rog/. Accessed: 2018-01-25. 1.3.1

[63] Laboratori Nationali Legnaro. Auriga bar detector. http://www.auriga.lnl.infn.it/. Accessed: 2018-01-25. 1.3.1

[64] Laboratori Nationali Legnaro. Auriga: the sensitivity. http://www.auriga.lnl.infn.it/auriga/detector/run1/sensitivity.html. Accessed: 2018-06-19. 1.5

[65] M. E. Gertsenshteĭn and V. I. Pustovoĭt. On the Detection of Low-Frequency Gravitational Waves. Soviet Journal of Experimental and Theoretical Physics, 16:433, 1963. 1.3.2

[66] R. Weiss. Electromagnetically Coupled Broadband Gravitational Antenna. LIGO-P720002v1, 1972. 1.3.2

[67] Gregory M Harry and the LIGO Scientific Collaboration. Advanced ligo: the next generation of gravitational wave detectors. Classical and Quantum Gravity, 27(8):084006, 2010. 1.3.2

[68] B P Abbott, R Abbott, R Adhikari, et al. Ligo: the laser interferometer gravitational-wave observatory. Reports on Progress in Physics, 72(7):076901, 2009. 1.3.2

[69] J. R. Smith and LIGO Scientific Collaboration. The path to the enhanced and advanced LIGO gravitational-wave detectors. Classical and Quantum Gravity, 26(11):114013, June 2009. 1.3.2

[70] G. M. Harry and LIGO Scientific Collaboration. Advanced LIGO: the next generation of gravitational wave detectors. Classical and Quantum Gravity, 27(8):084006, April 2010. 1.3.2, 1.6

[71] F Acernese, M Alshourbagy, P Amico, et al. Status of virgo. Classical and Quantum Gravity, 25(11):114045, 2008. 1.3.2

[72] F. Acernese, M. Agathos, K. Agatsuma, et al. Advanced Virgo: a second-generation interferometric gravitational wave detector. Classical and Quantum Gravity, 32(2):024001, January 2015. 1.3.2

[73] T. Accadia, F. Acernese, M. Alshourbagy, et al. Virgo: a laser interferometer to detect gravitational waves. Journal of Instrumentation, 7:3012, March 2012. 1.3.2

[74] M. Razzano. A very exciting ligo-virgo observing run draws to a close on the 25th august. Virgo Press Release. Accessed: 2018-06-20. 1.3.2

[75] B. Willke, P. Aufmuth, C. Aulbert, et al. The GEO 600 gravitational wave detector. Classical and Quantum Gravity, 19:1377–1387, April 2002. 1.3.2

[76] C Affeldt, K Danzmann, K L Dooley, et al. Advanced techniques in geo 600. Classical and Quantum Gravity, 31(22):224002, 2014. 1.3.2

[77] Y. Aso, Y. Michimura, K. Somiya, et al. Interferometer design of the KAGRA gravitational wave detector. Physical Review D, 88(4):043007, August 2013. 1.3.2

[78] K Kuroda, M Ohashi, S Miyoki, et al. Japanese large-scale interferometers. Classical and Quantum Gravity, 19(7):1237, 2002. 1.3.2

[79] H. Ward, J. Hough, G. P. Newton, et al. Laser interferometric sensing techniques for very small displacements - with applications to gravitational radiation detectors. IEEE Transactions on Instrumentation Measurement, 34:261–265, 1985. 1.3.2

[80] A. Abramovici, W. Althouse, J. Camp, et al. Improved sensitivity in a gravitational wave interferometer and implications for LIGO. Physics Letters A, 218:157–163, February 1996. 1.3.2

[81] K. Kawabe, S. Nagataki, M. Ando, et al. Demonstration of a recombined Fabry-Perot-Michelson interferometer with suspended mirrors. Applied Physics B: Lasers and Optics, 62:135–138, February 1996. 1.3.2

[82] A. Perot and C. Fabry. On the Application of Interference Phenomena to the Solution of Various Problems of Spectroscopy and Metrology. The Astrophysical Journal, 9:87, February 1899. 1.3.2, 1.3.2

[83] J Levine and JL Hall. Design and operation of a methane absorption stabilized laser strainmeter. Journal of Geophysical Research, 77(14):2595–2609, 1972. 1.3.2

[84] LIGO Scientific Collabration. Ligo instrument science white paper. LIGO-T1700231v2, 2017. 1.3.3, 1.3.4, 1.3.4

[85] S S Y Chua, B J J Slagmolen, D A Shaddock, and D E McClelland. Quantum squeezed light in gravitational-wave detectors. Classical and Quantum Gravity, 31(18):183001, 2014. 1.3.3

[86] LIGO Scientific Collabration. Ligo voyager upgrade concept. LIGO-M1100296-v2, 2011. 1.3.3

[87] LIGO Scientific Collabration. Ligo instrument science white paper. LIGO-T1400226v8, 2017. 1.3.3

[88] LIGO Scientific Collabration. Ligo-india, proposal of the consortium for indian initiative in gravitational-wave observations (indigo). M1100296-v2, 2017. 1.3.3

[89] J. Veitch, I. Mandel, B. Aylott, et al. Estimating parameters of coalescing compact binaries with proposed advanced detector networks. Physical Review D, 85(10):104045, May 2012. 1.3.3, 3

[90] David Blair, Li Ju, ChunNong Zhao, et al. The next detectors for gravitational wave astronomy. Science China Physics, Mechanics & Astronomy, 58(12):120405, 2015. 1.3.3, 4, 4.4, 4.4.2

[91] C. K. Mishra, K. G. Arun, B. R. Iyer, and B. S. Sathyaprakash. Parametrized tests of post-Newtonian theory using Advanced LIGO and Einstein Telescope. Physical Review D, 82(6):064010, September 2010. 1.3.4

[92] N. Yunes. Gravitational Waves from Compact Binaries as Probes of the Universe. In Resceu Symposium on General Relativity and Gravitation, (JGRG21), held September 26-29, 2011, at Tohoku University, Sendai, Japan, p.124, page 124, April 2012. 1.3.4

[93] N. Cornish, L. Sampson, N. Yunes, and F. Pretorius. Gravitational wave tests of general relativity with the parameterized post-Einsteinian framework. Physical Review D, 84(6):062003, September 2011. 1.3.4

[94] B. Sathyaprakash, M. Abernathy, F. Acernese, et al. Scientific objectives of Einstein Telescope. Classical and Quantum Gravity, 29(12):124013, June 2012. 1.3.4, 1.4.1

[95] P. Amaro-Seoane and L. Santamaría. Detection of IMBHs with Ground-based Gravitational Wave Observatories: A Biography of a Binary of Black Holes, from Birth to Death. The Astrophysical Journal, 722:1197–1206, October 2010. 1.3.4

[96] D. Keppel and P. Ajith. Constraining the mass of the graviton using coalescing black-hole binaries. Physical Review D, 82(12):122001, December 2010. 1.3.4

[97] K. G. Arun and C. M. Will. Bounding the mass of the graviton with gravitational waves: effect of higher harmonics in gravitational waveform templates. Classical and Quantum Gravity, 26(15):155002, August 2009. 1.3.4

[98] J. R. Gair, I. Mandel, M. C. Miller, and M. Volonteri. Exploring intermediate and massive black-hole binaries with the Einstein Telescope. General Relativity and Gravitation, 43:485–518, February 2011. 1.3.4

[99] T. Regimbau, T. Dent, W. Del Pozzo, et al. A Mock data challenge for the Einstein Gravitational-Wave Telescope. Physical Review D, 86(12):122001, December 2012. 1.10, 1.3.4

[100] A. Freise, S. Chelkowski, S. Hild, et al. Triple Michelson interferometer for a third-generation gravitational wave detector. Classical and Quantum Gravity, 26(8):085012, April 2009. 1.3.4

[101] S. Hild, S. Chelkowski, and A. Freise. Pushing towards the ET sensitivity using 'conventional' technology. ArXiv e-prints, October 2008. 1.3.4

[102] S Hild, M Abernathy, F Acernese, et al. Sensitivity studies for third-generation gravitational wave observatories. Classical and Quantum Gravity, 28(9):094013, May 2011. 1.3.4, 1.4.1, 4

[103] S. Hild, S. Chelkowski, A. Freise, et al. A xylophone configuration for a third-generation gravitational wave detector. Classical and Quantum Gravity, 27(1):015003, January 2010. 1.3.4

[104] K. Danzmann and LISA study Team. LISA: laser interferometer space antenna for gravitational wave measurements. Classical and Quantum Gravity, 13:A247–A250, November 1996. 1.3.5, 1.3.5

[105] P. Amaro-Seoane, H. Audley, S. Babak, et al. Laser Interferometer Space Antenna. ArXiv e-prints, February 2017. 1.11, 1.4.1

[106] T. Robson, N. Cornish, and C. Liu. The construction and use of LISA sensitivity curves. ArXiv e-prints, March 2018. 1.12

[107] E. J. Buis, S. Oemrawsingh, and G. Vacanti. Simulation of cosmological stochastic background in LISA. In Journal of Physics Conference Series, volume 154 of Journal of Physics Conference Series, page 012046, March 2009. 1.3.5

[108] M. Pitkin, S. Reid, S. Rowan, and J. Hough. Gravitational Wave Detection by Interferometry (Ground and Space). Living Reviews in Relativity, 14:5, July 2011. 1.3.5, 1.4.1, 1.4.2, 1.4.4

[109] M. Armano, H. Audley, G. Auger, et al. Sub-Femto-g Free Fall for Space-Based Gravitational Wave Observatories: LISA Pathfinder Results. Physical Review Letters, 116(23):231101, June 2016. 1.3.5

[110] P McNamara, S Vitale, K Danzmann, and on behalf of the LISA Pathfinder Science Working Team. Lisa pathfinder. Classical and Quantum Gravity, 25(11):114034, 2008. 1.3.5

[111] M Punturo, M Abernathy, F Acernese, et al. The Einstein Telescope: a third-generation gravitational wave observatory. Classical and Quantum Gravity, 27(19):194002, October 2010. 1.4

[112] S. A. Hughes and K. S. Thorne. Seismic gravity-gradient noise in interferometric gravitational-wave detectors. Physical Review D, 58(12):122002, December 1998. 1.4.1

[113] M. Beccaria, M. Bernardini, S. Braccini, et al. Relevance of Newtonian seismic noise for the VIRGO interferometer sensitivity. Classical and Quantum Gravity, 15:3339–3362, November 1998. 1.4.1, 1.4.2

[114] K. S. Thorne and C. J. Winstein. Human gravity-gradient noise in interferometric gravitational-wave detectors. Physical Review D, 60(8):082001, October 1999. 1.4.1

[115] M. G. Beker, G. Cella, R. Desalvo, et al. Improving the sensitivity of future GW observatories in the 1-10 Hz band: Newtonian and seismic noise. General Relativity and Gravitation, 43:623–656, February 2011. 1.4.1

[116] T. Creighton. Tumbleweeds and airborne gravitational noise sources for LIGO. Classical and Quantum Gravity, 25(12):125011, June 2008. 1.4.1

[117] E. J. Daw, J. A. Giaime, D. Lormand, M. Lubiński, and J. Zweizig. Long-term study of the seismic environment at LIGO. Classical and Quantum Gravity, 21:2255–2273, May 2004. 1.4.2

[118] Susana Custódio, Nuno A Dias, Bento Caldeira, et al. Ambient noise recorded by a dense broadband seismic deployment in western iberia. Bulletin of the Seismological Society of America, 104(6):2985–3007, 2014. 1.4.2

[119] P Saulson. Fundamentals of interferometric gravitational wave detectors,(1994). 1.4.2

[120] LIGO Scientific Collaboration, J. Aasi, B. P. Abbott, et al. Advanced LIGO. Classical and Quantum Gravity, 32(7):074001, April 2015. 1.4.2

[121] K. Somiya. Detector configuration of KAGRA-the Japanese cryogenic gravitational-wave detector. Classical and Quantum Gravity, 29(12):124007, June 2012. 1.4.2

[122] MV Plissi, CI Torrie, ME Husman, et al. Geo 600 triple pendulum suspension system: Seismic isolation and control. Review of scientific instruments, 71(6):2539–2545, 2000. 1.4.2

[123] S. Braccini, L. Barsotti, C. Bradaschia, et al. Measurement of the seismic attenuation performance of the VIRGO Superattenuator. Astroparticle Physics, 23:557–565, July 2005. 1.4.2

[124] F. Matichard, B. Lantz, R. Mittleman, et al. Seismic isolation of Advanced LIGO: Review of strategy, instrumentation and performance. Classical and Quantum Gravity, 32(18):185003, September 2015. 1.4.2

[125] AS Nowick and BS Berry. Anelastic relaxation in crystalline solids (academic, new york, 1972). Google Scholar, page 677, 1945. 1.4.3

[126] Jim Hough, Sheila Rowan, and B S Sathyaprakash. The search for gravitational waves. Journal of Physics B: Atomic, Molecular and Optical Physics, 38(9):S497, 2005. 1.4.3

[127] J.-Q. Fang and X.-H. Yu. A New Type of Cascading Synchronization for Halo-Chaos and Its Potential for Communication Applications. Chinese Physics Letters, 21:1429–1432, August 2004. 1.4.3

[128] Werner Heisenberg. Über den anschaulichen inhalt der quantentheoretischen kinematik und mechanik. In Original Scientific Papers Wissenschaftliche Originalarbeiten, pages 478–504. Springer, 1985. 1.4.4

[129] W. A. Edelstein, J. Hough, J. R. Pugh, and W. Martin. Limits to the measurement of displacement in an interferometric gravitational radiation detector. Journal of Physics E Scientific Instruments, 11:710, July 1978. 1.4.4

[130] B. P. Abbott, R. Abbott, T. D. Abbott, et al. Observation of Gravitational Waves from a Binary Black Hole Merger. Physical Review Letters, 116(6):061102, February 2016. 1.1, 1.5, 1.14, 2.2, 2.4, 2.4

[131] B. P. Abbott, R. Abbott, T. D. Abbott, et al. GW151226: Observation of Gravitational Waves from a 22-Solar-Mass Binary Black Hole Coalescence. Physical Review Letters, 116(24):241103, June 2016. 1.1, 1.5, 2.2, 2.4

[132] B. P. Abbott, R. Abbott, T. D. Abbott, et al. GW170104: Observation of a 50-Solar-Mass Binary Black Hole Coalescence at Redshift 0.2. Physical Review Letters, 118(22):221101, June 2017. 1.1, 1.5

[133] B. P. Abbott, R. Abbott, T. D. Abbott, et al. GW170608: Observation of a 19 Solar-mass Binary Black Hole Coalescence. The Astrophysical Journal Letters, 851:L35, December 2017. 1.1, 1.5

[134] B. P. Abbott, R. Abbott, T. D. Abbott, et al. GW170814: A Three-Detector Observation of Gravitational Waves from a Binary Black Hole Coalescence. Physical Review Letters, 119(14):141101, October 2017. 1.1, 1.15, 1.5, 2.2, 4

[135] B. P. Abbott, R. Abbott, T. D. Abbott, et al. GW170817: Observation of Gravitational Waves from a Binary Neutron Star Inspiral. Physical Review Letters, 119(16):161101, October 2017. 1.5, 2, 2.2, 2.2.1, 4, 4.3.1

[136] B. P. Abbott, R. Abbott, T. D. Abbott, et al. Multi-messenger Observations of a Binary Neutron Star Merger. Astrophysical Journal Letters, 848:L12, October 2017. 1.5, 2, 2.1, 2.2.1, 2.1, 2.3.1, 2.3.2, 2.3.3, 2.3, 2.4

[137] L. S. Finn. Detection, measurement, and gravitational radiation. Physical Review D, 46:5236–5249, December 1992. 1.6

[138] P. Jaranowski and A. Królak. Gravitational-Wave Data Analysis. Formalism and Sample Applications: The Gaussian Case. Living Reviews in Relativity, 15:4, March 2012. 1.6.1, 1.6.1, 1.6.1, 1.6.3

[139] J. Abadie, B. P. Abbott, R. Abbott, et al. First low-latency LIGO+Virgo search for binary inspirals and their electromagnetic counterparts. Astronomy & Astrophysics, 541:A155, May 2012. 1.6.1, 2

[140] S. Babak, R. Biswas, P. R. Brady, et al. Searching for gravitational waves from binary coalescence. Physical Review D, 87(2):024033, January 2013. 1.6.1

[141] L. Wen and B. F. Schutz. Coherent network detection of gravitational waves: the redundancy veto. Classical and Quantum Gravity, 22:S1321–S1335, September 2005. 1.6.1

[142] J. Veitch, V. Raymond, B. Farr, et al. Parameter estimation for compact binaries with ground-based gravitational-wave observations using the LALInference software library. Physical Review D, 91(4):042003, February 2015. 1.6.1, 2.2.3, 2.2.4, 3.1.1, 3.2

[143] B. Farr, V. Kalogera, and E. Luijten. A more efficient approach to parallel-tempered Markov-chain MonteÂ Carlo for the highly structured posteriors of gravitational-wave signals. Physical Review D, 90(2):024014, July 2014. 1.6.1

[144] Devinderjit Sivia and John Skilling. Data analysis: a Bayesian tutorial. OUP Oxford, 2006. 1.6.2, 1.6.2

[145] Phil Gregory. Bayesian Logical Data Analysis for the Physical Sciences: A Comparative Approach with Mathematica® Support. Cambridge University Press, 2005. 1.6.2

[146] R. Balasubramanian, B. S. Sathyaprakash, and S. V. Dhurandhar. Gravitational waves from coalescing binaries: Detection strategies and Monte Carlo estimation of parameters. Physical Review D, 53:3033–3055, March 1996. 1.6.3

[147] S. Fairhurst. Triangulation of gravitational wave sources with a network of detectors. New Journal of Physics, 11(12):123006, December 2009. 1.6.3, 4.3.3, 4.4, C

[148] P. Ajith and S. Bose. Estimating the parameters of nonspinning binary black holes using ground-based gravitational-wave detectors: Statistical errors. Physical Review D, 79(8):084032, April 2009. 1.6.3

[149] Linqing Wen and Yanbei Chen. Geometrical expression for the angular resolution of a network of gravitational-wave detectors. Physical Review D, 81(8):082001, 2010. 1.6.3, 4.4, 4.4.1, 4.4.1, C

[150] B. P. Abbott, R. Abbott, T. D. Abbott, et al. Prospects for Observing and Localizing Gravitational-Wave Transients with Advanced LIGO and Advanced Virgo. Living Reviews in Relativity, 19:1, February 2016. 1.6.3, 2.2, 4

[151] Stephen Fairhurst. Source localization with an advanced gravitational wave detector network. Classical and Quantum Gravity, 28(10):105021, 2011. 1.6.3, 3, 4, 4.3.1, 4.4, 4.4, C

[152] C. Cutler and É. E. Flanagan. Gravitational waves from merging compact binaries: How accurately can one extract the binary's parameters from the inspiral waveform\? Physical Review D, 49:2658–2697, March 1994. 1.6.3

[153] A. Królak, K. D. Kokkotas, and G. Schäfer. Estimation of the post-Newtonian parameters in the gravitational-wave emission of a coalescing binary. Physical Review D, 52:2089–2111, August 1995. 1.6.3

[154] R. Balasubramanian, B. S. Sathyaprakash, and S. V. Dhurandhar. Estimation of parameters of gravitational waves from coalescing binaries. Pramana, 45:L463–L470, November 1995. 1.6.3

[155] M. Vallisneri. Use and abuse of the Fisher information matrix in the assessment of gravitational-wave parameter-estimation prospects. Physical Review D, 77(4):042001, February 2008. 1.6.3

[156] M. Zanolin, S. Vitale, and N. Makris. Application of asymptotic expansions for maximum likelihood estimators errors to gravitational waves from binary mergers: The single interferometer case. Physical Review D, 81(12):124048, June 2010. 1.6.3

[157] H.-S. Cho and C.-H. Lee. Application of the effective Fisher matrix to the frequency domain inspiral waveforms. Classical and Quantum Gravity, 31(23):235009, December 2014. 1.6.3

[158] J. S. Bloom, D. E. Holz, S. A. Hughes, and K. Menou. Coordinated Science in the Gravitational and Electromagnetic Skies. In astro2010: The Astronomy and Astrophysics Decadal Survey, volume 2010 of Astronomy, 2009. 2

[159] D. A. Coulter, R. J. Foley, C. D. Kilpatrick, et al. Swope Supernova Survey 2017a (SSS17a), the optical counterpart to a gravitational wave source. Science, 358:1556–1558, December 2017. 2, 2.3.2

[160] M. Soares-Santos, D. E. Holz, J. Annis, et al. The Electromagnetic Counterpart of the Binary Neutron Star Merger LIGO/Virgo GW170817. I. Discovery of the Optical Counterpart Using the Dark Energy Camera. The Astrophysical Journal Letters, 848:L16, October 2017. 2, 2.3.2, 2.3.3, 5.2

[161] S. Valenti, David, J. Sand, et al. The Discovery of the Electromagnetic Counterpart of GW170817: Kilonova AT 2017gfo/DLT17ck. The Astrophysical Journal Letters, 848:L24, October 2017. 2, 2.3.2, 5.1, 5.1

[162] V. M. Lipunov, E. Gorbovskoy, V. G. Kornilov, et al. MASTER Optical Detection of the First LIGO/Virgo Neutron Star Binary Merger GW170817. The Astrophysical Journal Letters, 850:L1, November 2017. 2, 2.3.2

[163] I. Arcavi, G. Hosseinzadeh, D. A. Howell, et al. Optical emission from a kilonova following a gravitational-wave-detected neutron-star merger. Nature, 551:64–66, November 2017. 2, 2.3.2, 5.1, 5.1

[164] BP Abbott, R Abbott, TD Abbott, et al. Gravitational waves and gamma-rays from a binary neutron star merger: Gw170817 and grb 170817a. The Astrophysical Journal Letters, 848(2):L13, 2017. 2

[165] R. Margutti, E. Berger, W. Fong, et al. The Electromagnetic Counterpart of the Binary Neutron Star Merger LIGO/Virgo GW170817. V. Rising X-Ray Emission from an Off-axis Jet. The Astrophysical Journal Letters, 848:L20, October 2017. 2, 2.3.2

[166] A Goldstein, P Veres, E Burns, et al. An ordinary short gamma-ray burst with extraordinary implications: Fermi-gbm detection of grb 170817a. The Astrophysical Journal Letters, 848(2):L14, 2017. 2, 2.3.1

[167] NR Tanvir, AJ Levan, C Gonzalez-Fernandez, et al. The Emergence of a Lanthanide-rich Kilonova Following the Merger of Two Neutron Stars. The Astrophysical Journal Letters, 848:L27, October 2017. 2, 2.3.2, 3, 5.1, 5.1

[168] E. Chassande-Mottin, M. Hendry, P. J. Sutton, and S. Márka. Multimessenger astronomy with the Einstein Telescope. General Relativity and Gravitation, 43:437–464, February 2011. 2, 2.3.3, 2.3.4

[169] J. Kanner, T. L. Huard, S. Márka, et al. LOOC UP: locating and observing optical counterparts to gravitational wave bursts. Classical and Quantum Gravity, 25(18):184034, September 2008. 2

[170] C. D. Ott. Probing the core-collapse supernova mechanism with gravitational waves. Classical and Quantum Gravity, 26(20):204015, October 2009. 2

[171] Neal Dalal, Daniel E Holz, Scott A Hughes, and Bhuvnesh Jain. Short grb and binary black hole standard sirens as a probe of dark energy. Physical Review D, 74(6):063006, 2006. 2

[172] Bernard F Schutz. Determining the hubble constant from gravitational wave observations. Nature, 323(6086):310–311, 1986. 2, 4

[173] B. S. Sathyaprakash, B. F. Schutz, and C. Van Den Broeck. Cosmography with the Einstein Telescope. Classical and Quantum Gravity, 27(21):215006, November 2010. 2

[174] B. P. Abbott, R. Abbott, T. D. Abbott, et al. A gravitational-wave standard siren measurement of the Hubble constant. Nature, 551:85–88, November 2017. 2

[175] B. Abbott, R. Abbott, R. Adhikari, et al. Implications for the Origin of GRB 070201 from LIGO Observations. The Astrophysical Journal, 681:1419–1430, July 2008. 2

[176] B. Abbott, R. Abbott, R. Adhikari, et al. Search for gravitational waves associated with 39 gamma-ray bursts using data from the second, third, and fourth LIGO runs. Physical Review D, 77(6):062004, March 2008. 2

[177] J. Abadie, B. P. Abbott, R. Abbott, et al. Search for Gravitational-wave Inspiral Signals Associated with Short Gamma-ray Bursts During LIGO's Fifth and Virgo's First Science Run. The Astrophysical Journal, 715:1453–1461, June 2010. 2

[178] J. Abadie, B. P. Abbott, T. D. Abbott, et al. Implications for the Origin of GRB 051103 from LIGO Observations. The Astrophysical Journal, 755:2, August 2012. 2

[179] J. Abadie, B. P. Abbott, R. Abbott, et al. Search for Gravitational Waves Associated with Gamma-Ray Bursts during LIGO Science Run 6 and Virgo Science Runs 2 and 3. The Astrophysical Journal, 760:12, November 2012. 2

[180] J. Aasi, J. Abadie, B. P. Abbott, et al. Search for long-lived gravitational-wave transients coincident with long gamma-ray bursts. Physical Review D, 88(12):122004, December 2013. 2

[181] J. Aasi, B. P. Abbott, R. Abbott, et al. Methods and results of a search for gravitational waves associated with gamma-ray bursts using the GEO 600, LIGO, and Virgo detectors. Physical Review D, 89(12):122004, June 2014. 2

[182] J. Aasi, B. P. Abbott, R. Abbott, et al. Search for Gravitational Waves Associated with γ-ray Bursts Detected by the Interplanetary Network. Physical Review Letters, 113(1):011102, July 2014. 2

[183] B. Abbott, R. Abbott, R. Adhikari, et al. Search for Gravitational-Wave Bursts from Soft Gamma Repeaters. Physical Review Letters, 101(21):211102, November 2008. 2

[184] J. Abadie, B. P. Abbott, R. Abbott, et al. Search for Gravitational Wave Bursts from Six Magnetars. The Astrophysical Journal Letters, 734:L35, June 2011. 2

[185] J. Abadie, B. P. Abbott, R. Abbott, et al. Search for gravitational waves associated with the August 2006 timing glitch of the Vela pulsar. Physical Review D, 83(4):042001, February 2011. 2

[186] J. Aasi, B. P. Abbott, R. Abbott, et al. Searches for Continuous Gravitational Waves from Nine Young Supernova Remnants. The Astrophysical Journal, 813:39, November 2015. 2

[187] LIGO Scientific Collaboration, Virgo Collaboration, J. Abadie, et al. Implementation and testing of the first prompt search for gravitational wave transients with electromagnetic counterparts. Astronomy & Astrophysics, 539:A124, April 2012. 2

[188] P. A. Evans, J. K. Fridriksson, N. Gehrels, et al. Swift Follow-up Observations of Candidate Gravitational-wave Transient Events. The Astrophysical Journal Letters, 203:28, December 2012. 2

[189] J. Aasi, J. Abadie, B. P. Abbott, et al. First Searches for Optical Counterparts to Gravitational-wave Candidate Events. The Astrophysical Journal Letters, 211:7, March 2014. 2

[190] B. P. Abbott, R. Abbott, T. D. Abbott, et al. Localization and Broadband Follow-up of the Gravitational-wave Transient GW150914. The Astrophysical Journal Letters, 826:L13, July 2016. 2, 2.1, 2.2.2, 2.2.3, 2.2.4, 2.4, 4.3.2

[191] M. Yoshida, Y. Utsumi, N. Tominaga, et al. J-GEM follow-up observations of the gravitational wave source GW151226*. Publications of the Astronomical Society of Japan, 69:9, February 2017. 2

[192] The LIGO Scientific Collaboration, the Virgo Collaboration, B. P. Abbott, et al. Full Band All-sky Search for Periodic Gravitational Waves in the O1 LIGO Data. ArXiv e-prints, February 2018. 2

[193] B. P. Abbott, R. Abbott, T. D. Abbott, et al. All-sky search for periodic gravitational waves in the O1 LIGO data. Physical Review D, 96(6):062002, September 2017. 2

[194] B. Abbott, R. Abbott, R. Adhikari, et al. All-sky search for periodic gravitational waves in LIGO S4 data. Physical Review D, 77(2):022001, January 2008. 2

[195] J Aasi. Open call for partnership for the em identification and follow-up of gw candidate events, ligo m1300550-v3. Technical report, VIR-0494E-13,(LIGO, Pasadena, CA, 2013). URL (accessed 25 September 2015): https://dcc. ligo. org/LIGO-M1300550-v8/public.(Cited on page 6.). 2.1

[196] LIGO Scientific Collaboration and et al Virgo Collaboration. Ligo/virgo g298048: Fermi gbm trigger 524666471/170817529: Ligo/virgo identification of a possible gravitational-wave counterpart. GCN Circ, 21505, 2017. 2.1, 2.3.1

[197] LIGO Scientific Collaboration and et al Virgo Collaboration. Ligo/virgo g184098: Burst candidate in ligo engineering run data. GCN Circ, 18330, 2017. 2.1

[198] LIGO Scientific Collaboration and et al Virgo Collaboration. Ligo/virgo g211117: Identification of a gw cbc candidate. GCN Circ, 18728, 2017. 2.1

[199] LIGO Scientific Collaboration and et al Virgo Collaboration. Ligo/virgo g268556: Identification of a gw cbc candidate. GCN Circ, 20364, 2017. 2.1

[200] LIGO Scientific Collaboration and et al Virgo Collaboration. Ligo/virgo g288732: Identification of a gw binary merger candidate. GCN Circ, 21221, 2017. 2.1

[201] LIGO Scientific Collaboration and et al Virgo Collaboration. Ligo/virgo g297595: Identification of a gw binary merger candidate. GCN Circ, 21474, 2017. 2.1

[202] Y. Gürsel and M. Tinto. Near optimal solution to the inverse problem for gravitational-wave bursts. Physical Review D, 40:3884–3938, December 1989. 2.2, 4.4

[203] J. Veitch and A. Vecchio. Bayesian coherent analysis of in-spiral gravitational wave signals with a detector network. Physical Review D, 81(6):062003, March 2010. 2.2, 2.2.3, 4.4

[204] C. Röver, R. Meyer, and N. Christensen. Bayesian inference on compact binary inspiral gravitational radiation signals in interferometric data. Classical and Quantum Gravity, 23:4895–4906, August 2006. 2.2, 4.4

[205] Leo P. Singer, Larry R. Price, Ben Farr, et al. THE FIRST TWO YEARS OF ELECTROMAGNETIC FOLLOW-UP WITH ADVANCED LIGO AND VIRGO. The Astrophysical Journal, 795(2):105, October 2014. 2.2, 3, 3.2, 3.3

[206] B. D. Metzger and E. Berger. What is the Most Promising Electromagnetic Counterpart of a Neutron Star Binary Merger? The Astrophysical Journal, 746:48, February 2012. 2.2, 2.3.1, 2.2, 2.3.2, 2.3.3, 3

[207] Leo P Singer and Larry R Price. Rapid bayesian position reconstruction for gravitational-wave transients. Physical Review D, 93(2):024013, 2016. 2.2.1, 3.2, 3.6

[208] S. Klimenko, G. Vedovato, M. Drago, et al. Method for detection and reconstruction of gravitational wave transients with networks of advanced detectors. Physical Review D, 93(4):042004, February 2016. 2.2.2

[209] R. Essick, S. Vitale, E. Katsavounidis, G. Vedovato, and S. Klimenko. Localization of Short Duration Gravitational-wave Transients with the Early Advanced LIGO and Virgo Detectors. The Astrophysical Journal, 800:81, February 2015. 2.2.2, 2.2.3, 2.2.4

[210] V Necula, S Klimenko, and G Mitselmakher. Transient analysis with fast wilson-daubechies time-frequency transform. In Journal of Physics: Conference Series, volume 363, page 012032. IOP Publishing, 2012. 2.2.2

[211] S. Klimenko, I. Yakushin, A. Mercer, and G. Mitselmakher. A coherent method for detection of gravitational wave bursts. Classical and Quantum Gravity, 25(11):114029, June 2008. 2.2.2

[212] R. Lynch, S. Vitale, R. Essick, E. Katsavounidis, and F. Robinet. An information-theoretic approach to the gravitational-wave burst detection problem. ArXiv e-prints, November 2015. 2.2.3, 2.4

[213] Takamitsu Tanaka, Zoltán Haiman, and Kristen Menou. Witnessing the birth of a quasar. The Astronomical Journal, 140(2):642, 2010. 2.3

[214] R. Perna, D. Lazzati, and B. Giacomazzo. Short Gamma-Ray Bursts from the Merger of Two Black Holes. The Astrophysical Journal Letters, 821:L18, April 2016. 2.3

[215] X. Li, F.-W. Zhang, Q. Yuan, et al. Implications of the Tentative Association between GW150914 and a Fermi-GBM Transient. The Astrophysical Journal Letters, 827:L16, August 2016. 2.3

[216] B. Zhang. Mergers of Charged Black Holes: Gravitational-wave Events, Short Gamma-Ray Bursts, and Fast Radio Bursts. The Astrophysical Journal Letters, 827:L31, August 2016. 2.3

[217] Abraham Loeb. Electromagnetic counterparts to black hole mergers detected by ligo. The Astrophysical Journal Letters, 819(2):L21, 2016. 2.3

[218] B. J. Morsony, J. C. Workman, and D. M. Ryan. Modeling the Afterglow of the Possible Fermi-GBM event Associated with GW150914. The Astrophysical Journal Letters, 825:L24, July 2016. 2.3

[219] K. Murase, K. Kashiyama, P. Mészáros, I. Shoemaker, and N. Senno. Ultrafast Outflows from Black Hole Mergers with a Minidisk. The Astrophysical Journal Letters, 822:L9, May 2016. 2.3

[220] A. Janiuk, M. Bejger, S. Charzyński, and P. Sukova. On the possible gamma-ray burst-gravitational wave association in GW150914. New Astronomy, 51:7–14, February 2017. 2.3

[221] B. J. Kelly, J. G. Baker, Z. B. Etienne, B. Giacomazzo, and J. Schnittman. Prompt electromagnetic transients from binary black hole mergers. Physical Review D, 96(12):123003, December 2017. 2.3

[222] C. Kouveliotou, C. A. Meegan, G. J. Fishman, et al. Identification of two classes of gamma-ray bursts. The Astrophysical Journal Letters, 413:L101–L104, August 1993. 2.3.1

[223] E. Berger, D. B. Fox, P. A. Price, et al. A New Population of High-Redshift Short-Duration Gamma-Ray Bursts. The Astrophysical Journal, 664:1000–1010, August 2007. 2.3.1

[224] E. Berger, P. A. Price, S. B. Cenko, et al. The afterglow and elliptical host galaxy of the short γ-ray burst GRB 050724. Nature, 438:988–990, December 2005. 2.3.1

[225] A. M. Soderberg, E. Berger, M. Kasliwal, et al. The Afterglow, Energetics, and Host Galaxy of the Short-Hard Gamma-Ray Burst 051221a. The Astrophysical Journal, 650:261–271, October 2006. 2.3.1

[226] D. A. Frail, S. R. Kulkarni, R. Sari, et al. Beaming in Gamma-Ray Bursts: Evidence for a Standard Energy Reservoir. The Astrophysical Journal Letters, 562:L55–L58, November 2001. 2.3.1

[227] J. S. Bloom, D. A. Frail, and R. Sari. The Prompt Energy Release of Gamma-Ray Bursts using a Cosmological k-Correction. The Astronomical Journal, 121:2879–2888, June 2001. 2.3.1

[228] E. Berger, S. R. Kulkarni, and D. A. Frail. A Standard Kinetic Energy Reservoir in Gamma-Ray Burst Afterglows. The Astrophysical Journal, 590:379–385, June 2003. 2.3.1

[229] E. Nakar. Short-hard gamma-ray bursts. Physics Reports, 442:166–236, April 2007. 2.3.1, 2.3.3, 2.3.4

[230] O. Bromberg, E. Nakar, T. Piran, and R. Sari. Short versus Long and Collapsars versus Non-collapsars: A Quantitative Classification of Gamma-Ray Bursts. The Astrophysical Journal, 764:179, February 2013. 2.3.1

[231] E. Berger. Short-Duration Gamma-Ray Bursts. Annual Review of Astronomy and Astrophysics, 52:43–105, August 2014. 2.3.1

[232] N. Gehrels, C. L. Sarazin, P. T. O'Brien, et al. A short γ-ray burst apparently associated with an elliptical galaxy at redshift z = 0.225. Nature, 437:851–854, October 2005. 2.3.1

[233] J. X. Prochaska, J. S. Bloom, H.-W. Chen, et al. GRB 050724: secure host redshift from Keck. GRB Coordinates Network, 3700, 2005. 2.3.1

[234] D. B. Fox, D. A. Frail, P. A. Price, et al. The afterglow of GRB 050709 and the nature of the short-hard γ-ray bursts. Nature, 437:845–850, October 2005. 2.3.1

[235] J. Hjorth, D. Watson, J. P. U. Fynbo, et al. The optical afterglow of the short γ-ray burst GRB 050709. Nature, 437:859–861, October 2005. 2.3.1

[236] J. S. Villasenor, D. Q. Lamb, G. R. Ricker, et al. Discovery of the short γ-ray burst GRB 050709. Nature, 437:855–858, October 2005. 2.3.1

[237] J. Goodman. Are gamma-ray bursts optically thick? The Astrophysical Journal Letters, 308:L47–L50, September 1986. 2.3.1

[238] B. Paczynski. Gamma-ray bursters at cosmological distances. The Astrophysical Journal Letters, 308:L43–L46, September 1986. 2.3.1

[239] D. Eichler, M. Livio, T. Piran, and D. N. Schramm. Nucleosynthesis, neutrino bursts and gamma-rays from coalescing neutron stars. Nature, 340:126–128, July 1989. 2.3.1, 2.3.4

[240] R. Narayan, B. Paczynski, and T. Piran. Gamma-ray bursts as the death throes of massive binary stars. The Astrophysical Journal Letters, 395:L83–L86, August 1992. 2.3.1, 2.3.4

[241] S. Nissanke, M. Kasliwal, and A. Georgieva. Identifying Elusive Electromagnetic Counterparts to Gravitational Wave Mergers: An End-to-end Simulation. The Astrophysical Journal, 767:124, April 2013. 2.3.1, 2.3.2, 3, 3.5, 3.6, 4, 5

[242] C. Meegan, G. Lichti, P. N. Bhat, et al. The Fermi Gamma-ray Burst Monitor. The Astrophysical Journal, 702:791–804, September 2009. 2.3.1

[243] C. Meegan A. von Kienlin and A. Goldstein. Grb 170817a: Fermi gbm detection. GCN Circ, 21520, 2017. 2.3.1

[244] B.-B. Zhang, B. Zhang, H. Sun, et al. A peculiar low-luminosity short gamma-ray burst from a double neutron star merger progenitor. Nature Communications, 9:447, February 2018. 2.3.1

[245] A. H. Nitz, T. Dent, T. Dal Canton, S. Fairhurst, and D. A. Brown. Detecting Binary Compact-object Mergers with Gravitational Waves: Understanding and Improving the Sensitivity of the PyCBC Search. The Astrophysical Journal, 849:118, November 2017. 2.3.1

[246] V. Savchenko, C. Ferrigno, E. Kuulkers, et al. INTEGRAL Detection of the First Prompt Gamma-Ray Signal Coincident with the Gravitational-wave Event GW170817. The Astrophysical Journal Letter, 848:L15, October 2017. 2.3.1, 2.3.3

[247] L.-X. Li and B. Paczyński. Transient Events from Neutron Star Mergers. The Astrophysical Journal Letters, 507:L59–L62, November 1998. 2.3.2, 3

[248] S. R. Kulkarni. Modeling Supernova-like Explosions Associated with Gamma-ray Bursts with Short Durations. ArXiv Astrophysics e-prints, October 2005. 2.3.2

[249] S. Rosswog. Mergers of Neutron Star-Black Hole Binaries with Small Mass Ratios: Nucleosynthesis, Gamma-Ray Bursts, and Electromagnetic Transients. The Astrophysical Journal, 634:1202–1213, December 2005. 2.3.2

[250] BD Metzger, G Martínez-Pinedo, S Darbha, et al. Electromagnetic counterparts of compact object mergers powered by the radioactive decay of r-process nuclei. Monthly Notices of the Royal Astronomical Society, 406(4):2650–2662, 2010. 2.3.2

[251] D. Kasen, N. R. Badnell, and J. Barnes. Opacities and Spectra of the r-process Ejecta from Neutron Star Mergers. The Astrophysical Journal, 774:25, September 2013. 2.3.2

[252] Jennifer Barnes and Daniel Kasen. Effect of a high opacity on the light curves of radioactively powered transients from compact object mergers. The Astrophysical Journal, 775(1):18, 2013. 2.3.2, 3.1.1

[253] M. Tanaka and K. Hotokezaka. Radiative Transfer Simulations of Neutron Star Merger Ejecta. The Astrophysical Journal, 775:113, October 2013. 2.3.2

[254] L. Baiotti and L. Rezzolla. Binary neutron star mergers: a review of Einsteins richest laboratory. Reports on Progress in Physics, 80(9):096901, September 2017. 2.3.2

[255] M. Arnould, S. Goriely, and K. Takahashi. The r-process of stellar nucleosynthesis: Astrophysics and nuclear physics achievements and mysteries. Physics Reports, 450:97–213, September 2007. 2.3.2

[256] M. Branchesi. Multi-messenger astronomy: gravitational waves, neutrinos, photons, and cosmic rays. In Journal of Physics Conference Series, volume 718 of Journal of Physics Conference Series, page 022004, May 2016. 2.3.2, 2.3.4

[257] B. D. Metzger, A. Bauswein, S. Goriely, and D. Kasen. Neutron-powered precursors of kilonovae. Monthly Notices of the Royal Astronomical Society, 446:1115–1120, January 2015. 2.3.2

[258] Masaomi Tanaka, Kenta Hotokezaka, Koutarou Kyutoku, et al. Radioactively powered emission from black hole-neutron star mergers. The Astrophysical Journal, 780(1):31, 2014. 2.3.2

[259] Doron Grossman, Oleg Korobkin, Stephan Rosswog, and Tsvi Piran. The long-term evolution of neutron star merger remnants: Ii. radioactively powered transients. Monthly Notices of the Royal Astronomical Society, 439(1):757–770, 2014. 2.3.2

[260] N. R. Tanvir, A. J. Levan, A. S. Fruchter, et al. A 'kilonova' associated with the short-duration γ-ray burst GRB 130603B. Nature, 500:547–549, August 2013. 2.3.2, 3

[261] E. Berger, W. Fong, and R. Chornock. An r-process Kilonova Associated with the Short-hard GRB 130603B. The Astrophysical Journal Letters, 774:L23, September 2013. 2.3.2

[262] Bin Yang, Zhi-Ping Jin, Xiang Li, et al. A possible Macronova in the late afterglow of the 'long-short' burst GRB 060614. NATURE COMMUNICATIONS, 6:7323, 2015. 2.3.2

[263] Zhi-Ping Jin, Xiang Li, Zach Cano, et al. The light curve of the macronova associated with the long–short burst grb 060614. The Astrophysical Journal Letters, 811(2):L22, 2015. 2.3.2

[264] Zhi-Ping Jin, Kenta Hotokezaka, Xiang Li, et al. The 050709 macronova and the grb/macronova connection. arXiv preprint arXiv:1603.07869, 2016. 2.3.2

[265] M. R. Siebert R. J. Foley B. J. Shappee M. R. Drout J. S. Simon A. L. Piro D. A. Coulter, C. D. Kilpatrick and A. Rest. Ligo/virgo g298048: Potential optical counterpart discovered by swope telescope. GCN Circ, 21529, 2017. 2.3.2

[266] E. Berger D. J. Brout D. Brown R. E. Butler H.-Y. Chen R. Chornock E. Cook P. Cowperthwaite H. T. Diehl A. Drlica-Wagner M. R. Drout R. J. Foley W. Fong D. Fox J. Frieman R. Gruendl K. Herner D. Holz R. Kessler R. Margutti J. Marshall E. Neilsen M. Nicholl F. Paz-Chincon A. Rest M. Sako D. Scolnic N. Smith M. Soares-Santos D. Tucker V. A. Villar P. K. G. Williams B. Yanny S. Allam, J. Annis. Ligo/virgo g298048: Decam optical candidate. GCN Circ, 21530, 2017. 2.3.2

[267] et al. N. R. Tanvir, A. J. Levan. Ligo/virgo g298048: Vista/vircam detection of candidate counterpart. GCN Circ, 21544, 2017. 2.3.2

[268] C. McCully G. Hosseinzadeh S. Vasylyev M. Zalzman D. Poznanski (TAU) L.P. Singer (NASA/GSFC) S. Valenti (UC Davis) T. Piran (HUJI) D. Kasen-J. Barnes (UC Berkeley) I. Arcavi, D. A. Howell, Valenti et al. (LVC GCN 21531) W-f. Fong (UA) report an independent detection of the possible optical counterpart reported by Coulter et al. (LVC GCN 21529), Chornock et al. (LVC GCN 21530), and Melandri et al. (LVC GCN 21532). Ligo/virgo g298048: Las cumbres observatory detection of the possible optical counterpart in ngc 4993. GCN Circ, 21538, 2017. 2.3.2

[269] David Sand Leonardo Tartaglia Enrico Cappellaro Dan Reichart Josh Haislip Vladimir Kouprianov Sheng Yang, Stefano Valenti. Ligo/virgo g298048: Dlt40 optical candidate. GCN Circ, 21531, 2017. 2.3.2

[270] V.G.Kornilov N.Tyurina V.Shumkov D.Kuvshinov P.Balanutsa O.Gress A.Kuznetsov M.I.Panchenko A.V.Krylov I.Gorbunov V.M. Lipunov, E. Gorbovskoy. Ligo/virgo g298048: Master observations of the ngc 4993. GCN Circ, 21546, 2017. 2.3.2

[271] J. Hjorth D. J. Watson L. Amati L. A. Antonelli S. Ascenzi S. Benetti M.T. Botticella M. Branchesi (GSSI) S. Campana (INAF-OAB) E. Cappellaro (INAF-OAPD) S. Covino (INAF-OAB) P. D'Avanzo (INAF-OAB) V. D'Elia (INAF-ASDC) D. Fugazza (INAF-OAB) F. Getman (INAF-OAC) A. Grado (INAF-OAC) G. Greco (Urbino University/INFN Firenze) L. Limatola (INAF-OAC) M. Lisi (INAF-OAR) A. Melandri (INAF-OAB) L. Nicastro (INAF-IASF Bo) E. Palazzi (INAF-IAFS Bo) S. Piranomonte (INAF-OAR) L. Pulone (INAF-OAR) A. Rossi (INAF-IASF Bo) P. Schipani (INAF-OAC) G. Stratta (Urbino University/INFN Firenze) G. Tagliaferri (INAF-OAB) V. Testa (INAF-OAR) L. Tomasella (INAF-OAPD) S. Yang (INAF-OAPD) E. Brocato (INAF-OAR) on behalf of GRavitational Wave Inaf TeAm report: D. Malesani, E. Pian. Ligo/virgo g298048: Not near-infrared observations of sss17a. GCN Circ, 21591, 2017. 2.3.2

[272] P. A. Evans, S. B. Cenko, J. A. Kennea, et al. Swift and NuSTAR observations of GW170817: Detection of a blue kilonova. Science, 358:1565–1570, December 2017. 2.3.2, 2.3.3

[273] M. M. Kasliwal D. Cook S. Bradley Cenko J. Cannizzo S. Nissanke L. P. Singer, R. Lau and I. Arcavi. Ligo/virgo g298048: Gemini-south near-infrared photometry of the optical transient candidate. GCN Circ, 21552, 2017. 2.3.2

[274] B. J. Shappee K. Boutsia J. Bravo G. Prieto D. A. Coulter R. J. Foley C. D. Kilpatrick M. R. Siebert M. R. Drout, J. D. Simon and A. L. Piro. Ligo/virgo g298048: Magellan optical spectrum of the potential optical counterpart associated with ngc 4993. GCN Circ, 21547, 2017. 2.3.2

[275] M. R. Drout D. A. Coulter R. J. Foley C. D. Kilpatrick M. R. Siebert K. Boutsia J. Bravo G. Prieto J. D. Simon, B. J. Shappee and A. L. Piro. Ligo/virgo g298048: Magellan g-band imaging of the potential optical counterpart associated with ngc 4993. GCN Circ, 21551, 2017. 2.3.2

[276] S. Campana S. Covino (INAF-OAB) G. Greco M. Branchesi D. Fugazza L. Amati L. A. Antonelli S. Ascenzi M.T. Botticella E. Cappellaro V. D'Elia F. Getman A. Grado L. Limatola M. Lisi L. Nicastro E. Palazzi E. Pian S. Piranomonte (INAF-OAR) L. Pulone (INAF-OAR) A. Rossi (INAF-IASF Bo) G. Stratta (Urbino University/INFN Firenze) G. Tagliaferri (INAF-OAB) V. Testa (INAF-OAR) L . Tomasella (INAF-OAPD) S. Yang (INAF-OAPD) E. Brocato (INAF-OAR) on behalf of GRavitational Wave Inaf TeAm report: A. Melandri, P. D'Avanzo. Ligo/virgo g298048: Rem optical/nir observations. GCN Circ, 21556, 2017. 2.3.2

[277] M. M. Kasliwal, E. Nakar, L. P. Singer, et al. Illuminating gravitational waves: A concordant picture of photons from a neutron star merger. Science, 358:1559–1565, December 2017. 2.3.2, 5.1, 5.1

[278] D. N. Burrows, J. E. Hill, J. A. Nousek, et al. The Swift X-Ray Telescope. Space Science Reviews, 120:165–195, October 2005. 2.3.2

[279] A. A. Breeveld S. Campana S.B. Cenko E. Troja P.T. O'Brien (U. Leicester) S.D. Barthelmy (NASA/GSFC) A.P. Beardmore (U. Leicester) D.N. Burrows (PSU) G. Cusumano (INAF-IASF PA) A. D'Ai (INAF-IASFPA) P. D'Avanzo (INAF-OAB) V.D'Elia(ASDC) S.W.K. Emery (UCL-MSSL)-P. Giommi (ASI) C. Gronwall (PSU) H.A. Krimm (CRESST/GSFC/USRA) N.P.M. Kuin (UCL-MSSL) A.Y. Lien (GSFC/UMBC) F.E. Marshall (NASA/GSFC) A. Melandri (INAF-OAB) J.A. Nousek (PSU) S.R. Oates (U. Warwick) J.P. Osborne (U. Leicester) C. Pagani (U. Leicester) K.L. Page (U.Leicester) D.M. Palmer (LANL) M. Perri (ASDC)-J.L. Racusin (NASA/GSFC) B. Sbarufatti (INAF-OAB/PSU) M.H. Siegel (PSU) G. Tagliaferri (INAF-OAB) P. A. Evans, J.A. Kennea and A. Tohuvavohu (PSU). Ligo/virgo g298048: Swift uvot detection and xrt upper limits. GCN Circ, 21550, 2017. 2.3.2, 2.3.3

[280] M. M. Kasliwal S. M. Adams and N. Blagorodnova. Ligo/virgo g298048: Precise position of sss17a based on hst and gaia. GCN Circ, 21816, 2017. 2.3.2

[281] P. S. Cowperthwaite, E. Berger, V. A. Villar, et al. The Electromagnetic Counterpart of the Binary Neutron Star Merger LIGO/Virgo GW170817. II. UV, Optical, and Near-infrared Light Curves and Comparison to Kilonova Models. The Astrophysical Journal Letters, 848:L17, October 2017. 2.3.2, 5.1, 5.1

[282] K. W. Smith S. J. Smartt D. R. Young M. Coughlin T.-W. Chen J. Bulger L. Denneau H. Flewelling A. Heinze E. Kankare T. Lowe E. A. Magnier A. Rest B. Stalder A. S. B. Schultz C. W. Stubbs-J. Tonry C. Waters R. J. Wainscoat H. Weiland M. Willman (IfA)-D. E. Wright (QUB) K. C. Chambers, M. E. Huber. Ligo/virgo g298048: Pan-starrs izy photometry monitoring of sss17a/dlt17ck. GCN Circ, 21617, 2017. 2.3.2

[283] Yoshida M. Tanaka M. Terai T. Nakata F. Furusawa H. Koshida S. Utsumi Y. Kawabata K. S. Motohara K. Ohsawa R. Morokuma T. Yasuda N. (Univ. of Tokyo) Kawai N. Tominaga, N. and Y. Asakura. Ligo/virgo g298048: Subaru hsc z-band photometry confirms the fading nature of sss17a. GCN Circ, 21595, 2017. 2.3.2

[284] J. Kim Lim G. H. M. Lee S.-L. Kim M. Im, C. Choi and et al C.-U. Lee. Ligo/virgo g298048: Continued monitoring of the optical counterpart candidate. GCN Circ, 21632, 2017. 2.3.2

[285] S. Covino M. G. Bernardini M. Branchesi S. Campana V. D'Elia M. Della Valle Y. Z. Fan G. Ghirlanda G. Ghisellini L. Nava E. Palazzi A. Pescalli T. Piran S. Piranomonte O. S. Salafia R. Salvaterra G. Stratta G. Tagliaferri E. Troja-S. D. Vergani P. D'Avanzo, A. Melandri and Z. P. Zhin. Ligo/virgo g298048: Eso/vlt optical observations. GCN Circ, 21653, 2017. 2.3.2

[286] E. Berger P. K. G. Williams S. Allam J. Annis J. Garcia Bellido D. J. Brout D. Brown R. E. Butler H.-Y. Chen (Harvard) R. Chornock (Ohio University) E. Cook (TAMU) H. T. Diehl (Fermilab) A. Drlica-Wagner (Fermilab) Z. Doctor (U. Chicago) M. R. Drout (Carnegie) B. Farr (U Chicago) R. J. Foley (UCSC) W. Fong (Northwestern) D. Fox (Penn State)-J. Frieman (Fermilab/UChicago) M.S.S. Gill (Stanford) R. Gruendl (NCSA) K. Herner (Fermilab) D. Holz (UChicago) R. Kessler (UChicago) H. Lin (Fermilab) J. Marriner (Fermilab) R. Margutti (Northwestern) J. Marshall (TAMU) E. Neilsen (Fermilab) F. Paz-Chincon (NCSA) A. Rest (STScI) M. Sako (UPenn)-D. Scolnic (KICP) N. Smith (Arizona) M. Soares-Santos (BrandeisU) D. Tucker (Fermilab) V. A. Villar (Harvard) A. Walker (NOAO) B. Yanny (Fermilab) P. Lopes (UFRJ) F. Durret (IAP) M. Nicholl, P. S. Cowperthwaite and A. Loureno (UFRJ). Ligo/virgo g298048: Observed fading of optical counterpart sss17a. GCN Circ, 21580, 2017. 2.3.2

[287] R. Lau L. P. Singer and M. M. Kasliwal. Ligo/virgo g298048: Possible plateau in ks band revealed by continued gemini-south observations. GCN Circ, 21779, 2017. 2.3.2

[288] R. Chornock and et al E. Berger. Ligo/virgo g298048: Near-infrared fading from gemini-south. GCN Circ, 21684, 2017. 2.3.2

[289] J. Greiner P. Wiseman, T.-W. Chen and et al P. Schady. Ligo/virgo g298048: Grond photometry of candidate optical counterpart reveals brightening in the nir. GCN Circ, 21584, 2017. 2.3.2

[290] K. Bannister T. Murphy D. Kaplan D. Dobie, A. Hotan and C. Lynch. Ligo/virgo g298048: Askap observations of sss17a and ngc 4993 at 1.345 ghz. GCN Circ, 21639, 2017. 2.3.2

[291] B. J. Shappee, J. D. Simon, M. R. Drout, et al. Early spectra of the gravitational wave source GW170817: Evolution of a neutron star merger. Science, 358:1574–1578, December 2017. 2.3.2

[292] D. A. H. Buckley, I. Andreoni, S. Barway, et al. A comparison between SALT/SAAO observations and kilonova models for AT 2017gfo: the first electromagnetic counterpart of a gravitational wave transient - GW170817. Monthly Notices of the Royal Astronomical Society: Letters, 474:L71–L75, February 2018. 2.3.2, 2.3

[293] P. Vaisanen S. Potter (SAAO) E. Romero Colmenero (SAAO/SALT) S. Crawford (SAAO) D. Buckley (SAAO) J Cooke (Swinburne) Igor Andreoni M. Shara, T. Williams and Jirong Mao (YNAO) Tyler Pritchard (Swinburne). Ligo/virgo g298048: Salt optical spectra of the candidate optical/nir counterpart of the gravitational wave g298048 in ngc4993. GCN Circ, 21610, 2017. 2.3.2

[294] C. McCully, D. Hiramatsu, D. A. Howell, et al. The Rapid Reddening and Featureless Optical Spectra of the Optical Counterpart of GW170817, AT 2017gfo, during the First Four Days. The Astrophysical Journal Letter, 848:L32, October 2017. 2.3.2, 2.3

[295] K. Maguire M. T. Botticella M. Fraser C. Inserra E. Kankare S. J. Smartt K. W. Smith M. Sullivan S. Valenti O. Yaron-I. Manulis D. Young T.-W. Chen S. Campana S. Benetti L. Tomasella G. Leloudas J. Lyman, D. Homan and Z. Cano. Ligo/virgo g298048: epessto optical spectra of the candidate optical/nir counterpart of the gravitational wave g298048 in ngc4993. GCN Circ, 21582, 2017. 2.3.2

[296] S. Piranomonte M. Branchesi S. Campana E. Cappellaro S. Covino P. D'Avanzo A. Grado G. Greco A. Melandri E. Palazzi G. Stratta L . Tomasella L. Amati L. A. Antonelli S. Ascenzi S. Benetti M.T. Botticella D. Fugazza F. Getman L. Limatola M. Lisi L. Nicastro L. Pulone A. Rossi P. Schipani G. Tagliaferri V. Testa S. Yang L. Sbordone E. Pian, V. D'Elia and E. Brocato. Ligo/virgo g298048: Grawita vlt/x-shooter observations. GCN Circ, 21592, 2017. 2.3.2

[297] P. Cowperthwaite E. Berger J. Elias S. Heathcote J. Annis D. Tucker M. Soares-Santos R. Kessler M. Nicholl, C. Briceno and M Sako. Ligo/virgo g298048: Possible features in the spectrum of gw counterpart sss17a. GCN Circ, 21585, 2017. 2.3.2

[298] M. R. Drout, A. L. Piro, B. J. Shappee, et al. Light curves of the neutron star merger GW170817/SSS17a: Implications for r-process nucleosynthesis. Science, 358:1570–1574, December 2017. 2.3.2, 5.1, 5.1

[299] E. Elmer I. Andreoni, J. Cooke C. Lidman and T. Farrell. Ligo/virgo g298048: Aat/aao spectroscopic observations of the gw counterpart candidate sss17a/dlt17ck. GCN Circ, 21677, 2017. 2.3.2

[300] S. J. Smartt, T.-W. Chen, A. Jerkstrand, et al. A kilonova as the electromagnetic counterpart to a gravitational-wave source. Nature, 551:75–79, November 2017. 2.3.2, 2.3, 5.1, 5.1

[301] M. Nicholl, E. Berger, D. Kasen, et al. The Electromagnetic Counterpart of the Binary Neutron Star Merger LIGO/Virgo GW170817. III. Optical and UV Spectra of a Blue Kilonova from Fast Polar Ejecta. The Astrophysical Journal Letters, 848:L18, October 2017. 2.3.2, 2.3

[302] E. Pian, P. D'Avanzo, S. Benetti, et al. Spectroscopic identification of r-process nucleosynthesis in a double neutron-star merger. Nature, 551:67–70, November 2017. 2.3.2, 5.1, 5.1

[303] A. J. Levan, J. D. Lyman, N. R. Tanvir, et al. The Environment of the Binary Neutron Star Merger GW170817. The Astrophysical Journal Letters, 848:L28, October 2017. 2.3.2

[304] N.R. Tanvir O. Fox J. Hjorth S. B. Cenko A. S. Fruchter R. Ryan-Z. Cano A. deugarte Postigo P. Evans J. Greiner N. Kawai H. Khandrika A. Lien J. Lyman I. Mandel P. O'Brien J. Osborne E. Palazzi D. Perley E. Pian L. Piro T. Sakamoto S. Schulze S. Rosswog D. Steeghs P. Sutton A.J. Levan, E. Troja and D. Watson. Ligo/virgo g298048: Hubble space telescope observations. GCN Circ, 21781, 2017. 2.3.2

[305] E. Troja, L. Piro, H. van Eerten, et al. The X-ray counterpart to the gravitational-wave event GW170817. Nature, 551:71–74, November 2017. 2.3.2, 2.3.3, 5.1, 5.1

[306] B. D. Metzger. Kilonovae. Living Reviews in Relativity, 20:3, May 2017. 2.3.2

[307] D. Grossman, O. Korobkin, S. Rosswog, and T. Piran. The long-term evolution of neutron star merger remnants - II. Radioactively powered transients. Monthly Notices of the Royal Astronomical Society, 439:757–770, March 2014. 2.3.2

[308] B. D. Metzger and R. Fernández. Red or blue? A potential kilonova imprint of the delay until black hole formation following a neutron star merger. Monthly Notices of the Royal Astronomical Society, 441:3444–3453, July 2014. 2.3.2

[309] J. Barnes, D. Kasen, M.-R. Wu, and G. Martínez-Pinedo. Radioactivity and Thermalization in the Ejecta of Compact Object Mergers and Their Impact on Kilonova Light Curves. The Astrophysical Journal, 829:110, October 2016. 2.3.2

[310] M. Tanaka. Kilonova/Macronova Emission from Compact Binary Mergers. Advances in Astronomy, 2016:634197, 2016. 2.3.2

[311] D. Kasen, B. Metzger, J. Barnes, E. Quataert, and E. Ramirez-Ruiz. Origin of the heavy elements in binary neutron-star mergers from a gravitational-wave event. Nature, 551:80–84, November 2017. 2.3.2, 5.1

[312] C. D. Kilpatrick, R. J. Foley, D. Kasen, et al. Electromagnetic evidence that SSS17a is the result of a binary neutron star merger. Science, 358:1583–1587, December 2017. 2.3.2

[313] E. Nakar and T. Piran. Detectable radio flares following gravitational waves from mergers of binary neutron stars. Nature, 478:82–84, October 2011. 2.3.3

[314] T. Piran, E. Nakar, and S. Rosswog. The electromagnetic signals of compact binary mergers. Monthly Notices of the Royal Astronomical Society, 430:2121–2136, April 2013. 2.3.3

[315] K. Hotokezaka and T. Piran. Mass ejection from neutron star mergers: different components and expected radio signals. Monthly Notices of the Royal Astronomical Society, 450:1430–1440, June 2015. 2.3.3

[316] K. Hotokezaka, S. Nissanke, G. Hallinan, et al. Radio Counterparts of Compact Binary Mergers Detectable in Gravitational Waves: A Simulation for an Optimized Survey. The Astrophysical Journal, 831:190, November 2016. 2.3.3

[317] O. Gottlieb, E. Nakar, and T. Piran. The cocoon emission - an electromagnetic counterpart to gravitational waves from neutron star mergers. Monthly Notices of the Royal Astronomical Society, 473:576–584, January 2018. 2.3.3

[318] H. van Eerten, W. Zhang, and A. MacFadyen. Off-axis Gamma-ray Burst Afterglow Modeling Based on a Two-dimensional Axisymmetric Hydrodynamics Simulation. The Astrophysical Journal, 722:235–247, October 2010. 2.3.3

[319] A. Levan, P. Crowther, R. de Grijs, et al. Gamma-Ray Burst Progenitors. Space Science Reviews, 202:33–78, December 2016. 2.3.3

[320] T. Sakamoto S. B. Cenko E. Troja, L. Piro and A. Lien. Ligo/virgo g298048: Discovery of x-ray emission from sss17a in ngc4993. GCN Circ, 21765, 2017. 2.3.3

[321] E. Berger R. Chornock P. Cowperthwaite K. D. Alexander R. Margutti, W. Fong. Ligo/virgo g298048: Chandra x-ray observations. GCN Circ, 21648, 2017. 2.3.3

[322] M. Serino H. Negoro S. Ueno H. Tomida M. Ishikawa Y. Sugawara N.Isobe R. Shimomukai (JAXA) T. Mihara M. Sugizaki S. Nakahira W. Iwakiri M. Shidatsu M. Matsuoka (RIKEN) T. Yoshii Y. Tachibana S. Harita Y. Muraki K. Morita (Tokyo Tech) A. Yoshida T. Sakamoto Y. Kawakubo Y. Kitaoka T. Hashimoto (AGU) H. Tsunemi T. Yoneyama (Osaka U.) M. Nakajima T. Kawase A. Sakamaki (Nihon U.) Y. Ueda T. Hori A. Tanimoto S. Oda (Kyoto U.) Y. Tsuboi Y. Nakamura R. Sasaki (Chuo U.) M. Yamauchi C. Hanyu K Hidaka (Miyazaki U.) T. Kawamuro S. Sugita, N. Kawai and K. Yamaoka. Ligo/virgo g298048, fermi gbm trigger 524666471/170817.529: Maxi/gsc observations. GCN Circ, 21555, 2017. 2.3.3

[323] S. Sugita, N. Kawai, S. Nakahira, et al. MAXI upper limits of the electromagnetic counterpart of GW170817. Publications of the Astronomical Society of Japan, July 2018. 2.3.3

[324] F. Verrecchia, M. Tavani, I. Donnarumma, et al. AGILE Observations of the Gravitational-wave Source GW170817: Constraining Gamma-Ray Emission from an NS-NS Coalescence. The Astrophysical Journal Letter, 850:L27, December 2017. 2.3.3

[325] S. B. Cenko B. Sbarufatti S. Campana E. Troja S.D. Barthelmy A.P. Beardmore A. A. Breeveld D. N. Burrows G. Cusumano A. D'Ai P. D'Avanzo V.D'Elia S.W.K. Emery P. Giommi C. Gronwall H.A. Krimm N.P.M. Kuin A.Y. Lien F.E. Marshall (NASA/GSFC) A. Melandri (INAF-OAB) J.A. Nousek (PSU) S.R. Oates (U. Warwick) P.T. O'Brien (U. Leicester) J.P. Osborne (U. Leicester) C. Pagani (U. Leicester) K.L. Page (U.Leicester) D.M. Palmer (LANL) M. Perri (ASDC) J.L. Racusin (NASA/GSFC) M.H. Siegel (PSU) G. Tagliaferri (INAF-OAB) P. A. Evans, J. A. Kennea and A. Tohuvavohu. Ligo/virgo g298048: Possible x-ray detection with swift. GCN Circ, 21612, 2017. 2.3.3

[326] G. Hallinan K. P. Mooley and A. Corsi. Ligo/virgo g298048: Radio detection of sss17a at 3ghz with the vla/jagwar. GCN Circ, 21814, 2017. 2.3.3

[327] S. Martin F. E. Bauer M. Bremer S. Campana Z. Cano J. Corral-Santana P. D'Avanzo (INAF Brera) C. De Breuck (ESO) I. de Gregorio-Monsalvo (JAO) M. de Pasquale (Istanbul University) J. P. U. Fynbo (Dark Cosmology Centre) D. Garcia-Appadoo (JAO) D. Hartman (U. Clemson) J. Hjorth (Dark Cosmology Centre) P. Jakobsson (U. Iceland) D. A. Kann (IAA Granada) T. Kruehler (MPE Garching) R. Lekshmi (ARIES) A. J. Levan (U Warwick) A. Lundgren (JAO) D. Malesani (Dark Cosmology Centre) M. Michalowski (Adam Mickiewicz University) B. Milvang-Jensen (Dark Cosmology Centre) K. Misra (ARIES) S. R. Oates (U. Warwick) R. Sanchez-Ramirez (IAA Granada) M. Sparre (Heidelberg Institute for Theoretical Studies) R. L. C. Starling (U. Leicester) N. R. Tanvir (U. Leicester) C. C. Thoene (IAA Granada) S. Schulze, S. Kim and D. J. Watson. Ligo/virgo g298048: Alma observations. GCN Circ, 21747, 2017. 2.3.3

[328] S. Kim, S. Schulze, L. Resmi, et al. ALMA and GMRT Constraints on the Off-axis Gamma-Ray Burst 170817A from the Binary Neutron Star Merger GW170817. The Astrophysical Physical Journal Letters, 850:L21, December 2017. 2.3.3

[329] K. D. Alexander P. K. G. Williams and E. Berger. Ligo/virgo g298048: Alma upper limits on 98 ghz emission from sss17a. GCN Circ, 21750, 2017. 2.3.3

[330] K. W. Bannister, R. M. Shannon, J.-P. Macquart, et al. The Detection of an Extremely Bright Fast Radio Burst in a Phased Array Feed Survey. The Astrophysical Physical Journal Letters, 841:L12, May 2017. 2.3.3

[331] et al S. Goedhart, K. Mooley. Ligo/virgo g298048: Further meerkat observations of sss17a. GCN Circ, 21933, 2017. 2.3.3

[332] et al M. Bailes, I. Andreoni. Ligo/virgo g298048: Limits from an frb search of sss17a with the parkes 64m radio telescope. GCN Circ, 21899, 2017. 2.3.3

[333] I. Prandoni, M. Murgia, A. Tarchi, et al. The Sardinia Radio Telescope . From a technological project to a radio observatory. Astronomy & Astrophysics, 608:A40, December 2017. 2.3.3

[334] R. Beswick J. Moldon and Z. Paragi. Ligo/virgo g298048: Record of all e-merlin results to date on sss17a. GCN Circ, 21940, 2017. 2.3.3

[335] Tao An Philippe Bacon Rob Beswick Carolina Casadio Eric Chassande-Mottin Sandor Frey-Marcello Giroletti Peter Jonker Mark Kettenis Benito Marcote Arpad Szomoru Huib van Langevelde Zsolt Paragi, Ivan Agudo and Jun Yang. Ligo/virgo g298048: European vlbi network (evn) upper limit on 5 ghz compact emission from sss17a. GCN Circ, 21763, 2017. 2.3.3

[336] Tao An Philippe Bacon Rob Beswick Carolina Casadio Eric Chassande-Mottin Sandor Frey-Marcello Giroletti Peter Jonker Mark Kettenis Benito Marcote Javier Moldon Huib van Langevelde Arpad Szomoru Zsolt Paragi, Ivan Agudo and Jun Yang. Ligo/virgo g298048: Further european vlbi network (evn) observations of sss17a. GCN Circ, 21939, 2017. 2.3.3

[337] I. Andreoni K. Bannister J. Cooke D. Dobie D. Kaplan-C. Lynch A. Deller, M. Bailes and T. Murphy. Ligo/virgo g298048: Vlba observations of the possible counterpart sss17a in ngc 4993. GCN Circ, 21588, 2017. 2.3.3

[338] I. Andreoni K. Bannister J. Cooke D. Dobie D. Kaplan-C. Lynch A. Deller, M. Bailes and T. Murphy. Ligo/virgo g298048: Vlba upper limits at 8.7ghz for the gw counterpart sss17a/dlt17ck on august 20-21 ut. GCN Circ, 21850, 2017. 2.3.3

[339] K. S. Hirata, T. Kajita, M. Koshiba, et al. Observation in the Kamiokande-II detector of the neutrino burst from supernova SN1987A. Physical Review D, 38:448–458, July 1988. 2.3.4

[340] S. Ando, B. Baret, I. Bartos, et al. Colloquium: Multimessenger astronomy with gravitational waves and high-energy neutrinos. Reviews of Modern Physics, 85:1401–1420, October 2013. 2.3.4

[341] K. Ioka, S. Razzaque, S. Kobayashi, and P. Mészáros. TeV-PeV Neutrinos from Giant Flares of Magnetars and the Case of SGR 1806-20. The Astrophysical Journal, 633:1013–1017, November 2005. 2.3.4

[342] T. Pradier. Coincidences between gravitational wave interferometers and high energy neutrino telescopes. Nuclear Instruments and Methods in Physics Research A, 602:268–274, April 2009. 2.3.4

[343] M. Vietri. Ultrahigh Energy Neutrinos from Gamma Ray Bursts. Physical Review Letters, 80:3690–3693, April 1998. 2.3.4

[344] E. Waxman. High Energy Cosmic-Rays and Neutrinos from Cosmological Gamma-Ray Burst Fireballs. Physica Scripta Volume T, 85:117, 2000. 2.3.4

[345] J. S. Bloom, D. A. Perley, H.-W. Chen, et al. A Putative Early-Type Host Galaxy for GRB 060502B: Implications for the Progenitors of Short-Duration Hard-Spectrum Bursts. The Astrophysical Journal, 654:878–884, January 2007. 2.3.4

[346] Z. B. Etienne, Y. T. Liu, S. L. Shapiro, and T. W. Baumgarte. General relativistic simulations of black-hole-neutron-star mergers: Effects of black-hole spin. Physical Review D, 79(4):044024, February 2009. 2.3.4

[347] W. H. Lee and E. Ramirez-Ruiz. The progenitors of short gamma-ray bursts. New Journal of Physics, 9:17, January 2007. 2.3.4

[348] T. Karg, J. Alvarez-Muñiz, D. Kuempel, et al. Report from the Multi-Messenger Working Group at UHECR-2014 Conference. In Proceedings of International Symposium for Ultra-High Energy Cosmic Rays (UHECR2014), id.010021, ¡NUMPAGES¿13¡/NUMPAGES¿ pp., page 010021, 2016. 2.3.4

[349] E. Waxman and J. Bahcall. High Energy Neutrinos from Cosmological Gamma-Ray Burst Fireballs. Physical Review Letters, 78:2292–2295, March 1997. 2.3.4

[350] M. Ruffert, H.-T. Janka, K. Takahashi, and G. Schaefer. Coalescing neutron stars - a step towards physical models. II. Neutrino emission, neutron tori, and gamma-ray bursts. Astronomy and Astrophysics, 319:122–153, March 1997. 2.3.4

[351] Y. Sekiguchi, K. Kiuchi, K. Kyutoku, and M. Shibata. Gravitational Waves and Neutrino Emission from the Merger of Binary Neutron Stars. Physical Review Letters, 107(5):051102, July 2011. 2.3.4

[352] M. Ruffert and H.-T. Janka. Coalescing neutron stars - A step towards physical models. III. Improved numerics and different neutron star masses and spins. Astronomy and Astrophysics, 380:544–577, December 2001. 2.3.4

[353] M. Ruffert, H.-T. Janka, and G. Schaefer. Coalescing neutron stars - a step towards physical models. I. Hydrodynamic evolution and gravitational-wave emission. Astronomy and Astrophysics, 311:532–566, July 1996. 2.3.4

[354] L. Dessart, C. D. Ott, A. Burrows, S. Rosswog, and E. Livne. Neutrino Signatures and the Neutrino-Driven Wind in Binary Neutron Star Mergers. The Astrophysical Journal, 690:1681–1705, January 2009. 2.3.4

[355] S. Setiawan, M. Ruffert, and H.-T. Janka. Three-dimensional simulations of non-stationary accretion by remnant black holes of compact object mergers. Astronomy and Astrophysics, 458:553–567, November 2006. 2.3.4

[356] M. G. Aartsen, M. Ackermann, J. Adams, et al. The IceCube Neutrino Observatory: instrumentation and online systems. Journal of Instrumentation, 12:P03012, March 2017. 2.3.4

[357] M. Ageron, J. A. Aguilar, I. Al Samarai, et al. ANTARES: The first undersea neutrino telescope. Nuclear Instruments and Methods in Physics Research A, 656:11–38, November 2011. 2.3.4

[358] The Pierre Auger Collaboration. The Pierre Auger Cosmic Ray Observatory. ArXiv e-prints, February 2015. 2.3.4

[359] C. Finley E. Blaufuss R. Corley Z. Marka I. Bartos, S. Countryman and S. Marka. Ligo/virgo g298048: Found coincident icecube neutrino observation. GCN Circ, 21508, 2017. 2.3.4

[360] C. Finley E. Blaufuss R. Corley Z. Marka I. Bartos, S. Countryman and S. Marka. Ligo/virgo g298048: Update on icecube neutrino candidates — no coincidence with newest gw skymap. GCN Circ, 21568, 2017. 2.3.4

[361] A. Coleiro D. Dornic A. Kouchner T. Pradier M. Ageron, B. Baret. Ligo/virgo g298048 antares search. GCN Circ, 21522, 2017. 2.3.4

[362] A. Coleiro D. Dornic A. Kouchner T. Pradier M. Ageron, B. Baret. Ligo/virgo g298048 antares search (2). GCN Circ, 21631, 2017. 2.3.4

[363] E. Zas K. H. Kampert J. Alvarez-Muniz, F. Pedreira and M. Schimp. Ligo/virgo g298048: Pierre auger observatory neutrino follow-up. GCN Circ, 21686, 2017. 2.3.4

[364] A. Albert, M. André, M. Anghinolfi, et al. Search for High-energy Neutrinos from Binary Neutron Star Merger GW170817 with ANTARES, IceCube, and the Pierre Auger Observatory. The Astrophysical Journal Letters, 850:L35, December 2017. 2.3.4

[365] Florent Robinet. Omicron: an algorithm to detect and characterize transient events in gravitational-wave detectors. https://tds.ego-gw.it/?content=3&r=14693. Accessed: 2018-10-31. 2.4

[366] J. Annis, M. Soares-Santos, E. Berger, et al. A Dark Energy Camera Search for Missing Supergiants in the LMC after the Advanced LIGO Gravitational-wave Event GW150914. The Astrophysical Journal Letters, 823:L34, June 2016. 2.4

[367] V. Savchenko, C. Ferrigno, S. Mereghetti, et al. INTEGRAL Upper Limits on Gamma-Ray Emission Associated with the Gravitational Wave Event GW150914. The Astrophysical Journal Letters, 820:L36, April 2016. 2.4

[368] Imre Bartos, Tracy Huard, and Szabolcs Marka. James webb space telescope can detect kilonovae in gravitational wave follow-up. in prep., 2015. 3

[369] S. Kulkarni and M. M. Kasliwal. Transients in the local universe. In N. Kawai, T. Mihara, M. Kohama, and M. Suzuki, editors, Astrophysics with All-Sky X-Ray Observations, page 312, mar 2009. 3

[370] Darren J White, EJ Daw, and VS Dhillon. A list of galaxies for gravitational wave searches. Classical and Quantum Gravity, 28(8):085016, 2011. 3

[371] Laura K Nuttall and Patrick J Sutton. Identifying the host galaxy of gravitational wave signals. Physical Review D, 82(10):102002, 2010. 3

[372] XiLong Fan, Christopher Messenger, and Ik Siong Heng. A BAYESIAN APPROACH TO MULTI-MESSENGER ASTRONOMY: IDENTIFICATION OF GRAVITATIONAL-WAVE HOST GALAXIES. The Astrophysical Journal, 795(1):43, October 2014. 3, 3.1.1

[373] Imre Bartos, Arlin P S Crotts, and S. Márka. GALAXY SURVEY ON THE FLY: PROSPECTS OF RAPID GALAXY CATALOGING TO AID THE ELECTROMAGNETIC FOLLOW-UP OF GRAVITATIONAL WAVE OBSERVATIONS. The Astrophysical Journal, 801(1):L1, February 2015. 3

[374] Neil Gehrels, John K. Cannizzo, Jonah Kanner, et al. Galaxy Strategy for LIGO-Virgo Gravitational Wave Counterpart Searches. The Astrophysical Journal, (Lvc):1–8, 2015. 3

[375] Leo P Singer, H-Y Chen, DANIEL E Holz, et al. Going the distance: Mapping host galaxies of ligo sources in three dimensions using local cosmography and targeted follow-up. arXiv preprint arXiv:1603.07333, 2016. 3, 3.6

[376] Satoshi Miyazaki, Yutaka Komiyama, Hidehiko Nakaya, et al. Hyper suprime-cam. In SPIE Astronomical Telescopes+ Instrumentation, pages 84460Z–84460Z. International Society for Optics and Photonics, 2012. 3

[377] JP Bernstein, R Kessler, S Kuhlmann, et al. Supernova simulations and strategies for the dark energy survey. The Astrophysical Journal, (2):152, 2012. 3

[378] Nicholas Kaiser, Herve Aussel, Barry E. Burke, et al. Pan-starrs: A large synoptic survey telescope array. volume 4836, pages 154–164, 2002. 3

[379] Nicholas M Law, Shrinivas R Kulkarni, Richard G Dekany, et al. The palomar transient factory: system overview, performance, and first results. Publications of the Astronomical Society of the Pacific, 121(886):1395, 2009. 3

[380] Shaon Ghosh, Steven Bloemen, Gijs Nelemans, Paul J Groot, and Larry R Price. Tiling strategies for optical follow-up of gravitational wave triggers by wide field of view telescopes. arXiv preprint arXiv:1511.02673, 2015. 3

[381] Javed Rana, Akshat Singhal, Bhooshan Gadre, Varun Bhalerao, and Sukanta Bose. An enhanced method for scheduling observations of large sky error regions for finding optical counterparts to transients. The Astrophysical Journal, 838(2):108, 2017. 3, 3.1, 3.6

[382] S. Nissanke, J. Sievers, N. Dalal, and D. Holz. Localizing Compact Binary Inspirals on the Sky Using Ground-based Gravitational Wave Interferometers. The Astrophysical Journal, 739:99, October 2011. 3

[383] C. L. Rodriguez, B. Farr, V. Raymond, et al. Basic Parameter Estimation of Binary Neutron Star Systems by the Advanced LIGO/Virgo Network. The Astrophysical Journal, 784:119, April 2014. 3

[384] The sloan digital sky survey. https://www.sdss.org/. Accessed: 2018-10-30. 3.1

[385] Leo Singer, Larry Price, and Antony Speranza. Optimizing optical follow-up of gravitational-wave candidates. arXiv preprint arXiv:1204.4510, 2012. 3.1

[386] Leo P Singer, Hsin-Yu Chen, Daniel E Holz, et al. Supplement:going the distance: Mapping host galaxies of ligo and virgo sources in three dimensions using local cosmography and targeted follow-up(2016, apjl, 829, l15). The Astrophysical Journal Supplement Series, 226(1):10, 2016. 4, 3.1.1

[387] H.-Y. Chen and D. E. Holz. Facilitating follow-up of LIGO-Virgo events using rapid sky localization. The Astrophysical Journal, August 2015. 3.2, 4

[388] LSST Science Collaboration, P. A. Abell, J. Allison, et al. LSST Science Book, Version 2.0. ArXiv e-prints, December 2009. 3.3, 5, 5.2

[389] Weimin Yuan, Chen Zhang, H Feng, et al. Einstein probe-a small mission to monitor and explore the dynamic x-ray universe. arXiv preprint arXiv:1506.07735, 2015. 3.4

[390] JRP Angel. Lobster eyes as x-ray telescopes. In Space Optics Imaging X-Ray Optics Workshop, volume 184, pages 84–86. International Society for Optics and Photonics, 1979. 3.4

[391] B. Zhang. Early X-Ray and Optical Afterglow of Gravitational Wave Bursts from Mergers of Binary Neutron Stars. The Astrophysical Journal Letters, 763:L22, January 2013. 3.4, 3.4

[392] Michael Coughlin and Christopher Stubbs. Maximizing the probability of detecting an electromagnetic counterpart of gravitational-wave events. Experimental Astronomy, 42(2):165–178, 2016. 3.5

[393] P. S. Cowperthwaite and E. Berger. A Comprehensive Study of Detectability and Contamination in Deep Rapid Optical Searches for Gravitational Wave Counterparts. The Astrophysical Journal, 814:25, November 2015. 3.6

[394] K. Cannon, R. Cariou, A. Chapman, et al. Toward Early-warning Detection of Gravitational Waves from Compact Binary Coalescence. The Astrophysical Journal, 748:136, April 2012. 4

[395] J. Mills, V. Tiwari, and S. Fairhurst. Localization of binary mergers with gravitational-wave detectors of second and third generation. ArXiv e-prints, August 2017. 4

[396] Wen Zhao and Linqing Wen. Localization accuracy of compact binary coalescences detected by the third-generation gravitational-wave detectors and implication for cosmology. arXiv preprint arXiv:1710.05325, 2017. 4, 4.3.2

[397] R. Voss and T. M. Tauris. Galactic distribution of merging neutron stars and black holes - prospects for short gamma-ray burst progenitors and LIGO/VIRGO. Monthly Notices of the Royal Astronomical Society, 342:1169–1184, July 2003. 4

[398] M. Dominik, K. Belczynski, C. Fryer, et al. Double Compact Objects. I. The Significance of the Common Envelope on Merger Rates. The Astrophysical Journal, 759:52, November 2012. 4

[399] S. Vitale, W. Del Pozzo, T. G. F. Li, et al. Effect of calibration errors on Bayesian parameter estimation for gravitational wave signals from inspiral binary systems in the advanced detectors era. Physical Review D, 85(6):064034, March 2012. 4.3.3

[400] L. Lindblom. Optimal calibration accuracy for gravitational-wave detectors. Physical Review D, 80(4):042005, August 2009. 4.3.3

[401] L. Lindblom, J. G. Baker, and B. J. Owen. Improved time-domain accuracy standards for model gravitational waveforms. Physical Review D, 82(8):084020, October 2010. 4.3.3

[402] H.-Y. Chen and D. E. Holz. Finding the One: Identifying the Host Galaxies of Gravitational-Wave Sources. ArXiv e-prints, December 2016. 4.4

[403] Z. Ivezic, J. A. Tyson, B. Abel, et al. LSST: from Science Drivers to Reference Design and Anticipated Data Products. ArXiv e-prints, May 2008. 5, 5.2, 5.2, 5.1

[404] LSST Science Collaboration, P. Marshall, T. Anguita, et al. Science-Driven Optimization of the LSST Observing Strategy. ArXiv e-prints, August 2017. 5, 5.2

[405] I. Arcavi. The First Hours of the GW170817 Kilonova and the Importance of Early Optical and Ultraviolet Observations for Constraining Emission Models. The Astrophysical Journal Letters, 855:L23, March 2018. 5.1

[406] I. Andreoni, K. Ackley, J. Cooke, et al. Follow Up of GW170817 and Its Electromagnetic Counterpart by Australian-Led Observing Programmes. Publications of the Astronomical Society of Australia, 34:e069, December 2017. 5.1, 5.1

[407] V. A. Villar, J. Guillochon, E. Berger, et al. The Combined Ultraviolet, Optical, and Near-infrared Light Curves of the Kilonova Associated with the Binary Neutron Star Merger GW170817: Unified Data Set, Analytic Models, and Physical Implications. The Astrophysical Journal Letters, 851:L21, December 2017. 5.1, 5.1

[408] M. C. Díaz, L. M. Macri, D. Garcia Lambas, et al. Observations of the First Electromagnetic Counterpart to a Gravitational-wave Source by the TOROS Collaboration. The Astrophysical Journal Letters, 848:L29, October 2017. 5.1, 5.1

[409] L. Hu, X. Wu, I. Andreoni, et al. Optical observations of LIGO source GW 170817 by the Antarctic Survey Telescopes at Dome A, Antarctica. Science Bulletin, Vol. 62, No.21, p.1433-1438, 2017, 62:1433–1438, October 2017. 5.1, 5.1

[410] A. S. Pozanenko, M. V. Barkov, P. Y. Minaev, et al. GRB 170817A Associated with GW170817: Multi-frequency Observations and Modeling of Prompt Gamma-Ray Emission. The Astrophysical Journal Letters, 852:L30, January 2018. 5.1, 5.1

[411] Y. Utsumi, M. Tanaka, N. Tominaga, et al. J-GEM observations of an electromagnetic counterpart to the neutron star merger GW170817. Publications of the Astronomical Society of Japan, 69:101, December 2017. 5.1, 5.1

[412] A. Perego, D. Radice, and S. Bernuzzi. AT 2017gfo: An Anisotropic and Three-component Kilonova Counterpart of GW170817. The Astrophysical Journal Letters, 850:L37, December 2017. 5.1